# Applied synthesis and characterisation of nanoparticles

**This thesis is submitted in partial fulfilment of the**
**requirements for the degree of Doctor of Philosophy (Chemistry).**

Joseph C. Bear

**2014**

I, Joseph Bear confirm that the work presented in this thesis is my own. Where information has been derived from other sources, I confirm that this has been indicated in the thesis.

Signed:

# Abstract

This thesis covers three areas of development of nanomaterials synthesis; namely the synthesis of superhydrophobic polymer-nanoparticle composites (chapter 3), the synthesis of doped quantum dots for catalysis and photoluminescence enhancement (chapter 4) and the synthesis of magnetic iron oxide nanoparticles from inexpensive, readily available reagents (chapter 5). Details of characterisation and analytical techniques and synthetic methods used are given in chapter 2, and the thesis summarised in chapter 6.

Superhydrophobic polymer-nanoparticle composites represent a class of material which combine the superhydrophobicity of the polymer with the functionality of incorporated nanoparticles. Reactive oxygen species generated by photocatalytic nanoparticles degrade organic matter, and thus degrade the polymer, resulting in a loss of superhydrophobicity. In this chapter, a general method for the incorporation of hydrophobically ligated nanoparticles into a superhydrophobic poly(dimethylsiloxane) polymer matrix *via* AACVD is demonstrated. This resulted in a highly effective, robust titania nanoparticle-poly(dimethylsiloxane) composite for photocatalysis, along with, to the best of the author's knowledge, the first superparamagnetic-superhydrophobic polymer composite.

Chapter 4 deals with the synthesis and characterisation of a quantum dot based photoactivated catalyst vector which releases $Cu^+$ *via* UV irradiation, the first of its kind. The catalytic activity was evaluated using “click” chemistry under UV irradiation, with quantum dots being recoverable and able to undergo several catalytic cycles. A mechanism for the photoluminescence and copper release is also postulated. The copper is incorporated into the shells of quantum dots *via* the decomposition of single source metal-dithiocarbamates.

Chapter 5 details a method for the synthesis of iron oxide nanoparticles for magnetic hyperthermia, but from reagents obtained from the high street. A low cost synthesis was developed and the resulting nanoparticles functionalised with an amphiphilic polymer and tested for magnetic hyperthermia.

# Acknowledgements

Firstly, I would like to thank my primary supervisor Professor Ivan Parkin, whose inspiration, patience and encouragement have been utterly invaluable. I also want to take this opportunity to thank my secondary and tertiary supervisors Professor Quentin Pankhurst and Professor Kerry Chester who have been there whenever I have required them with advice, support and requests for the odd bit of chemistry. Thanks to Dr. Graeme Hogarth for an excellent collaboration and advice.

One of the main reasons that my time spent at UCL has been enjoyable has been the amazing friendly atmosphere of UCL chemistry, particularly in the in the Parkin, Carmalt and Hogarth groups. My thanks go to you all in no particular order: Raul, Carlos, Sacha, Iman, Shishir, Anna, Clair, Allie, Will, Emma, Michael P, Michael W, Sandeep, Davinder, Penny, Ralph, Jared, Emily, Charlie, Veronica, Caroline, Nick, Matt, Joe, Pragna, Hazel, Anastasia, Cynthia, Andreas, Ben, Sanjay, Kris, Andy, Anu, Nadia, Leanne and Nuruzzaman.

I would also like to extend my thanks to my colleagues at the Royal Institution and UCL Cancer Institute for all their help and understanding of my fly-by-night visits, namely: Cristina, Paul, Daniel, Sam, George, Richard, Luke, Roxanne, Bettina, Maha, Alex, Liz, Jenny, Tiziana, Tom, Enrique and Maria.

I extend special thanks to Drs. Colin Crick and Nathan Hollingsworth for their excellent help, friendship, advice (career as well as personal!) and skill on completing some enjoyable science during my time at UCL- my heartfelt thanks to you both. Dr Ian Watts and Dr Steve Firth have been marvellous in terms of helping me with instrumentation, and the logging of the department's chemical weapon precursors. Also thanks to my colleagues at the University of Leeds, Queen Mary, University of London and Manchester Metropolitan university, Dr Mike Ward, Dr Russell Binions, Marc-Krystelle Mafina and Mark Frost, with whom I hope to continue working with in the future.

I have been lucky enough to work with some excellent people during the course of my Ph.D, to which I thank my supervisors from my first research forays from the University of East Anglia for their never-ending support, namely Professor Thomas Nann, Dr Andrew Mayes, Dr Greg Wildgoose, Ben Piggott and the late Dr Brian Hills, inspirations all.

Dr Paul McNaughter has been a fantastic friend over the last five years, on which we have shared many escapades and adventures, from crazy nights in the lab dancing to Duran Duran to driving to events we're terribly late for at 100 mph in the bat-mobile, wonderful memories.

My Church friends from St Marks', Battersea rise deserve a special mention for being bastions of faith throughout my PhD, with special mention to Dr. Peter and Corinne Marchand who helped me settle into Church life in London as well as at UCL- thank you. Special mention must also go to my long-suffering housemate of two years, Chris May, who is an all round excellent chap even though he decided to move to Slough after leaving me for his wife.

Rixy, Tudor, Steph and Rob- you guys are such fantastic friends and thank you for the laughs, games and visits to ridiculous, Bond villain-esque pirate islands!

Last but by no means least, I wish to thank my family for their unwavering support through seven years of university. So Mum, Dad, Alex, Nan, Grandad- thank you. My Aunt Nicola and John have been amazing in simultaneously putting me up and putting up with me for the final year of my PhD and deserve a special mention. Lastly, I thank my girlfriend Anna for her constant love and support.

# Table of Contents

## Table of Contents

# Index of figures

# Index of Tables

# List of abbreviations

| | |
|---|---|
| AC | Alternating Current |
| AACVD | Aerosol Assisted Chemical Vapour Deposition |
| ATR-FTIR | Attenuated Total Reflectance – Fourier Transform Infrared |
| CCD | Charge-Coupled Device |
| CHFS | Continuous Hydrothermal Flow Synthesis |
| CVD | Chemical Vapour Deposition |
| DLS | Dynamic Light Scattering |
| DLVO | Derjaguin, Landau, Verwey and Overbeek |
| DNA | Deoxyribonucleic Acid |
| EDS | Energy Dispersive X-Ray Spectroscopy |
| EELS | Electron Energy Loss Spectroscopy |
| EFTEM | Energy-filtered Transmission Electron Microscopy |
| ESCA | Electron Spectroscopy for Chemical Analysis |

| | |
|---|---|
| EXAFS | Extended X-Ray Absorption Fine Structure |
| FEG | Field Emission Gun |
| FRET | Förster Resonance Energy Transfer |
| FTIR | Fourier Transform Infrared |
| HFCVD | Hot Filament Chemical Vapour Deposition |
| HRTEM | High Resolution Transmission Electron Microscopy |
| ICP-AES | Inductively Coupled Plasma – Atomic Emission Spectroscopy |
| ILP | Intrinsic Loss Power |
| NMR | Nuclear Magnetic Resonance |
| PDMS | Poly(dimethylsiloxane) |
| PMMA | Poly(methyl methacrylate) |
| PTFE | Poly(tetrafluoroethylene) |
| QD - QW | Quantum Dot – Quantum Well |
| SAED | Selected Area Electron Diffraction |
| SAR | Specific Absorption Rate |

| | |
|---|---|
| SEM | Scanning Electron Microscopy |
| SILAR | Successive Ion Layer Absorption and Reaction |
| SPR | Surface Plasmon Resonance |
| SQUID | Superconducting Quantum Interference Device |
| TCSPC | Time-Correlated Single Photon Counting |
| TEM | Transmission Electron Microscopy |
| TEOS | Tetraethyl Orthosilicate |
| TGA | Thermogravimetric Analysis |
| UV/vis | Ultraviolet/visible |
| XANES | X-Ray Absorption Near Edge Structure |
| XAS | X-Ray Absorption Spectroscopy |
| XPS | X-Ray Photoelectron Spectroscopy |
| XRD | X-Ray Diffraction |

# Chapter 1: Introduction

## 1.1. Nanoparticulate science: An overview

Nanoparticles are materials in the 1-100 nm size range, which exhibit nanoscopic, size-dependent properties. These size dependent properties are many-fold, from superparamagnetism of $Fe_3O_4$ nanoparticles to bright, visible photoluminescence of CdSe quantum dots. Thus, the potential applications of nanoparticles are as diverse as the materials and methods from which they are synthesised. Particles can be classified by size as coarse (10,000-2,500 nm), fine (2,500-100 nm) and ultrafine (1-100 nm) nanoparticles. This thesis deals with the syntheses, functionalisation methods and application of various types of ultrafine nanoparticles.

Nanoparticulate materials have been utilised for thousands of years for properties such as fine lustres on jewellery or pottery. The most notable example being the Roman Lycurgus cup (currently in the British museum), has a purple lustre now known to be caused by the surface plasmon resonance (SPR) of incorporated gold and silver nanoparticles showing the Ancients' excellent empirical understanding of metallurgy.[1] Michael Faraday (1791-1867) was the first chemist to recognise that this lustre was caused by colloidal gold, published in 1857.[2] Richard Feynmann's after-dinner lecture of 1959 is seen as one of the catalysts which brought the vast potential of nanoscience to the wider scientific community, namely the potential for operation on the molecular and atomic scale.[3] Subsequent discoveries such as buckminsterfullerene and advances in electron microscopy such as the design of the scanning tunnelling microscope and nanolithography have accelerated interest and development in the field.

Since then, nanoscience and nanoparticulate science has advanced at an incredible pace, driven largely by consumer demand for smaller and more powerful electronic devices. Currently, the terms “nanoscience” and “nanotechnology” have come to encompass particulate science, nanostructured devices and atomic scale manipulation of matter.

Nanoscience has attracted a great deal of attention from scientists, but commercially successful applications have thus-far been limited. However, the unique properties offered by nanoparticles remain highly desirable for commercialisation, with a great deal of effort now focussed on the large-scale generation of high performance, cost-effective materials. Nanoparticles themselves are of great interest in the areas of medicine,[4–7] computing,[8,9] energy materials,[10–15] sensing and detection,[16–18] and catalysis.[19–22]

## 1.2. Colloidal nanoparticles

Colloidal stability is a very desirable property for a nanoparticle dispersion as this allows for solution phase chemistry to take place, and for nanoscopic properties to be conserved, as properties such as SPR are quenched in agglomerated particle dispersions. Colloidal stability is given to nanoparticles by ligands (section 1.3).

Many nanoscopic properties increase with decreasing nanoparticle diameter, often linearly down to around 20 nm, beyond which nanoparticle properties become increasingly similar to the molecular/atomic scale. Nanoparticles can be composed of many different materials, with the term nanocrystals encompassing crystalline examples. Proteins can be thought of as well defined nanoparticles, as they possess similar size dimensions and techniques for their quantification and analysis. Protein manipulation techniques such as gel electrophoresis and size exclusion chromatography are frequently used for colloidal inorganic nanoparticles.[23,24]

Nanoparticles syntheses are engineered to maximise the performance of the product. Nanoparticle monodispersity is desirable as all of the particles will respond in exactly the same way to an external stimulus and maximise performance. For example, the photoluminescence emission profile of polydisperse quantum dots will be much broader than that of a monodisperse sample, leading to poor photoluminescence quantum yields due to a range of emitted wavelengths.

## 1.3 Nanoparticle stabilisation

Nanoscopic properties of nanoparticles are maximised when nanoparticles are separate; *i.e.* they are not aggregated or agglomerated. Indeed, many nanoparticle based sensors have been based on nanoparticle agglomeration to alter a property such as SPR or photoluminescence in the presence of a desired analyte.[25,26]

In order to achieve this in a dispersion, nanoparticles require ligand stabilisation, as they tend to aggregate due to intrinsic attractive van der Waals forces. Ligands serve multiple functions, including: stabilising the high energy surfaces of nanoparticles, imparting dispersibility in different solvents, providing sites for chemical functionalisation and conjugation and preventing nanoparticle agglomeration. Generally speaking, there are two types of ligand; low-molecular weight, highly charged species or high molecular weight, sterically hindering molecules and polymers. Ligands which are small and highly charged such as 3-mercaptopropionic acid adhere closely to nanoparticles and impart charge to the nanoparticle surface. Nanoparticles will therefore repel one another due to electrostatic charge repulsion, the theory of which was laid down by Derjaguin, Landau, Verway and Overbeek (DLVO).[27,28]

Electrostatically stabilised nanoparticles have a surface charge which encourages coulombic repulsion between nanoparticles. Increasing the nanoparticle surface charge leads to greater the inter-particle electrostatic repulsion. Therefore nanoparticles with a high surface charge exhibit greater stability in colloidal dispersion. In an aqueous system, ions form a double layer around individual nanoparticles, with a layer of tightly bound ions with the opposite charge to the surface charge, followed by a larger, diffuse layer of ions. Coulombic repulsions occur between double layers of different nanoparticles, preventing aggregation. The zeta potential is a measurement of the electric double layer (between the nanoparticle surface and the edge of the diffuse layer (the slipping plane)) and is indicative of colloidal stability.[29] The formation of the double layer is dependent on the ionic strength of the solution; too low and a double layer of ions will be unable to form and too high the ionic strength of the solution will collapse the double layer, causing nanoparticle aggregation.

Ligands with greater steric bulk such as polymeric ligands or fatty acids prevent nanoparticle agglomeration by creating a physical barrier between nanoparticles, preventing inter-particle interactions. Sterically stabilised nanoparticles tend to be more resistant to changes in pH and ionic strength than ionically stabilised nanoparticles. It is noteworthy that ligands for inorganic nanoparticles tend to be organic,[30–33] although some inorganic examples have been recorded.[34]

## 1.4 Nanoparticle synthesis

The synthesis of nanoparticles can be divided into two categories: the bottom-up and the top-down approaches. The top-down method is seen as the physical approach, which involves breaking down bulk material into nanoparticles through techniques such as acid-etching,[35] ball-milling[36,37] and laser ablation.[38,39] Conversely, the bottom-up method relies on chemical nucleation to form nanoparticles from molecular precursors. Electrochemical methods,[40] sonolysis,[41,42] thermal decomposition[43–46] and co-precipitation[47–49] all fall into this category.

The advantages of a bottom-up approach are that the nucleation and crystal growth stages of nanoparticle formation can be carefully controlled, leading to reduced polydispersity in the final product, properties not easily controlled by top-down approaches.

Polydispersity is defined as the degree of which particle sizes differ with respect to each other, which is often detrimental to nanoparticle properties. So monodispersity is desired as the entire sample will behave in the same way, thus the effectiveness of the nanoparticle properties will be amplified.

All same size nuclei should be subjected to the same reaction conditions and monomer concentrations and therefore grow at the same rate. It is important for particle monodispersity to have a very brief single nucleation period (separate to crystal growth), as different size nuclei growing at the same rate will lead to a polydisperse product. Also, if same-size nuclei grew at different rates, a broadening of the particle size distribution occurs.

The mechanism for monodisperse particle nucleation and growth was laid down by Viktor K. LaMer in 1950 to describe the nucleation and growth of sulphur sols,[50,51] and is still used as the standard model today, although different to transition metal nanoparticle syntheses.[52]

The LaMer model involves three broad stages, all of which should be separate if monodisperse particles are to be synthesised. The first stage is the increase of nanoparticle monomer (precursor) concentration to supersaturation (figure 1.1, stage I). Nucleation cannot occur until the nucleation energy barrier is surmounted and the condition of supersaturation [concentration] is satisfied (figure 1.1, stage II). Once the nucleation conditions are satisfied, bonds are formed rapidly between nanoparticle monomers and the monomer concentration begins to decrease as nanoparticles grow. In order to obtain a monodisperse product, it is important that nucleation is a single event, otherwise nanoparticles grow at different rates. After nucleation, there is a rapid decline in the concentration of monomers as nanoparticles grow, with nanoparticles above a critical radius ($r_C$) growing at the expense of those below $r_C$. As monomers are consumed, the model enters the final stage, crystal growth (figure 1.1, stage III). Crystal growth is diffusion controlled, with rates of growth determined by the rate of monomers diffusing to the nanoparticle surface.

At equilibrium concentration, nanoparticles are subject to Ostwald ripening, which leads to a broadening of the size distribution of nanoparticles. Ostwald ripening is a state in which larger nanoparticles grow at the expense of smaller ones. In a broad size distribution of nuclei, Ostwald ripening can decrease the polydispersity of a sample as small particles dissolve away and large nanoparticles grow.

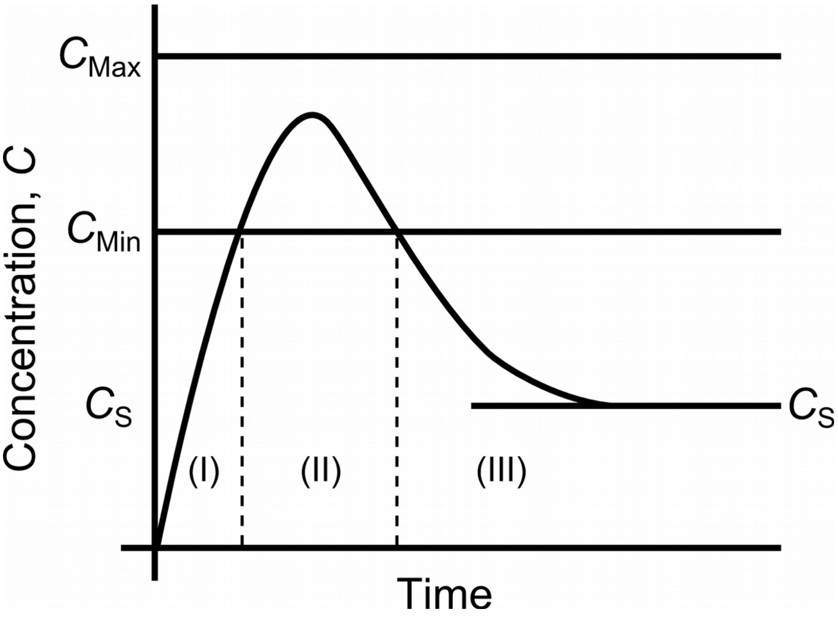

**Figure 1.1**: The LaMer model of nanoparticle nucleation and growth separated into three distinct phases: increase in concentration of monomer (stage I), nucleation of a supersaturated solution (stage II) and crystal growth by diffusion (stage III). The plot shows changes in concentration which satisfy supersaturation (between $C_{max}$ and $C_{min}$) and equilibrium concentration ($C_S$) where Ostwald ripening becomes the primary method of nanoparticle growth. Re-drawn from ref.[53]

### 1.4.1 Nanoparticle nucleation

As previously stated, nucleation occurs after the formation of a supersaturated solution of nanoparticle monomers and there is enough energy in the system to overcome the nucleation barrier. Classical nucleation theory treats the formed nuclei as bulk material, with a negative term favouring bond formation (the difference in bulk free energy per volume between the bulk and formed phases, "$\Delta G_V$") and a positive term for the energy required to form a new surface "$\Delta G_S$", as in equation 1.

$$\Delta G = \Delta G_S + \Delta G_V = 4\pi r^2\gamma - \frac{4}{3}\pi r^3 \Delta G_V \qquad \text{Equation 1}$$

This equation assumes a spherical nanoparticle of radius "r" and surface energy per unit area "γ". If a plot of Gibbs free energy "ΔG" against particle radius, a maximum is achieved at a critical nanoparticle radius, "$r_C$". This leads to an important consequence; nanoparticle nuclei larger in size than "$r_C$" will grow whereas nuclei smaller than "$r_C$" will dissolve back into solution.

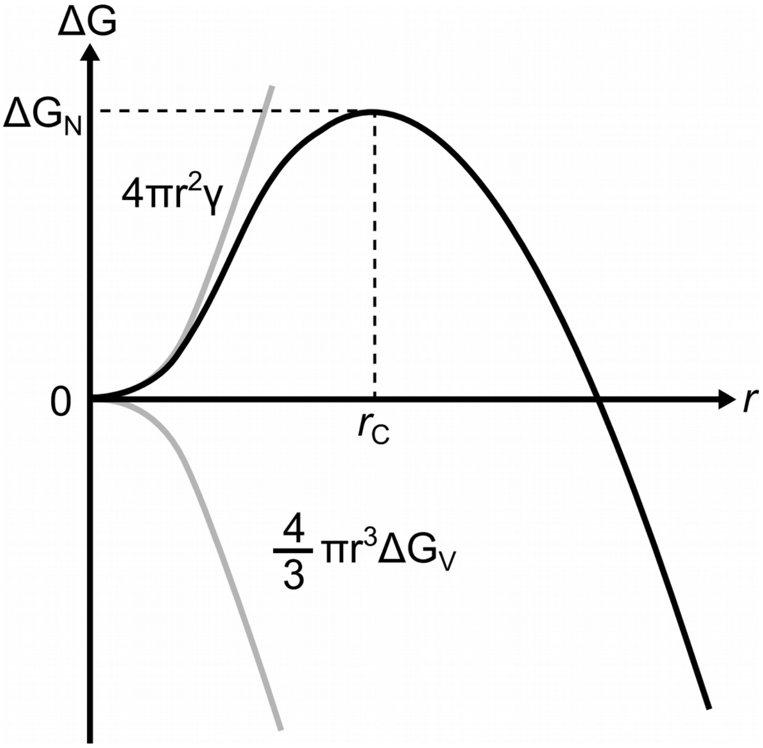

**Figure 1.2**: Plot of Free energy against nanoparticle nucleus radius showing the maximum at the critical radius "$r_C$" and free energy maximum, "$\Delta G_N$". Re-drawn from ref.[52]

The formed nuclei with sizes above the critical radius then consume monomers in the crystal growth phase of the LaMer model, described in section 1.4.

### 1.4.2 Nanoparticle crystal growth

The final stage in the LaMer model is crystal growth. Nuclei larger than the critical radius "$r_C$" grow until all monomers have been consumed, *via* an intermediate state. This process is temperature dependent, with high temperatures yielding fast crystal growth. Kinetically, crystal growth is a slow process when compared to nucleation and proceeds for homogeneous and uniform particle size increases at relatively low temperatures.[54]

Crystal growth is diffusion controlled, with monomers diffusing from bulk solution to an interfacial layer close to the surface of the nanocrystal ("flux", "$I_{diff}$") which can be modelled using Fick's law (equation 2). This is represented in figure 1.3 which shows the diffusion controlled equilibrium between the interfacial concentration of monomers at a nanoparticle surface, "$[C]_i$" and the bulk monomer concentration in solution, "$[C]_b$". Monomers then react or desorb from the surface according to the rates "$k_{des}$" and "$k_r$".[54] This is valid for a reaction sphere (boundary at "$[C]_i$") of radius "σ". "D" is the diffusion coefficient according to the Stokes-Einstein-Debye equation.

$$I_{diff} = 4\pi\sigma^2 J = 4\pi\sigma^2 D \frac{d[C]}{d\sigma} \qquad \text{Equation 2}$$

At equilibrium monomer concentration, "$[C]_e$", growth will occur at the nanoparticle surface with "$[C]_e = k_{des}/k_r$" according to the Gibbs-Thomson relation (equation 3) which relates "$[C]_e$" to the concentration of monomer at an infinitely flat surface, "$[C]_\infty$".

$$[C_e] = [C_\infty]\exp\left\{\frac{2\gamma V_m}{rRT}\right\} \qquad \text{Equation 3}$$

At the pure diffusion limit, "$[C]_i = [C]_e$" as the monomer will react instantaneously with the nanoparticle surface ($k_r << k_{des}$). At the pure reaction limit, monomers will diffuse to the surface and react according to the reactivity and concentration of adsorbates in solution, so "$[C]_i = [C]_b$". However, instances of crystal growth almost always occur in between these imposed limits. The instantaneous size-dependent growth rate is given in equation 4:

$$\frac{dr}{dt} = DV_m \left( \frac{[C]_b - [C]_\infty \exp\left(\frac{2\gamma V_m}{rRT}\right)}{\left(r + \frac{D}{k_r}\right)} \right) \qquad \text{Equation 4}$$

This equation takes into account surface and volume terms with respect to diffusion of monomers to and from the surface. It also shows the temperature dependence of the rate of crystal growth meaning faster growth will occur at higher temperatures.

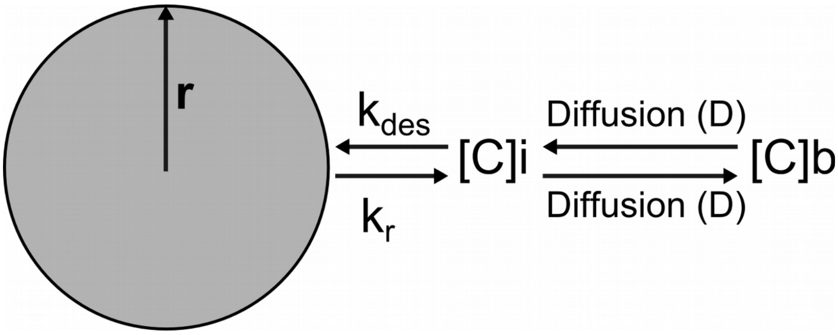

**Figure 1.3**: Diagram illustrating the transport of monomers to and from a nanoparticle surface, with an intermediate "interfacial" concentration, [C]i, which differs from the bulk monomer concentration, [C]b due to the consumption of monomers by nanoparticles. The rate of growth of the nanoparticles from [C]i is governed by two rates, $k_{des}$ and $k_r$. Re-drawn from ref.[54]

## 1.5 Methods of nanoparticle synthesis

As stated in section 1.4, the methods for the synthesis of nanocrystals are manyfold, and an in-depth discussion of every synthetic method is beyond the scope of this thesis. Therefore, this section focusses on the methods used for the synthesis of the majority of nanoparticles used in this thesis, namely reduction of a metal salt, the “heat-up” and “hot-injection” methods.

### 1.5.1 Reduction of a metal salt

The reduction of a metal salt used in the synthesis of gold nanoparticles is an example of a co-precipitation synthesis where the formation of a solid interface drives the reaction towards the formation of nanocrystals.[48,55,56] A classical example of this is described for the co-precipitation synthesis of magnetite iron(II, III) oxide nanocrystals in section 5.1.

The Brüst-Schiffrin method uses a two-phase solvent system containing tetraoctylammonium bromide as the surfactant, sodium borohydride as the reductant and gold(III) chloride as the gold source. The tetraoctylammonium bromide forms a complex with $Au^{3+}$ ions in toluene, before reduction to Au(0) with an aqueous solution of sodium borohydride. In the original synthesis, alkyl thiol molecules are added to act as a preliminary reducing agent to reduce $Au^{3+}$ to $Au^{+}$ before the sodium borohydride reduction.[57] Alkyl thiol molecules are highly effective surfactants for gold nanoparticles due to the high affinity of gold surfaces for thiol molecules. Thus they are also able to impart longer-term colloidal stability to the gold nanoparticles than tetraoctylammonium bromide whose affinity for gold surfaces is altogether weaker.[58] Thiol ligands can also be added post synthesis, increasing nanoparticle longevity in solution. The synthesis is described in section 2.2.4.1.

### 1.5.2 The “heat-up” method

The “heat-up” method has been widely used to synthesise a variety of nanocrystals including: metal oxides,[59–62] metal sulphides,[63–65] coinage metal nanoparticles,[66–68] and quantum dots.[69–72] The “heat-up” method usually consists of the high temperature decomposition of a metal complex or salt in the presence of surfactants and a high boiling point solvent. Mechanistic elucidation has been attempted by several groups, but the mechanism of nucleation and growth seems to be unique to the system under scrutiny with surfactants playing different roles in the reaction mechanisms. Nevertheless, a general mechanism as ascribed by Kwon and Hyeon[52] can be applied to reactions which feature the formation of a complex *in situ*, followed by burst nucleation and size focussing by Ostwald ripening. The suggested model is based on the nanoparticle nucleation and growth theories laid down in sections 1.4.1 and 1.4.2, and supported by computational simulations.

### 1.5.3 The “hot-injection” method

The hot-injection method adheres closely to the LaMer model, and has enjoyed widespread use in the synthesis of quantum dots, notably for the seminal organometallic syntheses of CdSe and InP quantum dots.[73–77] The hot-injection method involves either the separation of two precursors which make up the final material, or the injection of a ll precursors into a hot solution so that supersaturation and nucleation can be achieved at a single stroke. One of the precursors is heated in a high boiling point solvent (often a precursor complex is synthesised *in situ*) to a temperature which, on injection of the other precursor, will be high enough to overcome the nucleation barrier and cause instantaneous burst nucleation.

Rapid injection of the cold solution of secondary nanoparticle precursor causes burst nucleation to occur, whilst instantaneously lowering the temperature of the system. This prevents multiple nucleations by providing a distinct energy barrier between the nucleation and crystal growth phases. In this way, a monodisperse population of nanoparticles is achieved. To prevent a prolonged period of crystal growth and a broadening of the nanoparticle size distribution, the solution is cooled rapidly to room temperature. With quantum dots, it is the length of the growth period that is critical in tuning the resultant size and therefore emission wavelength which can be monitored by UV/vis spectroscopy.

## 1.6 Noble metal nanoparticles

Noble metal nanoparticles are perhaps the most studied nanoparticles due to their ease of synthesis,[78–81] longevity in colloidal suspension,[32,33] and optical properties.[6,82,83] Although noble metal salts were utilised by the ancients in glass, the first synthesis in colloidal solution was by Michael Faraday in the mid-nineteenth century.[2] Developments in electron microscopy and synthetic methods such as the Turkevich and Brüst-Schiffrin syntheses[57,84] have led to size-tunable gold nanoparticles for numerous applications including sensing,[18,85,86] photodynamic therapy[87,88] and catalysis.[19,89–91]

Noble metal nanoparticles such as gold and silver exhibit SPR. This manifests itself as a purple/red colour in gold colloidal dispersions, and is caused by the oscillation of electrons through the entire nanoparticle due to interaction with a specific wavelength of light. SPR in gold nanoparticles was modelled by Mie by solving Maxwell's equations for a sphere interacting with light, which approximates nanoparticle size to the wavelength of incident light.[92]

Noble metal nanoparticles tend to have a high affinity for sulphur containing ligands, which facilitates ligand exchange reactions and promotes longevity in colloidal suspension. This has allowed for a plethora of applications in bio-conjugation, and certainly fundamental work in the field of noble metal nanoparticles has underpinned the proliferation of nanoparticle research in the last twenty years.[58,93,94]

## 1.7 Semiconductor nanocrystals

semiconductor nanocrystals exhibit bright, size-dependent photoluminescence due to the quantum size effect. These nanocrystals, known as quantum dots, were first identified in a glass matrix by Alexei Ekimov in tandem with theoretical work by Louis E. Brus. [95–97] Since the development of organometallic routes for their synthesis, research activity has increased exponentially.[98–102] This activity is driven by the potential applications of quantum dots, particularly for the electronics and biomedical imaging industries.[12,103–106] Research has focussed on the development of techniques for the improvement of quantum yield, reduction of photo-bleaching and oxidation and new, less toxic materials for quantum dots.[107–110]

The photoluminescence of quantum dots is attributed to the quantum size effect, which describes the crossover between the molecular and bulk properties within semiconductors (figure 1.4). As quantum dots become smaller in size, nanoscopic properties become more pronounced, and the bandgap energy levels become quantised in nature. Therefore, a definite energy gap between the valence and conduction band appears, and when this bandgap corresponds to the visible region of the spectrum, visible photoluminescence can occur.

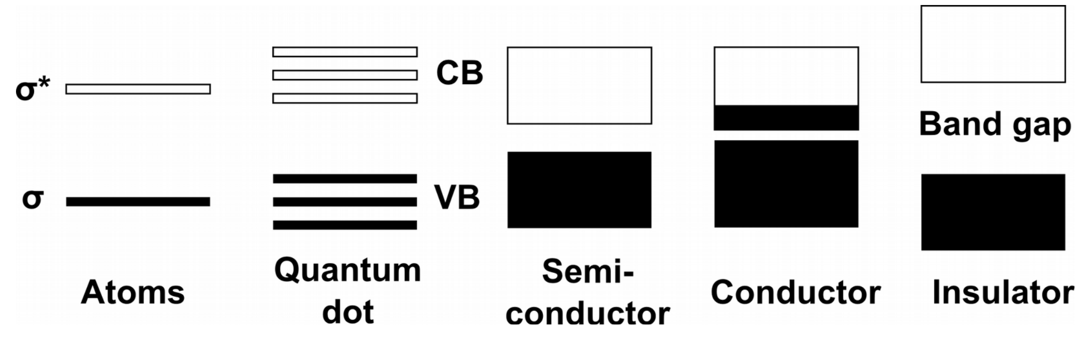

**Figure 1.4**: Representation of the variation in semiconductor bandgaps due to quantisation caused by the quantum size effect. Quantum effects increase with reducing size. Re-drawn from ref.[111]

In a semiconductor, the valence and conduction bands either side of the Fermi level are populated by electrons and electron holes. In quantum dots, incident radiation causes the formation of an exciton (electron-hole pair) by promotion of an electron from the valence band to the conduction band. The electron then has to emit the absorbed radiation in order for electron-hole recombination to occur. However, there are numerous ways for this radiation to be emitted, through radiative and non-radiative processes with photoluminescence being a radiative exciton recombination process.[112]

A consequence of the quantum size effect is that the wavelength of emission is size tunable, as you are altering the area of exciton quantum confinement and therefore the bandgap. The smaller the diameter of the quantum dot the smaller the bandgap and the bluer the emission wavelength. This size dependent emission of quantum dots can be related to the intrinsic semi-conducting properties of the bulk material using the Brus equation (equation 5). The bandgap of the quantum dot, "$E_{gap}^{QD}$" and the bandgap of the bulk material, "$E_{gap}^{B}$" are related to the quantum dot radius, "r" using the material dependent effective masses of a pseudoelectron, "$m_e$" (which is far less than the real electron mass) and hole, "$m_h$". These approximations hold as long as the unit cell remains the same in any cluster and the bulk material. "$\varepsilon_0$" is the permittivity of free space, "$\varepsilon_B$" the permittivity of the bulk material and "*e*" is the elementary charge.

$$E_{gap}{}^{QD} = E_{gap}{}^{B} + \frac{h^2}{8r^2}\left(\frac{1}{m_e} + \frac{1}{m_h}\right) - \frac{1.8e^2}{4\pi\varepsilon_0\varepsilon_B r}$$ Equation 5

The quantum yield of quantum dots can be vastly improved by shelling the quantum dot cores with a shell of another semi-conducting material. The most effective shelling materials have the same or complementary lattice structures to the core, and are designed to prevent oxidation of the core material and remove surface defects which act as electron "traps" and decrease quantum yield. A review on recent advances quantum dot shelling techniques and materials, as well as the theory behind shelling with different bandgap materials can be found in chapter 4 of this thesis.

## 1.8 Magnetic nanoparticles

Magnetic nanoparticles have received a great deal of interest in the literature, mainly due to their potential applications in magnetic hyperthermia,[113–116] data storage,[9,42] catalysis,[117–119] drug delivery[120–122] and as contrast agents in magnetic resonance imaging[123–125] amongst others. Most ferromagnetic materials cease to have multiple magnetic domains (areas in the material of aligned magnetic moments) below a certain size and become superparamagnetic at room temperature. This size transition differs for different magnetic materials, but is usually in the region of 20 nm.[126]

In multi-domain materials, long-range order of magnetic materials will cease above the Néel temperature and the material exhibits paramagnetic behaviour. Superparamagnetic nanoparticles have magnetic anisotropy, and are magnetised in an “easy” (single) direction per nanoparticle.

Above the blocking temperature, superparamagnetic nanoparticles are single domain units and don't interact as the thermal energy is large enough to overcome the magnetic anisotropy barrier. Therfore superparamagnetic nanoparticles exhibit no magnetic hysteresis and zero coercivity, and no net magnetisation outside an applied magnetic field.[127,128] They react instantaneously to an applied magnetic field, aligning along the “easy” axes, and revert to their random, no-overall magnetic moment when said field is removed.

Magnetic hyperthermia is a practical utilisation of superparamagnetism, with a detailed description found in section 5.2.

## 1.9 Summary

Developments in nanoparticle syntheses, functionalisation strategies and applications have increased exponentially over the last two decades, with many advances in the fields of medicine, imaging and therapy currently in clinical trials.[129,130] The field of energy materials has also benefitted, with advances in photocatalysis, solar cells, light harvesting and data storage. The proliferation of the field has come with developments in characterisation techniques such as electron microscopy, atomic force microscopy, high energy X-ray and scattering techniques. However, nanoparticles and nanomaterials have yet to achieve their potential or fulfil their promise as the next generation of medicines or molecular machines due to challenges with toxicity and nanoscale engineering. Recent progress in the elucidation of synthetic mechanisms,[131] control over shape anisotropy,[132] new functionalisation strategies[133] and a plethora of accessible composite materials[134] has solidified the position of nanomaterials at the forefront of technology development.

# Chapter 2: Techniques, Methods and Materials

## Preface

The following chapter details the methods and materials used in all experimental chapters, namely chapters 3, 4 and 5. This includes detailed protocols of each of synthetic methods used, and details of purity and procurement of all chemicals used. Analytical techniques common to multiple experimental chapters are detailed here, including: electron microscopy, electron energy loss spectroscopy, energy dispersive X-Ray spectroscopy, X-Ray photoelectron spectroscopy, UV/vis and photoluminescence spectroscopy, Mössbauer spectroscopy and superconducting quantum interference device magnetometry. The basic principles of the AACVD process are also outlined.

# 2.1 Techniques

## 2.1.1 Electron microscopy

“It is poor comfort to hope that human ingenuity will find ways of overcoming this limit”- Ernst Abbe (1840-1905) on the limitations of light microscopy.

Transmission electron microscopy (TEM) is a very powerful analytical weapon in the nanoparticle chemist's arsenal, and the main analytical technique used in this thesis. It allows the sample to be imaged and scrutinised directly, with fine structural and compositional information easily attainable with high kV instruments with integrated secondary detection techniques such as energy dispersive X-ray spectroscopy (EDS) and electron energy loss spectroscopy (EELS). TEM differs from scanning electron microscopy (SEM) in that it detects transmitted electrons, meaning that electrons are scattered elastically and inelastically from a beam passing through the sample, rather than looking at backscattered and secondary electrons from a sample surface, which are detected in SEM. Therefore, information obtained from SEM gives details on the 3D structure of the surface of the analyte which TEM cannot, but lacks the penetration to show the crystalline composition of materials.

### 2.1.1.1 Principles and overview

The concept of electron microscope came about due to the limitations of light microscopy. At the beginning of the 20th century, light microscopy was reaching the limits of resolution, as a physical limit imposed by the wavelength of light. It wasn't until the idea of using higher energy electrons for microscopy was proposed a few years years after de Broglie first theorised the wave-like properties of electrons, that microscopy continued to advance. The first commercial TEMs were produced in the 1930s, with the Metropolitan Vickers EM1 being the first example in 1936. The electron microscope has seen continued improvement, with high resolution TEM and atomic column imaging realised in the mid-1970s.[135]

One of the main limitations in improving the resolving power of high resolution transmission electron microscopes (HRTEMs) is designing electron lenses. Electron lenses and samples introduce spherical and chromatic aberrations respectively, although these can be used as an advantage when “tilting” a sample or focussing the microscope. Another noteworthy limitation of the TEM is the tiny fraction of the sample that is examined; a consequence of the greater resolution afforded by the electron microscope. The TEM system also requires the sample to be placed under high vacuum, and the sample can be damaged by the electron beam, due to the ionising effect of high energy electrons.

As already stated, the TEM requires an electron beam rather than a light source in order to image samples. The majority of the electron beam passes through the sample, but it is those electrons which interact with the sample allow the TEM image to be formed and makes spectroscopies such as EDS, EELS and Auger electron spectroscopy possible. The electron beam is formed through either field emission or thermionic sources. Briefly, a thermionic source is made of a material which, when heated, emits electrons due to the natural barrier which preventing their emission being overcome. This barrier is termed the work function “Φ”. So an ideal thermionic source needs to have a high melting temperature and a low work function, such as lanthanum hexaboride ($LaB_6$, $\Phi = 2.4$ eV, operating temperature = 1,700 K) or tungsten ($\Phi = 4.32$ eV, operating temperature = 2,700 K). Field emission produces a beam when an intense electric field is applied to a thin filament of material, and therefore Φ is lowered to allow electrons to tunnel out, forming the electron beam. Tungsten wire is the most commonly used field emission source.[135]

The electron beam is controlled and focussed through the use of apertures and lenses before and after the electron beam interacts with the sample. Electron images are “seen” through the interaction of the electron beam with a phosphorescent screen, usually consisting of a film of micrometre size zinc sulphide microparticles. In modern instruments, a charge-coupled device (CCD) is used to record images digitally, and powerful software packages allow easy manipulation and analysis of TEM images and SAED patterns.

Apertures are circular annular metal discs which block electrons which have been scattered away from the main electron beam axis at several points before and after the sample. They help to improve the resolution of the image, although the trade-off is that the smaller the aperture, the more the electron beam is condensed, so fewer electrons are detected and the darker the image appears on the phosphorescent screen.

Electron lenses behave in the same way as converging optical lenses. They focus the electron beam and must be aligned in order for a focussed image to be formed. Lenses manipulate the electron beam through the use of electromagnets and can be controlled by altering the current that flows through the lens. From the top down, a TEM has a set of condenser, objective and projector lens. The condenser lens set is responsible for primary beam formation, whilst the objective and projector lenses focus the scattered electrons which pass through the sample and expand the beam onto the phosphorescent screen. Additional coils known as stigmators help correct beam astigmatism, a lens aberration which causes the electron beam to have different focal points in orthogonal directions, leading to defocussing of the image.

#### 2.1.1.2 Interaction of electrons with the sample

High energy electrons are able to remove inner shell electrons from atoms, resulting in a degree of ionisation. This in turn leads to a number of processes that can occur within the sample, which are summarised in figure 2.1. Characteristic X-rays, Auger electrons and secondary electrons all give information about the nature of the sample, and can be detected and analysed using spectroscopy.

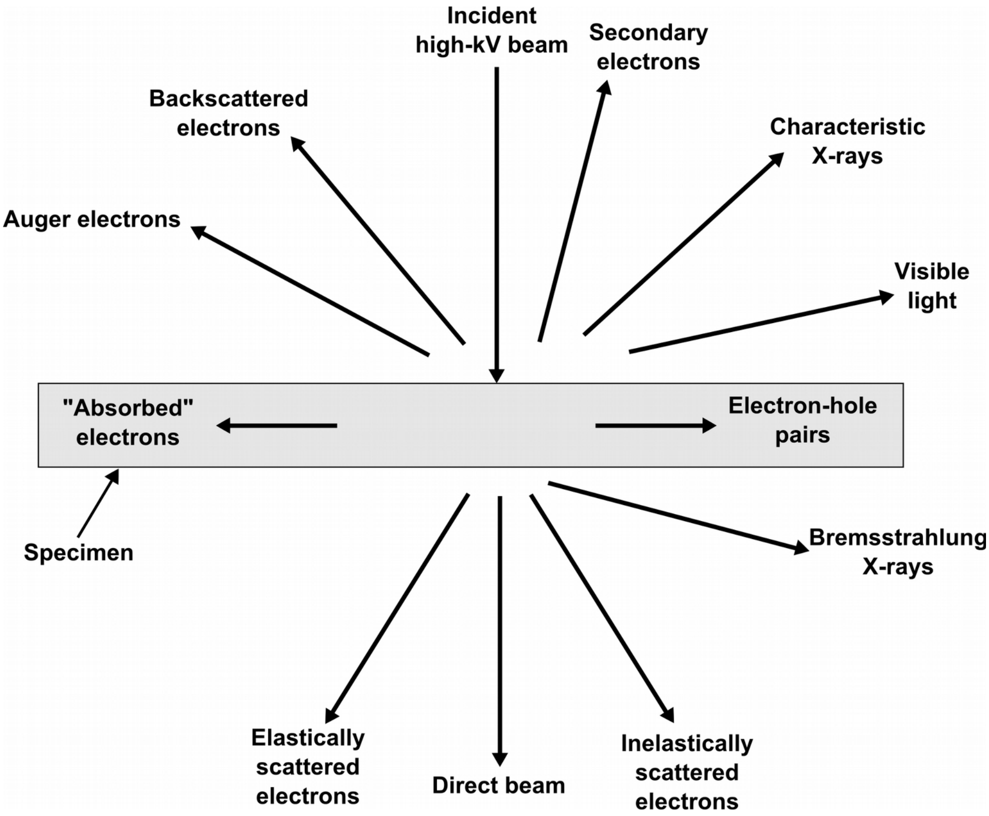

**Figure 2.1**: Different kinds of scattered electrons and other products obtained from the interaction of an incident electron beam with a scattering analyte. Secondary electrons are the primary imaging electrons for SEM, whilst TEM relies on forward scattering electrons. Characteristic X-Rays are used for EDS spectroscopy, whilst inelastically scattered electrons are used in EELS. Re-drawn from ref.[135]

### 2.1.1.3 TEM imaging

For imaging purposes, electrons which do not deviate far from the main electron beam, *i.e.* elastically scattered electrons, form the image, with dark areas indicating where scattering has occurred. Electrons are scattered by repulsive interactions from the electron cloud and by the nuclei in the sample, and scatter strongly because they are charged particles. The amount of forward scattered electrons, *i.e.* electrons detected in TEM, deviating 1-10° from the main electron beam, is dependent on the thickness of the sample, as the thicker the sample, the few the number of coherent, forward scattered electrons.

Contrast is also a very important variable when considering an analyte for TEM. Scattering intensity is dependent on the thickness, density and crystallinity of the sample. Electron poor elements or non-crystalline species often image poorly on the TEM (*i.e.* polymers, DNA), as their electron clouds are diffuse. Therefore, for polymeric or biological samples, staining techniques with heavy metal solutions such as tungstic oxide or osmium tetroxide are employed.

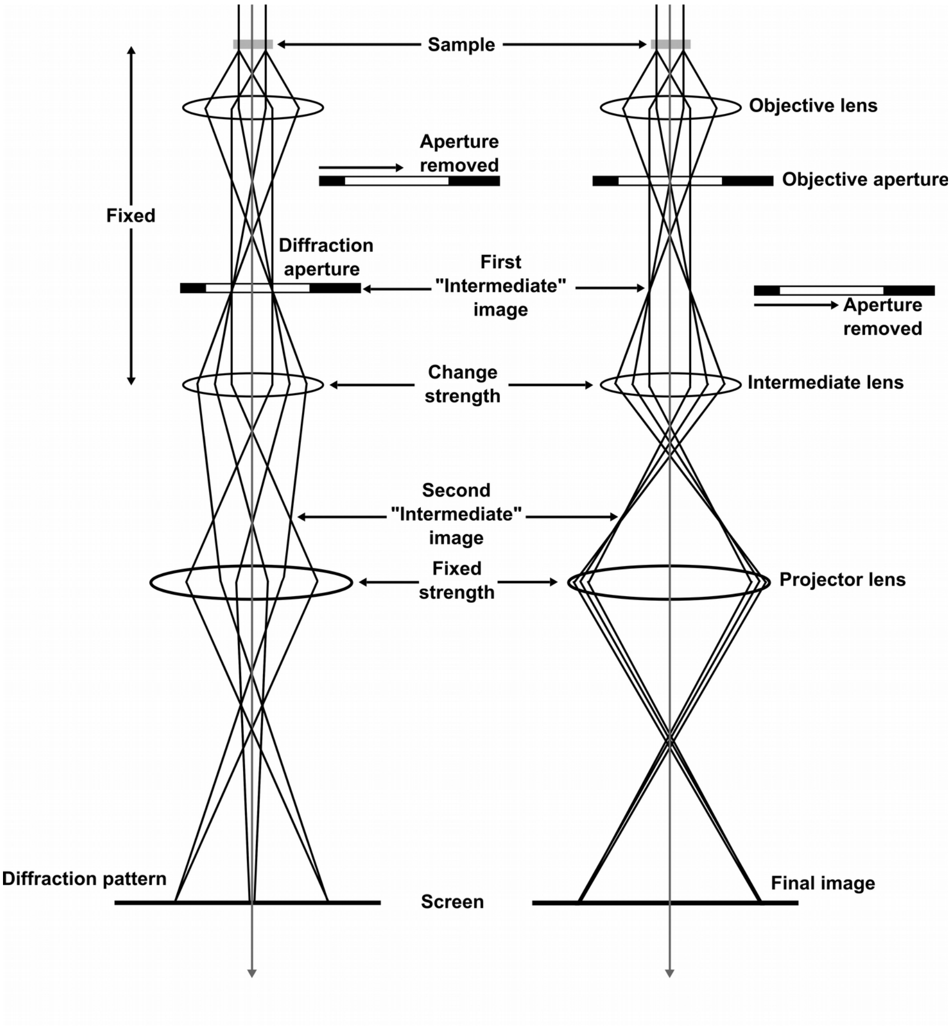

**Figure 2.2**: Simplified schematic of a TEM, with diffraction mode depicted on the left with a concentrated beam and imaging mode on the right with a more diffuse beam for imaging. Re-drawn from ref.[135]

Figure 2.2 shows the main imaging modes of the TEM with the different apertures and lenses showing a diffuse, spread beam for imaging, and a concentrated direct beam for electron diffraction.

### 2.1.1.4 Scanning electron microscopy

SEM is a complementary technique to TEM, in which scattered electrons are utilised in a different way. TEM is a *transmission* technique so relies on forward scattered electrons, whereas SEM is a *scanning* technique, and secondary electrons are used as the primary imaging source. A low energy electron beam is scanned over the surface of the sample, with the beam's position as well as detected electrons combined to form a raster pattern, and thus an image. This means highly dense, thick samples can be imaged, and very detailed information about surface composition can be obtained.

### 2.1.1.5 Microscope instrumentation details

Several microscopes were used in the work described in this thesis: TEM images were recorded using a Jeol JEM 1200EX with a 4 megapixel Gatan Orius SC200 CCD camera at an acceleration voltage of 120 kV at the School of Anatomy, University College London. HRTEM measurements were collected using a Philips CM200 FEG (field emission gun) TEM fitted with a Gatan GIF 200 imaging filter for EELS and an Oxford Instruments UTW EDS detector running ISIS software at the Leeds EPSRC Nanoscience and Nanotechnology Research Facility and a Jeol 2100 HRTEM with a $LaB_6$ source operating at an acceleration voltage of 200 kv with an Oxford Instruments X-Max EDS detector running AZTEC software at the Department of Chemistry, University College London. Micrographs were taken on a Gatan Orius CCD. Samples for TEM were prepared by drop-casting a suspension of nanoparticles in *n*-hexane solvent onto a 400 Cu mesh lacy carbon film TEM grid (Agar Scientific Ltd).

SEM images were recorded on a Jeol JSM-6301F operating at 5kV at the Department of Archaeology, University College London. Samples were vacuum sputtered with a very thin film of gold to improve surface electrical conductivity.

#### 2.1.1.6 EELS and EDS

Electron energy loss spectroscopy (EELS) and energy dispersive X-Ray spectroscopy (EDS) are seen as complementary techniques, as both are commonly used as secondary detection techniques within a TEM. They are seen as complementary as EDS provides information on the composition of analytes and is much more sensitive to heavier elements, whereas EELS gives much more detailed information on chemical bonding and atomic composition and works best with very sharp excitation edges, which tend to be elements of low atomic mass.

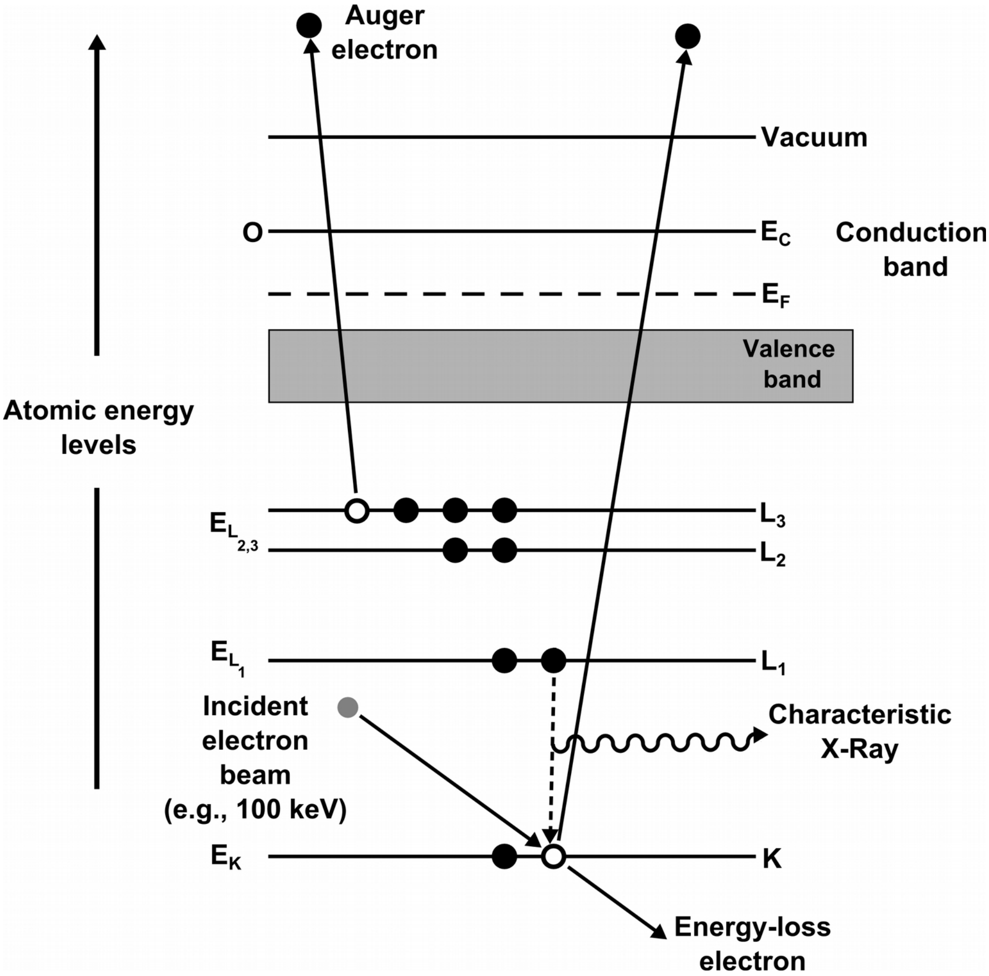

**Figure 2.3**: The process of inner shell ionisation of an atom by an incident electron beam. Processes used in EDS (emission of a characteristic X-Ray), Auger electron spectroscopy (absorption of an X-Ray and subsequent ejection by a higher energy electron) and electron energy loss spectroscopy (inelastically scattered electrons). "$E_C$" is the conduction band, "$E_F$" is the Fermi level and "L" and "K" denote electron shells. Re-drawn from ref.[135]

When an electron beam interacts with a sample, several processes occur, as illustrated in figure 2.1. EDS makes use of the characteristic X-rays, which are unique to each element. When an electron beam is applied to a sample, incoming electrons can cause the ejection of a core electron in the sample through excitation, leaving an electron hole in the core (ionisation). Consequently, a higher energy electron from an outer shell then loses energy to occupy the core-electron hole to gain the lowest energy electronic configuration. The electron does this with emission of a characteristic X-ray of energy corresponding to the difference in energy levels between the core and outer shell electrons. Emitted X-rays are unique in energy for each element and each shell, so atomic identification and elemental composition measurements are possible. As previously stated, EDS is more sensitive to heavier elements, due to a greater number of outer electrons which can emit X-Rays.

Auger electrons are emitted in a similar way, albeit the characteristic X-Ray is absorbed by another outer shell electron after emission, which in turn is ejected.

EELS utilises inelastically scattered electrons, *i.e.* electrons which have lost energy and have been slightly and randomly deflected by the sample. Inelastically scattered electrons are scattered through a few processes, namely phonon scattering, plasmon scattering and inner shell ionisation. The degree of deflection and energy loss are characteristic of elements in the sample.

A typical EELS spectrum will show the energies of inelastically scattered electrons, with a zero loss peak, a plasmon resonance peak and core loss electron peaks. The zero loss peak contains a mixture of inelastic and elastically forward scattered electrons, and is used to calibrate the spectrometer. The low loss region containing the plasmon resonance region and the core loss electron peaks carry the most useful information. Plasmons are wave-like oscillations of weakly bound electrons, and are specific to each element, whilst the core loss region (high loss region) details electrons which have interacted with tightly bound, core electrons.[135]

By choosing an electron energy window, it is possible to study electrons that have only interacted with particular electrons from particular elements in the sample. These electrons can be imaged to produce an elemental map. The technique is known as Energy-filtered Transmission Electron Microscopy (EFTEM) and is invaluable for analysis of core/shell nanoparticles.

#### 2.1.1.7 Selected area electron diffraction

Selected area electron diffraction (SAED) is a technique which utilises the electron beam within a TEM to analyse crystalline samples. When electrons pass through a single crystalline sample, the sample acts as a diffraction grating, diffracting elastically scattered electrons into spots around the central beam, according to Bragg's law. When analysing nanoparticles, elastically scattered electrons tend to form rings, as many individual spots from different randomly orientated nanoparticles coalesce. The electron diffraction pattern is directly comparable to the X-ray diffraction (XRD) powder pattern, but much smaller areas and crystals of fixed crystallographic orientation can be analysed within the TEM. The distance between rings can be measured and assigned, the key difference with XRD being the scattering angles involved, with larger diffraction angles used in XRD. This means that we can directly assign materials according to their SAED patterns.

SAED patterns were acquired on a Jeol 2100 HRTEM with a $LaB_6$ source operating at an acceleration voltage of 200 kV, at the University College London, and a Philips CM200 FEG TEM, at the Leeds EPSRC Nanoscience and Nanotechnology Research Equipment Facility.

### 2.1.2 X-Ray techniques

#### 2.1.2.1 X-ray photoelectron spectroscopy

X-ray photoelectron spectroscopy (XPS) or electron spectroscopy for chemical analysis (ESCA) is a surface analysis technique which uses the photoelectric effect to perform qualitative and quantitative electronic spectroscopy on surfaces and powders.[136] The technique involves firing an X-ray beam at a given sample and angle, and measuring the intensity and number of ejected electrons from electron shells from atoms within the sample. The energy of emitted electrons (must be below the energy of the incident beam) are specific to elements in the sample and sensitive to oxidation states. The interaction of electrons with a sample is a very similar to EDS, except it is incident X-rays not electrons which are used (figure 2.1). XPS spectra are collected as intensity against electron energy (electron kinetic energy), but are usually displayed as intensity against electron binding energy. This is due to the electron kinetic energy being dependent on the X-ray excitation source. It is linked to the electron binding energy (an intrinsic property of a material) using the following equation (equation 6):

$$E_B = h\nu - E_K - W \qquad \text{Equation 6}$$

Where "$E_B$" is the electron binding energy, "$E_K$" is the electron kinetic energy, "hυ" the energy of the incident of incident X-rays and "W" the work function of the spectrometer. Electrons which escape without loss contribute to the standard lines in the XPS spectrum, whilst inelastically scattered with energy loss contribute to the background of the spectrum. Relaxation of outer shell electrons to lower energy configurations leads to characteristic X-rays and thus X-ray fluorescence. Auger electrons may also be generated by the absorption of the characteristic X-rays by outer shell electrons and their subsequent ejection.

XPS requires ultra high vacuum conditions, typically $< 10^{-9}$ mbar, and as such volatile species may not be analysed. As previously stated, XPS is a surface analysis technique, and as such the penetration depth is limited by various processes that occur in the material, preventing the escape of photoelectrons.

XPS was performed using a Thermo Scientific K-alpha spectrometer with monochromated Al Kα radiation, a dual beam charge compensation system and constant pass energy of 50 eV (spot size 400 μm). Survey scans were collected in the range 0-1200 eV. High-resolution peaks were used for the principal peaks of Ti (2p), O (1s), N (1s), C (1s), Fe (2p), Au (4f), Cu (2p), Cd (3d), Se (3d), In (3d), P (2p), Zn (2p), Hg (4f) and S (2p). The peaks were modelled using sensitivity factors to calculate nanoparticle composition using CASA XPS software.

### 2.1.2.2 X-Ray absorption spectroscopy

X-Ray absorption spectroscopy (XAS) is a technique which requires intense radiation, and provides information concerning specific elements and bonding modes in analytes. XAS is very sensitive to chemical bonding modes, elemental oxidation states, co-ordination numbers and bond distances of nearest neighbours. Unlike XRD, XAS does not require a crystalline sample. XAS is divided into two regimes: X-Ray absorption near-edge spectroscopy (XANES) and extended X-Ray absorption fine structure spectroscopy (EXAFS). As XAS probes atomic energy levels, it requires high energy, synchrotron radiation for completion.

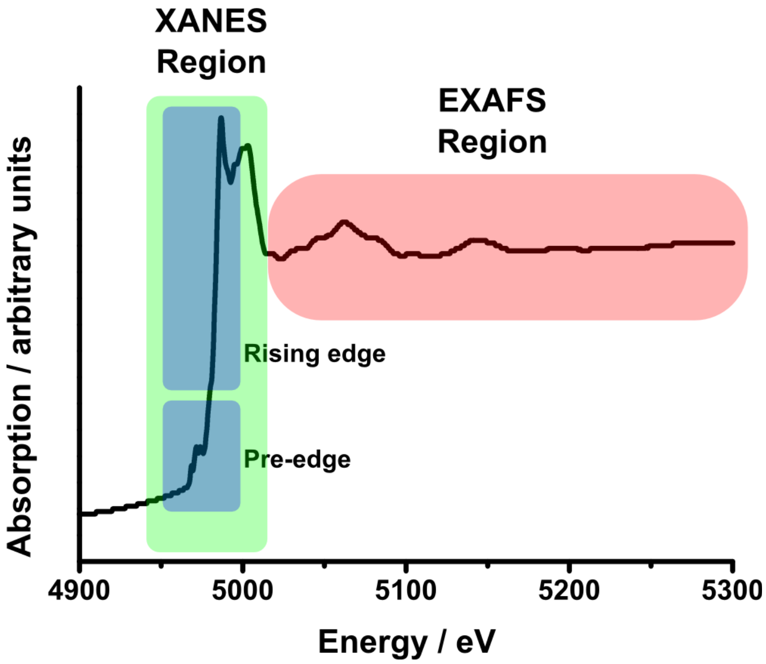

**Figure 2.4**: XAS spectrum of an anatase titania with highlighted pre-edge, rising edge, XANES and EXAFS regions highlighted.

X-rays are absorbed by core electrons above and equal to the binding energies of those electrons in the sample, which ejects a photoelectron (described in section 2.1.2.1). Electrons then lose energy *via* X-Ray fluorescence and the Auger effect. XANES is very sensitive to co-ordination chemistry and oxidation states whereas EXAFS is more sensitive to bond distances and co-ordination numbers of atoms surrounding the target element. The XANES region is typically in the energy range of 50-100 eV, whilst EXAFS occurs after the elemental "edge" (the lowest unoccupied energy level above the Fermi level) at energy ranges > 150 eV.[137]

EXAFS measurements were recorded at the UK Synchrotron, Diamond, by Dr Andreas Kafizas. EXAFS was conducted in flourescence mode over the 4800 – 5600 eV range to assess the K-line of Ti. Patterns were normalised and modelled using Athena and Demeter softwares respectively.

### 2.1.3 Spectroscopic techniques

#### 2.1.3.1 UV/visible and photoluminescence spectroscopy

UV/vis and photoluminescence spectroscopies are the principal techniques for the determination of the optical properties of fluorophores and quantum dots. UV/vis spectroscopy is used to determine the band-edge of quantum dots, from which the Stokes' shift can be determined using the UV/vis and photoluminescence spectra (figure 2.5). This is important as it is indicative of how much photon energy is lost by radiative and non-radiative processes. Determination of the band edge allows quantum dot samples to be analysed by photoluminescence emission spectroscopy as the excitation source can excite the quantum dots at the band edge maximum, thus maximising photoluminescence response.

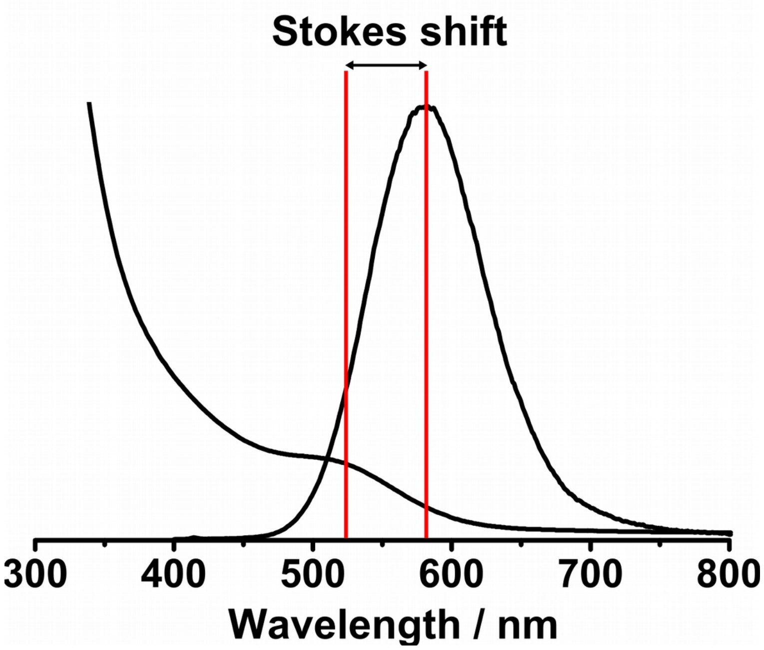

**Figure 2.5**: UV/vis and photoluminescence spectra of an InP/ZnS-CdS sample in *n*-hexane showing the Stokes shift between the absorption band edge (UV/vis, left) and emission spectrum maximum (photoluminescence, right). The band edge is defined as $\text{abs}_{\text{max}}$ on the first shoulder of the absorption peak (shown).

Photoluminescence spectroscopy is used to examine the excitation and emission characteristics of quantum dots and can be used to observe phenomena such as surface trap states and red or blue shifting. The emission profile can also give information on the polydispersity and shape of the quantum dot sample. When combined with UV/vis spectroscopy, photoluminescence spectroscopy can be used to calculate quantum yield (section 4.2).

### 2.1.3.2 UV/visible spectroscopy

UV/vis spectroscopy deals with the absorption/reflectance of photons by electrons in molecular and solid species, from which electronic transitions and therefore colour changes can be scrutinised. UV/vis spectroscopy deals with the area of the electromagnetic spectrum from the near infrared to the ultraviolet, generally in wavelength range 190 - 1200 nm. Absorption spectra are subject to the Beer-Lambert law, which relates the pathlength of the sample, sample concentration and extinction coefficient to absorption.

A typical UV/vis spectrometer has two sources; a deuterium lamp which emits in the region of 190 - 400 nm and a tungsten lamp which emits between 300 - 2,500 nm. In this way there is a transition period where one bulb takes over from the other. A UV/vis spectrometer is a dispersive instrument, so after passing through a monochromator, the beam is dispersed by an optical "chopper" which then passes through the sample and a background "control" which usually consists of the solvent. This allows for subtraction of the solvent background and thus any masking effects the solvent may have. After interaction with the sample, the resultant photons are detected using a photomultiplier tube. The difference between incident and transmitted photons in the sample minus the background results in the UV/vis spectrum. UV-vis spectra were recorded using a Perkin Elmer Lambda 25 UV/Vis spectrometer single beam instrument over a range of 250–1000 nm.

#### 2.1.3.3 Photoluminescence spectroscopy

Photoluminescence spectroscopy is used to measure fluorescence excitation and emission in molecules and substances. Molecules possess distinct electronic states populated by vibrational energy states. Fluorescence spectroscopy is designed to probe these energy states through the excitation of electrons in a singlet ground state to an excited singlet state *via* the absorption of radiation and the subsequent emission of absorbed energy as a photon. In the excited state, the electron can undergo radiative and non-radiative relaxation processes such as losing energy to vibrational levels of the solvent (heat, radiative) or decay *via* inter-system crossing to a triplet state and phosphorescence. Phosphorescence is a longer lived process than fluorescence, due to inter-system crossing between a singlet and triplet state being formally forbidden (change in multiplicity). Nevertheless, phosphorescence (μs - s) and fluorescence (ns) occur on fast time-scales.

A typical spectrophotometer requires a high energy source such as as a xenon arc lamp or a laser for activation. A laser has an incredibly narrow emission wavelength and therefore doesn't require an excitation monochromator, but the excitation wavelength cannot be changed without changing the laser. A xenon arc source is a continuous wave source with a near constant emission intensity over the 300 - 800 nm wavelength range. Coupled with an excitation and emission monochromators, this allows excitation and emission spectra to be recorded by keeping the wavelength emitted from one monochromator and varying the other. Fluorescence emission is recorded at a right angle to the sample as the intensity of the incident radiation would saturate a detector in the same plane as the incident radiation. Photoluminescence spectra were recorded using an Horiba-Jobin Fluorolog-3 fluorometer with a TCSPC attachment.

### 2.1.3.4 Photoluminescence lifetime spectroscopy

Time-correlated single photon counting (TCSPC) in combination with a laser excitation source, is used to determine the rate of decay from excited electronic states to ground states of fluorescent species. This can be used to analyse multiple features in fluorescence spectra generated from different analytes/processes in solution. The resultant decay curve generates a fluorescence lifetime, "$\tau$" with longer lifetimes indicating a more complicated fluorescence decay pathway (*via* electron trap states or phosphorescence).

### 2.1.3.5 Mössbauer spectroscopy

Mössbauer spectroscopy is a very sensitive technique for the detection of different chemical oxidation states and chemical environments for a given element. In order to do this, Mössbauer spectroscopy requires the absorption and emission of $\gamma$ radiation by nuclei within a solid lattice. The radiation required can only be produced by a radioactive nucleus of the same type, hence the use of $^{57}$Co (which decays to an excited isotope of $^{57}$Fe) for iron Mössbauer spectroscopy.

Mössbauer spectra are recorded as intensity against mm $s^{-1}$, as there is no way of tuning the emitted quanta of radiation to the emitter, so the necessary tuning required for monochromatic radiation sources is achieved *via* the Doppler effect, hence the source is moved back and fourth. The sensitivity of Mössbauer is such that very subtle changes in nuclear environment can be detected, so obtained spectra typically show three types of nuclear interaction: isomer shift, quadrupole and hyperfine (Zeeman) splitting.

### 2.1.3.6 The Mössbauer effect

When a molecule emits a quantum of energy ($E_v$), the emitted photon must have a momentum ($E_v/c$) which will have an equal and opposite recoil momentum ($-E_v/c$). The energy associated with the recoil ($E_R$) is calculated using the kinetic energy relation (Kinetic energy = $mv_R^2/2$, where $v_R$ is the recoil velocity, and m the mass). At lower energy with emitters of normal molecules or atoms, $v_R$ is small and thus $E_R$ is negligible. However, $\gamma$ radiation is very high energy, and as such, $v_R$ and therefore $E_R$ becomes significant. The energy of $\gamma$ quanta ($E_\gamma$) all stems from the transition of the nucleus from its excited state to ground state. Therefore, this process is solely responsible for the emission and must also provide $E_R$. If the nuclear transition is called $E_t$, then for emission:

$$E_\gamma = E_t - E_R \qquad \text{Equation 7}$$

Therefore, $E_\gamma$ is much less than $E_t$. There is a significant amount of recoil energy when an atom absorbs an emitted γ quantum of energy $E_\gamma$. If a γ quantum excites a nucleus with transition energy $E_t$, then $E_\gamma$ must be greater than $E_t$ by an amount equal to $E_R$, so that:

$$E_\gamma = E_t + E_R \qquad \text{Equation 8}$$

Molecules in the gas or liquid phases which emit γ quanta cannot reabsorb them, as $E_\gamma$ and $E_t$ will not be the same (figure 2.6). However, in a rigid, solid lattice, the recoil energies of the lattice are quantised throughout the lattice, insofar as the lattice behaves as a single entity. Therefore, we revert to a situation where "m" in the kinetic energy relation becomes large, and $v_R$ and $E_R$ become negligible, so that $E_\gamma$ will equal $E_t$ (figure 2.6). In reality, this is not always the case, as lattice vibrational modes become excited by γ radiation, so a small window known as the recoil free fraction which gives rise to the Mössbauer spectrum. As is the case with dampening vibrations in all spectroscopic methods, higher resolution Mössbauer spectra can be obtained at lower temperatures.[138]

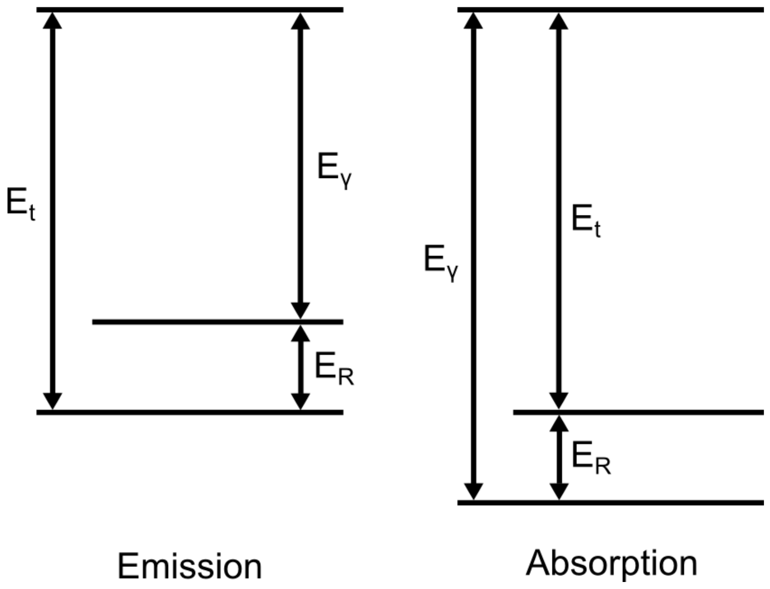

**Figure 2.6**: Energy level diagrams for emission and absorption of γ radiation. Re-drawn from ref.[138]

### 2.1.3.7 The Mössbauer spectrum

The nuclear transition energy, $E_t$, depends on a number of factors, such as the electronic environment of the nucleus, and magnetic and electric field gradients at the nucleus. It is these subtle environmental features which allows for the extraction of more detailed information on nuclei in the sample.

We can measure these subtle changes in $E_t$ using the Doppler effect as the energies of the emitted quanta are controlled by the use of an oscillating source. The source's position is measured relative to the sample, hence the Mössbauer spectra is recorded as intensity against mm $s^{-1}$. The relative motion modulates the energy of the quanta received by the sample, and when this energy equals $E_t$ in the sample, radiation is absorbed. A schematic of a typical Mössbauer spectrometer is shown in figure 2.7.

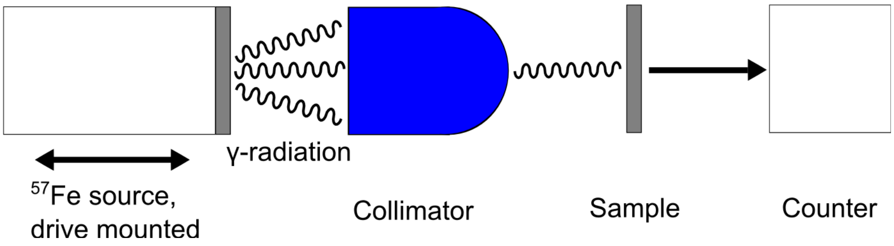

**Figure 2.7**: Schematic of a typical Mössbauer spectrometer, re-drawn from ref.[138]

The isomer shift (δ) in the Mössbauer spectrum arises from the interaction of a nucleus with electrons surrounding it, as the size of the nucleus is different in the ground state compared to the excited state. The isomer shift is dependent on the electron density at the nucleus, although some nuclei are bigger than others in the ground/excited state so the isomer shift may be positive or negative. Therefore, we can say that isomer shift is dependent on oxidation states in the sample.

If a nucleus has a nuclear spin greater than 1/2, then it has a quadrupole moment, and will be affected by any electric field gradient at the nucleus. This splits the Mössbauer signal due to the formation of an asymmetric electric field. In the case of

$^{57}$Fe, the spectrum will split into a doublet due to the loss of degeneracy in the excited 3/2 state.

Hyperfine splitting occurs when the nuclear magnetic moment interacts with a magnetic field at the nucleus to split the nuclear energy levels. A nucleus with spin I experiences a loss of degeneracy, and splits into 2I + 1 energy levels in the presence of an external magnetic field, known as the Zeeman effect. Transitions from the ground state to excited state are allowed so long as $\Delta m_I = 0$ or 1. So for a nucleus with excited state spin 3/2, (such as $^{57}$Fe) will split the Mössbauer signal into four, and the ground state, spin 1/2 will split into two, there are six transitions and so the spectrum splits into six separate peaks.[138]

Mössbauer spectroscopy was carried out using a SEE Co. Model W302 Resonant Gamma Ray Spectrometer, with a $^{57}$Co(Rh) gamma ray source operating at 300 K.

### 2.1.4 Other techniques

#### 2.1.4.1 Super conducting quantum interference device (SQUID)

SQUID magnetometers are able to measure extremely small magnetic fields (as low as $10^{-15}$ T). Measurements are made by moving the magnetic sample through a set of measurement coils, thus inducing a current in those coils. The current causes a signal coil to produce a magnetic field which in turn influences the current in a closed superconducting loop containing two Josephson junctions (the SQUID itself). The current in the SQUID is affected by changes in magnetic flux as low as one half of a magnetic flux quantum *i.e.* approximately $10^{-15}$ Wb (hence the sensitivity of the technique). The resulting voltage across the SQUID is processed to determine the magnetisation of the sample.[139] Magnetisation data in this thesis was taken using a Quantum Design MPMS SQUID VSM Magnetometer (San Diego, USA) at 300 K using a field range of ± 7 Tesla.

### 2.1.4.2 Chemical vapour deposition

Chemical vapour deposition (CVD) is used to describe the branch of chemistry concerning the formation of a thin solid film on the surface of a substrate by the chemical reaction of precursors in the vapour phase.[140] Chemical reactions occur both in the gas phase and on the surface of the substrate, and can be further promoted by heat, UV-irradiation or plasma.

The basic CVD process can be broken down into a number of steps, which detail chemical and physical processes that occur throughout the process. The first step is the transport of the CVD precursors from the main gas flow into the reactor. This includes the nebulisation/atomisation of a precursor solution into the gas phase. This can be achieved using various methods such as: using ultrasound to create an aerosol (AACVD), direct liquid injection into a heated reactor, use of an atomiser and vaporisation of solid sources. Once vapourised, the precursors undergo gas phase reactions (figure 2.8) which form reactive intermediate species (step 2). These are transported by the carrier gas to the [heated] substrate in the reaction chamber, constituting step 3.

Gas phase intermediates and precursors are then adsorbed onto the surface of the substrate, and diffuse to nucleation and crystal growth sites, leading to film formation. Nucleation sites are areas within which crystals have begun to nucleate and often form on defects within the substrate, so crystal growth can be templated, leading to tunable crystal phase deposition. For example, if a rutile $TiO_2$ surface is deposited on a glass substrate, any subsequent titania depositions will template that crystal structure, even if conditions favourable for anatase titania growth are used, hence the difficulty in the synthesis of anatase/rutile junctions.[141]

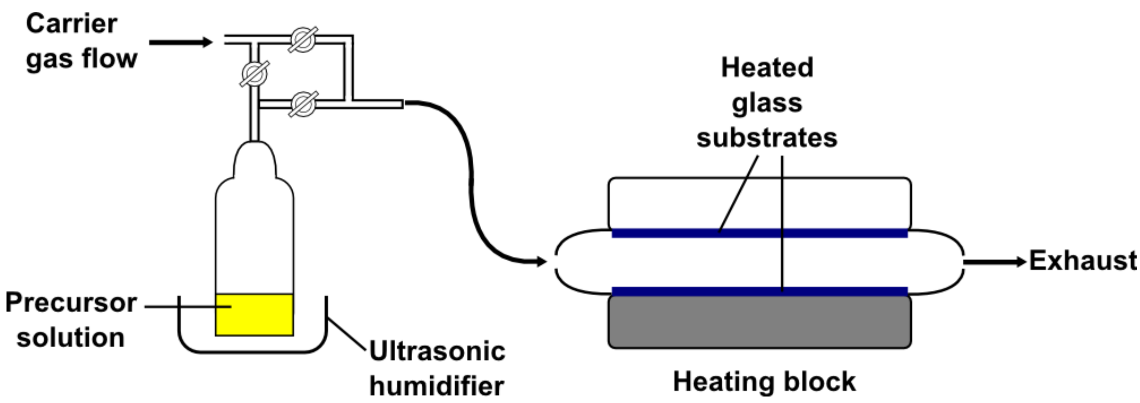

**Figure 2.8**: Schematic of an AACVD reactor.

The final step (step 4) involves the transport of the by-products of the CVD process out of the CVD reactor chamber *via* the exhaust and carrier gas.

It is noteworthy that in nanoparticluate depositions, thermophoretic effects are important in determining how and where the nanoparticles deposit. In the AACVD system used in this thesis, the glass substrates are placed above one another in the CVD reactor and the deposition occurs exclusively on the upper glass plate. In the gaseous phase, particles will preferentially move in the direction of decreasing temperature. This is due to particles having a higher average velocity at hotter points in the reactor, so they move away faster, hence upper glass plate depositions.

### 2.1.4.3 Other instrumental details

Raman spectra were taken over the range 400 – 4000 cm$^{-1}$ on a Renishaw Raman System 1000 using an argon ion laser ($\lambda$ = 514 nm) calibrated against the emission lines of neon. FTIR-ATR measurements were taken over 650 - 4000 cm$^{-1}$ on a Perkin-Elmer Spectrum-100 (Ge crystal) equipped with a universal ATR attachment. NMR samples were prepared by dissolving the analyte in $CDCl_3$ (2 ml) in a borosilicate glass NMR tube and obtained on a Brüker AV- 600 MHz spectrometer, operating at 295 K and 600.13 MHz ($^1$H). Dynamic light scattering size measurements were collected using a

Malvern Zetasizer Nano-ZS. X-ray diffraction patterns were obtained on a PanAlytical diffractometer using Co Kα radiation, $\lambda = 1.789010$ Å. Thermogravimetric analyses were obtained on a TA instruments TGA Q500 V6.7 with $N_2$ carrier gas between 25 and 1000 °C at a heating rate of 10 °C $min^{-1}$ at Queen Mary, University of London.

## 2.2 Synthesis of nanoparticles

### 2.2.1 Synthesis of iron oxide nanoparticles

Iron oxide nanoparticles were synthesised according to two different methods, both based on the thermal decomposition of iron salts in the presence of long chain alkyl surfactants in high boiling point solvents. These methods, along with co-precipitation are reviewed in chapter 5, and experimental details are as follows:

### 2.2.1.1 Synthesis of iron oxide nanoparticles from iron(III) acetylacetonate

~8 nm iron oxide nanoparticles were prepared from the decomposition of iron(III) acetylacetonate according to Lattuada and Hatton,[142] using an improved version of the synthesis realised by Sun and Zeng.[43] Briefly, iron(III) acetylacetonate (0.706 g, 2 mmol) and 1,2-tetradecanediol (2.30 g, 10 mmol), oleic acid (1.91 ml, 6 mmol), oleylamine (1.97 ml, 6 mmol) and benzyl ether (20 ml, 105.2 mmol) were added to a 250 ml three-necked flask and stirred thoroughly at room temperature giving a red/brown mixture. The reaction mixture was evacuated/back-filled with nitrogen 3 times before heating to 100 ºC at a rate of 2.5 ºC $min^{-1}$, and held at 100 ºC for 45 minutes. The reaction mixture was then heated to 200 °C at a rate of 2.5 ºC $min^{-1}$ and held at 200 ºC for 2 hours, before heating to 300 ºC for one hour before cooling to room temperature. Ethanol (2 × 50 ml) was added to the resultant black suspension, before centrifugation (504 × *g* for 10 minutes). The solid black precipitate was re-dispersed in the desired organic solvent (15 ml total).

### 2.2.1.2 Synthesis of iron(III) oleate

Iron(III) oleate was prepared, according to Park *et. al.*[45] Briefly, a suspension of iron(III) chloride hexahydrate (10.8 g, 40 mmol) and sodium oleate (36.5 g, 120 mmol) in a solvent mixture of *n*-hexane (140 ml), deionised water (60 ml) and ethanol (80 ml) was heated to 70 ºC for 4 hours. The organic layer was separated and washed with 3 × 30 ml portions of distilled water to remove sodium chloride. The dark organic layer was dried *in vacuo* to remove *n*-hexane, yielding the iron(III) oleate complex as a waxy solid. It is difficult to quantify the yield of oleate species as they do not crystallise, excess sodium oleate has the same solubility as the final product and the absorption of excess solvent can be beneficial to the nanoparticle formation process, so removing it could be detrimental to the monodispersity of the final product (section 5.1).[143]

### 2.2.1.3 Synthesis of iron oxide nanoparticles from iron(III) oleate

For ~15 nm particles: iron(III) oleate (18.0 g, 20 mmol) and oleic acid (2.35 ml, 10 mmol) were dissolved in 1-octadecene (100 g, 396.1 mmol) and stirred thoroughly at room temperature. The reaction mixture was heated to 320 ºC at a rate of 3.3 ºC min$^{-1}$ under nitrogen and held at 320 ºC for one hour. The resulting black dispersion was allowed to cool to room temperature before addition of ethanol (250 ml) to precipitate the particles. The dispersion was centrifuged at 504 × *g* for 10 minutes, giving solid particle precipitates. If the precipitate was not solid, excess oleate-type species were removed by washing with ethanol (2 × 80 ml). The supernatant was discarded and the solid particle precipitates dispersed in the desired organic solvent (30 ml total).

Nanoparticle size can be controlled by the ratio of oleic acid to iron(III) oleate in the reaction, with larger nanoparticle sizes achieved with a higher ratio of oleic acid to iron(III) oleate.[45]

### 2.2.2 Synthesis of iron oxide nanoparticles using high street reagents

#### 2.2.2.1 Synthesis of iron palmitate

Iron palmitate was prepared, according to Park *et. al.*[45] Briefly, a suspension of homogenised iron tablets (20 tablets each containing 14 mg of iron as iron gluconate) and soap (assumed to be 65 % sodium palmitate, 0.321 g, 1.15 mmol) in a solvent mixture of *n*-hexane (140 ml), deionised water (60 ml) and ethanol (80 ml) was heated to 70 °C for 4 hours. The organic layer was separated and washed with 3 × 30 ml portions of distilled water to remove sodium chloride. The dark organic layer was dried *in vacuo* to remove *n*-hexane, yielding the iron palmitate complex as a brown, waxy solid.

#### 2.2.2.2 Synthesis of iron oxide nanoparticles from iron palmitate

Iron palmitate (2 g, 2.4 mmol) and olive oil (0.59 ml, 1.2 mmol of oleic acid) were dissolved in 1-octadecene (15.8 g, 62.5 mmol) or shark liver oil (20 ml) and stirred thoroughly at room temperature. The reaction mixture was heated to 320 °C at a rate of 3.3 °C min$^{-1}$ under nitrogen and held at 320 °C` for 1 hour. The resulting black dispersion was allowed to cool to room temperature before addition of ethanol (100 ml) to precipitate the particles. The dispersion was centrifuged at 600 × *g* for 10 minutes, giving solid particle precipitates. If the precipitate was not solid, excess oleate-type species were removed by washing with ethanol (2 × 80 ml). The supernatant was discarded and the solid particle precipitates dispersed in the desired organic solvent (20 ml total).

### 2.2.3 Synthesis of other metal oxide nanoparticles

#### 2.2.3.1 Cobalt oxide nanoparticles

Cobalt oxide nanoparticles were synthesised according to the procedure described by Park *et al.*[45] The synthesis involved the decomposition of cobalt(II) oleate, which was synthesised using the same procedure in section 2.2.2.2, replacing iron(III) chloride hexahydrate with cobalt(II) chloride hexahydrate (6.35 g, 26.7 mmol). The quantity of sodium oleate was also reduced, as the desired product is cobalt(II) oleate (24.3 g, 80 mmol). This process yielded a waxy purple solid. It is noteworthy that cobalt(II) oleate degrades in air unlike iron or nickel variants, so should be decomposed as soon as synthesised.

Decomposition of cobalt(II) oleate followed the same procedure and conditions as the decomposition of iron(III) oleate, yielding a green dispersion of “bullet” shaped anisotropic cobalt oxide nanoparticles.

#### 2.2.3.2 Nickel oxide nanoparticles

Nickel oxide nanoparticles were synthesised according to the procedure described by Park *et al.* [45] The synthesis involves the decomposition of nickel(II) oleate, which was synthesised using the same procedure in section 2.2.2.2, replacing iron(III) chloride hexahydrate with nickel(II) chloride hexahydrate (6.34 g, 26.7 mmol). The quantity of sodium oleate was also reduced, as the desired product is nickel(II) oleate (24.3 g, 80 mmol).This process yielded a bright green solid.

Decomposition of nickel(II) oleate followed the same procedure and conditions as the decomposition of iron(III) oleate, yielding a grey dispersion of spherical nickel oxide nanoparticles.

### 2.2.3.3 Titanium dioxide nanoparticles

Titanium dioxide nanoparticles were synthesised according to a process developed by Cozzoli *et al.*[144] Briefly, oleic acid (39.3 ml, 123.9 mmol) was purged with nitrogen for 1 hour at room temperature in a closed 250 ml round bottomed flask. Titanium(IV) isopropoxide (1.48 ml, 5 mmol) was added and stirred for 10 minutes, giving a yellow solution. A triethylamine (1.12 ml, 8 mmol) in ethylene glycol (4.49 ml, 80.6 mmol) solution was added, and the reaction vessel heated to 100 °C and stirred for 48 hours.

Ethanol (2 × 40 ml) was added to the resultant orange solution, which precipitated the white anatase titania particles. The particles were obtained as a solid pellet after centrifugation at 504 × *g* for 10 minutes and were then washed with portions of ethanol (3 × 40 ml) before re-dispersion in chloroform (30 ml).

### 2.2.3.4 Titanium dioxide nanoparticles (CHFS)

Hydrothermally synthesised anatase nanoparticles were provided by Dr. Christopher Tighe and Prof. Jawwad Darr (UCL) as an aqueous slurry.[145] The aqueous slurry was subsequently lyophilised and used as a white powder.

### 2.2.3.5 Titanium dioxide nanoparticles (CHFS) functionalisation

Anatase nanoparticles were heated to 80 °C in excess oleic acid (38.1 ml, 120 mmol), with a catalytic amount of triethylamine (1.12 ml, 8 mmol) for 24 hours.

Ethanol (100 ml) was added to the resultant white suspension, which precipitated the anatase particles. The particles were obtained as a solid pellet after centrifugation at 504 × *g* for 10 minutes and were then washed with portions of ethanol

(2 × 80 ml) before re-dispersion in $CHCl_3$ (30 ml).

### 2.2.4 Metal nanoparticles

#### 2.2.4.1 Gold nanoparticles

Au nanoparticles were synthesised using an adapted "Brüst-Schiffrin" method, described by Palgrave and Parkin.[146] Briefly, a solution of gold(III) chloride trihydrate (0.146 g, 0.43 mmol) in deionised water (15 ml) was mixed with a solution of tetraoctylammonium bromide (1.04 g, 1.90 mmol) in toluene (40 ml) under vigorous stirring, forming a two phase system.

To reduce $Au^{3+}$, a solution of sodium borohydride (0.190 g, 5.02 mmol) in deionised water (25 ml) was added dropwise over 30 minutes. During this time, the solution turned from orange to colourless to purple, indicating the formation of gold nanoparticles. The toluene layer was separated and washed with 2 × 50 ml portions of 1 mol $dm^{-3}$ sulphuric acid solution and deionised water (100 ml). The toluene layer was dried over sodium sulphate (~5 g) and diluted to 100 ml with toluene.

To increase the longevity of colloidal stability, 1-dodecanethiol (20 ml, 8.34 mmol) was added to tetraoctylammonium bromide functionalised gold nanoparticles in toluene (100 ml)  were heated to 60 °C for 24 hours. The nanoparticles were precipitated with ethanol ((2 × 200 ml) and centrifuged at 504 × *g* for 10 minutes, and re-dispersed in toluene (50 ml).

#### 2.2.4.2 Nickel nanoparticles

Nickel nanoparticles were prepared according to Carenco *et al.* with modifications.[66] Briefly, nickel(II) acetylacetonate (2.0 g, 7.8 mmol) was dissolved in ten equivalents of oleylamine (25.58 ml, 78 mmol). Trioctylphosphine (2.76 ml, 6.24 mmol) was added, and the mixture subjected to 3 vacuum/nitrogen flushes. The mixture was heated to 100

°C at a rate of 3.0 °C $\mathrm{min}^{-1}$. The mixture was subjected to 3 further vacuum/nitrogen flushes whilst the temperature was maintained at 100 °C for 30 minutes. The temperature was then raised to 220 °C at a rate of 3.0 °C $\mathrm{min}^{-1}$ and maintained for two hours. The resulting black dispersion was allowed to cool to room temperature before addition of ethanol (80 ml) to precipitate the particles. The Ni particles were then centrifuged at 504 × *g* for 10 minutes, giving solid particle precipitates. The supernatant was discarded and the solid particle precipitates dispersed in chloroform (15 ml total).

### 2.2.5 Quantum dots

Quantum dots were synthesised using the air-sensitive hot-injection synthesis, the theory of which is discussed in section 1.4. The methods described herein for the synthesis of cadmium selenide and indium phosphide involve the injection of cold selenium/phosphorus-surfactant into a hot solution of the respective metal-surfactant mixture. This allows for an instantaneous and distinct nucleation and crystal growth phases, and a monodisperse product.

#### 2.2.5.1 CdSe quantum dots

CdSe quantum dot cores were synthesised using a modified procedure Cadmium oxide (0.0514g, 0.4 mmol), hexadecylamine (1.928 g, 8 mmol), 1-dodecylphosphonic acid (0.2203 g, 0.88 mmol) and trioctylphosphine oxide (3.7114 g, 9.6 mmol) were subjected to 3 vacuum/nitrogen flushes before rapid heating (10 °C $\mathrm{min}^{-1}$) under nitrogen to 320 °C. The temperature was maintained at 320 °C until the solution became colourless.

A degassed suspension of selenium powder (0.315 g, 4 mmol) in trioctylphosphine (8 ml, 17.9 mmol) was injected into the mixture in order to initiate nucleation. This lowered the temperature to 270 °C, which was maintained for two minutes to allow the crystals to grow (~ 4 nm diameter, emission wavelength $\lambda = 590$ nm). The reaction flask was immediately cooled by placing in a water bath (~ 90 °C) then cooled to room temperature. Chloroform (10 ml) was injected, and the CdSe quantum dots were precipitated with ethanol (2 × 40 ml) and centrifuged at 504 × *g* for 10 minutes. The supernatant was then re-suspended in *n*-hexane (10 ml).

### 2.2.5.2 CdSe/ZnS core/shell quantum dots using diethylzinc

ZnS shells were grown around CdSe quantum dot cores according to the process developed by Roullier *et al.* [71] Briefly, a solution of diethylzinc (1.325 ml of a 1.0 mol $dm^{-3}$ stock solution in hexanes), 1,1,1,3,3,3-hexamethyldisilathiane (360 μl, 1.71 mmol) and trioctylphosphine (10 ml, 22.4 mmol) were added to an oven-dried Schlenk flask in a glovebox due to the pyrophoric nature of diethylzinc and obnoxious odour of 1,1,1,3,3,3-hexamethyldisilathiane.

Separately, a 250 ml three necked round bottom flask was charged with trioctylphosphine oxide (3.71 g, 7.2 mmol) and hexadecylamine (1.93 g, 8 mmol). The flask was heated to 150 °C with stirring for 1 hour and held *in vacuo*. After cooling to 70 °C, the core dispersion in *n*-hexane (described above) was injected and evacuated/re-filled with nitrogen 3 times before heating to 160 °C under nitrogen. The shelling solution was added slowly over one hour, before the flask was cooled to room temperature. Chloroform (4 ml) was added, before precipitation of the quantum dots with ethanol (50 ml) and centrifugation ( 504 × *g* for 5 minutes). The quantum dots were dispersed in *n*-hexane (10 ml) and stored in the dark prior to use.

In order to tune wavelength emission, UV/vis spectroscopy can be used. If the desired wavelength of emission is reached before all of the shelling precursor is added, then the reaction can be rapidly quenched by immersing the flask in cold water.

### 2.2.5.3 CdSe/ZnS core/shell quantum dots using zinc(II) diethyldithiocarbamate

Core/shelling of CdSe cores using single source zinc(II) diethyldithiocarbamate was completed using a procedure developed by Deflethsen and Døssing.[147] Briefly, zinc(II) diethyldithiocarbamate (0.507 g, 1.40 mmol) was subjected to 3 vacuum/nitrogen flushes before injection of 1-octadecene (10 ml, 31.25 mmol), trioctylphosphine (3 ml, 6.73 mmol) and oleylamine (3 ml, 9.12 mmol). The CdSe quantum dot dispersion in *n*-hexane was injected, and the dispersion heated to 70 °C at a rate of 2.2 °C $\text{min}^{-1}$ and *n*-hexane removed *in vacuo*. The dispersion was then heated to 120 °C at a rate of 2.2 °C $\text{min}^{-1}$ and maintained at that temperature for two hours. The reaction was allowed to cool to room temperature before addition of ethanol (60 ml) and the CdSe/ZnS quantum dots isolated by centrifugation at 504 × *g* for 10 minutes. The quantum dots were washed twice with ethanol (2 × 60 ml) to remove any unbound surfactants and unreacted diethyldithiocarbamates, and dispersed in *n*-hexane (15 ml).

### 2.2.5.4 CdSe modified shelling procedure with metal dithiocarbamate species

The modified procedure for the forming of composite quantum dot shells involved the addition of a mixture of zinc(II) diethyldithiocarbamate and metal dithiocarbamate species according to the procedure above. Metal dithiocarbamate species were prepared through the salt metathesis reaction between sodium diethyldithiocarbamate trihydrate (2.65 g, 11.74 mmol) and the corresponding metal chloride (*i.e.* copper(II) chloride, 1 g, 5.87 mmol) in deionised water (40 ml).[148,149] The reaction was stirred for 2 hours, during which a precipitate of black copper(II) diethyldithiocarbamate formed. The product was filtered under reduced pressure and washed with deionised water (3 × 30 ml), before dissolution in dichloromethane (50 ml). The black solution was stirred with magnesium sulphate for 30 minutes, after which the mixture was filtered and the filtrate dried *in vacuo*. The product was then re-crystallised from chloroform.

Yield 1.84 g, 87%. Anal. Calc. for $C_{10}H_{20}N_2S_4Cu$**:** C, 33.36; H, 5.60; N, 7.78.

Found: C, 33.33; H, 5.58; N, 7.74.

### 2.2.5.5 InP quantum dots

Indium phosphide quantum dots were synthesised according to Xu *et al.*[69] Briefly, a nitrogen-purged Schlenk flask was charged with stearic acid (28.5 mg, 0.1 mmol), zinc undecylenate (86 mg, 0.2 mmol), indium(III) chloride (22 mg, 0.1 mmol) and hexadecylamine (48 g, 0.2 mmol). 1-octadecene (2 ml) was added, and the mixture vacuum/back filled with nitrogen 3 times before heating to 270 °C. On reaching 270 °C, a solution of tris(trimethylsilyl)phosphine (1 ml, 0.1M) in 1-octadecene was rapidly injected, and the solution heated at 240 °C for 20 minutes to allow the quantum dots to grow. The flask was then placed in water to cool to room temperature, before addition of toluene (4 ml). InP quantum dots were precipitated with ethanol (~ 80 ml) and isolated by centrifugation (5 minutes at 3000 × *g*). The quantum dots were washed twice with ethanol (2 × 60 ml) to remove any unbound surfactants, and dispersed in *n*-hexane (10 ml).

### 2.2.5.6 InP/ZnS quantum dots

A shell of ZnS was synthesised by the thermal decomposition of zinc(II) diethyldithiocarbamate according to a modified procedure by Xu *et al.*[150] Briefly, the three-necked flask containing the InP cores synthesised in 2.2.5.5 was charged with zinc(II) diethyldithiocarbamate (72 mg, 0.2 mmol), zinc undecylenate (180 mg - amount used in 2.2.5.5). The mixture was subjected to 3 vacuum/nitrogen flushes before heating at 180 °C for 10 minutes, then annealed at 240 °C for 20 minutes. The reaction was cooled to room temperature before addition of ethanol (60 ml) and the InP/ZnS quantum dots isolated by centrifugation at 3000 × *g*. The quantum dots were washed twice with ethanol (2 × 60 ml) to remove any unbound surfactants and unreacted diethyldithiocarbamates, and dispersed in *n*-hexane (10 ml).

### 2.2.5.7 InP modified shelling procedure with metal dithiocarbamate species

The modified procedure for the forming of composite quantum dot shells involved the addition of a mixture of zinc(II) diethyldithiocarbamate and a metal dithiocarbamate according to the procedure above.

### 2.2.6 Miscellaneous nanoparticle processes

### 2.2.6.1 Amphiphilic polymer nanoparticle coating and hyperthermia testing

Nanoparticle amphiphilic polymer coating was carried out according to a protocol developed by Lees *et al.*[151] Although described here solely for the phase transfer of iron oxide nanoparticles from hexane to water, this process is applicable for the phase transfer/functionalisation of any hydrophobically ligated nanoparticles

Briefly, iron oxide nanoparticles in hexane (5 ml) were precipitated with ethanol (~100 ml), centrifuged and the solid residue re-dispersed in chloroform (10 ml). Poly(maleic anhydride-*alt*-1-octadecene) (10 mg) was dissolved in chloroform (10 ml) and added under vigorous stirring to the nanoparticle dispersion and left to stir for 1 hour. The chloroform was removed slowly *in vacuo* (750 mbar, 25 °C water bath) and then subsequently placed under a ~$10^{-2}$ mbar vacuum for 24 hours. 20 ml of a 0.1 mol $dm^{-3}$ solution of tetramethyl ammonium hydroxide was added, and left overnight to react. Once the nanoparticles were fully dispersed, the dispersion was acidified to pH 8 with acetic acid before concentration with centrifuge filters (Centriprep YM-10, 10 kDa MW cutoff for 3 × 20 minute cycles at 3000 × *g*).

Aqueous dispersions of amphiphilic polymer coated nanoparticles (concentration 1 mg/ml) were exposed to an alternating magnetic field of strength 6.6

kA/m and frequency 945 kHz in a water-cooled 6-turn coil 36 mm in length with an internal diameter of 18 mm. Temperature readings were recorded using fibre-optic thermocouples.

#### **2.2.6.2 Functionalisation of gold nanoparticles with silica**

Silica coating of gold nanoparticles utilised adapted procedures described by Darbandi *et al.*[152] and hydrophobised according to Pastoriza-Santos *et al.*[153] Briefly, Igepal® CO-520 (26 ml) and the gold nanoparticles in toluene (described above, 16 ml) were added to cyclohexane (400 ml) under vigorous stirring. Tetraethylorthosilicate (0.24 ml, 1.07 mmol) and (3-mercaptopropyl) trimethoxysilane (0.24 ml, 1.29 mmol) were added and the solution stirred for 30 minutes. Ammonia solution (16 μl, 33 wt% in water) was quickly added and the dispersion stirred for 24 hours to allow silane polymerisation to be completed.

The microemulsion system was broken by addition of acetone (~ 200 ml) and centrifuged at 504 × *g* for 10 minutes. The precipitated gold/silica particles were washed with butanol (~50 ml), 2-propanol (~50 ml), ethanol (~50 ml) and methanol (~50 ml) in that order. The resulting particles were dispersed with sonication in ethanol.

The particles were hydrophobised using trimethoxy(octadecyl) silane (2.4 % solution in 3 ml chloroform). Gold/silica particles in ethanol (15 ml) were mixed with ammonia solution (300 μl, 33 wt % in water) and added dropwise to the trimethoxy(octadecyl) silane solution under vigorous stirring. After 24 hours, the hydrophobic particles were centrifuged at 504 × *g* for 10 minutes, washed with ethanol (15 ml) and dispersed in chloroform (15 ml).

### **2.2.7 Catalytic processes**

#### **2.2.7.1 Photodegredation of Resazurin dye**

Poly(dimethylsiloxane) (PDMS)-titania nanoparticle composites were evaluated for photocatalytic activity through the photo-induced decomposition of Resazurin ® dye. [154] Briefly, glycerol (0.3 g, 3.26 mmol), hydroxyethyl cellulose (0.045 g, 0.0005 mmol) and Resazurin ® dye (4 mg) were added to a 1:1 v/v solution of water and methanol (ml) with 3g of this solution applied to two square inches of the surfaces under scrutiny, including a float glass control. UV irradiation ($\lambda = 365$ nm, 3.40 eV) was applied, and the dye degradation monitored via UV-vis spectroscopy.

### 2.2.7.2 Reaction of nickel nanoparticles with ammonia-borane complex

Ammonia-borane ($H_3N{:}\rightarrow BH_3$) is a promising hydrogen storage material due to its ability to liberate 3 equivalents of hydrogen for every equivalent of ammonia-borane (section 3.7). The catalytic activity of nickel nanoparticle containing superhydrophobic surfaces using the protocol developed by Li *et al.*[155] Briefly, ammonia-borane complex (0.1 g, 3.24 mmol) was dissolved in deionised water in a Schlenk flask fitted with a hose for hydrogen collection under water. One square inch of glass was cut and placed in the solution, and the hose placed under a glass measuring 100 ml measuring cylinder to collect evolved hydrogen. Finally, the Schlenk flask was sealed with a stopper with high vacuum grease.

### 2.2.7.3 Catalytic testing of CdSe/ZnS-CuS quantum dots

The catalytic activity of CdSe/ZnS-CuS quantum dots was tested using the “click” reaction between benzyl azide and phenyl acetylene. To a suspension of quantum dots (3.33 mg, 5 wt %) in *n*-hexane (1ml) phenyl acetylene (109.8 µL, 1 mmol) was added with stirring. Benzyl azide (62.5 µL, 66.5 mg, 0.5 mmol) was then added to the solution and the mixture irradiated for a set time. Upon completion $CDCl_3$ (2 ml) was added and the sample yield ascertained by $^1H$ NMR immediately.

### 2.2.8 Aerosol assisted chemical vapour deposition

Aerosol assisted chemical vapour deposition (AACVD) of superhydrophobic surfaces was undertaken according to Crick *et al.*[156,157] AACVD of superhydrophobic surfaces and nanoparticle incorporation is discussed in detail in chapter 3, section 3.1. The two components of Sylgard-184 ® Silicone Elastomer (0.70 g) were dissolved in an arbitrary volume of chloroform (40 ml) with rapid stirring. The chloroform dispersed nanoparticles (all of the above in separate experiments) were added to the solution and the total volume of precursor was made up to 70 ml. To prevent premature curing the mixture was used immediately after stirring for deposition studies. Nanoparticle dispersions in chloroform were added at this stage, with a portion of chloroform replaced with a nanoparticle suspension (~ 0.1 g in 10 ml of chloroform).

Depositions were carried out in a cold-walled horizontal bed chemical vapour deposition (CVD) reactor. The reactor contained top and bottom plates, both comprised of $SiO_2$ coated barrier glass (dimensions: 145 x 45 x 5 mm; barrier thickness 50 nm) supplied by Pilkington NSG. A carbon block on which the bottom plate was placed heated the CVD reactor. The top plate was positioned 8 mm above and parallel to the bottom plate, the complete assembly was enclosed within a quartz tube. The aerosol of the precursor solution was generated using a PIFCOHEALTH ultrasonic humidifier with an operating frequency of 40 kHz and 25 W of power. The aerosol generated was moved to the reactor using a nitrogen gas flow *via* PTFE (polytetrafluoroethylene) and glass tubing, where it entered between the top and bottom plates. The reactor waste gas left *via* an exhaust. Nitrogen flow carried the vapour from the flask until all liquid was gone, which took typically 45 minutes per deposition.

The heated carbon block was then turned off and allowed to cool to room temperature, the nitrogen flow was left on for a further 10 minutes. The cooled plates were removed and handled in air. The deposition of the films occurred to the top plate. The reactor temperature was maintained at 390 °C throughout the deposition, as measured by a thermocouple in the carbon heater block.

## 2.3 Materials

In this section, chemicals are listed by chapter and their purities and manufacturer are recorded.

### 2.3.1 Solvents

All solvents were used as received, unless stated otherwise, and are listed in the following table:

| Solvent | Manufacturer | Purity |
|---|---|---|
| Acetone | VWR Ltd. | Min. 99 % |
| Benzyl ether | Sigma Aldrich Ltd. | 98 % |
| 1-Butanol | Fisher Scientific Ltd. | 99.9 % |
| Chloroform | Sigma Aldrich Ltd. | HPLC grade, ≥ 99.8 % |
| Cyclohexane | Sigma Aldrich Ltd. | ACS reagent, ≥ 99 % |
| Dichloromethane | Sigma Aldrich Ltd. | ACS reagent, ≥ 99.5 % |
| Ethanol | Fisher Scientific Ltd. | ≥ 97 % |
| Ethylene glycol | Sigma Aldrich Ltd. | ≥ 99 %, Reagent + |
| *n*-hexane | Sigma Aldrich Ltd. | Laboratory reagent, ≥ 95 % |
| Methanol | Fisher Scientific Ltd. | ≥ 99.5 % |
| 1-Octadecene | Sigma Aldrich Ltd. | Technical grade, 90% |
| Phenyl ether | Sigma Aldrich Ltd. | ≥ 99 % |
| 2-Propanol | Fisher Scientific Ltd. | ≥ 99.5 % |
| Toluene | Sigma Aldrich Ltd. | ACS Reagent, ≥ 99.5 % |
| Water (distilled) | ELGA DV25 Purelab option 15.0 Ω M cm. | |

**Table 2.1**: Common laboratory solvents used.

### 2.3.2 Chapter 3 materials

| Chemical | Manufacturer | Purity |
|---|---|---|
| Sylgard-184® Silicone Elastomer | Univar Speciality Consumables | - |
| Gold(III) chloride hydrate | Alfa Aesar | 49.96 % Au |
| Triethylamine | Alfa Aesar | 99 % |
| Iron(III) chloride hexahydrate | VWR International Ltd. | 98 % |
| Oleic acid | Sigma Aldrich Ltd. | Technical grade, 90% |
| Oleylamine | Sigma Aldrich Ltd. | Technical grade, ≤ 70% |
| Sodium oleate | Sigma Aldrich Ltd. | ≤ 82% fatty acid content |
| Trioctylphosphine | Sigma Aldrich Ltd. | Technical grade, 90% |
| Trioctylammonium bromide | Sigma Aldrich Ltd. | 98 % |
| Titanium(IV) isopropoxide | Sigma Aldrich Ltd. | 97 % |
| Cobalt(II) chloride hexahydrate | Sigma Aldrich Ltd. | Reagent grade |
| Nickel(II) acetylacetonate | Sigma Aldrich Ltd. | 95 % |
| Igepal ® CO-520 (average $M_n$ = 441) | Sigma Aldrich Ltd. | - |
| Tetraethyl orthosilicate | Sigma Aldrich Ltd. | ≥ 99.0 % |
| Trimethoxy-(octadecyl)silane | Sigma Aldrich Ltd. | Technical grade, 90% |
| (3-Mercaptopropyl) trimethoxysilane | Sigma Aldrich Ltd. | 95 % |
| 2-Hydroxyethyl cellulose | Sigma Aldrich Ltd. | Average $M_w$ ~ 90,000 |
| Glycerol | Sigma Aldrich Ltd. | 99.5 % |
| Resazurin ® dye | Sigma Aldrich Ltd. | 92 % |
| Sodium borohydride | Sigma Aldrich Ltd. | ≥ 96 % |

**Table 2.2**: Reagents used in chapter 3.

### 2.3.3 Chapter 4 materials

| Chemical | Manufacturer | Purity |
|---|---|---|
| Cadmium(II) oxide | Alfa Aesar | 98.9 % |
| Copper(II) chloride | Sigma Aldrich Ltd. | 99.995 %, trace metal basis |
| 1-Dodecylphosphonic acid | Alfa Aesar | 95 % |
| Hexadecylamine | Alfa Aesar | Technical grade, 90% |
| Oleylamine | Sigma Aldrich Ltd. | Technical grade, ≤ 70% |
| Selenium powder, 200 mesh | Acros | 99.5+ % |
| Sodium diethyldithiocarbamate trihydrate | Sigma Aldrich Ltd. | ≥ 99.995 %, trace metal basis |
| Stearic acid | Sigma Aldrich Ltd. | Reagent grade, 95 % |
| Trioctylphosphine | Sigma Aldrich Ltd. | Technical grade, 90% |
| Trioctylphosphine oxide | Sigma Aldrich Ltd. | Technical grade, 90% |
| Tris(trimethylsilyl)phosphine | Sigma Aldrich Ltd. | 95 % |
| Indium(III) chloride | Sigma Aldrich Ltd. | 98 % |
| Zinc(II) diethyldithiocarbamate | Sigma Aldrich Ltd. | 97 % |
| Zinc undecylenate | Sigma Aldrich Ltd. | 98 % |

**Table 2.3**: Reagents used in chapter 4.

In the preparation of the trioctylphosphine-Se stock solution, 1-octadecene was dried over sodium and subjected to 3 freeze-pump-thaw cycles before use.

# Chapter 3: Superhydrophobic polymer-nanoparticle composites by aerosol assisted chemical vapour deposition

## Preface

For a surface to be superhydrophobic, the water contact angle must exceed 150°, otherwise it is defined as hydrophobic ($150° < x < 90°$) or hydrophilic ($90° < x < 0°$). Superhydrophobic surfaces have a plethora of uses in many industrial and everyday applications, from clothing to self-cleaning windows,[158–160] with the eventual goal being multi-functional surfaces.

The use of nanoparticles to do this is a very viable method with a great deal of literature precedent. However, retention of superhydrophobicity and nanoscopic properties has proven difficult, in part due to photocatalytically active nanoparticles destroying the superhydrophobic matrix in which the nanoparticles are housed. Nanoparticle surface contact is also challenging, as the matrix often encapsulates the nanoparticles completely.

In this chapter, developments in superhydrophobic polymer and superhydrophobic polymer-nanoparticle composite surfaces are reviewed. Subsequent experimental work paved the way for a general method for the synthesis of a novel class of superhydrophobic polymer thin films with embedded nanoparticles, which is presented here. These materials combine the superhydrophobic nature of silicone polymer matrices and the properties of the nanoparticles for photocatalysis, magnetic applications, or high surface area catalysis. The films themselves are deposited using a one-pot aerosol assisted chemical vapour deposition process, and are characterised using electron microscopy, energy dispersive X-ray spectroscopy, water contact angle and bouncing measurements and EELS elemental mapping. We show that these materials demonstrate multifunctional behaviour through magnetic, catalytic and superhydrophobic measurements. The synthesis of the first magnetic/ superhydrophobic composite is also presented.

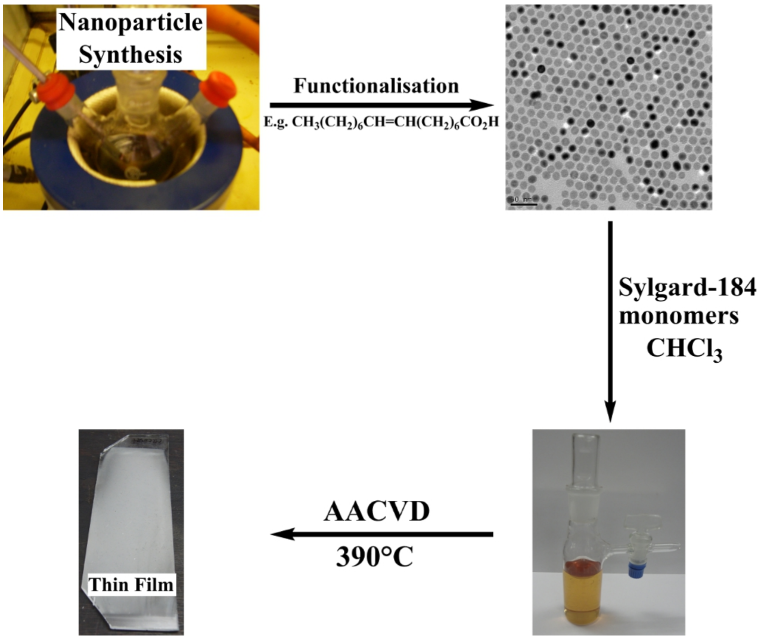

**Figure 3.1**: Scheme illustrating the preparation of superhydrophobic polymer-nanoparticle composites.

## 3.1 Superhydrophobic surfaces- An introduction

Superhydrophobic surfaces have received a great deal of interest in the literature for their numerous industrial and commercial applications. Most take their inspiration from nature, with the "Lotus effect" being the most well known example.[161] The superhydrophobicity of lotus leaves stems from the rough, waxy cuticle layer on top of the leaf. Other natural examples in nature include the wings of certain insects, fruit and lizards.[160,162] All of these examples require extreme water repellency to prevent bacterial or fungal adhesion, as the contact area with the surface is dramatically reduced. Bacteria or fungal spores may also be washed off by water droplets running over the surface, a very important process for plants and one which has been mimicked in superhydrophobic anti-bacterial surfaces.[163,164]

The definition of superhydrophobicity is determined by the water contact angle, which is the angle between the plane of a surface and the tangent made by the water droplet at the solid-liquid-air interface, figure 3.2. For a surface to be superhydrophobic, the water contact angle must exceed 150°, otherwise it is defined as hydrophobic ($150° < x < 90°$) or hydrophilic ($90° < x < 0°$).

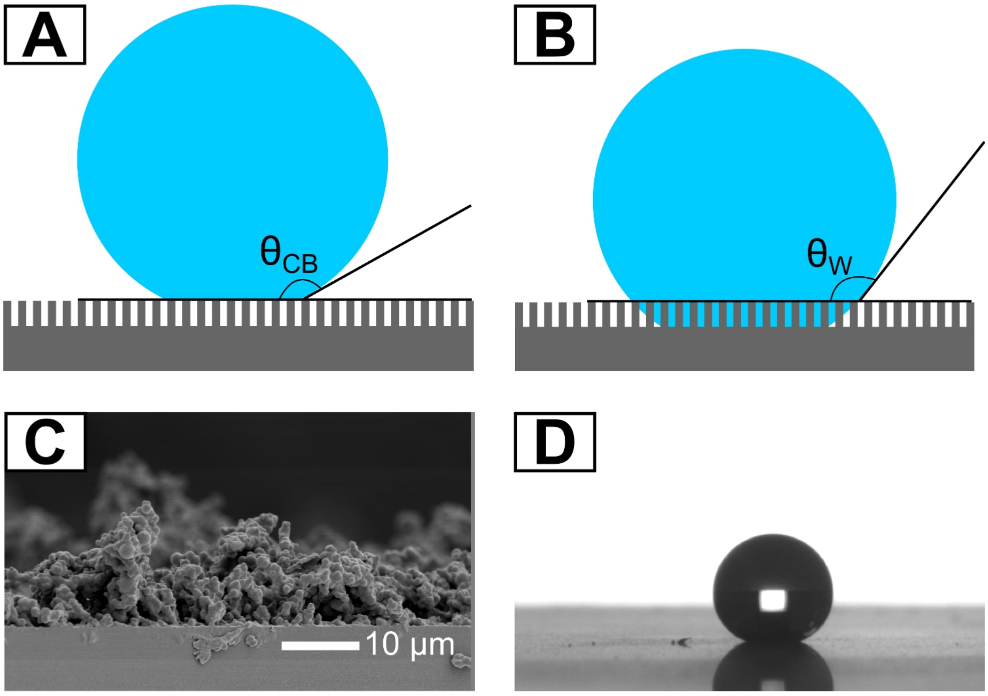

**Figure 3.2**: A) The Cassie-Baxter model of surface wetting details a highly rough, microstructured surface with air trapped beneath the water droplet, B) The Wenzel model shows no air underneath the droplet, but the water contact angle is exacerbated by the surface roughness versus the interfacial tension of the surface and the droplet, C) An SEM micrograph of a rough, superhydrophobic poly(dimethylsiloxane) (PDMS) surface on a glass substrate and D) A sessile water droplet on the surface in C).

Superhydrophobicity can be modelled using two methods: the Wenzel[165] and the Cassie-Baxter.[166] The Wenzel model makes use of the interfacial tension between the water droplet and the solid surface, and applies when a surface is micro- or nanostructured, and the water droplet is in intimate contact with the surface with no trapped air underneath. The contact angle the water droplet makes with the surface is dependent on the roughness ratio of the surface “r”, and so the contact angle is exacerbated with increasing surface roughness (equation 9):

$$\cos\theta_W = r\cos\theta \qquad \text{Equation 9}$$

Where "$\theta_W$" is the contact angle due to the Wenzel effect, and "$\theta$" the predicted contact angle. Increased microstructuring of the surface exacerbates the contact angle whether it is above or below 90°, so hydrophilic surfaces become more hydrophilic and hydrophobic surfaces become more hydrophobic.

The Cassie-Baxter model is also a consequence of micro/nanostructuring whereby air is trapped under the water droplet. This means that friction is drastically reduced, so water can easily "roll off" the surface. This state is reached when the surface roughness is such that the droplet is suspended from just the rough "spikes" on the surface. The equation for the Cassie-Baxter state is given below:

$$\cos\theta_D = -\frac{E_D}{\gamma_{LA}} = f_1\cos\theta_E - f_2 \qquad \text{Equation 10}$$

Where "$\theta_D$" is the contact angle due to the Cassie-Baxter effect, "$f_1$" and "$f_2$" are the interfacial energies, "$E_D$" is the total energy associated with the Cassie-Baxter model, "$\gamma_{LA}$" is the liquid-air interfacial energy and "$\theta_E$" is the static contact angle for the solid-liquid interface. It is noteworthy that this equation reduces to the Wenzel model when "$f_2$" = 0. The Cassie-Baxter equation accounts for the contact the water droplet has at the solid-liquid interface as well as the air-solid interface. The Cassie-Baxter model can be simplified to assume that the solid-liquid interface is flat, as in figure 3.2, A).[167]

$$\cos\theta_D = \varphi(\cos\theta_E + 1) - 1 \qquad \text{Equation 11}$$

Where "$\varphi$" is the fraction of the solid which is in contact with the liquid. The Cassie-Baxter state will revert to the Wenzel state when "$\cos\theta > (\varphi - 1)/(r - \varphi)$", when the contact area of the water droplet is large.

### 3.1.1 Superhydrophobic surface synthesis with polymers: a review

As previously stated, superhydrophobic surfaces have many potential uses, including: antimicrobial surfaces,[163,168,169] self-cleaning surfaces,[164,170,171] anti-icing coatings,[172,173] waterproofing,[174,175] oil-water separation devices,[176–178] anti-corrosive coatings,[179,180] microfluidics[181] and anti-reflective coatings.[162,182] These properties are achieved using a variety of techniques and materials, too numerous for the scope of this thesis. The work presented concerns the methods and use of polymers for superhydrophobic surfaces and nanoparticle incorporation therein.

The main requirement for a superhydrophobic polymeric surface that obeys the Cassie-Baxter model of surface wetting is high surface roughness. The main way this is achieved on a flat substrate is through templating- *i.e.* the formation of a nano or micro template which imparts high levels of roughness to the surface for the polymer to coat.

The most successful and widely used methods for the formation of polymeric superhydrophobic surfaces use methods such as dip-coating, spin-coating and drop-casting. These methods are easy to apply, and require solution based polymers for completion.

Dip-coating is effective for chemical reactions or polymerisations at substrate surfaces due to the prolonged contact time with the substrate. It is also effective for completely coating the substrate, and dependent on the total immersion time, the thickness of films can be tuned easily. For example, polymers such as silicones are dissolved in a volatile solvent and a suitably prepared substrate is immersed in the solution. The silicone polymer then hydrogen bonds with hydroxyl groups on the surface of a substrate (*i.e.* glass), before undergoing a condensation when heat is applied. Surface functionalisation with hydrophobic molecules (such as fluoroalkyl molecules) can then be added *via* silane condensation (Figure 3.3).

Polymerisation of alkoxysilanes can also give superhydrophobic surfaces, as can the addition of acrylate monomers.[183,184] Silica based surfaces have received a great deal of attention in the literature for the formation of hydrophobic surfaces due to their non-toxic nature, facile functionalisation and ease of polymerisation of alkoxysilanes. Superhydrophobic silica surfaces range from simple systems such as silica nanoparticles dispersed in a matrix, to multi-layer systems composing organic and inorganic phases.[185] Optically transparent superhydrophobic silica films were prepared by Shang *et al.* which compared differing ratios of tetraethylorthosilicate (TEOS) and methacryloxypropyltrimethoxysilane, TEOS and methyltriethoxysilane and TEOS with base catalysis to form silica films upon dip coating. The silica films were then functionalised with chlorotrimethylsilane and tridecafluoro-1,1,2,2-tetrahydrooctyldimethylchlorosilane to impart superhydrophobicity.[186] Rough superhydrophobic transparent films were similarly prepared by Mahadik *et al.* with varying dip coating times. The authors found that superhydrophobicity increased linearly with increasing immersion time, with contact angles of 172° reported.[187]

Superhydrophobic silica has also been used to coat fabrics and fibres.[175,183,185,188] One of the most successful examples uses positively charged 3-aminopropyl triethoxysilane anchoring points on the surface of the fibres which attracts negatively charged silica nanoparticles to create the surface.[189] By dip-coating a fabric substrate into a solution of poly(dimethyl siloxane) PDMS monomers (figure 3.3), a superhydrophobic, oil-water separation device was prepared with reported water contact angles of 150°.[159] Use of fluorinated hydrophobic monomers with siloxane head groups is also a viable route to superhydrophobic fabrics.[190]

Superhydrophobic poly(ethylene) surfaces have been prepared by polymerisation on the surface of a silica substrate with an embedded catalyst by dip coating, with the thickness of the film controlled by the immersion time. Using this method, Han *et al.* produced films with water contact angles of 165°, using two different catalytic systems.[191]

Dip-coating with poly(electrolyte) polymer solutions has led to superhydrophobic films formed by layer-by-layer assembly. A substrate is dipped into two solutions alternately; one a positively charged, cationic polymer (e.g. poly(ethyleneimine)) and a negatively charged, anionic polymer (poly(acrylic acid)).

Liu *et al.* utilised this method to incorporate nanoparticulate silver into a superhydrophobic surface for a marine, anti-biofouling coating.[191] Layer-by-layer assembly has been used in conjunction with silica nanoparticles to increase surface roughness.[192] Han *et al.* used polyethyleneimine with poly(acrylic acid) coated zirconia nanoparticles to form the rough surface, with contact angles of 170° reported.[193] Superhydrophobic polymer surfaces such as poly(diallyldimethyl-ammonium chloride)-sodium silicate/ poly(acrylic acid) can also be transparent, leading to water repellent coatings for windows.[182] Other systems including poly(vinylpyrrolidone) (PVP)/ poly(methacrylic acid) and poly(ethyleneimine)/ poly(2-vinyl-4,4-dimethylazalactone) gave contact angles of 155.6° and 155° respectively.[194,195]

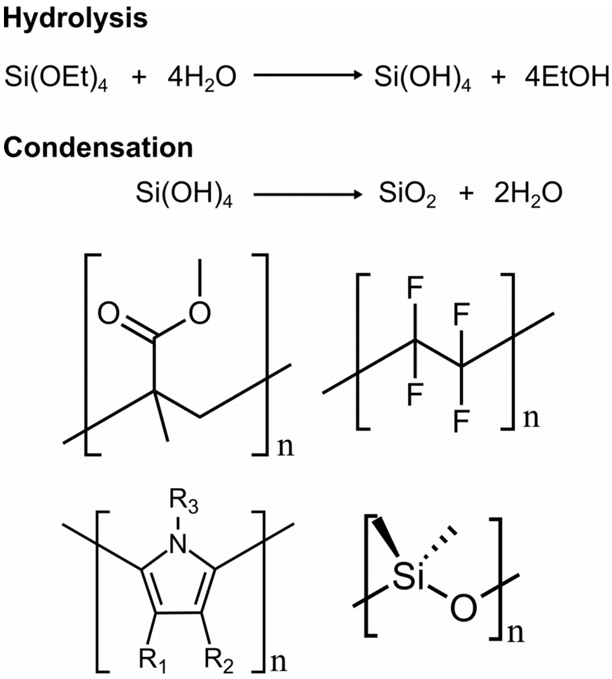

**Figure 3.3**: Top): Reaction scheme of tetraethylorthosilicate (TEOS) with water. The reaction proceeds *via* hydrolysis and a subsequent condensation. Bottom), clockwise from top left): poly(methyl methacrylate) (PMMA), poly(tetrafluoroethylene) (PTFE), poly(alkyl pyrrolidone) and poly(dimethylsiloxane) (PDMS).

Spin-coating uses a spinning disc controlled by an electric motor on which the substrate is placed. The polymer solution is then pipetted onto the spinning substrate, giving even surface coverage.

A notable example which uses spin coating and combines superhydrophobicity with photocatalytic activity was demonstrated by Wang *et al.*[196] The authors describe the synthesis of a copper(II) iodide - poly(aniline) polymer. The superhydrophobic surface was prepared on glass by spin-coating an ethanol suspension of the monomer onto a glass substrate. Due to the electron transfer between π and π* orbitals of the poly(aniline), electrons are able to transfer from the π* orbitals of the poly(aniline) to the conduction band of the copper(II) iodide, and the transfer of electron holes to the π orbitals of the poly(aniline). This allows for the generation of hydroxyl radicals for the photodegradation of Rhodamine B. The authors report a pre-irradiation water contact angle of 160.3°, which is tunable depending on the ratio of poly(aniline) to copper(II) iodide.

Poly(methyl methacrylate) (PMMA, figure 3.3) have seen widespread use for superhydrophobic surfaces, although intrinsically hydrophilic. Bernagozzi *et al.*[197] used poly(styrene) beads to template a PMMA superhydrophobic surface through drop-casting. Drop-casting involves dropping a solution of polymer onto a substrate and allowing the solvent to evaporate, whether that be in air, under elevated temperatures or *in vacuo*. Using this templating method, the authors reported maximum water contact angles of ~170°. Cyclohexane is used to dissolve the poly(styrene) template, leaving roughened PMMA due to its insolubility. Superhydrophobic PMMA surfaces have been achieved using spin coating,[198] in combination with poly(urethane) and fluorinated poly(urethane),[184] in conjunction with roughened silica ($SiO_2$),[174,199] and by cast-moulding with other materials such as silver or alumina.[200–202]

Polymers such as poly(tetrafluoroethylene) (PTFE) can be moulded or formed into nano or microparticles to form rough, superhydrophobic surfaces, also *via* templating. Spray coating is an effective method for preparing PTFE surfaces, with electrospraying (substrate attached to a power source) of Teflon ® PTFE-30[203] and conventional spraying (creating a poly(phenylene sulphide)/PTFE hybrid on a magnetic steel-composite surface (maximum contact angle 164°) for drag reduction in liquid-floated rotor micro-gyroscopes) widely used.[204]

PTFE surfaces have also been successfully prepared using etching processes, notably argon-plasma etching. This involves using ions to etch down into the surface, dramatically increasing surface roughness. The etching depth using this approach is tunable, so roughness can be limited to a few nanometres without altering the properties of the bulk material.[205] Indeed, plasma etching has seen success in the synthesis of poly(ethylene) surfaces.[206] Argon-oxygen etching has been used to synthesise superhydrophobic PTFE surfaces extensively, with high water contact angles reported.[207–209]

Poly(alkylpyrrole) (figure 3.3) has a high tendency to form fractal surfaces, which have a high roughness factor upon polymerisation on the substrate. Other systems which react in this way include waxy alkyl-ketene dimers[210] and co-polymers of sodium *p*-toluene sulphate.[211,212] Poly(alkylpyrrole) is deposited by the electrodeposition of alkylpyrrole (where the alkyl group is a long-chain hydrocarbon), and polymerisation occurs on the surface of the substrate. Yan *et al.* demonstrated superhydrophobic surfaces composed of poly(alkylpyrrole) in combination with sodium *p*-toluene sulphate yields highly spiked surfaces with contact angles greater than 150°.[211] Superhydrophobic poly(1-*n*-octadecylpyrrole) films have also been synthesised *via* electrodeposition.[213] Fluorinated derivatives have also been demonstrated, with increased effectiveness in hydrophobicity, as well as additional properties such as resistance to acid/alkali corrosion.[214]

There have been few examples of comparative studies of different polymers for the synthesis of superhydrophobic surfaces, but one such study compared the effectiveness of poly(styrene), PMMA, poly(urethane urea), EPOXY resin, poly(carbonate) and a poly(dimethylsiloxane-urea) copolymer. Samples were prepared by spin coating a polymer film directly onto the substrate, followed by two silica layers, then a final polymer/silica hybrid layer. The first and final polymer layers contained the aforementioned polymers in nanoparticulate form, which formed the microstructure of the surface. Contact angles with the three layer system are summarised in table 3.1 below:

| Polymer | Polymer Static water contact angle (°, 3 layers) |
|---|---|
| Poly(styrene) | 173.7 ± 0.5 |
| Poly(methylmethacrylate) | 172.9 ± 1.2 |
| Poly(urethaneurea) | 170.8 ± 1.7 |
| Poly(carbonate) | 164.6 ± 1.9 |
| Poly(dimethylsiloxane-urea) | 172.6 ± 1.2 |
| Epoxy resin | 174.8 ± 0.7 |

**Table 3.1**: Summary of the water contact angles obtained for the polymer films described by Yilgor *et al.* [184] The synthesis involves the templating of the polymer on the substrate, then the sequential layering of silica then a parent polymer/silica final layer.

Chemical vapour deposition (CVD) is a chemical process which involves the exposure of a [usually heated] substrate to a volatile mixture of precursors which then react or decompose, forming a film on the substrate. Many inorganic materials may require a further annealing step in order to aid crystallisation. A detailed description of the CVD process is given in section 2.1.4.2.

Aerosol-assisted chemical vapour deposition (AACVD) requires the formation of an aerosol composed of a solvent and precursors. The aerosol is then carried over to the heated reaction chamber *via* a carrier gas, where the precursors react/decompose onto a heated substrate, forming a film. CVD methods for the synthesis of surfaces usually yields flat films due to the way in which the reactants are uniformly physisorbed onto the surface, and as such rough surfaces often prove elusive. To counter this, precursors which have a tendency to form rough surfaces, such as nanoparticle dispersions or monomers for rough, polymeric films are utilised.[157] Superhydrophobic films by CVD is an area of great interest simply due to the need for large surfaces to be coated in superhydrophobic material, and CVD is a viable industrial route thereof.

PTFE has been used successfully for superhydrophobic surfaces by CVD, primarily with a post-deposition treatment as CVD films of PTFE tend to be very flat. Nevertheless, PTFE has a very low surface energy with respect to water, with water contact angles of approximately 100° reported on flat substrates.[203,209,215] Post-deposition treatments can raise the water contact angle to < 160°, such as the use of sandpaper to mechanically abrade a PTFE surface.[216] PTFE surfaces have also been roughened using plasmas, amongst other techniques described earlier.[209]

Hot filament chemical vapour deposition (HFCVD) uses a hot filament to decompose a stream of reagents before deposition on a lower temperature substrate. HFCVD was used by Thieme *et al.* to deposit PTFE onto alumina substrates, and compared this with the deposition of 1,3,5-trivinyltrimethylcyclotrisiloxane with di-*tert*-butyl peroxide as an initiator.[200] The resultant polymer surfaces (PTFE and fluorine free-poly(siloxane)) exhibited water contact angles of 151° and 153° respectively. HFCVD has also been used in conjunction with a tungsten catalyst to form superhydrophobic PTFE surfaces from the decomposition of hexafluoropropylene oxide, giving contact angles greater than 160°.[217]

Fluorocarbon surfaces have also been prepared by the pyrolysis of hexafluoropropylene oxide on silicon substrates at low temperatures (200-300 °C).[218] The authors also propose a mechanism for the formation of the poly(fluorocarbon) surface by way of formation and subsequent polymerisation of difluorocarbene. Water contact angles increased with temperature, with angles as high as 172.7 ° reported for the film deposited at 300 °C.

Crick and Parkin prepared superhydrophobic (PDMS) films by the deposition of PDMS monomers from commercially available Sylgard -184®. The PDMS monomers have a platinum based curing mechanism, which is activated at higher temperatures, hence the 300-360 °C used for the deposition. It is notable that depositions occurred on the top-plate of the reactor, due to thermophoretic effects, as PDMS particles migrate away from the heat source. The contact angle increases from 95° for a flat, dip-coated PDMS surface to 167° for the rough, AACVD-high temperature cured surface.[156] Crick and Parkin also produced a model for the definition of superhydrophobic surfaces based on water bouncing.[219] The authors also investigated the effect of the surface tension of the water on the number of bounces using solutions of sodium dodecyl sulphate and lanthanum(III) chloride.[220]

Thermally activated deposition encompasses CVD techniques which are activated by temperature, including atmospheric (APCVD) and reduced pressure CVD. Examples of APCVD processes are relatively limited in the literature, but some examples using polymers such as PTFE and inorganic films have been recorded. APCVD has been used to deposit tungsten diselenide thin films from tungsten hexachloride and diethyl selenide, creating hydrophobic surfaces with water contact angles of 135-145°. The surface structures (tungsten selenide needles) were not conducive for the Cassie-Baxter model, moreover promoting a Wenzel type interaction, thus the observed high droplet-surface adherence.[221] Oddly, morphologies obtained by other transition metal-diselenide systems have proven ineffective in producing superhydrophobic surfaces.[222–224] Stallard *et al.* used a novel atmospheric pressure plasma enhanced chemical vapour deposition system to form highly ordered, rough poly(siloxane) films.[225] Hexamethyldisiloxane was introduced into a nitrogen/helium plasma stream which is then used to form the poly(siloxane) films on a silica substrate. The reported water contact angles fluctuated from 150° to 100° across the substrate, attributed to proximity of the glow discharge plasma.

The use of polymers for superhydrophobic surfaces and the composites thereof will continue to develop, with improvements in roughness, applicability, durability, transparency and function to the fore.

### 3.1.2 Superhydrophobic polymer-nanoparticle composites: a review

Polymer-nanoparticle composites have been used for numerous applications, including: anti-microbial surfaces,[226,227] drug delivery,[228,229] bio-conjugation,[230,231] Förster resonance energy transfer (FRET),[232] anti-icing coatings,[172] anti-corrosive coatings,[233] and thermochromic coatings.[234] Compared to polymer-nanoparticle composites, examples of superhydrophobic polymer-nanoparticle composites are relatively few and far between.

One of the main functions of the addition of nanoparticles to superhydrophobic surfaces is increasing the surface roughness, and this is indeed evident in the literature. The use of silica nanoparticles to roughen surfaces of superhydrophobic polymers such as poly(styrene),[235,236] co-polymers such as poly(styrene-co-acrylic acid) and poly(styrene-co-maleic anhydride)[237,238] and poly(diallyldimethylammonium chloride)-silicate/ poly(acrylic acid)[238] and poly(sodium-4-styrene sulphate)/poly(allylamine hydrochloride) polyelectrolyte layers.[122,239] PTFE nanoparticles in SU-8 (Microchem, UV-curable polymer) photoresist ® have also been synthesised, in a polymer-polymer nanoparticle system, with water contact angles of >165° reported.[240] Applications for these surfaces appear to be limited, albeit as an academic exercise in increasing the water contact angle and surface superhydrophobicity. Cao *et al.* prepared superhydrophobic surfaces using a mixture of organosilane modified silica particles and poly(styrene-co-butyl methacrylate-co-glycidyl methacrylate) in a toluene/acetone solvent system, which was subsequently applied to the surface using a spray gun and cured for 12 hours.[172] The resultant surfaces had static water contact angles of 144-158°, and were tested by coating a satellite dish with the polymer-particle composite and exposing it to freezing rain. Changeable hydrophobic/superhydrophobic polymer systems have been created using pH responsive polymers attached to silica nanoparticles. [241]

A novel application of silica nanoparticles in poly(alkylsiloxane) solution was described by Manoudis *et al.*[233] A suspension of nanoparticles and polymer in white spirit was used to coat marble for anti-corrosive applications on buildings and monuments, with contact angles of 162° reported.

Sparks *et al.* used nanoparticle-laden superhydrophobic poly(thiol-ene) resins to form superhydrophobic surfaces on glass substrates in a one-pot reaction. The films were synthesised using an acetone/tetrahydrofuran solution of pentaerythritol tetra(3-mercaptopropionate) and a mixture of triallyl isocyanurate and 2,4,6,8-tetramethyl-2,4,6,8-tetravinylcyclotetrasiloxane with silica nanoparticles. A photoinitiator (2,2-dimethoxy-2-phenylacetophenone) was used to cure the composite (5 minutes under a UV flood lamp operating at 17 mW / cm$^2$), after spraying onto glass substrates. Higher water contact angles (up to 158.3°) were reported when the concentrations of silica nanoparticles in the composite were increased.[242]

The use of magnetron sputtering to deposit polymers over nanoparticles forming rough, superhydrophobic films with contact angles close to 180°. Kylián *et al.* utilised a vacuum system for the deposition of nanoparticles *via* a gas aggregation source before subsequent PTFE deposition *via* a radiofrequency magnetron sputterer from a PTFE target with argon gas.[243] The morphology was very rough and spherical in nature (analogous to the morphologies seen by SEM in this chapter, *vide infra*), hence the high water contact angles achieved. Transparent superhydrophobic surfaces have application in the window coatings where water repellent and anti-icing coatings are desirable. Thin, single silica particle-polymer superhydrophobic composites have been synthesised, mostly based on thin layers of silica nanoparticles encased in polymers such as poly(styrene),[235] perfluorodecyltriethoxysilane[244] and poly(sodium-4-styrene sulphate)/poly(allylamine hydrochloride).[245] Similar systems have also been prepared with alumina nanoparticles.[246]

Superhydrophobic/ anti-microbial surfaces have been prepared using polymer nanoparticle composites. Although polymeric fibres containing silver nanoparticles have been tested successfully for anti-microbial activity,[169,226,227,247] there is a dearth of superhydrophobic polymer-nanoparticle composite examples.

Recently, Xu *et al.* synthesised high density poly(ethylene) on precision woven nylon mesh with incorporated photocatalytic titania nanoparticles under high temperature and pressure. The authors show that on UV irradiation, the mesh became hydrophilic, and on heating, superhydrophobicity was restored. In this way, the UV activated photocatalytic system exhibits reversible superhydrophobicity, albeit in a convoluted manner.[171]

## 3.2 Problem overview

Ideal superhydrophobic polymer-nanoparticle composites require the superhydrophobic features of the polymer film and nanoparticle surface protrusion in order to preserve the function of the incorporated nanoparticles. This surface protrusion also increases surface roughness.[235] The photocatalytic degradation of organic species such as bacteria on such surfaces tends to quickly degrade both the polymer and any organic species, thus quickly rendering the surface useless. Therefore, a superhydrophobic polymer-nanoparticle composite which possesses photocatalytic activity and sustainable superhydrophobicity is highly desirable. A general, one-pot method for the synthesis of superhydrophobic polymer-nanoparticle surface coatings would also open up superhydrophobic surfaces to catalytic applications due to their high surface area.

In this chapter, a superhydrophobic polymer-nanoparticle composite was synthesised using the AACVD of commercially available Sylgard-184 ® monomer, with a platinum based curing agent along with hydrophobically ligated titania nanoparticles to provide photocatalytic activity. All precursors were dissolved in a chloroform solution, and carried over to the substrate in a 360 °C reaction chamber, forming the superhydrophobic PDMS-titania nanoparticle composite. This one-pot AACVD approach was then applied to different types of nanocrystal incorporation, with magnetic, gold, metal-oxide and nickel nanocrystals incorporated. The catalytic activity of the nickel nanocrystals in the dehydrogenation of ammonia-borane is also evaluated.

## 3.3 Results and discussion

### 3.3.1 Synthesis and characterisation of titania nanoparticles

In this work, nanoparticles were synthesised using two different methods. The first involved the functionalisation of titania nanoparticles synthesised using continuous flow hydrothermal synthesis (CHFS) with oleic acid, and the other a slow hydrolysis based on the method developed by Cozzoli *et al.*[144] The synthesis of slow hydrolysis nanoparticles involves the slow hydrolysis of titanium(IV) isopropoxide with water generated *in situ* from the esterification of oleic acid and ethylene glycol (solvent). In this way, the titania hydrolysis is slow, and the nanoparticles capped by oleic acid. For detailed experimental details, see section 2.2.3.3.

CHFS nanoparticles were prepared by the hydrothermal reaction of titanium(IV) bis(ammonium lactato) dihydroxide with superheated water described elsewhere.[145] The resultant aqueous slurry was lyophilised before use, yielding a fine white powder. The surface of these particles was functionalised using oleic acid, rendering them dispersible in chloroform. It was hypothesised that the surface of the nanoparticles is populated by titanol (Ti-OH) groups which can be esterified with the carboxylic acid and a catalytic amount of base (triethylamine). However, the titanium(IV) bis(ammonium lactato) dihydroxide used in the CHFS synthesis acts as a capping agent, hence no R-OH stretches were observed in the IR spectrum of lyophilised CHFS titania nanoparticles (figure 3.4). Therefore, the oleic acid exchanges with lactic acid moeities on the titania nanoparticle surfaces and imparts dispersibility. It has also been shown that carboxylic acid containing species are effective at ligating nanoparticles, without forming covalent interactions with the surface. From FTIR spectroscopy, this was evident (Figure 3.4).

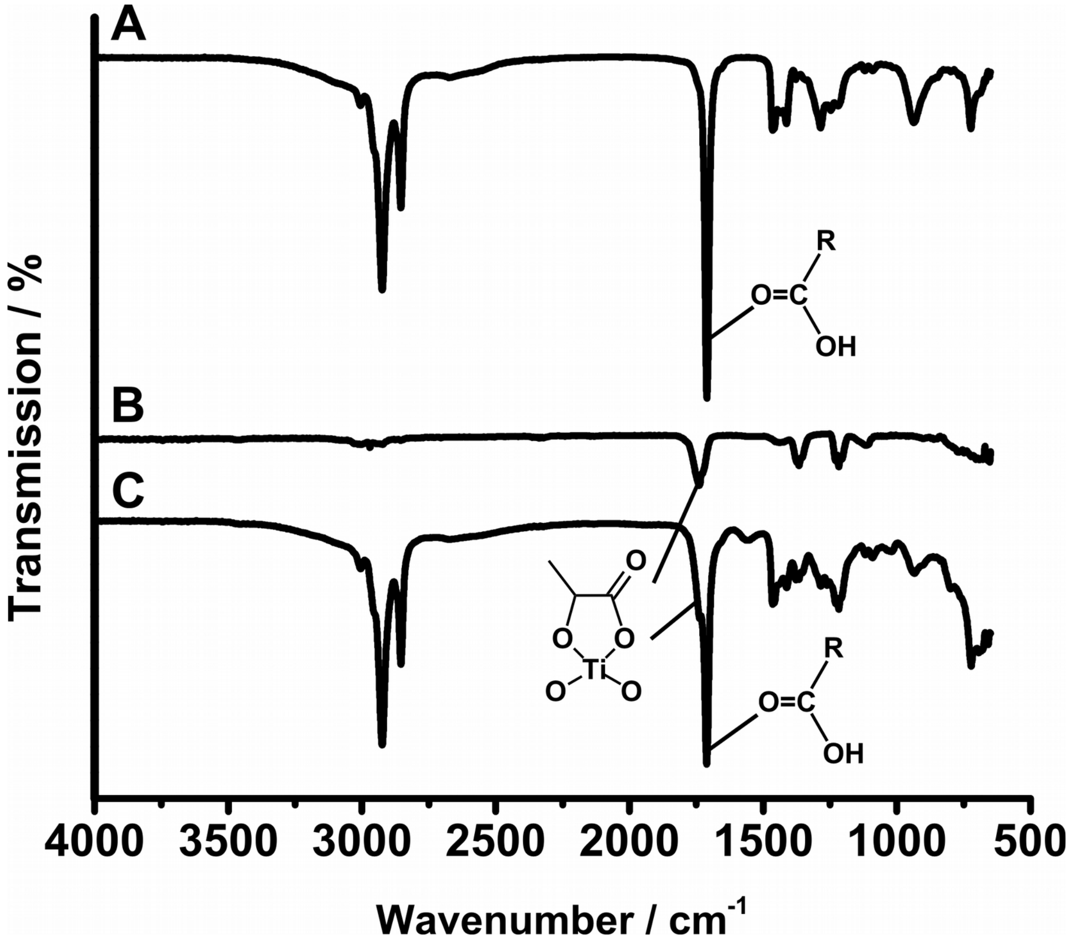

**Figure 3.4:** ATR-FTIR spectra of: A) oleic acid, B) unfunctionalised CHFS anatase $TiO_2$ nanoparticles and C) oleic acid functionalised CHFS anatase $TiO_2$ nanoparticles showing carboxylic acid and titanium(IV) bis(ammonium lactato) dihydroxide capping functionality at the nanoparticle surface.

Figure 3.4 shows a typical ATR-FTIR spectrum of oleic acid functionalised anatase nanoparticles with the spectra of pure oleic acid and unfunctionalised titania nanoparticles for comparison. C-H stretching vibrations from the oleic acid are evident at 2924 and 2854 cm$^{-1}$ respectively. The shoulder at 2954 cm$^{-1}$ can be attributed to the asymmetric stretching of the terminal $CH_3$ group of the oleic acid chains. The weak band at 3004 cm$^{-1}$ is assigned as the olefinic C-H stretch.[248]

The strong peak in the carbonyl stretching region (1710 cm$^{-1}$) is attributed to free oleic acid molecules which are ionically attracted to titania nanoparticle surfaces. The sharp band at 1740 $cm^{-1}$ observed in the titania nanoparticle spectrum is attributed to titanium(IV) bis(ammonium lactato) dihydroxide used in the nanoparticle synthesis, and also explains why no broad R-OH stretches are observed <3000 $cm^{-1}$ (figure 3.4).

CHFS and slow hydrolysis synthesised nanoparticles were characterised by TEM. Both sets of nanoparticles showed well dispersed, shape-anisotropic nanoparticles. The average size of the CHFS and slow hydrolysis synthesised nanoparticles was 13.2 nm ± 5.62 nm and 4.2 nm ± 1.27 nm respectively. EDS was used to confirm the elemental composition of the two samples (figure 3.5). Copper emanated from the copper TEM grid, and phosphorus, sulphur and chlorine are from the CHFS process. Silicon is a standard contaminant obtained from glass.

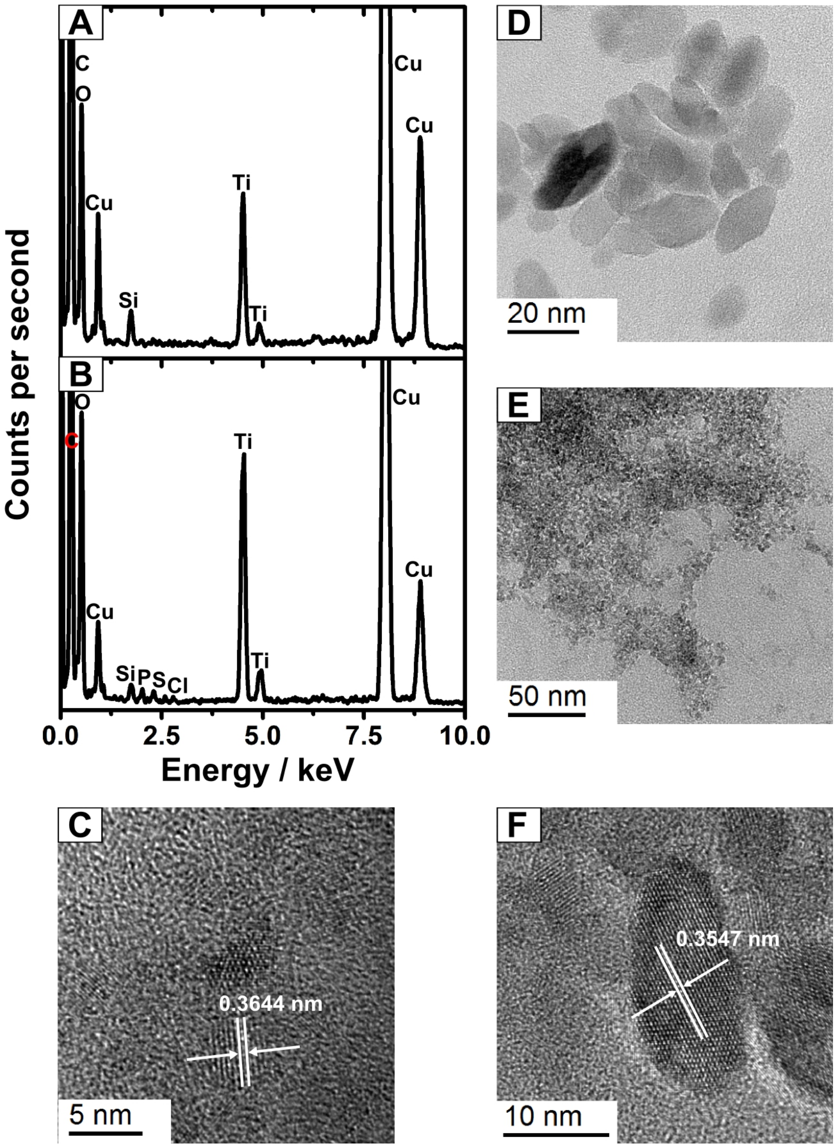

**Figure 3.5**: A) EDS spectrum of slow hydrolysis synthesised titania nanoparticles, B) EDS spectrum of CHFS synthesised titania nanoparticles, C) and E) HRTEM and TEM images of slow hydrolysis synthesised titania nanoparticles and D) and F) TEM and HRTEM images of CHFS synthesised titania nanoparticles.

HRTEM analysis showed *d*-spacings of 0.3547 nm and 0.3644 nm for the CHFS and slow hydrolysis nanoparticles respectively, corresponding to the <101> plane of anatase titania.

XRD analysis also confirmed the composition of the nanoparticles, assigned as anatase titania (figure 3.6).

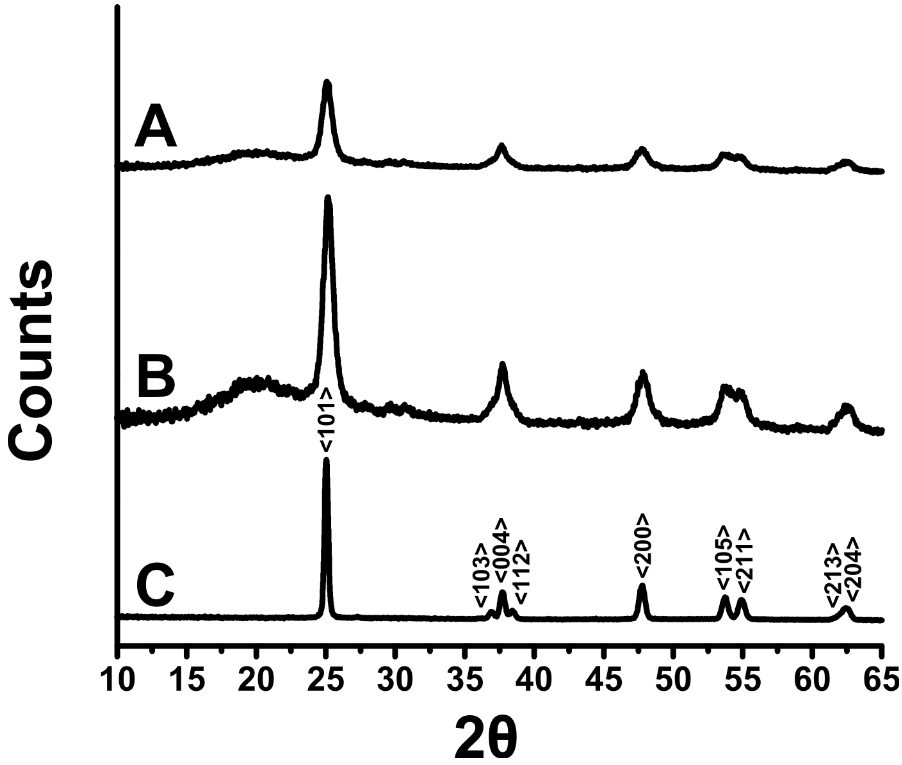

**Figure 3.6**: XRD patterns of: A) anatase titania nanoparticles synthesised *via* slow hydrolysis, B) anatase titania nanoparticles synthesised *via* continuous flow hydrothermal synthesis and C) anatase $TiO_2$ standard, Sigma Aldrich (≤ 99.5%, trace metal basis).

### 3.3.2 Synthesis, characterisation and catalytic testing of PDMS- titania nanoparticle composites

PDMS-titania nanoparticle precursor composites were synthesised using a dispersion of functionalised titania nanoparticles (0.5 g) with Sylgard-184® elastomers and monomers in chloroform (~ 40 ml) by AACVD deposition. Detailed experimental protocols can be found in section 2.2.7.3.

It is noteworthy that the composite deposition occurred on the top plate. This is due to thermophoretic effects, which causes particulate matter to move away for a heat source. In the CVD reactor, this means that aerosol droplets move away from the bottom plate, and adsorb preferentially onto the top glass plate.[140] The high temperature (360 °C) within the CVD reactor is necessary for fast aerosol evaporation (occurs readily above 150 °C) and for the polymer to cure and form the surface (above 250 °C). Deposition times were typically around 35 minutes, depending on transfer rate of solution. The reactor was then left to cool to room temperature. Plain PDMS depositions provided a white-opaque film that allowed less than 15% visible light transmission.

The resultant films were analysed by several methods, including: SEM, TEM, EFTEM, water contact angle measurements, EXAFS, XRD, EDS, water bouncing measurements, Raman spectroscopy and photocatalytic dye degredation studies. Where appropriate, PDMS- titania nanoparticle composites are compared to superhydrophobic PDMS films without nanoparticles.

SEM micrographs showed a typically rough, pronounced microstructure, with surface protrusions around 3-5 μm in length. The film comprised a series of interlinked silicone microparticles attached to the glass substrate. The high surface roughness combined with the low surface energy of the native polymer film rendered them superhydrophobic. Plain PDMS films and microstructure can be observed in figure 3.7.

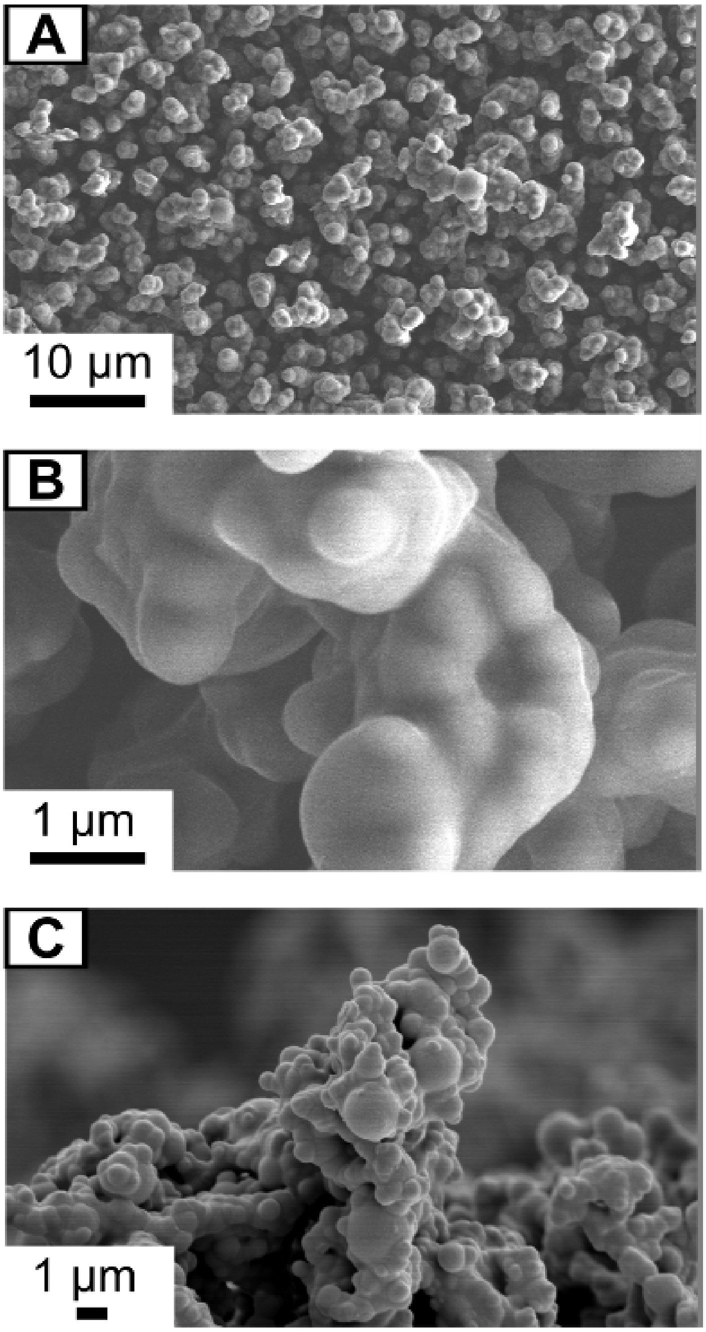

**Figure 3.7**: SEM micrographs of superhydrophobic PDMS films: A) Top-down, B) an individual silica sphere and C) Side-on image showing the bulbous microstructure.

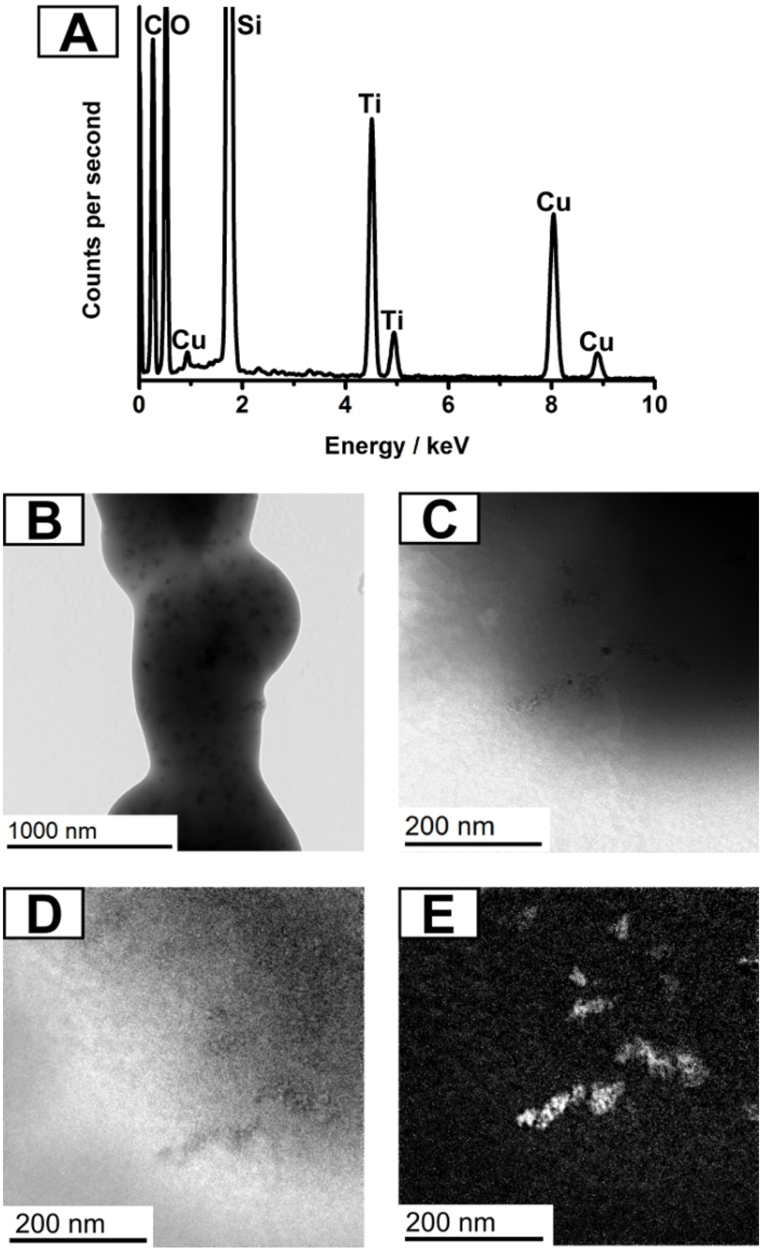

**Figure 3.8:** A) EDS spectrum of $TiO_2$ nanoparticle-PDMS composite, B) TEM image of $TiO_2$ nanoparticles dispersed in the composite, C), D) and E) show the zero loss C), silicon map D) and titanium map E) EFTEM analysis for the $TiO_2$ nanoparticle-PDMS composite. Silicon and titanium are shown in white in D) and E).

TEM analysis showed the titania nanoparticles dispersed evenly throughout the polymer. EFTEM analysis also confirmed the presence of titanium in the nanoparticles and their random dispersion throughout the silicon matrix (figure 3.8). Similar atomic ratios (Ti:Si:O) were seen throughout the film by EDS, with an average atomic ratio of 5:1 for Si:Ti.

XRD analysis showed no discernible reflection due to the low density of the nanoparticle material embedded within the polymer. However, XAS analysis of the K-line fluorescence of Ti (4800 – 5400 eV) confirmed that the nanoparticles embedded within the polymer were of the anatase $TiO_2$ phase. This is evident in figure 3.9 (XANES analysis shown) when comparing the titania nanoparticles in PDMS against rutile and anatase standards. EXAFS analysis (not shown) for the embedded nanoparticles was normalised and modeled in *R*-space ($r^2 = 0.050$, suitability of fitted data). A contraction relative to the bulk powder was observed, where the average bond distance decreased from 1.964 to 1.905 Å in the first Ti-O shell.

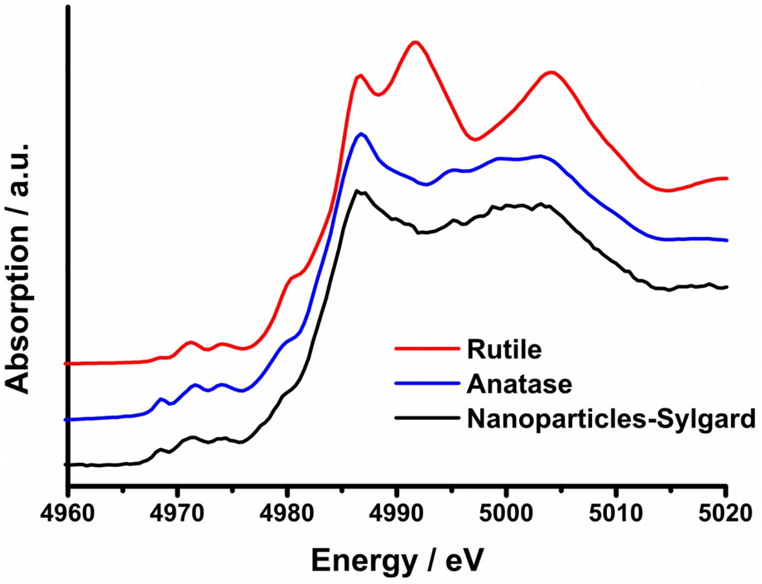

**Figure 3.9**: XAS of anatase CHFS nanoparticle-PDMS composite with comparative spectra of anatase and rutile standard powders, showing the presence of anatase titania in the nanoparticle-PDMS composite.

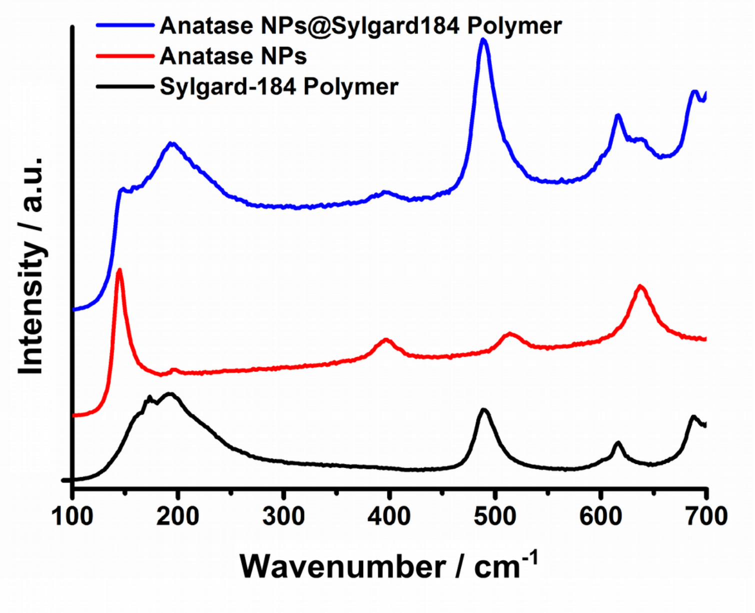

**Figure 3.10**: Raman spectra of: Anatase titania nanoparticles-PDMS composite, anatase titania nanoparticles and plain superhydrophobic PDMS (Sylgard-184 ®) polymer. The Raman spectra of the titania-PDMS composite clearly shows features of the polymer and anatase titania nanoparticles.

Raman spectroscopy also confirmed the presence of anatase titania nanoparticles in both the CHFS and slow hydrolysis titania nanoparticle-PDMS composites. Raman Shifts characteristic of anatase $TiO_2$ were observed with $E_g$ modes at 146, 197 and 639 $cm^{-1}$ and a $B_{1g}$ mode at 516 $cm^{-1}$.[144,249] Importantly, the signal at 397 $cm^{-1}$ and $E_g$ modes at ~158 $cm^{-1}$ and 630 $cm^{-1}$ from the particles were clearly observable in the Raman spectrum of the titania nanoparticle-PDMS composites (figure 3.10).

Average water contact angles were measured at 162°, with a maximum angle of 167° achieved. Water tilt angles for the surface were below 5°. Water bouncing measurements showed an average of seven bounces of water droplets cast onto the surface.[219]

Prior to dye degradation studies, the resistance of the composite to UV irradiation was assessed. Irradiating the superhydrophobic films with UV light ($\lambda$ = 254 nm, 4.88 eV) for two hours gave a slight reduction of these water contact angles to 160°. The number of bounces achieved by water droplets fell slightly to an average of six. The small reduction in water contact angle and water bouncing can be attributed to the partial photo-induced wetting of the titania nanoparticles apparent on the surface of the PDMS. However, these water contact angles remained unchanged (160° average) with further irradiation (tested for 48 hours in total at $\lambda = 254$ nm), therefore showing no degredation to the superhydrophobic microstructure. The fraction of contact between titania nanoparticles and water droplet was small enough for it not to reduce the water contact angles further, as the primary contact of water is made with hydrophobic polymer and trapped air. It should also be noted that extensive UV-irradiation (254 nm, 48 hours) had no detectable physical effects on the PDMS.

The photocatalytic activity of nanoparticle embedded superhydrophobic films was tested against the breakdown of dye molecules (Resazurin).[250,251] The established method developed by Kafizas *et al.* uses aqueous solutions, but this was exchanged for a 1:1 methanol:water mixture to ensured full wetting of the superhydrophobic surface (see section 2.2.7.1). Following irradiation with UV light ($\lambda = 365$ nm, 3.40 eV), the resazurin dye was completely discoloured after 90 minutes (figure 3.11). Superhydrophobic PDMS films with no embedded nanoparticles did not show any dye degradation over this period. Thin films of crystalline titanium dioxide deposited using thermal CVD required 80 minutes for full dye decomposition.[154] Therefore, the photocatalytic activity of the polymer composite films is comparable to that of flat titanium dioxide films.

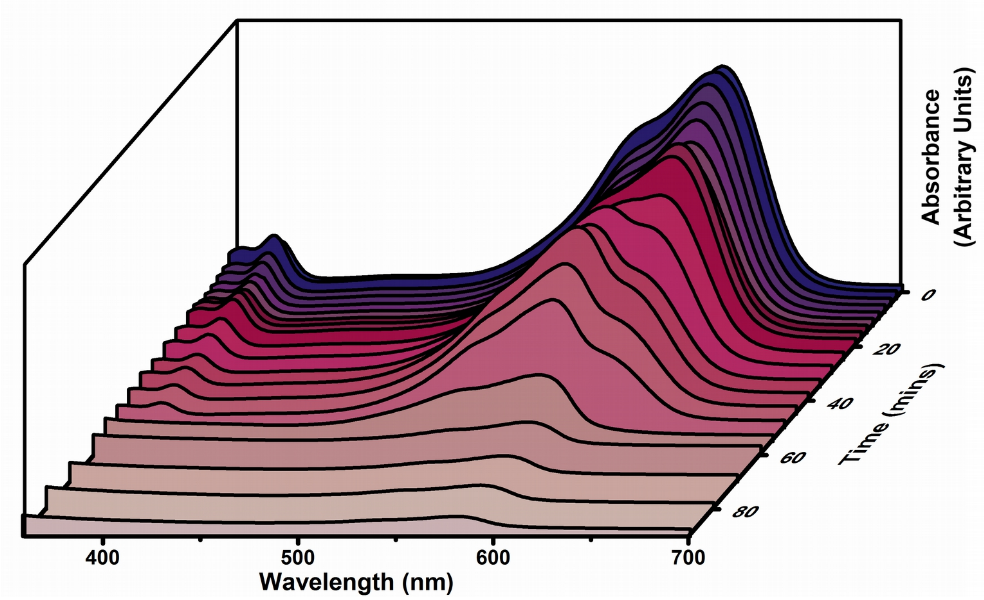

**Figure 3.11**: UV/vis composite of the degradation of Resazurin dye in water:methanol on the CHFS titania nanoparticle PDMS composite. A complete degradation of the dye was observed after 80 minutes.

### 3.3.3 Summary

The nanoparticle-PDMS films were able to exhibit both superhydrophobicity and photocatalysis, even after extensive periods of UV-irradiation. This occurs as the exposed surface consists mainly of the polymer matrix that supports these particles, thereby preventing a significant reduction of the surface hydrophobicity on irradiation. Further to this, the polymer matrix is made up of a PDMS type polymer that resists photocatalytic breakdown caused by the embedded nanoparticles. The result is a surface that self-cleans using superhydrophobic and hydrophilic-photocatalytic mechanisms in tandem. This is the first example of a surface which incorporate such features, and show dual functionality after extensive UV-irradiation. Thus, these composites have potential as commercial self-cleaning films.

## 3.4 Development of a general method for the synthesis of superhydrophobic polymer-nanoparticle composites

The relative ease at which titania nanoparticles could be incorporated into PDMS polymers by AACVD naturally led onto the development of a general method for the synthesis of nanoparticle-PDMS composites. There are a plethora of nanoparticle syntheses which use fatty acid ligands and therefore render nanoparticles dispersible in chloroform. Nanoparticles can therefore be incorporated into the aforementioned AACVD system, however it was found that thermally sensitive nanoparticles or nanoparticles susceptible to oxidation such as CdSe/ZnS core/shell quantum dots are unsuitable for incorporation due to the high temperatures in the CVD reactor. The PDMS is cured using a platinum based curing agent, a process which can be disrupted by certain metal nanoparticles such as gold. In the case of gold, a silica coating was employed to prevent this. The silica coat was grown onto the gold nanoparticles *via* microemulsion the polymerisation of TEOS, and the Au/$SiO_2$ nanoparticles hydrophobised by reaction with trimethoxy(octadecyl) silane.

### 3.4.1 A general method for the synthesis of general PDMS-nanoparticle composites

Hydrophobically ligated nanoparticles were synthesised according to protocols listed in chapter 2. CoO, Ni, CdSe/ZnS, $Fe_3O_4$, $SiO_2$ and Au/$SiO_2$ were the nanoparticles synthesised and deposited. Approximately 0.1 g of nanoparticles were used per deposition in the same way as the titania nanoparticles, except that the reactor temperature was increased to 390 °C to increase the PDMS curing rate. It was found that CdSe/ZnS nanoparticles were completely destroyed and prevented the curing of the polymer, yielding a patchy film of cadmium oxide. Commercially available $SiO_2$ nanoparticle powder (Sigma Aldrich, 99.8%) were functionalised with oleic acid in the same way as the CHFS nanoparticles (section 2.2.3.5). They were incorporated successfully into the PDMS, however there was no discernible difference between superhydrophobic PDMS films and silica nanoparticle-PDMS composites by any analytical techniques, including microscopy and water contact angle measurements. Therefore, CdSe/ZnS and $SiO_2$ PDMS composites are not discussed further in this work.

Nanoparticles and nanoparticle-PDMS composites were characterised in the same way as the titania nanoparticles using: TEM, HRTEM, EFTEM, SEM, water contact angle measurements, water bouncing measurements, SQUID, DLS and EDS.

In terms of application, the uses of superhydrophobic nanoparticle-PDMS composites are currently fairly limited. However, due to the highly rough microstructure, the surface area of the composite is very high, leading to high surface area catalysis. Nickel nanoparticle-PDMS composites were evaluated for just that, through the nickel-catalysed dehydrogenation of ammonia-borane complex in water. Despite the limited applications, the first example of a superhydrophobic, magnetic surface was synthesised as well as the elucidation of a general method for the synthesis of superhydrophobic surfaces with nanoscopic properties.

### 3.4.2 Synthesis and characterisation of CoO, Ni, $Fe_3O_4$, Au/$SiO_2$ nanoparticles

CoO and $Fe_3O_4$ nanoparticles were synthesised according to Park *et al.*[45] with modifications. The method is based on the synthesis and thermal decomposition of metal-oleate species in high boiling point solvent in the presence of oleic acid. This method produces highly monodisperse nanoparticles as shown by TEM images in figure 3.12.

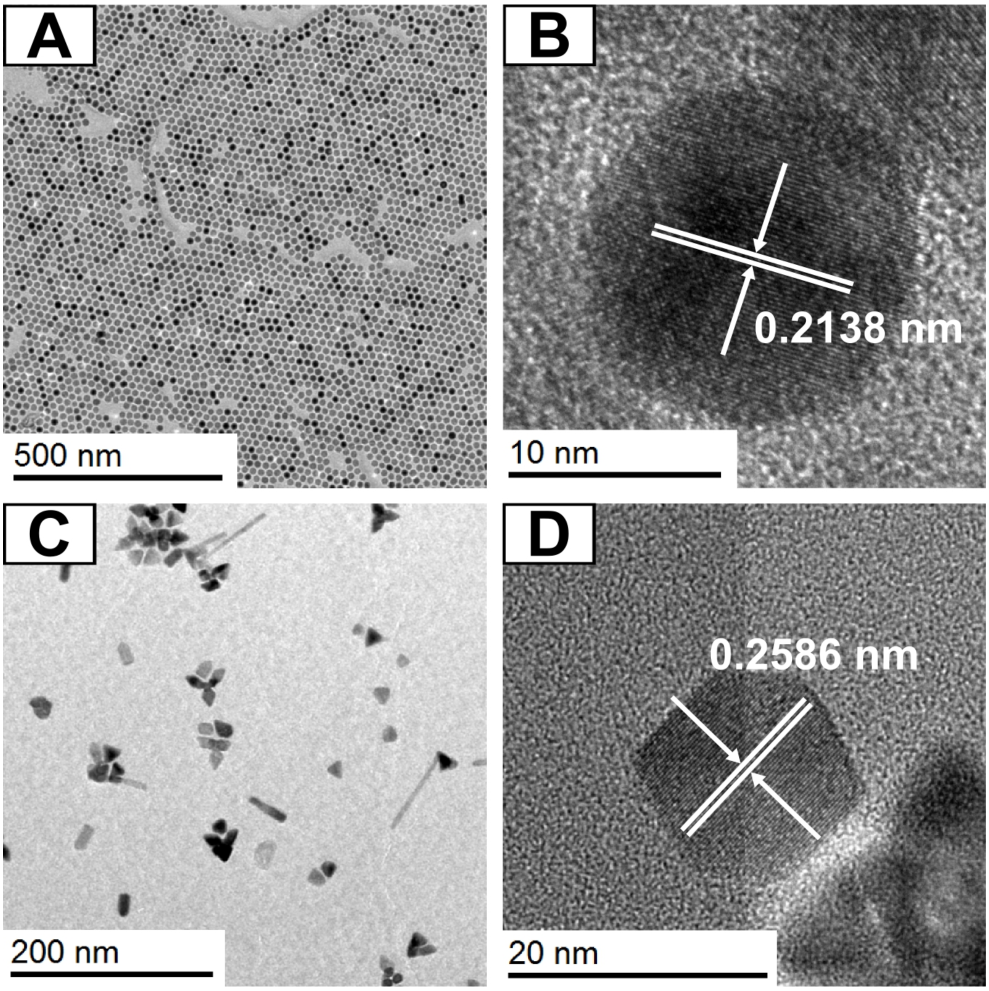

**Figure 3.12**: TEM and HRTEM images of: A/B) $Fe_3O_4$ nanoparticles and C/D) CoO nanoparticles showing lattice *d*-spacings of 0.214 nm and 0.259 nm respectively.

The nanoparticles demonstrated a range of shapes, even with clear similarities in their syntheses. This is clearly observable in the rhomboid CoO and spherical $Fe_3O_4$ nanoparticles. The "rhomboid"-like morphology of the CoO nanoparticles is due to the nature of the cobalt-oleate complex before decomposition. Much like other nanoparticle ligands, oleic acid adheres to certain crystal planes of different materials in nanoparticle syntheses, thus promoting directional growth. It is noteworthy that the metal-oleate derived nanoparticles had a vast excess of oleic acid/oleate species in solution, the removal of which is non-trivial. This adversely affected HRTEM measurements, through carbon contamination of the detector. The TEM grids were plasma cleaned to remove organic matter before analysis and easy imaging of the particles was made possible. HRTEM analysis of the $Fe_3O_4$ and CoO nanoparticles yielded *d*-spacings of 0.214 nm and 0.259 nm, corresponding to <400> of $Fe_3O_4$ and <002> of CoO respectively.[45]

EDS was used to analyse the elemental composition of the nanoparticles (figure 3.13). The elemental composition of each type of nanoparticles showed desired ratios and well within error limits. Large copper and carbon peaks emanate from the carbon coated copper TEM grid. The silicon peak is a standard contaminant in TEM/EDS systems, and it was confirmed that silicon was part of the sample in the Au/$SiO_2$ system, by comparing against a background spectrum (not shown).

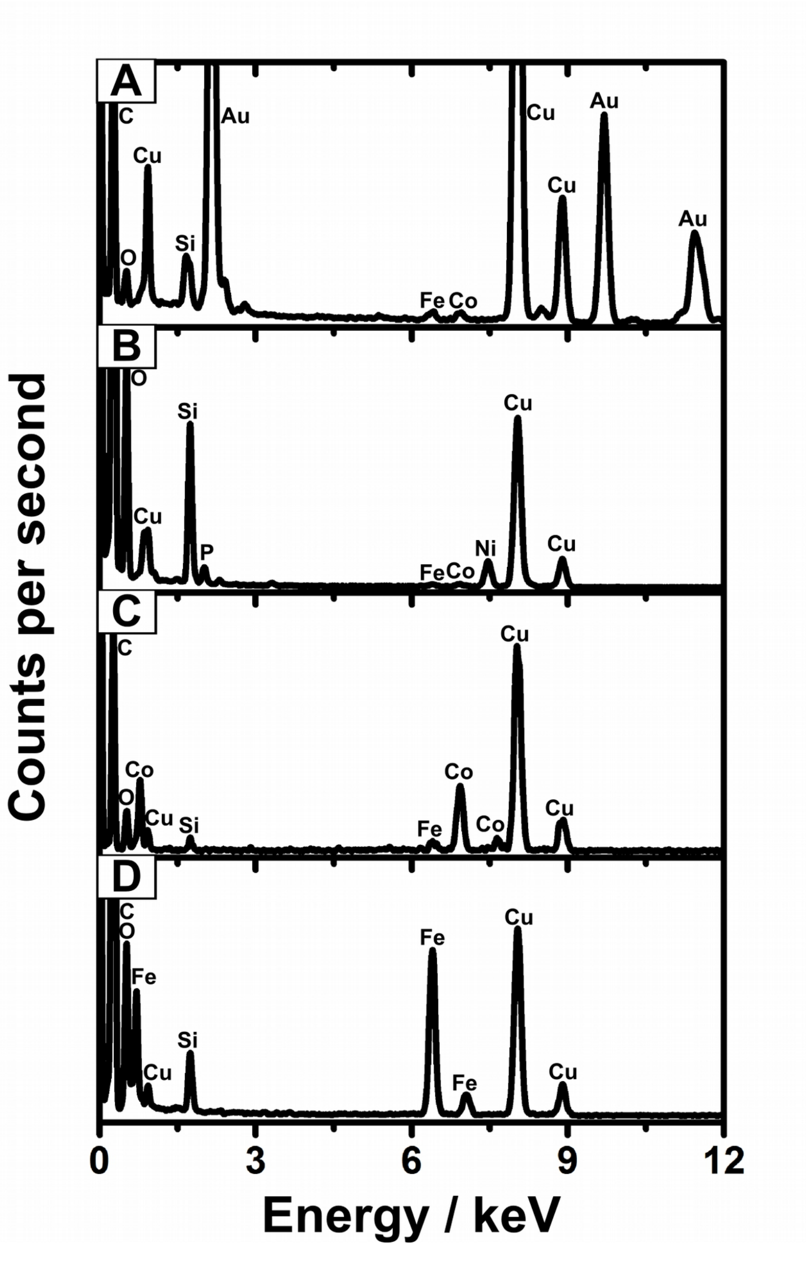

**Figure 3.13**: EDS spectra of: A) Au/$SiO_2$ nanoparticles, B) Ni nanoparticles, C) CoO nanoparticles and D) $Fe_3O_4$ nanoparticles.

Nickel nanoparticles were synthesised according to Carenco *et al.*[66] The synthesis uses trioctylphosphine as the solvent and oleylamine as the surfactant. A nickel-amine complex, similar to iron or cobalt-oleate is formed and decomposed *in situ*, forming the nanoparticles. The relatively low temperature of the synthesis (220 °C) avoids the synthesis of nickel phosphide nanocrystals.[252] TEM analysis showed spherical nanoparticles, with lattice *d*-spacings of 0.185 nm recorded, corresponding to <111> of Ni (figure 3.14).[253] EDS analysis also confirmed the presence of Ni in the nanoparticles (figure 3.13).

Gold nanoparticles were synthesised using a modified Brüst-Schiffrin method according to Palgrave and Parkin.[146] The method involved the reduction of gold(III) chloride hydrate with sodium borohydride in the presence of tetraoctylammonium bromide in a toluene-water solvent mixture. The tetraoctyl ammonium bromide acts as a surfactant and imparts dispersibility in toluene to the gold nanoparticles. The AACVD of Brüst-Schiffrin gold nanoparticles stabilised by tetraoctylammonium bromide with PDMS monomers prevented the formation of a superhydrophobic film, potentially due to interference with the platinum based curing agent.

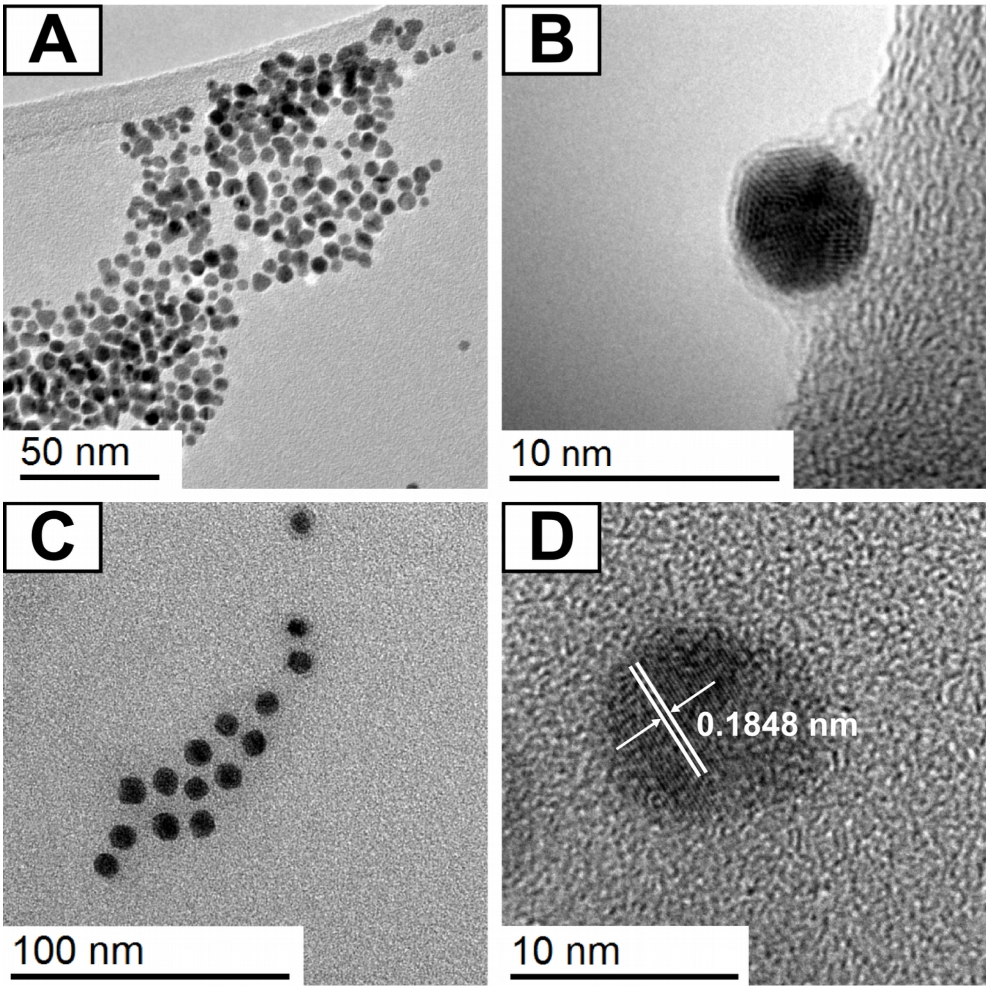

**Figure 3.14**: TEM images of: A) Au/$SiO_2$ nanoparticles, B) An HRTEM image of a single Au/$SiO_2$ nanoparticle, C) Ni nanoparticles and D) An HRTEM image of a single Ni nanoparticle showing *d*-spacings of 0.185 nm.

A successful superhydrophobic nanoparticle-PDMS composite was synthesised using $SiO_2$ nanoparticles, which didn't interfere with the polymer curing system. Therefore, gold nanoparticles were silica coated with a silica coat according to the method developed by Darbandi *et al.*[152] Briefly, the gold nanoparticles are silica coated using microemulsion polymerisation of TEOS. A water in cyclohexane microemulsion system was formed with Igepal ® CO-520 creating a nanoreactor within which the polymerisation occurred. The size of the microemulsion droplet limited the degree of silica polymerisation and ensured individual nanoparticles were coated by individual silica spheres. Gold nanoparticles transfer from the cyclohexane into the water microemulsion droplets through amphiphilic intercalation with the surfactant layer and Igepal ® CO-520 (figure 3.15).[152]

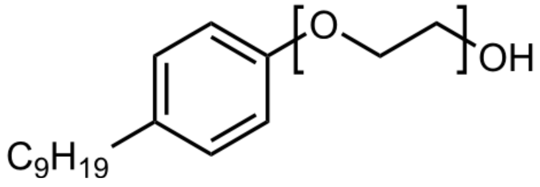

**Figure 3.15**: Chemical structure of Igepal ® CO-520.

The microemulsion was stirred vigorously, and the silica polymerisation catalysed with the addition of ammonia solution. Silica polymerisation was allowed to continue for 24 hours, before the addition of acetone which broke the microemulsion. The Au/$SiO_2$ nanoparticles were then recovered *via* centrifugation, before washing in different alcohols to remove excess silanes and organic solvent. It is noteworthy that the addition of (3-mercaptopropyl)trimethoxysilane aided the adherence of silica to the Au nanoparticle surfaces due to the strong affinity of gold surfaces for thiol moieties.

In order to be compatible with the AACVD system, the Au/$SiO_2$ nanoparticles were treated with trimethoxy(octadecyl) silane which attached itself *via* the trimethoxy groups to the Si-OH groups on the Au/$SiO_2$ surface. In the same way, ammonia solution was used to catalyse this reaction.

TEM micrographs of Au nanoparticles and functionalised Au/$SiO_2$ nanoparticles showed spherical nanoparticles with a low polydispersity index (figure 3.14).

| Material | Average Particle Diameter, nm | Shape | Synthesis |
|---|---|---|---|
| CoO (Periclase structure) | 13.0 ± 2.02 | Rhomboid | Thermal Decomposition |
| $Fe_3O_4$ (Magnetite) | 13.5 ± 1.11 | Spherical | Thermal Decomposition |
| Ni | 9.00 ± 1.92 | Spherical | Thermal Decomposition |
| Au | 5.3 ± 1.55 | Spherical | Chemical Reduction |
| CHFS $TiO_2$ | 13.1 ± 5.62 | Spherical/Elliptical | Hydrothermal Synthesis |
| Slow hydrolysis $TiO_2$ | 4.20 ± 1.27 | Spherical/Elliptical | Low Temperature Hydrolysis |

**Table 3.2**: Summary of the materials, nanoparticle sizes, shapes and synthesis methods used in the synthesis of superhydrophobic nanoparticle-PDMS composites.

The hydrodynamic diameters of the nanoparticles was investigated by DLS. The hydrodynamic diameter is larger than the nanoparticle core size given by TEM (Table 3.2), and is a good indicator of colloidal stability (figure 3.16).

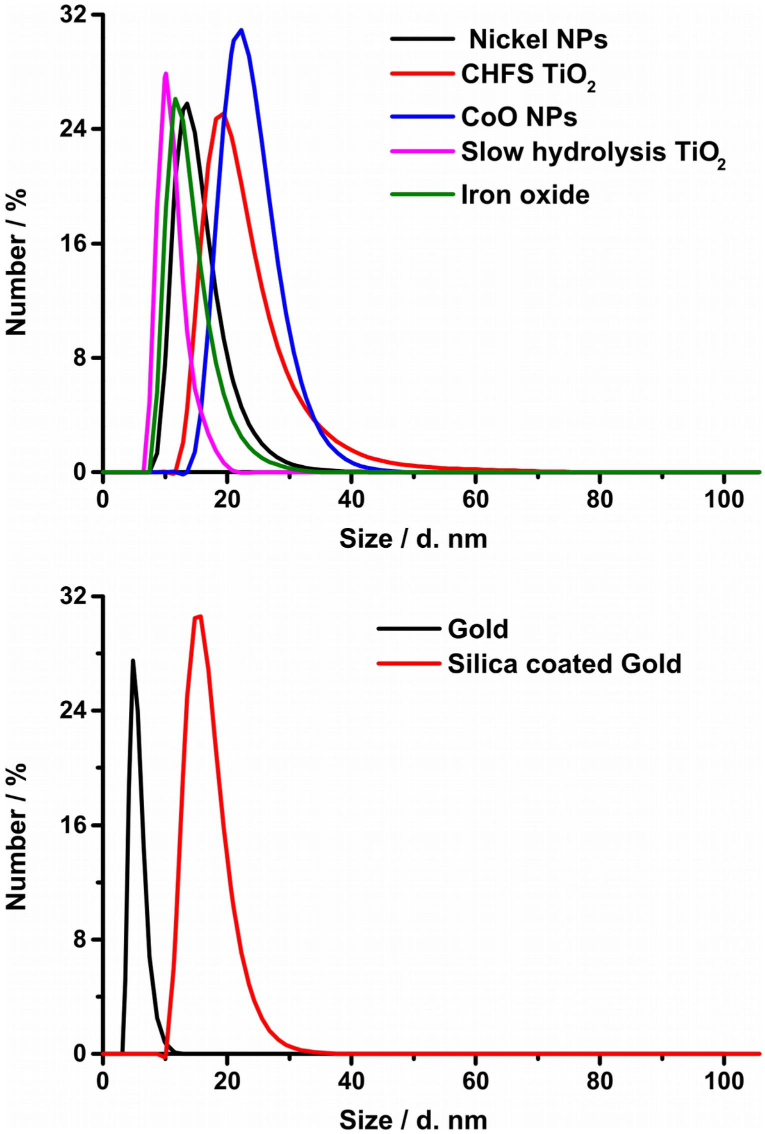

**Figure 3.16**: Top) DLS spectra of: Ni, $TiO_2$, CoO and $Fe_3O_4$ nanoparticles in chloroform and bottom) Au nanoparticles synthesised using the Brüst-Schiffrin method compared to hydrophobised $SiO_2$ coated Au nanoparticles showing an increase indicative of silica coating and subsequent hydrophobisation.

### 3.4.3 Synthesis and characterisation of PDMS- CoO, Ni, $Fe_3O_4$, Au/$SiO_2$ nanoparticle composites

The AACVD of nanoparticles with the Sylgard-184 ® silicone polymer (PDMS, figure 3.3) was carried out *via* the direct incorporation of chloroform dispersible nanoparticles into polymer precursors. The polymer curing proceeds *via* a platinum catalysed process within the CVD reactor and is promoted by the high temperature of the CVD process. The AACVD deposition resulted in highly rough surfaces composed of agglomerations of polymer particles. The process can be described as CVD as there is a vapour phase curing of the polymer that takes place during the depositions. Incorporation of $TiO_2$, $SiO_2$ and $SiO_2$-coated Au nanoparticles were not observed to interfere with the polymer curing mechanism. High concentrations of particles (up to 0.3 g of nanoparticles per 0.7 g of polymer) in the CVD precursor could be tolerated before any visible change in the films were detected. CoO, $Fe_3O_4$ and Ni nanoparticles partially interfered with the polymer curing and a lower concentration of these particles had to be used (less than ~ 0.05 g, ~ 0.1 g and 0.08 g) in order to deposit viable superhydrophobic films.

The visual texture of the superhydrophobic polymer films with nanoparticles incorporated remained unaltered except in colour, which was dependent on concentration and the type of nanoparticle used. The hydrophobicity of the films was shown to be unaltered by incorporation of the nanoparticles with films averaging 162° static water contact angles and an average number of water droplet bounces of seven. A reduction in hydrophobicity was observed for polymer films with high concentrations of nanoparticles (~ 0.3 g of nanoparticles per 0.7 g of polymer) due to partial interference with the polymer curing mechanism. Indeed, SEM micrographs with nanoparticle concentrations specified appeared to be no different to the microstructures observed for plain PDMS films or titania nanoparticle-PDMS composites (figure 3.17).

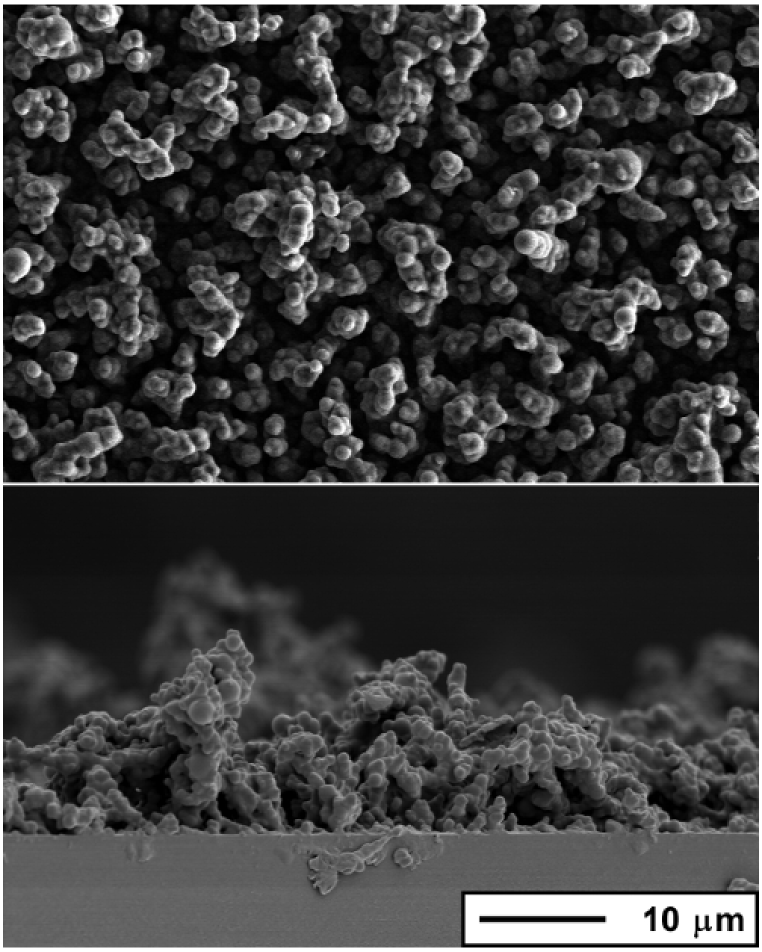

**Figure 3.17**: SEM image of PDMS with $TiO_2$ nanoparticles incorporated, deposited *via* AACVD using a substrate temperature of 390°C. The deposition used 0.2 g of nanoparticles and 0.7 g of Sylgard-184 ® polymer precursor. The scale bar is applicable for both top-down and side-on images.

The presence of the given nanoparticles in the PDMS films was primarily confirmed by TEM. The overall thickness of the films were between 2-4 μm which hindered the use of TEM and atomic force microscopy, but thin enough portions were obtained by carefully removing a small portion of the film, sonication in chloroform (1 ml) and drop-casting onto a TEM grid. The pronounced difference in contrast of crystalline materials such as $Fe_3O_4$ and CoO compared to the PDMS also improved micrograph quality.

The excess oleate species in the CoO and Ni nanoparticle samples was found to have a highly detrimental effect on the formation of a nanoparticle containing aerosol in the AACVD process. This was due to the attraction of the nanoparticles to the non-volatile oleate species, over the more polar carrier-solvent (chloroform), which hindered their transfer from the aerosol generator to the CVD reactor. It was found that the particles tended to aggregate within “bulbs” of PDMS formed by the curing of the polymer, which allowed the nanoparticles to protrude from the surface.

The PIFCOHEALTH ultrasonic humidifier generated an average aerosol droplet size of ~3μm at 40 kHz frequency and 25W power with chloroform as the solvent. The solvent within these droplets invariably evaporated between the reservoir and the CVD reactor, thus shrinking the size of the droplet. The nanoparticles were well dispersed through the aerosol solution, and tended to agglomerate according to the decreasing size of the aerosol droplet. Upon contact with the heated glass substrate, the carrier solvent evaporated rapidly, leaving a spherical agglomeration of particles. The PDMS monomers (also contained in the droplet) then cured around the particles, forming the aforementioned PDMS “bulbs”. This can be seen by the TEM micrographs of the nanoparticles, particularly in the case of $Fe_3O_4$, which cured nicely into “clusters” (figure 3.18).

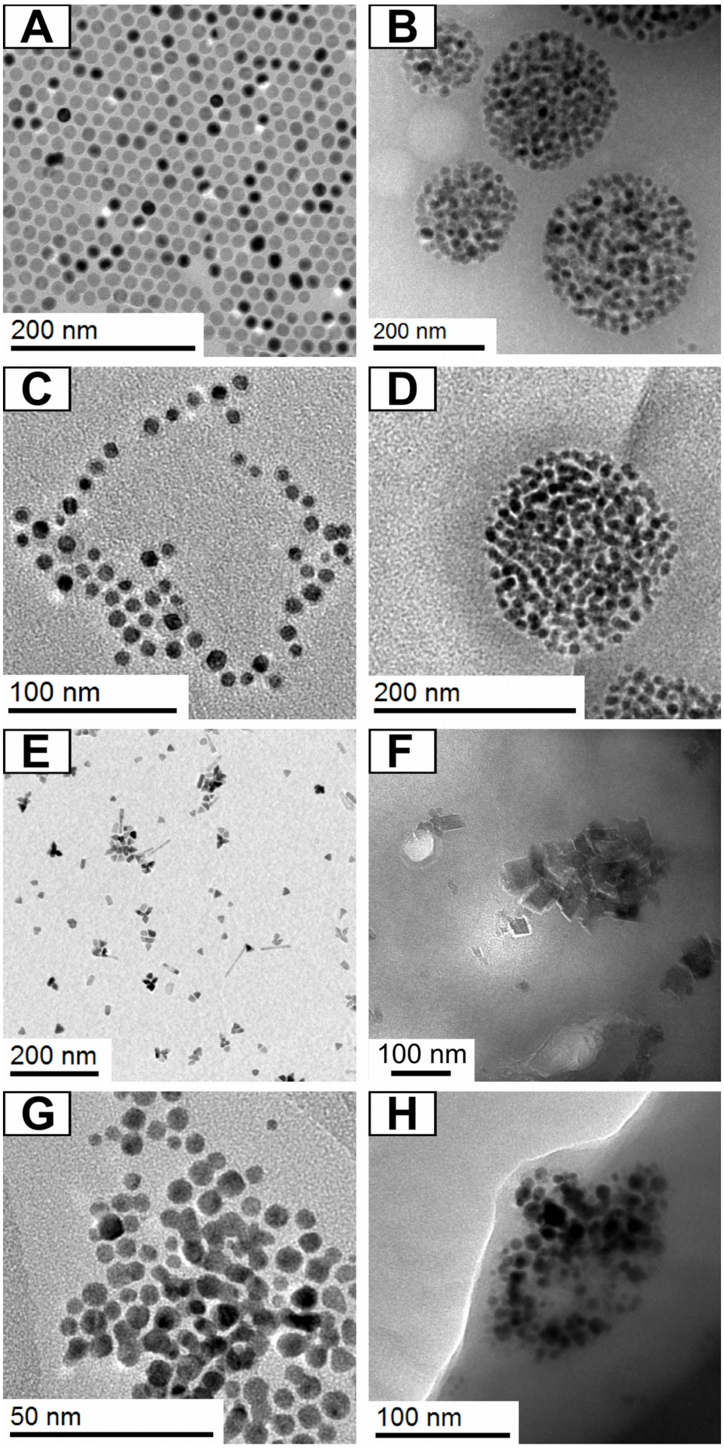

**Figure 3.18**: TEM images showing: A/B) $Fe_3O_4$ , C/D) Ni, E/F) CoO, and G/H) Au/$SiO_2$ nanoparticles. The particles are shown prior to depositions (left column, A, C, E and G) and as deposited embedded in the PDMS films *via* AACVD (B, D, F and H).

The encapsulating nature of the film protects the nanoparticles from degradation, so the film can retain both functional properties and microstructure, with no change in properties in air over 6 months. The films also proved to be physically robust, substantial pressure was required remove the films even with the use of a steel scalpel blade.

Nanoparticle morphologies and sizes remain unaltered by the CVD process, as evidenced by TEM micrographs of the "rhomboid" CoO particles (figure 3.18). Their rhomboid shape can clearly be seen in all of the systems studied. However, it is noteworthy that due to the high temperature of the CVD reactor (390 °C), particles which are susceptible to high temperature degradation/oxidation are not suitable such as CdSe quantum dots. The nanoparticles were further characterised using EDS after deposition. EDS analysis definitively showed the presence and encapsulation of particles in silica due to the massive increase in silicon relative to the particulate elements (figure 3.19).

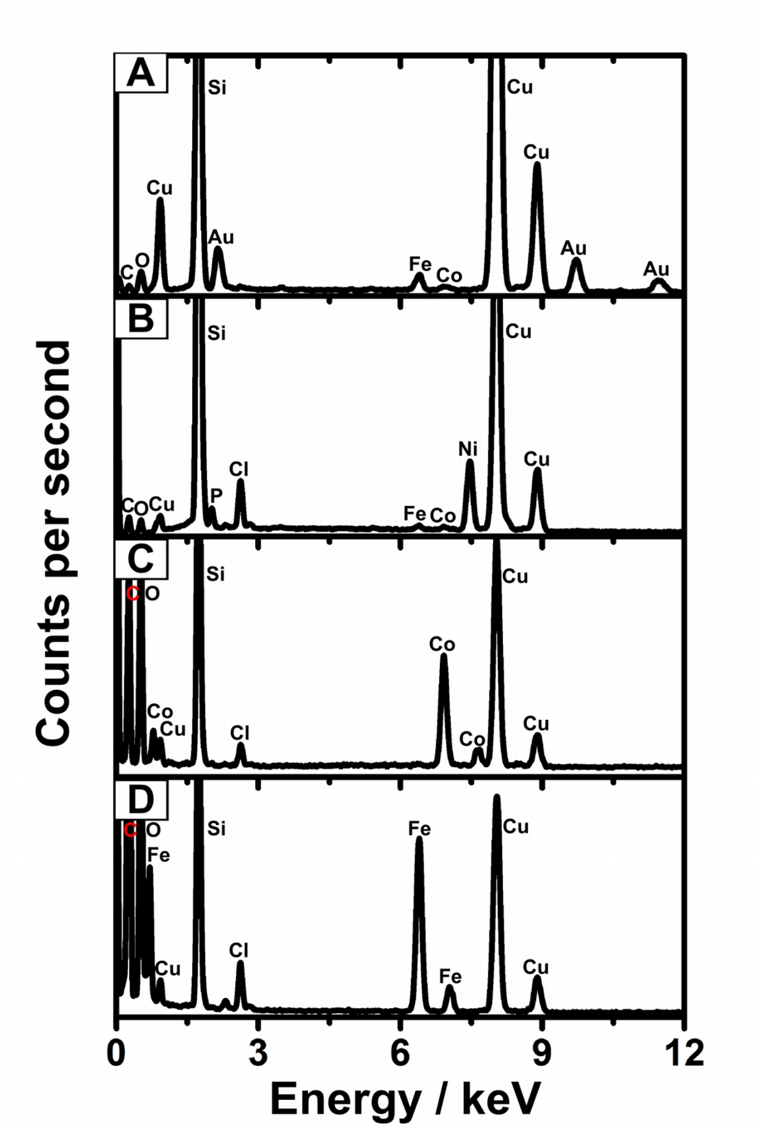

**Figure 3.19**: EDS spectra of: A) Au/$SiO_2$- PDMS composite, B) Ni-PDMS composite, C) CoO-PDMS composite and D) $Fe_3O_4$-PDMS composite.

EELS elemental mapping images were collected to identify certain elements due to loss of energy of inelastically scattered electrons. Figure 3.20 shows the TEM image for $Fe_3O_4$ nanoparticles in the PDMS film with the silicon and iron jump ratios. The images are filtered to eliminate electrons which lost energy from a particular element (*i.e.* iron and silicon), so the highlighted parts of the image are from the target element. Iron in the $Fe_3O_4$ nanoparticles is clearly visible in this figure, and are confirmed as the sole source of iron in the composite. From the silicon EELS image, the $Fe_3O_4$ nanoparticles appear to have been coated in a uniform layer of silicon during the CVD/polymer curing process.

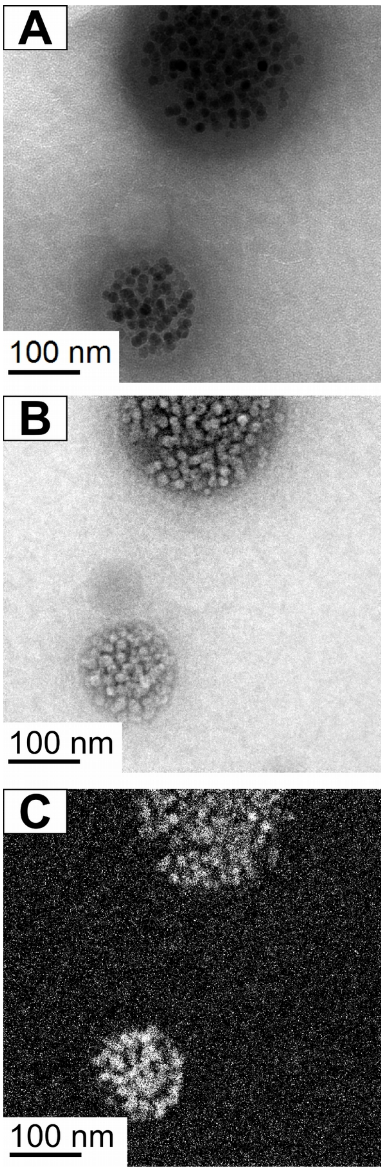

**Figure 3.20**: EELS elemental mapping images of $Fe_3O_4$ -PDMS composite. A) is a zero loss TEM image, B) the silicon elemental map and C) the iron elemental map. Silicon and iron are shown in white in images B) and C) respectively.

The magnetisation of $Fe_3O_4$ nanoparticles in the film sample was analysed using SQUID magnetometry. Hysteresis loops (and therefore magnetic moments) of 1 ml of $Fe_3O_4$ particle aerosol/monomer solution (dried *in vacuo*) in chloroform and one square inch of $Fe_3O_4$ film were acquired at 300 K. The $Fe_3O_4$ film sample was prepared by removing one square inch of film from the glass and placing inside the SQUID sample tube. The hysteresis loop indicates that the $Fe_3O_4$ is superparamagnetic in colloidal suspension and in the films, due to their small crystallite size (< 20 nm). A saturation magnetisation of the PDMS-$Fe_3O_4$ film was calculated from SQUID measurements to be 0.00137 emu for 0.7 mg of film (1.96 emu/g). For $Fe_3O_4$ nanoparticles, a saturation magnetisation of 0.06749 emu for 1.6 mg (42.2 emu/g) of dried powder. Calculating the percentage concentration by mass ((1.96 / 42.2) × 100) gives an estimated mass concentration of 4.6 % of $Fe_3O_4$ in the polymer film (figure 3.21).

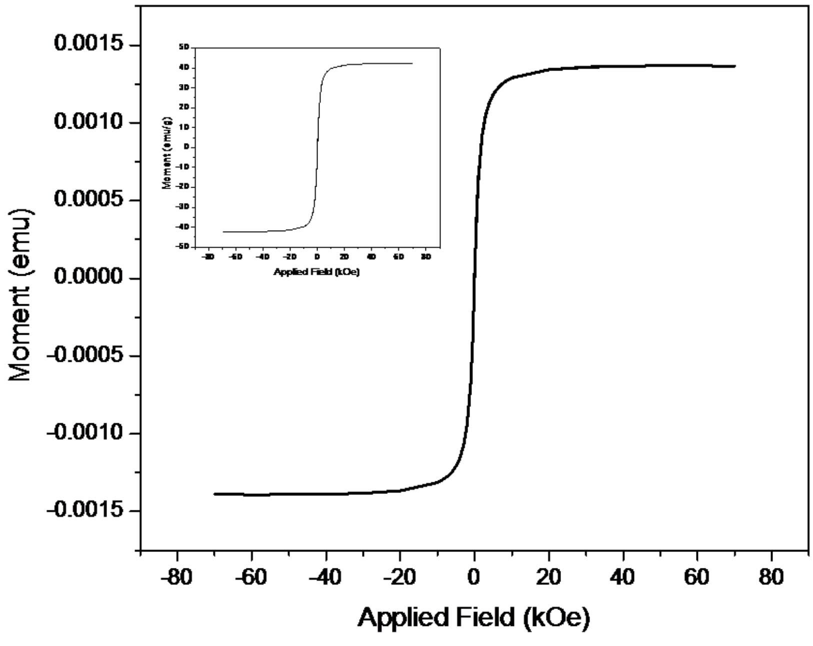

**Figure 3.21**: Magnetic hysteresis loop from SQUID analysis at 300K for polymer and $Fe_3O_4$ composite with data from $Fe_3O_4$ powder standard (inset).

The catalytic activity of nanoparticle-embedded superhydrophobic materials was tested using a protocol described by Li *et al.*[155] The composite films were able to breakdown dye at similar rates to those seen for flat films of titanium dioxide deposited using CVD. This is due to the highly rough surface microstructure of the superhydrophobic materials allowing for a large area of surface-dye contact (see Crick *et al.*).[156] The nickel nanoparticles were also tested using the hydrolytic dehydrogenation of $NH_3BH_3$. The catalytic testing was carried out using superhydrophobic polymer films (25 x 25 mm substrate size) with Nickel nanoparticles incorporated. These substrates were submerged in an aqueous solution of $NH_3BH_3$ (0.1 g in 10 ml of water) in a sealed Schlenk flask with the evolved gas collected and volume measured. The volume of hydrogen gas evolved was 18 ml during 24 hours of running the experiment. The above examples show the potential for these surfaces to be used as an approach toward high surface area catalysts, without the need for using the pure substance. Although the nanoparticles were encapsulated by the polymer, some protruded through (effectively forming part of the microstructure) hence catalytic activity was observed.

## **3.5 Summary**

In this chapter, the synthesis of superhydrophobic, photocatalytic polymer-nanoparticle composites was demonstrated, and a general method for the synthesis of superhydrophobic polymer- nanoparticle composites developed. The synthesis involved the AACVD of a chloroform solution of Sylgard-184 ® monomers, curing agent and hydrophobically ligated nanoparticles. The deposition occurred at 360 °C in a cold-walled CVD reactor on the top of two glass substrate sheets due to thermophoretic effects. Due to the nature of the PDMS, the polymer retained its superhydrophobicity after UV irradiation, even when containing anatase $TiO_2$ nanoparticles, a potent photocatalyst. The photocatalytic potential of the PDMS-anatase nanoparticle composites was successfully demonstrated upon photodegradation of Resazurin dye. The potential of these surfaces for anti-bacterial, self-cleaning surfaces is hereby demonstrated with obvious application in sterile environments such as hospitals. Anti-bacterial tests for this material are the subject of ongoing research, and field testing in hospitals is the next logical step.

The method was then extended to CoO, Ni, $Fe_3O_4$, Au/$SiO_2$ nanoparticles to demonstrate the versatility of this technique, and in doing so, to the author's knowledge, created the world's first magnetic, superhydrophobic thin film. There were however limitations to this technique; namely nanoparticles which are thermally sensitive or susceptible to oxidation such as CdSe/ZnS quantum dots do not survive the high temperatures required and untreated gold nanoparticles prevent the polymer from curing.

The PDMS-nickel nanoparticle composite exhibited a good catalytic response in the dehydrogenation of ammonia-borane complex. 18 $cm^2$ of hydrogen gas evolved during 24 hours of running the experiment, with an initial Ni nanoparticle loading of 0.05 g. Of course, much of the aerosol reaction mixture is not deposited on the glass substrate, so the actual nanoparticle loading is significantly lower.

The nanoparticles and PDMS-nanoparticle composites were characterised using a variety of techniques including: XRD, XAS, EDS, TEM, EFTEM, SEM, water contact angle measurements, ATR-FTIR, and SQUID measurements. Electron microscopy and elemental analysis techniques showed that nanoparticles cured in PDMS bulbs, and dye degradation and SQUID measurements showed the unequivocal retention of nanoparticle properties post-synthesis. The future of these composites to provide functionality and superhydrophobicity for a myriad of applications is bright. If the PDMS coating could be made transparent, then nanocrystals with thermochromic properties such as monoclinic vanadium(IV) oxide for energy saving windows can be envisaged. High surface area catalysis is another area of use for these composites as “dip” catalysts, as shown by the catalytic dehydrogenation of ammonia-borane.

# Chapter 4: Doping copper into the shells of quantum dots through the decomposition of metal dithiocarbamates

## Preface

Quantum dots are a class of semi-conducting nanocrystals with size tunable photoluminescence properties. There have been great efforts to improve quantum yields, photostability, functionalisation strategies, longevity in colloidal suspension and to reduce toxicity. This chapter focusses on the synthesis of quantum dots and doping metals into their shells. This is achieved by decomposing single-source precursors, metal-dithiocarbamate complexes, onto the surfaces of quantum dot cores in the presence of surfactants.

Metal-dithiocarbamate complexes are promising candidates for shelling materials for quantum dots as they are air stable and offer an alternative to pyrophoric organometallic reagents. By using a mixture of zinc and metal dithiocarbamates in differing ratios, Hg, Cd, Cu and In were doped into the shells of CdSe (II-VI) and InP (III-V) quantum dots. Depending on the metal, there were differing effects on the photoluminescence of the resulting quantum dots. On shelling, the quantum yields generally improved, with quantum yields as high as 0.72 reported for CdSe/ZnS-CdS quantum dots. However, certain systems such as CdSe/ZnS-CuS saw an increase in surface defects due to poorer lattice matching and a blue-shift in photoluminescence emission. The copper doped CdSe/ZnS-CuS quantum dots were, however, shown to be effective in catalysing “click” chemistry under UV irradiation. The quantum dots produced a 100% yield in the “click” reaction between benzyl azide and phenylacetylene in *n*-hexane and were recoverable after precipitation with ethanol and centrifugation. In this way, several reaction cycles were achieved, with catalytic turnover numbers of 625 reported.

Mechanisms for the photoluminescence changes and catalysis seen in the CdSe/ZnS-CuS examples are postulated. Quantum dot samples were characterised by: TEM, HRTEM, EFTEM, EDS, XPS, photoluminescence spectroscopy, UV/vis spectroscopy, quantum yield measurements and photoluminescence lifetime measurements.

## 4.1 Improving quantum yields of quantum dots *via* shelling

One of the main obstacles to high photoluminescence quantum yields in quantum dots are surface defects which act as electron "traps", and prevent electron-hole recombination. These surface defects act as pathways for fast non-radiative de-activation channels for photogenerated excitons, thus reducing quantum yield. However, prevention of exciton recombination is desirable for applications such as photocatalytic water splitting, as good electron-hole separation is required for reduction and oxidation reactions involved in that process.[254] Classical materials for quantum dots such as II-VI materials tend to be highly toxic and susceptible to oxidation such as cadmium selenide, so require the overgrowth of a shell for many applications. Quantum dot shells tend to be composed of similar materials, with desired bandgaps,[255] lower toxicity[107] and effective crystalline lattice matching between core and shell.[256]

It is imperative that effective shelling materials have a crystalline structure analogous or similar to the core in order to prevent lattice defects forming on the core/shell interface.[255] Lattice mismatch occurs primarily due to differences in bond lengths between atoms in the core and shell. During a shell synthesis, there is a maximum quantum yield which is attained during the epitaxial (layer-by-layer) growth of a shell, found to be < 2 monolayers for CdSe/ZnS[257] and ~ 2.2 monolayers for CdSe/CdS quantum dots, with CdSe/CdS having a lower lattice mismatch.[258] Shells in this order of size yield highly luminescent quantum dots, but at the cost of increased quantum dot susceptibility to oxidation. Post-shell synthesis, an annealing step can also be effective in removing defects and improving lattice matching.[255]

Shelling materials can be chosen such that the photoluminescence can be preserved/affected in a variety of different ways. This is achieved by manipulation of bandgaps to create hierarchical structures whereby the exciton exists between the smallest energy gap of the conduction and valence bands of connecting shelling materials. This can be visualised by looking at a typical Type I system, CdSe shelled with ZnS in figure 4.1:

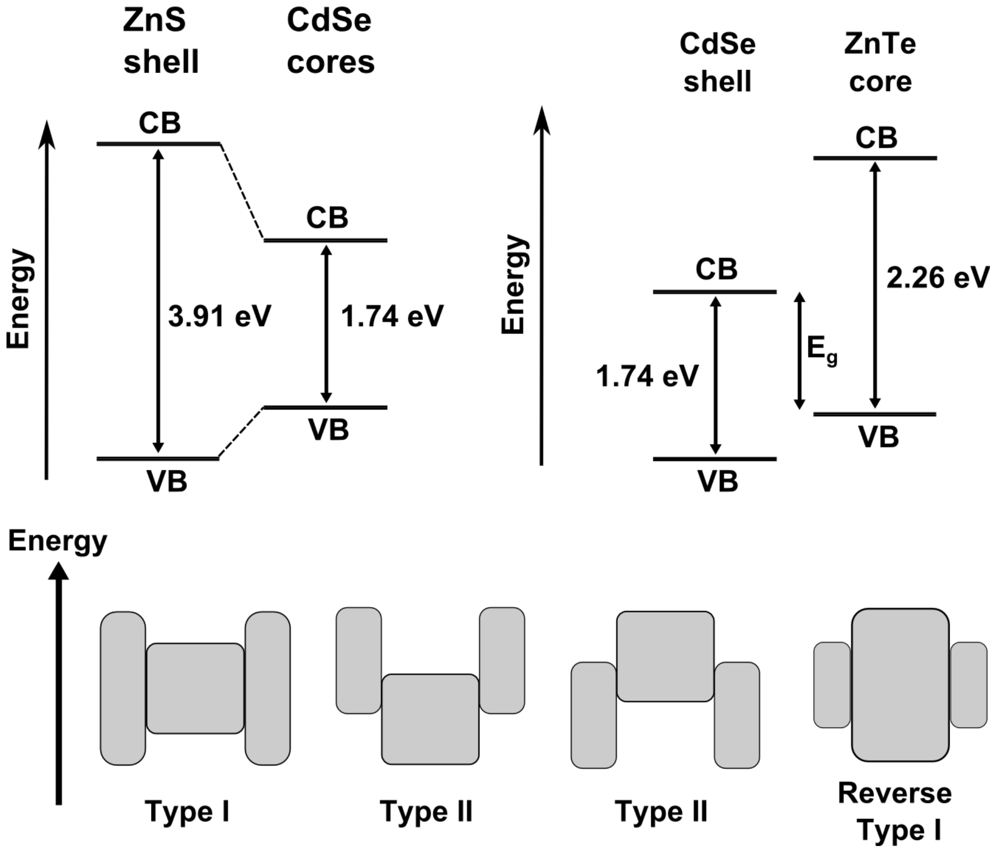

**Figure 4.1**: Top left) Type I CdSe/ZnS quantum dot system with the smallest conduction band-valence band energy gap confining photoluminescence to the CdSe core. Top right) Type II ZnTe/CdSe system with the smallest energy gap being between the conduction band of the CdSe shell and the valence band of the ZnTe core. In this way, Type II systems tend to exhibit highly red-shifted photoluminescence. Bottom) Single-shell band gap configurations, with the grey rectangles indicating the positions of the core and shell bandgaps.

The smallest energy gap between any adjacent core/shell bandgaps in a Type I system resides in the core. So for the CdSe/ZnS system in figure 4.1, the addition of the ZnS will not alter the photoluminescence emission wavelength drastically, but due to surface defect elimination and exciton leaking into the shell, the effective diameter of the quantum dot increases, and a small red-shift is observed. A reverse type I system confines the photoluminescence to the shell, so a large red-shift is expected on shelling. Type I systems have excellent electron-hole wavefunction overlap within the core, giving the greatest probability that electron-hole recombination will occur at the band edge of the material.[112,255]

Type II systems are brought about when core/shell material band gaps are offset with respect to one another, either above or below the bandgap of the core. The smallest energy gap between core and shell is therefore between the conduction band of the shell and the valence band of the core, as in ZnTe/CdSe in figure 4.1. Again, this leads to a significant red-shift as the charge carriers are confined mostly in separate domains of the quantum dot, *i.e.* one in the core and shell. This physical separation leads to poorer wavefunction overlap between electron and hole, and therefore a longer excited state lifetime. Longer excited state lifetimes give non-radiative pathways (*i.e.* not photoluminescence emission) a greater chance to occur, thus reducing quantum yield. Materials used for type II shells tend to have poorer lattice matching between core and shell, so surface defects and general complexity of the system leads to more non-radiative decay pathways.

Type III systems are a further class of quantum dot core/shell heterostructure where the bandgaps of the core and shell have no overlap whatsoever.[255] To date, there is no literature precedent for type III core/shell quantum dots.

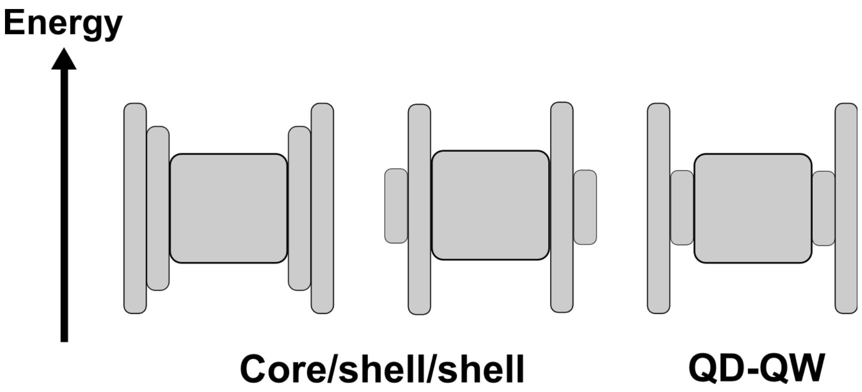

**Figure 4.2**: Bandgap diagrams showing core/shell/shell quantum dots and quantum dot-quantum well configurations. The rectangles represent the bangap energies of the core and shells of core/shell/shell quantum dots.

On top of these structures, research into multiple-shell structures has led to vastly improved lattice matching between core and shell and therefore improved quantum yields (figure 4.2).[255] QD-QW systems employ a layer of a material with a smaller bandgap than the core and the outer shell, so the exciton is effectively confined in two dimensions. Examples include CdS/HgS/CdS,[259] ZnS/CdS/ZnS[260] and the reverse QD-QW system CdSe/ZnS/CdSe, showing two distinct emissions from the core and the shell.[102]

In terms of synthesis of a quantum dot shell, it is important to first consider the material and the effect it will have on the quantum dot photoluminescence and overall quantum yield. The effect of ligands, concentration and synthesis temperature are very important in affecting the growth, lattice matching, thickness and overall crystallinity of the final shell. There are also obstacles to overcome, such as the solubility of monomer (too high and shell growth will not occur), the binding strength of the core surface ligands and if homogeneous nanoparticle nucleation of the shell reagents occurs.[261]

The choice of ligand and the removal of ligands from the core synthesis are paramount when considering a shell synthesis. Ligands used in the core synthesis may not prevent dissolution or Ostwald ripening of the quantum dots at high temperature.

Therefore in some shell syntheses it is vital that excess ligands/monomers are removed and replaced with appropriate alternatives. For example, for the growth of a ZnS shell on CdSe cores require weakly co-ordinating alkyl amines and trioctylphosphine oxide.[147,261,262]

The concentration of shelling reagents should be such as to match the concentration of reagents in the latter stages of quantum dot core synthesis. Concentrations can also be estimated as to grow monolayers of atoms around the quantum dot cores.[147,261]

Shell synthesis temperatures of 200 - 260 °C are typical for many syntheses, although new organometallic methods coupled with single-source precursors have led to the development of crystalline quantum dot shells grown at significantly lower temperatures.[64,147,150,263] This is advantageous as it prevents the nucleation of any nanoparticles composed of the shelling reagents. Shelling temperature is also important due to the rate of Ostwald ripening. Smaller nanoparticles have a higher rate of Ostwald ripening, and so require lower temperatures for shell formation. However, it is often desirable to use higher temperatures to remove shell defects and attain maximum shell crystallinity and therefore maximise quantum yield.

## 4.2 Quantum yield determination

One of the inherent challenges in nanoparticle chemistry is the inability to determine the concentration of nanoparticle dispersions accurately. This is in part due to the composition of individual nanoparticles, with complex contributions from material concentration gradients in the core, surface defects and ligands. These properties vary from nanoparticle to nanoparticle due to overall sample polydispersity, shape anisotropy and so forth. However, the determination of the concentration and size of gold nanoparticles by UV/vis spectroscopy has literature precedent.[264]

For quantum dots, the quantum yield represents a universal method for the determination of how effective a fluorophore a sample of quantum dots is, independent of concentration and the Beer-Lambert law. Quantum yield, "$\Phi$" is defined as the number of photons emitted divided by the number of photons absorbed (equation 12).

$$\Phi = \frac{photons\ emitted}{photons\ absorbed} \qquad \text{Equation 12}$$

The standard method of quantum yield determination involves comparing the analyte, in this case the quantum dots to a standard fluorophore of known quantum yield,"$\Phi_{ST}$" at wavelength "$\lambda$", which is ideally identical to the analyte. This method involves creating a linear plot of absorption (determined by UV/vis) against integrated fluorescence intensity of several diluted samples of standard with solvent refractive index "n". In this way, a calibration line of a fixed gradient, "gradient$_{ST}$" is created which will pass through the origin if no fluorescence self-absorption occurs (*i.e.* the concentration of the standard solution is below a certain threshold). This process is then repeated for the analyte, obtaining "gradient$_X$". The quantum yield of the analyte, "$\Phi_X$" can then be determined by taking the ratio of the gradients according to equation 13. Accurate quantum yield determination using this method requires the standard calibration to be performed before every batch of samples as it removes instrument noise.

$$\Phi_X = \Phi_{ST}\left(\frac{Gradient_X}{Gradient_{ST}}\right)\left(\frac{{n_X}^2}{{n_{ST}}^2}\right) \qquad \text{Equation 13}$$

Modern spectrofluorometers are increasingly being fitted with integrating spheres; a tool which allows for the direct measurement of absolute quantum yield. The light scattered by the interior of an integrating sphere is evenly scattered over all angles, and comes into contact with the sample housed within the integrating sphere. The processes is repeated for a reference (solvent) and the integrated difference between the two lines corresponds to the absolute quantum yield, equation 12.[265]

## 4.3 Quantum dot shelling- a brief review

The overgrowth of shells onto semiconductor quantum dots has been the subject of intensive research, due to the increase in quantum yields,[266] reduction in cytotoxicity,[267] resistance to oxidation[255] and tunable photoluminescence to a wider spectral range [268–271] that shelling with a suitable material affords (section 4.1). Shelling also opens up a greater range of applications due to the harsher conditions the quantum dots can tolerate. The need for greater control over size and photoluminescence properties of quantum dots has in turn proliferated the need for new quantum dot shells, synthetic routes for shells and new shelling materials. It is noteworthy that the literature on this subject is vast, and the information in this section provides key developments and highlights in the development of quantum dot shell synthesis.

Initial quantum dot shelling experiments, dating back to the mid-1980s, focussed on the detection of surface defects and the effects of the addition of rudimentary shells. For example, Spanhel *et al.* such as a $CdS/Cd(OH)_2$ system showed a marked increase in fluorescence quantum yield, with yields of up to 50% reported, and two thousand times more stable in photoanodic corrosion measurements than a CdS core sample.[272] Other early methods focussed on the effects of quantum dot ligands, with silver sulphide[273] and triethylamine[272] and exotic ligands such as fullerenes tested.[274] A notable example of the early use of ligands for the modification of quantum dot surfaces is the use of dithiocarbamate anions for CdS nanoparticles.[272] Kamat and Dimitrijevic found the addition of dithiocarbamate anions to a colloidal suspension of CdS quantum dots decreased the quantum yield and the photoluminescence decay lifetime of the CdS. On pulse laser excitation, electron transfer from the CdS forms dithiocarbamate radicals which then dimerise, which led to much reduced photoanodic corrosion of the CdS.[275] The majority of the pre-organometallic routes to quantum dot shells focussed on the precipitation of salts from solution, activated by processes such as changes in pH[259] or radical generation.[276]

The overgrowth of a ZnS shell for CdSe quantum dots, a type I system, was first realised by Kortan *et al.* in 1990.[277] The authors also report a reverse type I system by growing a CdSe shell onto a ZnS seed. This synthesis is based on the formation of an inverse micellular system based on dioctyl sulfosuccinate sodium salt, more commonly known as AOT, within which shells are grown *via* the slow injection of metal alkyl species, sodium sulphide and zinc perchlorate. Spectroscopically, a red shift is observed on shelling, typical of a type I system.

The development of shells of II-VI semi-conducting nanocystals have been at the forefront of the field, driven mainly by the ease of the synthesis of high quantum yield CdSe quantum dots *via* hot-injection, see section 2.2.5. The first organometallic routes for the synthesis of quantum dots *via* the hot-injection method opened the possibility of the mass production of quantum dots.[72,98,278] This series of synthetic breakthroughs allowed quantum dots to be scrutinised and developed in research laboratories across the world, in turn leading to organometallic routes towards quantum dot shells.

One of the first, widely used organometallic routes for the synthesis of a shell was developed by Hines and Guyot-Sionnest[279] and Dabbousi *et al.*[72] for the synthesis of CdSe/ZnS quantum dots. This method involved the slow injection of 1,1,1,3,3,3-hexamethyldisilathiane and diethyl zinc in trioctylphosphine into a solution of CdSe cores in a nitrogen purged flask at elevated temperature (140 - 220 °C). The amount of precursor required and the shelling temperature was calculated from the size and shape of the cores determined by TEM and small angle X-ray scattering. Modifications to this method include the use of syringe drivers for uniform shell growth[262] and the use of *in-situ* UV/vis spectroscopy so the shelling process can be tuned dependent on the emission wavelength required.[71] This route has been used successfully over a large range of quantum dot sizes, even for shell growth onto CdSe clusters.[280]

Fatty acid salts of zinc and elemental sulphur have also enjoyed success in epitaxial ZnS shell growth, as their reactivity is lower than that of diethyl zinc or 1,1,1,3,3,3-hexamethyldisilathiane.[102,281,282] A recent example of the combination of zinc-fatty acid salts with 1-dodecanethiol for the synthesis of $CuInS_2$/ZnS quantum dots was developed by Booth *et al.* The authors used the decomposition of zinc oleate in the presence of tetrahedral $CuInS_2$ quantum dots capped with 1-dodecanethiol and found that at elevated temperatures (230 °C initially, then annealed for 4 hours at 220 °C), a crystalline ZnS shell was formed.[283] The use of zinc-fatty acid complexes with elemental sulphur (and derivatives) represents a less hazardous route than the use of pyrophoric metal alkyl compounds, but require multiple injection steps for completion.

Gas/solution interface reactions, notably those with gases such as hydrogen sulphide in combination with metal alkyl compounds or metal salts have also been documented, but often require an annealing step to ensure crystallinity of the final product.[284] Zhang *et al.* prepared large semi-conducting shells through soft acid-base manipulation of single-source precursors to synthesise an array of core/shell nanocrystals, often with high lattice mismatches.[285]

Pan *et al.* described the synthesis of CdSe nuclei in the size range 1.2 - 1.5 nm which were subsequently shelled with CdS. Both core and shell syntheses were carried out at 140 - 180 °C in an autoclave using cadmium myristate and selenourea/thiourea as precursors, oleic acid as a surfactant, and a toluene/water two-phase solvent system.[286]

So far, the shape of the resultant quantum dot shells has assumed to be spherical. However, there have been papers published on the effects of shell shape anisotropy on nanoparticle quantum yield. McBride *et al.* proposed a “bullet” shaped shell through the growth of ZnS along the <001> crystal plane, and found this to be critical in preparing quantum dots with a quantum yield of 100 %.[287] Xie *et al.* grew tetrapod shaped ZnTe/CdSe and ZnTe-CdS nanocrystals by alternating injections of Cd-oleate in 1-octadecene and selenium in 1-octadecene at 215 °C and Cd-oleate and sulphur solutions at 235 °C.[288] The directional growth of the CdSe onto the ZnTe was templated by the surfactants (oleylamine). As far as optical properties are concerned, the authors noted an absorption band at 650 nm which is attributed to the CdSe arms for the ZnTe/CdSe tetrapods, and indicative of a type II system.

Anisotropic growth of CdS shells on CdSe spherical core nanoparticles has been shown by several groups, particularly focussing on the growth of CdSe/CdS nanorods.[282,289] It was found by several groups that low reaction temperatures and the slow injection of alkyl cadmium and 1,1,1,3,3,3-hexamethyldisilathiane (with a ratio slightly biased in favour of the 1,1,1,3,3,3-hexamethyldisilathiane) facilitated the growth of CdSe/CdS nanorods. Epitaxial growth on a single facet has been elucidated to the directing effects of surfactants and lattice mismatching on certain facets. Quantum yields of 0.7 have been reported, with high control over the rod length.[255,290] Surfactant directing effects have also been demonstrated in CdSe/CdS nanorods at elevated temperatures (< 350 °C) *via* hot-injection.[289] Further evidence for the increase in quantum yield afforded by anisotropic shell growth has been evidenced by tetrapod growth of CdTe/CdSe nanocrystals *via* multiple injection steps of different precursors and annealing steps. In this way, Chin *et al.* reported the tuning of character of the resultant quantum dot from a type I to a type II quantum dot system through altering the shape (with quantum yields of 0.82 reported), potentially leading to band tunable quantum dot nanostructures for myriad applications.[109]

Chemical bath deposition techniques have been used for the sequential deposition of shells onto quantum dots, a technique known as the successive ion layer absorption reaction (SILAR) method.[102] SILAR was originally developed for the deposition of reagents onto the surface of thin films.[291,292] Precursors are added gradually *via* a syringes, and the build up of the layer is monitored by UV/vis spectroscopy. [102,293] Recently, Hao *et al.* reported incredibly high quantum yields (~ 0.95) for CdSe/ZnS quantum dots by the deposition of ZnS *via* the SILAR method, directed by trioctylphosphine.[266] The authors report the maximum quantum yield is maintained after the growth of three monolayers and maintained on the deposition of a further three layers. Trioctylphosphine dissolves excess selenium at the quantum dot surface and activates the zinc and sulphur precursors (zinc oleate and elemental sulphur). Quantum dots have also been deposited as thin films *via* the SILAR method by several groups to make quantum dot sensitised solar cells.[110,294]

Single-source molecular precursors have enjoyed a renaissance as precursors for quantum dot shell synthesis, rather than as precursors for quantum dot cores where they have been largely superseded by dual precursor based hot-injection syntheses. Pioneering work by O'Brien and co-workers into single-source precursors for quantum dots (in particular III-V and II-VI materials) laid the foundation for single-source shell precursors. Examples for II-VI quantum dots include the syntheses of: zinc(II) heterocyclic piperidine, zinc(II) tetrahydroquinoline dithiocarbamates,[295] zinc(II) diethyldithiocarbamate,[296] zinc(II) *bis*(hexylmethyldithiocarbamate) for ZnS,[297] lead(II) xanthate for PbS,[70] zinc(II) *bis*(diethyldiselenocarbamate) and zinc(II) ethyl(diethyldiselenocarbamate) for ZnSe,[296] cadmium(II) ethylxanthate[263] and cadmium(II) *bis*(hexylmethyldithiocarbamate) for CdS,[298] cadmium(II) ethyl(diethyldiselenocarbamate) for CdSe[299] and indium(III) *tris*(di-*tert*-butyl phosphide) decomposed in 4-ethylpyridine for III-V InP quantum dots.[300] This work led directly to the use of as single-source precursors, mainly metal dithiocarbamate species for the synthesis of quantum dot shells.

Metal-dithiocarbamate shell precursors are viable alternatives to multiple injection based organometallic reagents as they are air-stable compounds which have low decomposition temperatures.[149] This allows the formation of a metal sulphide shell at low temperatures, which eliminates the nucleation of metal sulphide nanoparticles. One of the first example of the use of zinc(II) diethyldithiocarbamate as a shell precursor for CdSe cores was by Wang *et al.*[301] in a microcapillary reactor heated to 150 °C and 240 °C depending on the composition of the shelling precursor solution. The authors used either a trioctylphosphine- zinc(II) diethyldithiocarbamate or 1-octadecene- zinc(II) diethyldithiocarbamate solution at the aforementioned synthesis temperatures to affect shelling. Further work by Luan *et al.* utilised a trioctylphosphine-oleylamine -1-octadecene-zinc(II) diethyldithiocarbamate mixture at 80 - 160 °C in a microfluidic reactor for highly luminescent CdSe/ZnS quantum dots.[302]

Other quantum dots such as ternary $CuInS_2$ and InP have been coated using the thermal decomposition of zinc(II) diethyldithiocarbamate in the presence of surfactants, giving good improvement in quantum yield. In particular, the synthesis of InP/ZnS quantum dots by Xu *et al.* used zinc undecylenate in the core InP synthesis which, along with hexadecylamine, forms a layer of zinc around the InP core which facilitates the lattice matching between core and ZnS shell (grown using zinc(II) diethyldithiocarbamate).[150] Variation in the concentration of zinc undecylenate provides high control over quantum dot size, and therefore emission wavelength. The use of zinc(II) diethyldithiocarbamate has been investigated by Dethlefsen and Døssing in an oleylamine, 1-octadecene and trioctylphosphine mixture, with shell thickness, decomposition temperature and photoluminescence of the resultant CdSe/ZnS scrutinised.[147]

Other metal-dithiocarbamate species (akin to those mentioned as precursors for quantum dots) for the synthesis of quantum dot shells have been investigated, full details of which are beyond the scope of this thesis, but can be found in the following review articles.[112,149,255]

Core/shell/shell systems borrow from the shelling methods listed, but require multiple shell growth stages for completion, which require isolation of the quantum dots before each growth phase. Core/shell/shell systems allow core and shell materials which may have poor lattice matchings to have a strain reducing intermediate layer, thus reducing surface defect formation.[255] This could potentially allow the synthesis of quantum dots with incredibly high photoluminescence quantum yields, matching the best organic dyes. One of the first examples of a core/shell/shell system is CdSe/ZnSe/ZnS in which the ZnSe layer acts as a lattice adapter for the ZnS, achieving quantum yields of up to 0.85.[257] The shells were synthesised by multiple injection steps of organometallic precursors. In this way, CdS/HgS/CdS colloids have been prepared by Dorfs and Eychmüller,[303] and III-V InAs/ZnCdS prepared by Allen *et al.*[269] Indeed, improvements in quantum yield over a wide spectral range have been enjoyed by many core/shell/shell[256,257] and QD-QW systems.[259,303,304]

## 4.4 Problem overview

The proliferation of the field of semi-conducting nanocrystals has seen their use in numerous catalytic processes, such as photocatalytic water splitting,[254,305] oxygen reduction,[306] quantum dot sensitised solar cells[14,99,307] and photocatalytic dye degradation.[15,308] In these applications, quantum dots are often used in combination with other nanoparticles, material supports and surfaces.[105,309,310]

The use of gold nanoparticles in various organic transformations in fine chemical synthesis has been the subject of a recent review,[91] and metal oxide nanocrystals have also been shown to be effective.[311] However, there are relatively few examples of the use of quantum dots for catalysing organic reactions.[22,312] with most being supported in polymer or carbon matrices.[15] The use of colloidal quantum dots for the catalysing organic transformations is largely unexplored, with the majority of the literature focussing on organic carbon dots.[313]

Bridging the gap between molecular homogeneous and heterogeneous catalysis is a new frontier in the field of catalysis, combining fast reaction rates and turnover numbers of homogeneous catalysts with re-usability and recoverable nature of homogeneous catalysts. In this chapter, the synthesis of type-I core/shell quantum dots with a hybrid shell (CdSe/ZnS-CuS) is realised *via* the decomposition of a mixture of zinc(II) and copper(II) diethyldithiocarbamate species. The catalytic potential of the resultant core/shell quantum dots was tested *via* the Huisgen 3 + 2 cycloaddition “click” reaction between benzyl azide and phenylacetylene under UV irradiation. A mechanism for this and alterations in photoluminescence emission are postulated.

Further work led to the development of a general method for the doping of any metal into the shell of II-VI and III-V quantum dots *via* the decomposition of different metal-dithiocarbamate species (namely Cu, Cd and Hg). Changes in photoluminescence emission and quantum yield are documented, including the synthesis of infrared emitting CdSe/ZnS-HgS quantum dots.

## 4.5 Results and discussion

### 4.5.1 Synthesis of CdSe/ZnS-CuS quantum dots

CdSe quantum dots were synthesised using the standard hot-injection method described in chapter 2, section 2.2.5.3 and shelled according to a modified procedure outlined by Dethlefsen and Døssing.[147] The Cu-doping of the ZnS shell used in this study was achieved using a new, one-pot low-temperature thermal decomposition of air-stable precursors in the presence of alkyl surfactants. The Cu dopant and ZnS shelling material were introduced as a stoichiometric mixture of copper(II) diethyldithiocarbamate and zinc(II) diethyldithiocarbamate respectively. Their use as dopant vectors in quantum dot shells is underexplored, given the wide array of metal dithiocarbamates, spanning the entirety of the periodic metals this shell-doping method has great scope given the myriad of new materials that can be formed.

CdSe cores were shelled by the decomposition of zinc(II) diethyldithiocarbamate and copper(II) diethyldithiocarbamate in the following molar ratios; 1:1(**I**), 1:3 (**II**), 1:7 (**III**), 1:15 (**IV**) and 1:0 (**V**). The total molar quantity of shell precursor was identical to that required for the CdSe/ZnS, equivalent to three monolayers (approximate increase of 1.8 nm in quantum dot diameter). [147]

| Ratio (Zn:Cu) | | Zinc(II) diethyldithiocarbamate | | Copper(II) diethyldithiocarbamate | |
|---|---|---|---|---|---|
| Ratio | Sample | g | mmol | g | mmol |
| 1:1 | Sample (**I**) | 0.254 | 0.700 | 0.252 | 0.700 |
| 1:3 | Sample (**II**) | 0.380 | 1.05 | 0.126 | 0.350 |
| 1:7 | Sample (**III**) | 0.443 | 1.23 | 0.0630 | 0.175 |
| 1:15 | Sample (**IV**) | 0.475 | 1.31 | 0.0315 | 0.0875 |
| 1:0 | Sample (**V**) | 0.507 | 1.40 | 0 | 0 |

**Table 4.1**: Differing ratios of zinc to copper dithiocarbamates used to shell CdSe quantum dots.

The presence of Cu in the quantum dots was shown by XPS. The molar ratios of Cu to Zn used in the quantum dot shelling relates directly to the intensity of the Cu and Zn signals in the XPS spectra (figure 4.3). The Cu2p$_{3/2}$ and Cu2p$_{1/2}$ peaks for all samples are reported as 933.18 and 952.88 eV respectively, which is indicative of the presence of Cu$^{+}$.[314] Other elements in the quantum dots were also analysed, and binding energy peak positions recorded as follows: (Cd3d- Cd3d$_{5/2}$ 405.4 eV, 411.49 eV Cd3d$_{3/2}$, Se3d- Se3d$_{5/2}$ 54.8 eV, Se3d$_{3/2}$ 56.1 eV, Zn2p- Zn2p$_{3/2}$ 1021.8 eV, Zn2p$_{1/2}$ 1045 eV and S2p- S2p$_{3/2}$ 161.85 eV, S2p$_{1/2}$ 162.85 eV).

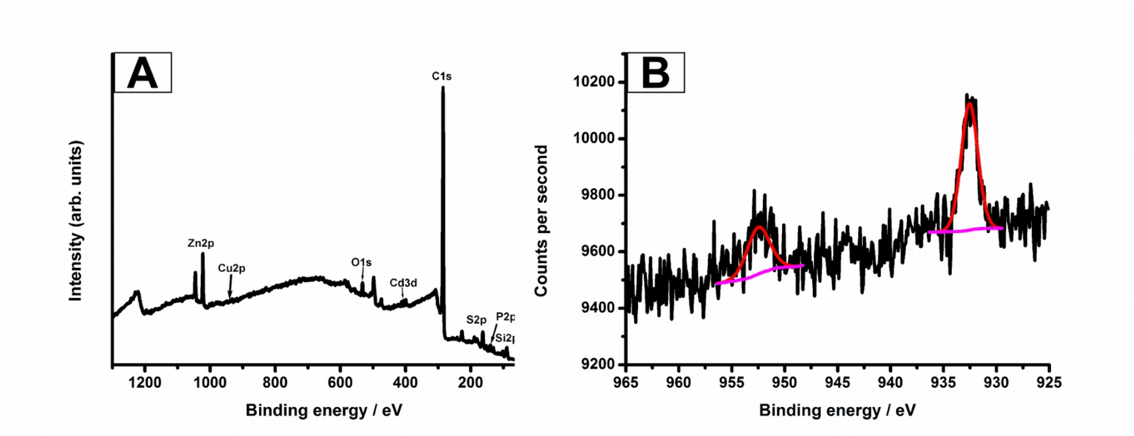

**Figure 4.3**: A) XPS survey spectrum of sample (II), CdSe/ZnS-CuS quantum dots with dithiocarbamate ratio 3:1 and B) Cu2p scan of the same sample, showing $Cu^+$ character.

XPS was also used to determine the relative elemental percentages for all CdSe/ZnS-CuS samples, calibrated against adventitious carbon. Samples were prepared for XPS by drop-casting a colloidal suspension of quantum dots in *n*-hexane onto a heated glass substrate.

| Sample | Cd, at. % | Se, at. % | S, at. % | Zn, at.% | Cu, at.% |
|---|---|---|---|---|---|
| Sample (**I**) | 2.12 | 7.28 | 73.3 | 13.2 | 4.07 |
| Sample (**II**) | 3.08 | 4.27 | 67.2 | 23.6 | 1.80 |
| Sample (**III**) | 2.93 | 5.11 | 64.2 | 27.02 | 0.700 |
| Sample (**IV**) | 1.79 | 7.87 | 59.1 | 30.75 | 0.520 |
| Sample (**V**) | 14.4 | 12.6 | 23.9 | 49.0 | 0 |

**Table 4.2**: Elemental composition of CdSe/ZnS-CuS quantum dots determined by quantitative XPS.

EDS analysis (table 4.3 and figure 4.5) confirmed the presence of all of the elements in the structure (Cd, Se, Zn, S and Cu), versus CdSe/ZnS quantum dots. Quantitative EDS and XPS analyses showed the amount of Cu loading on the quantum dots, all of which were low in comparison to the stoichiometric amounts of shelling reagents used (Table 4.1 and 4.2). XPS analysis gave higher Cu to Zn ratios than EDS, thus suggesting the majority Cu sites are located on the quantum dot surface. We can also infer that the CdSe cores have a preferential affinity for ZnS over CuS shelling due to the higher amount of Zn in the system. It is noteworthy that EDS samples were analysed on gold TEM grids rather than the standard copper to avoid masking of the copper signal.

Discrepancies from the expected values can be attributed to the relatively poor atom efficiency of zinc diethyldithiocarbamate in its conversion to ZnS and its ability to coordinate to nanoparticle surfaces.[315] A greater amount of sulphur compared to zinc in the copper-doped samples suggests it is zinc that is replaced by copper in the ZnS lattice; a trend which is reversed for CdSe/ZnS potentially due to better lattice matching of CdSe/ZnS over CdSe/ZnS-Cu. Further characterization of samples I-V by TEM showed all samples to be monodisperse with an average diameter of 3.7 - 4.1 nm, compared with cores of ~2.7 nm in diameter (figure 4.4). HRTEM measurements showed highly crystalline structures with *d*-spacings corresponding to the <111> crystal plane of CdSe (Figure 4.4, inset).

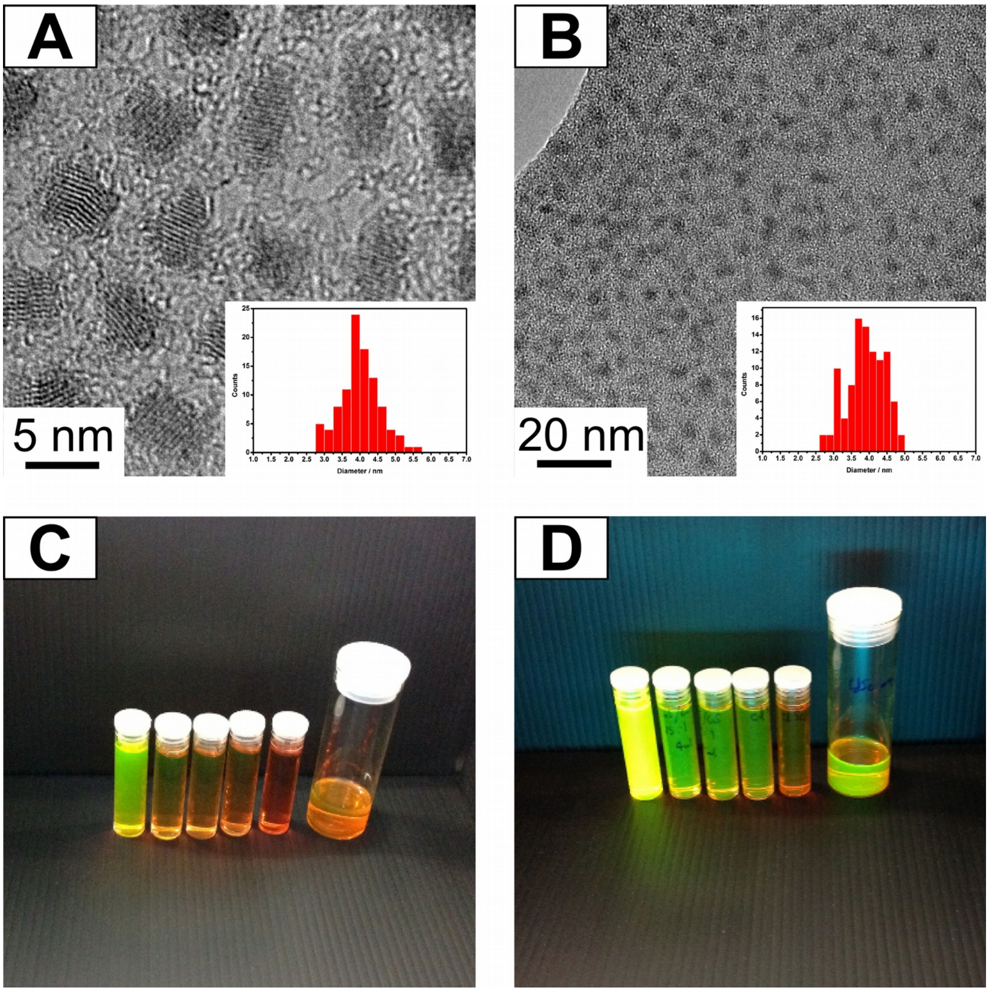

**Figure 4.4**: TEM micrographs of: A) Sample V, CdSe/ZnS quantum dots with nanoparticle size histogram (inset), B) Sample III, CdSe/ZnS-CuS 7:1 with histogram (inset), Photographs of samples I-V and CdSe quantum dot cores with D) and without C) 365 nm UV illumination.

| Sample | Average wt % Cu | % Doping |
|---|---|---|
| Sample (**I**) | 1.20 | 3.11 |
| Sample (**II**) | 0.670 | 1.52 |
| Sample (**III**) | 0.350 | 1.18 |
| Sample (**IV**) | 0.140 | 0.400 |
| Sample (**V**) | 0 | 0 |

**Table 4.3**: Elemental composition of CdSe/ZnS-CuS quantum dots determined by quantitative EDS.

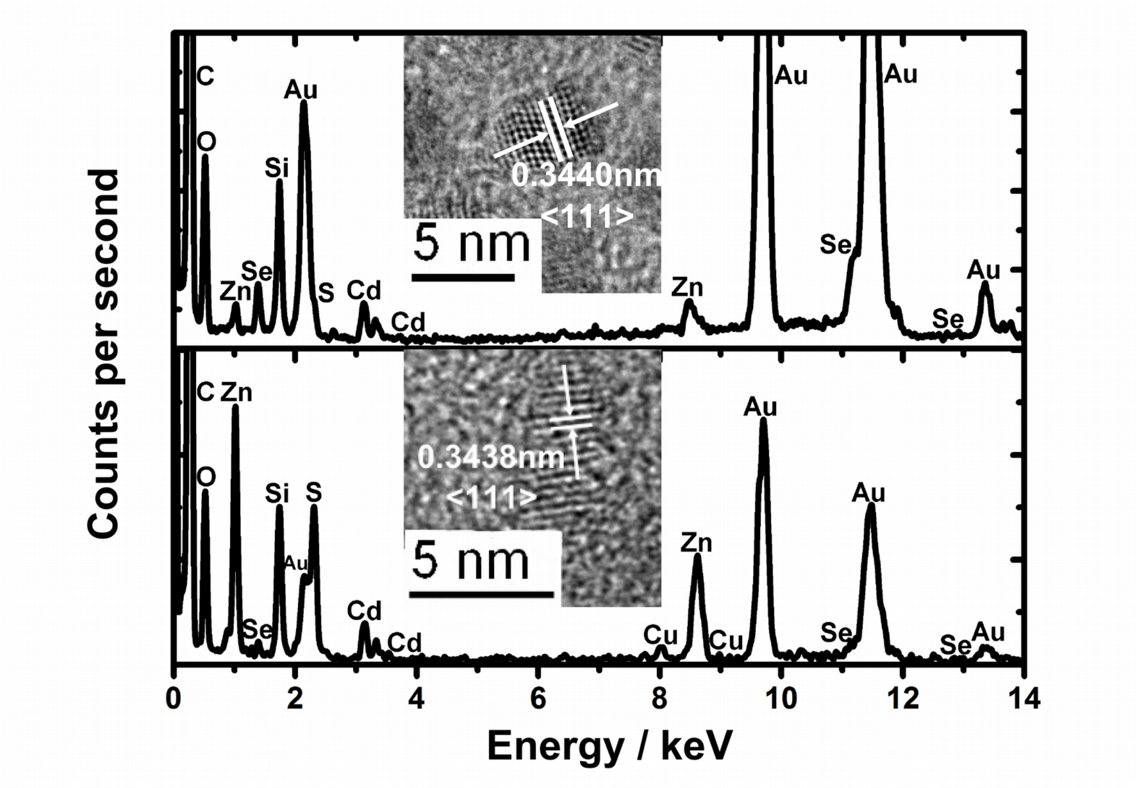

**Figure 4.5**: Top) EDS analysis of sample (V), CdSe/ZnS and inset) HRTEM of an individual CdSe/ZnS nanocrystal showing the <111> crystal plane. Bottom) EDS analysis of sample (III), CdSe/ZnS-CuS 7:1 and inset) HRTEM of an individual CdSe/ZnS-CuS nanocrystal showing the <111> crystal plane.

Figure 4.6 shows the absorption and photoluminescence spectra of samples I-V. When Cu is introduced to the ZnS shell, a blue shift in luminescence and a decrease in quantum yield were observed. This is in stark contrast to a pure ZnS shell, where a significant increase in quantum yield and a red-shift in luminescence is observed. In the case of sample I, the photoluminescence was completely quenched. Furthermore, Cu-doped samples did show an increased near-infrared photoluminescence band at approximately 1.8 eV (660 nm) (figure 4.6 B)), which had a significantly longer luminescence life-time compared with the band-edge luminescence (figure 4.6 D)). If we assume that $Cu^+$ ions have been doped into the ZnS shell (which is reasonable given the low levels of Cu found in the particles experimentally), figure 4.6 C represents the energy levels in the quantum dots.[316–319] Cu-doped ZnS does luminescence in the blue/green region of the spectrum due to S and Zn vacancies and a level introduced by the $Cu^+$.[318] This luminescence is not visible in the spectra and is most likely quenched by the CdSe core or not intense enough to be detected. The near-infrared luminescence at *ca.* 1.8 eV (660 nm) is well known in CdSe nanocrystals and can be assigned to Se or Se/Cd (di)vacancies probably located at the boundary between core and shell.[317,320]

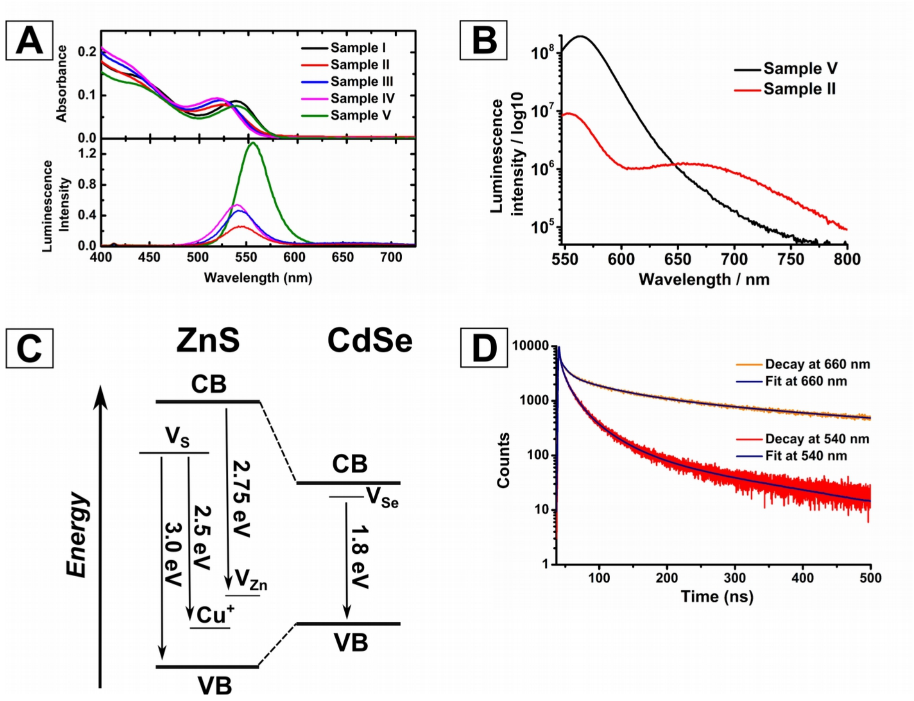

**Figure 4.6**: A) UV/vis and photoluminescence spectra of samples (I-V), B) Photoluminescence spectra of samples II and V sample clearly showing a second, broad emission band centred at 660 nm for sample II, C) Proposed photoluminescence energy level diagram and D) example photoluminescence decay measurements at 540 nm and 660 nm, illustrating the long-lived Cu-induced feature at 660 nm.

The blue-shift in the core luminescence may be due to a “shrinking” of the CdSe core or changes in its dielectric environment. Given the low levels of Cu doping, the Cu in the “shelling” reagents partially exchanged against Cd. This is plausible bearing in mind work on Cu-activation of chalcogenides and cation exchange.[314,321] The “shrinking” theory is further supported by the increase in the near-infrared photoluminescence, which indicates that the number of defect states in the core has been increased – especially at the interface between core and shell. This is also evident from the decrease in quantum yield commensurate with the level of copper doping (Table 4.4).

| Sample | Quantum yield at 540 nm, % | Quantum yield at 660 nm, % | Combined quantum yield, % | Photoluminescence lifetime ($\tau_1$) at 540 nm / ns | Photoluminescence lifetime ($\tau_1$) at 660 nm / ns |
|---|---|---|---|---|---|
| Sample (**I**) | 2.44 | 1.15 | 3.59 | 3.17 | 23.8 |
| Sample (**II**) | 1.98 | 0.885 | 2.865 | 3.02 | 26.6 |
| Sample (**III**) | 1.61 | 0.666 | 2.276 | 4.53 | 20.7 |
| Sample (**IV**) | ~0.05 | 1.86 | 2.56 | 3.99 | 28.1 |
| Sample (**V**) | 5.84 | - | 5.84 | 0.288 | - |

**Table 4.4**: Quantum yield and photoluminescence lifetime measurements of CdSe/ZnS-CuS samples. Quantum yield measurements were taken against Rhodamine-6G in ethanol.

As Cu in the ZnS shell has $Cu^+$ character, excitation of the quantum dots is likely to oxidise the Cu dopants releasing $Cu^+$ into solution. The mechanism of release likely involves photo-oxidation of the doped ZnS shell under release of Cu, Zn and $SO_x^{y-}$ ions. The proposed mechanism was supported by the detection of Cu using inductively coupled plasma-atomic emission spectroscopy (ICP-AES, Table 4.5). A quantum dot suspension of sample I in *n*-hexane was irradiated with 254 nm overnight, with a counterpart quantum dot dispersion kept in the dark. The quantum dots were precipitated with ethanol, centrifuged and the supernatant evaporated for nitric acid digestion and analysis. It was shown that the irradiated sample leached *ca*. fourteen times as much Cu compared to the dark sample, which supports the hypothesis of photo-oxidation promoted $Cu^+$ release (Table 4.5). It is noteworthy that the amount of copper leached is small (1033 ng ± 10 % from an estimated total quantum dot mass of 16.2 mg).

| Sample | Amount of Cu / ng | Total mass of quantum dots/ mg |
|---|---|---|
| Sample I, 1:1 (254 nm irradiation) | 1033 | 16.2 |
| Sample I, 1:1 (Dark) | 70.6 | 13.2 |
| Solvent control | 12.9 | - |
| Blank tube | 0.257 | - |

**Table 4.5**: ICP-AES measurements of sample I, CdSe/ZnS-CuS 1:1 quantum dots with and without 254 nm irradiation, showing the leaching of copper into solution via photo-oxidation of the quantum dot shell.

A practical way of utilising the generated $Cu^+$ species is Huisgen 3 + 2 cycloaddition which is known to be catalysed by $Cu^+$ sites more readily than $Cu^{2+}$. Common literature procedures start with a $Cu^{2+}$ salt and use a reducing agent to generate $Cu^+$ *in situ* for catalysis.[322] Commonly used *in situ* reducing agents such as sodium ascorbate derivatives have drawbacks for bio-conjugate applications due to separate reactions with protein side-chains.[323,324] Tasdalen and Yagci have shown that separate UV activators can be used to reduce $Cu^{2+}$ to $Cu^+$ in a two component system, however the selectivity of the photo-reducing agent is unclear.[325] A system that can release $Cu^+$ in a controlled manner without the need for a reducing agent would be highly advantageous in bioconjugate applications, although compatibility in an aqueous environment is required.

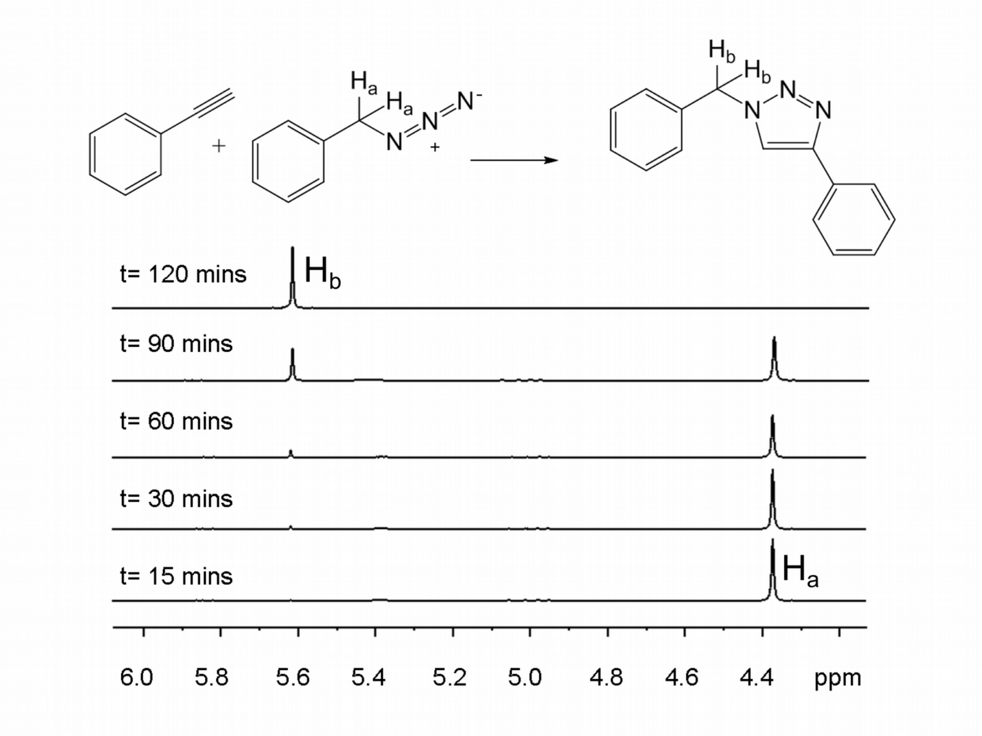

**Figure 4.7**: Top) Reaction scheme and resulting "click" product between phenyl acetylene and benzyl azide. Protons monitored by $^1$H NMR are labelled Ha and Hb respectively, with Ha diminishing with the emergence of Hb as the reaction proceeds. Bottom) following the "click" reaction *via* $^1$H NMR spectroscopy.

The "click" reaction in question was between phenyl acetylene and benzyl azide in *n*-hexane (figure 4.7). CdSe/ZnS-CuS quantum dots were also dispersed in *n*-hexane and stirred thoroughly with the "click" reactants throughout the duration of the reaction, and irradiated with 254 nm, 365 nm or visible light irradiation.

The reaction was monitored (figure 4.7) by the ratio of $^1$H NMR peaks from the azide as it was converted to the triazole. Sample I was tested first as EDS and XPS analyses (tables 4.2 and 4.3) confirmed a higher proportion of Cu in the ZnS shell. A concentration with 5 mol % of Cu was shown to have reached > 99 % yield by two hours. Due to its insolubility in *n*-hexane, the triazole can be separated from the catalyst by filtration. Analysing aliquots at timed intervals shows 1 %, 2 %, 8 %, 35 % and 100 % of triazole formed at 15, 30, 60, 90, and 120 minutes respectively. The slow initial product formation suggests there is an activation period after irradiation of 60 minutes. Presumably this initial inactivity is due to the quantum dots being kept in the dark prior to use, and this activation period could be postulated to be the time required for the release of $Cu^+$ ions and therefore rate limiting (table 4.5).

Catalytic activity is determined by the turnover number, which is defined in organometallic catalysis as the number of moles of reactant a catalyst can covert before becoming inactive. The turnover number was calculated by multiplying the yield by the number of moles of product formed, divided by the number of moles of copper used in the reaction. Similarly, the turnover frequency is the turnover per unit time and calculated by dividing the turnover number by the reaction time in hours.

Performing the "click" reaction in the dark (without any irradiation) gave a 22 % yield. Therefore, it is postulated that on irradiation, the quantum dots photo-oxidise with S being oxidised to $SO_x^{y-}$. This causes the Cu to form a complex with the azide and eventually acting as a sacrificial electron-acceptor and subsequently, the "click" reaction occurs.

Reducing the quantum dot loading of sample I to give 0.32 mol % of Cu (5 wt % of sample I) the reaction reaches > 99 % after 8 hrs. Sample I displays no sign of reduced activity after 3 cycles showing the quantum dot core is able to release catalytic $Cu^+$ over a prolonged period. A "cycle" is defined as a period in which a 100% yield is obtained with introduced reagents (at an initial benzyl azide concentration of 0.5 mmol/ml). On comparison, the lower level of doping in sample II reduces the mol % Cu to 0.16 % for 5 wt % of quantum dots in the reaction; this reduction has no detrimental effect giving >99 % yield after 8 hours with a turnover number of 625. Reactions involving samples III and IV (5 wt %) show a sharp decline in yield and this can be correlated to the low proportion of Cu doping in these samples. The assumption that the catalysis is taking place on a Cu centre is supported by sample V whereby no reaction took place without the presence of Cu sites. The reaction also proceeds with visible light activation with a > 99 % yield after 3 hours using sample I (5 mol % Cu).

| Catalyst | Quantum dot wt. % | Cu (mol. %) | Time (hrs) | Yield (%) + hʋ[d] | Turnover number | Turnover frequency ($hr^{-1}$) | Yield (%) no hʋ |
|---|---|---|---|---|---|---|---|
| none | 0 | 0 | 8 | <0.1 | 0 | 0 | 0 |
| Sample (**I**) | 77.2 | 5.00 | 2 | >99 | 20 | 10 | 22 |
| Sample (**I**) | 5.00 | 0.320 | 8 | >99a,<br>>99b,<br>>99c | 309 | 37 | 11 |
| Sample (**II**) | 5.00 | 0.160 | 8 | >99 | 625 | 78 | 5 |
| Sample (**III**) | 5.00 | 0.120 | 8 | 7.50 | 61 | 8 | <0.1 |
| Sample (**IV**) | 5.00 | 0.0400 | 8 | 1.30 | 32 | 4 | <0.1 |
| Sample (**V**) | 5.00 | 0 | 8 | <0.1 | 0 | 0 | <0.1 |

**Table 4.6**: Summary of Huisgen cycloaddition, yields are calculated by $^1H$ NMR and are averages of three samples. [a], [b], [c] are repeats using the same catalyst, [d] hʋ used; 257 nm 980 µW/$cm^{-1}$.

## 4.6 Summary and future work

The CdSe/ZnS-CuS quantum dots synthesised in the first part of this chapter were found to be highly effective as vectors for $Cu^+$ induced “click” chemistry catalysis. Copper release proceeds *via* photo-oxidation of the shell, allowing azide species to form complexes with $Cu^+$ ions and affect the “click” reaction. Although not true catalysts in themselves, it is stressed that these quantum dots are the first of their kind and as such bridge the gap between homogeneous and heterogeneous catalysis, combining facile catalyst recoverability with higher turnover frequencies compared to heterogeneous catalysts.

The photoluminescence profiles and quantum yields indicate that there is an increase in surface defects between core and shell, which is supported by longer-lived photoluminescence lifetime measurements (Table 4.4).

The doping of copper into the shells of CdSe/ZnS quantum dots led to further investigation of core/shell quantum dots systems, with the doping of mercury, cadmium and indium into the shells of CdSe/ZnS and InP/ZnS quantum dots *via* cadmium(II) diisobutyldithiocarbamate, indium(III) tris(diisobutyldithiocarbamate) and mercury(II) diethyldithiocarbamate. There was little difference to the host core lattices on shelling, due in no small part to the thin nature of the shells as evidenced by TEM (figure 4.8, E and F). There were marked effects on the overall photoluminescence profiles, lifetimes and quantum yields of all of the composites. Notably, the CdSe/ZnS-CdS quantum dots exhibited a large increase in quantum yield, achieving a maximum of 0.72 for a 7:1 ratio of Zn to Cd. The photoluminescence profiles increased incrementally with the amount of Cd doping (figure 4.8, A). This is due to Cd defects at the CdSe surface filled and a better lattice matching between core and shell. This is supported by a greater magnitude of red-shift than standard ZnS shelling as the effective diameter of the quantum dot is increased due to defect elimination.

In doping had a similar effect in InP-ZnS-$In_2S_3$ systems, with a higher recorded quantum yield (0.427 versus 0.337 for InP/ZnS). However for CdSe/ZnS-$In_2S_3$ systems, there was no real shift in photoluminescence (figure 4.8, C), and quantum yields were depressed. This is attributed to poor lattice matching and reduced ligand-shell affinity, with only low ratios of In to Zn dispersible in organic solvents. Similar results were seen for the corresponding InP-ZnS-CdS samples.

Perhaps the most interesting photoluminescence results were obtained for CdSe/ZnS-HgS quantum dots, as the photoluminescence was red-shifted some 200 - 400 nm form the core emission. Although the for this red-shift is currently unclear, the formation of a HgSe/ZnS, a HgS/ZnS or a composition in between those two states seems the most likely, forming a QD-QW structure, or a Type II system, both potentially leading to a large red-shift. The core/shell/shell theory is supported by the spontaneous decomposition of mercury(II) diethyldithiocarbamate on exposure to CdSe cores, producing the red-shift. It is then reasonable to assume that the zinc(II) diethyldithiocarbamate decomposes on top of the mercury layer, possibly with some cationic exchange. The spontaneous decomposition is attributed to the affinity mercury has for selenium, a fact which makes it a potent neurotoxin.[326] Although InP/ZnS-HgS exhibits some red-shifting, it is not of the magnitude experienced by CdSe/ZnS-HgS, suggesting a different band structure.

The elucidation of band-gap structures for the aforementioned quantum dots as well as their compositions and mechanisms for photoluminescence are the subject of ongoing investigations, as is the range of tunable emission wavelengths available (figure 4.8, D).

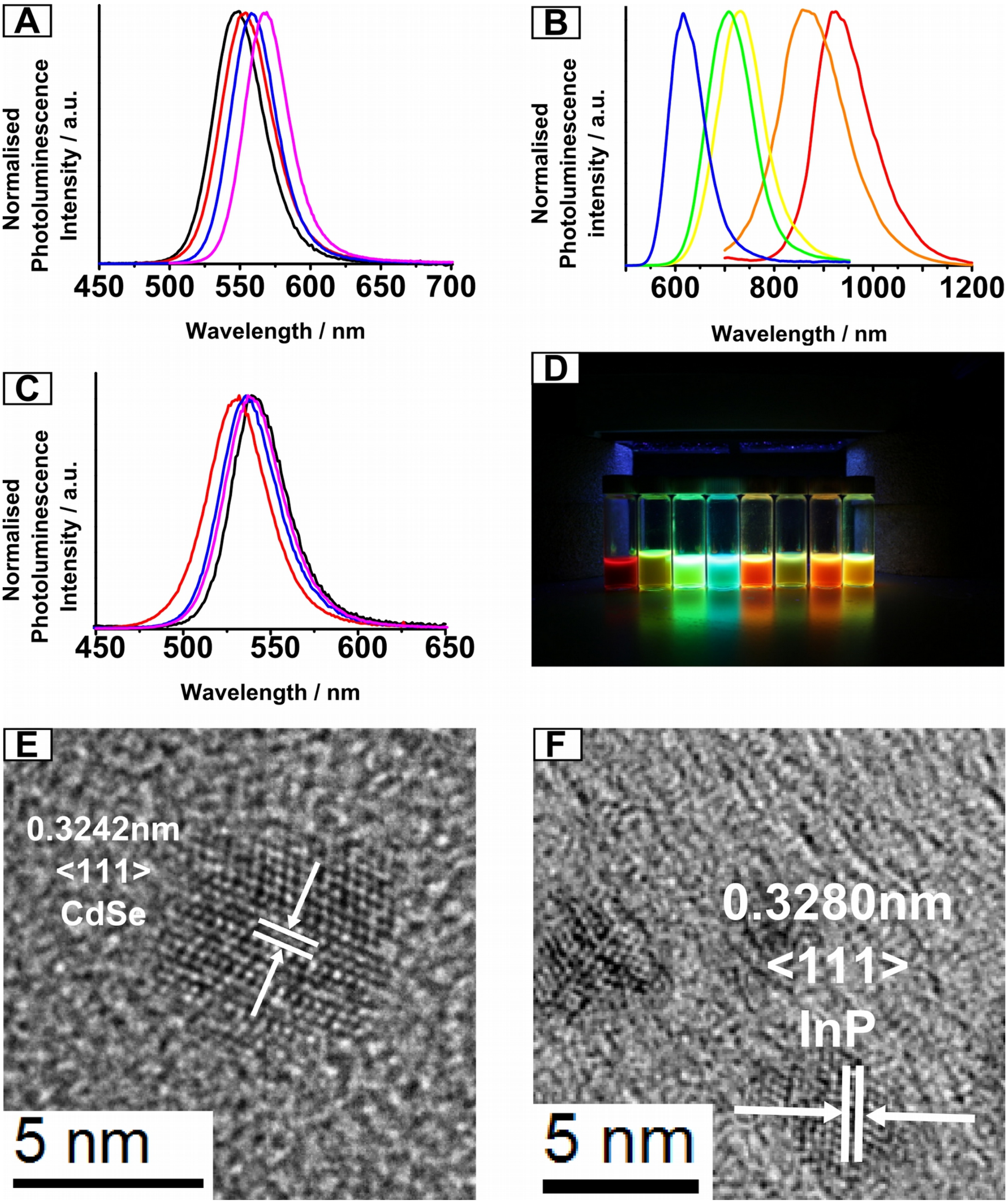

**Figure 4.8**: A) Photoluminescence spectra showing red shifting on addition of increasing amounts of Cd into ZnS quantum dot shells, B) For Hg doping, C) for In doping, E) HRTEM micrograph of CdSe/ZnS-HgS quantum dot with <111> CdSe crystal plane and F) HRTEM micrograph of an InP/ZnS-CdS quantum dot, showing the <111> crystal plane of InP.

# Chapter 5: Iron oxide nanoparticles synthesised from high street reagents

## Preface

The following chapter describes advances made in the synthesis of iron oxide nanomaterials from high street reagents. The aim was to be able to synthesise iron oxide nanomaterials more cheaply than conventional syntheses in order to make the synthesis of high quality nanomaterials more accessible for a greater number of laboratories and chemical industry. The synthesis route investigated was a “heat-up” method (chapter 1, section 1.5.2) based on the thermal decomposition of iron-fatty acid complexes in high boiling point solvent. The resulting nanomaterials were characterised using: XRD, XPS, TEM, HRTEM, EDS, SAED, SQUID, ATR-FTIR and Mössbauer spectroscopy. The effectiveness of the obtained nanomaterials were evaluated as magnetic fluid hyperthermia agents after transfer to water *via* an amphiphilic polymer.

In this chapter, thermal decomposition methods for the synthesis of iron oxide nanoparticles are introduced and reviewed, and the technique of magnetic hyperthermia explored.

## 5.1 Iron oxide nanomaterial synthesis, an introduction

Research into the synthesis of iron oxide nanomaterials has been focussed primarily on the synthesis of iron(III) and iron(II, III) oxides, however there are sixteen known iron oxide and oxyhydroxide minerals.[327] This chapter will focus on the synthesis of both iron(III) and iron(II, III) oxide, as they have a large magnetic moment and as such are of most interest for magnetic hyperthermia.[328] Ideal nanoparticles for magnetic hyperthermia applications should have: a large magnetic moment, a low polydispersity index, an average size below 20 nm and be composed of non-toxic materials.[126,329,330]

Iron oxide nanomaterials can be synthesised using a variety of methods, from physical "top-down" methods such as: ball-milling, acid etching and inkjet printing to "bottom-up" methods such as: thermal decomposition, co-precipitation, electrochemical methods and sol-gel syntheses.[42] "Top-down" methods, as discussed in chapter 1.4, tend to yield large, polydisperse nanoparticles with large shape anisotropy.

The most effective iron oxide nanoparticles for magnetic hyperthermia have been based on the co-precipitation method. This method involved the ageing of $Fe^{2+}$ and $Fe^{3+}$ salts in basic, aqueous solution in order to precipitate magnetite ($Fe_3O_4$) nanocrystals according to the following chemical equation:

$$Fe^{2+}_{(aq)} + 2Fe^{3+}_{(aq)} + 8OH^{-}_{(aq)} \rightarrow Fe_3O_{4(s)} + 4H_2O_{(l)}$$

When nucleating nanocrystals using this method, only kinetic factors are controlled, so control over size and shape are limited. There is an initial "burst" nucleation stage, after which the crystal growth phase is uncontrolled, so proceeds according to Ostwald ripening.[56] This leads to a broad size distribution of nanoparticles. Therefore it is necessary to separate the two phases in order to synthesise monodisperse nanoparticles, as monodisperse nanoparticle nuclei growing at a constant rate will eliminate Ostwald ripening, yielding a population of monodisperse nanoparticles. It is therefore necessary to have a short burst nucleation stage, to avoid multiple nucleations at different times, which leads to Ostwald ripening.

In the co-precipitation method, numerous studies have been undertaken in order to control nanoparticle shape and size. Changing synthesis parameters such as the pH, temperature, ionic strength, $Fe^{2+}$ to $Fe^{3+}$ ratio, and indeed the metal salts used.[42,48,331] The addition of nanoparticulate surfactants and chelating agents control size by passivating nanoparticle surfaces, preventing further growth or Ostwald ripening, as well as providing dispersibility in aqueous or organic solvents.[43,142,332–334] Co-precipitation also allows for large amounts of nanocrystals to be synthesised in comparison to other methods, often at the expense of nanoparticle monodispersity.[335–337]

The advent of high temperature syntheses yielding large quantities of monodisperse iron oxide nanoparticles sparked renewed interest in developing synthetic methods for the synthesis of monodisperse nanocrystals.[43–45,142] First attempts focussed on the use of iron pentacarbonyl as the iron source, but this has obvious drawbacks relating to the by-products obtained from its decomposition.[338,339]

In their landmark paper, Sun and Zeng described the synthesis of highly monodisperse nanocrystals in high boiling point solvent from the decomposition of iron(III) acetylacetonate in the presence of alkyl surfactants.[43] The process involves the dissolution of iron(III) acetylacetonate and 1,2-hexadecanediol in diphenyl ether in the presence of oleic acid and oleyl amine, before elevation of the temperature to 265 ºC under nitrogen for thirty minutes (figure 5.1). This method yields monodisperse magnetite nanoparticles readily dispersible in organic solvents due to the highly oleophilic nature of oleic acid and oleyl amine, the nanoparticle ligands. It is postulated that the 1,2-hexadecanediol reduces a portion of the $Fe^{3+}$ to $Fe^{2+}$ before supersaturation is achieved, and provides an oxygen source for the nanocrystals.

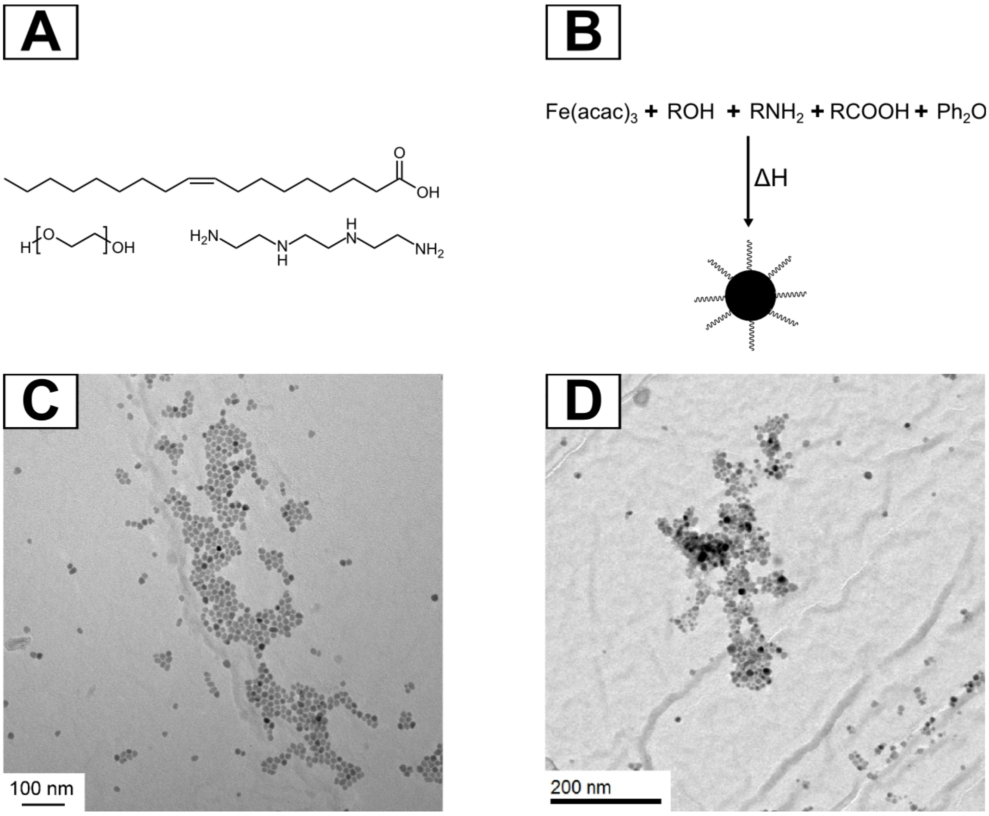

**Figure 5.1**: A) Top: Oleic acid, bottom left: polyethylene glycol and bottom right: triethylenetetramine, B) Schematic for the synthesis of iron oxide nanocrystals where "R" is a fatty alkyl group, re-drawn from ref.[43] TEM images of $Fe_3O_4$ nanoparticles synthesised using: C) poly(ethylene glycol) and D) triethylenetetramine.

Sun and Zeng also used a seed-mediated growth method involving the use of smaller iron oxide seeds to grow larger nanocrystals in the presence of 1-octadecanol, as it is energetically more favourable to grow on the surface of existing nanocrystals than nucleate new nanoparticles.

Many groups have looked to improve this synthesis and exert greater control over the size, shape and monodispersity of the product. Notably, Lattuada and Hatton showed that the commercially expensive 1,2-hexadecanediol could be replaced by 1,2-tetradecanediol, thus reducing the cost of the process.[142] Sun *et al*. demonstrated that a substitution of a portion of the iron (III) acetylacetonate with different metal acetylacetonates such as manganese or cobalt led to differences and significant improvement in magnetic moment, with no detriment to product yield or particle monodispersity.[44] Shape anisotropy can also be induced using the thermal decomposition method by varying reactant concentration, synthesis temperature and surfactant type.[132,333,340,341]

Other methods borrowed from this type of thermal decomposition synthesis, including polyol methods, hot injection and decomposition of single-source precursors.[342,343] The blanket term “polyol methods” also include syntheses in which the solvent acts as the surfactant and reducing agent. The term stems from the use of polyethylene glycol derivatives as the solvent, reducing agent and surfactant (figure 5.1). Polyethylene glycol allows nanoparticles to be readily dispersible in a wide variety of solvents, as diverse in polarity as hexane and water. This astonishing property is also a hindrance when trying to remove excess polyethylene glycol, as it is very difficult to precipitate the nanoparticles with salt or a miscible solvent with a different polarity and subsequently re-disperse in fresh solvent.

The use of 2-pyrrolidone has been shown to be an effective solvent, reducing agent and nanoparticle stabilising agent.[344,345] Li *et al*. elucidated a mechanism for nanoparticle formation based on the elimination of carbon monoxide from 2-pyrrolidone, and its subsequent re-arrangement into an azetidine species.[345] This then hydrolyses iron(III) chloride to iron oxyhydroxide (FeOOH), which subsequently reacts with carbon monoxide, producing magnetite $Fe_3O_4$. The synthesis of iron oxide nanomaterials has also been documented in ionic liquids (figure 5.2).[346]

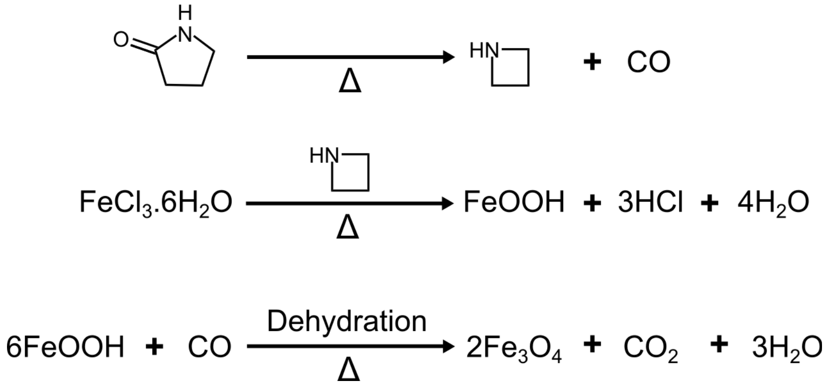

**Figure 5.2**: Reaction of 2-pyrrolidone with iron(III) chloride to form magnetite $Fe_3O_4$ *via* an azetidine intermediate formed from the elimination of carbon monoxide. Re-drawn from ref.[345]

One of the problems in the modification of iron oxide nanocrystals for conjugation purposes is the need to have nucleophilic amine groups on the surface.[347] Difficulties stem from the fact that iron oxides are often stabilised by carboxylic acid groups which are acidic and therefore negatively charged in aqueous solution. Amine groups are basic and are positively charged in solution, and so by switching between the two, nanoparticles must have a neutral charge and therefore a zeta potential of zero, which leads to irreversible aggregation. Qu *et al*. used the thermal decomposition of iron(III) acetylacetonate in triethylenetetramine to yield amine-functionalised $Fe_3O_4$ nanoparticles with a low polydispersity index.[348] The authors then demonstrated the versatility of the amine functionalities by attaching streptavidin and subsequently making use of the strong biotin-streptavidin affinity for protein separation.

Although the hot-injection method has received more attention in the synthesis of semi-conducting quantum dots, it has been shown to be effective for the synthesis of iron oxide nanoparticles. The theory of the hot injection method has its roots in the model postulated by LaMer. Ho *et al*. used the hot injection of iron(III) acetylacetonate in benzyl ether at 290 °C at various injection rates to form monodisperse magnetite nanocubes and polyhedra.[349] The final particle shape was determined in the final "crystal growth" phase of the LaMer model, where a dearth of monomer units led to preferential growth on high energy facets, and thus nanocubes were grown. Herman *et al*. used the hot-injection of the iron sandwich complex bis(Z5-1,3,5-exo-6-

tetramethylcyclohexadienyl) iron(II) at 300 °C into an oleyl amine/1-octadecene solution to form iron/iron oxide core/shell nanoparticles.[350] This process is noteworthy as a hot-injection, single source method, and changing the surfactant to dimercaptosuccinic acid renders the nanoparticles water dispersible.

Examples of the decomposition of single source precursors for iron oxide nanocrystals are few and far between. Investigations by the O'Brien group into the synthesis of iron pivalate clusters have yielded good quality superparamagnetic iron oxide nanoparticles[351] as well as other metal oxide nanocrystals.[73,352] Aside from the aforementioned use of iron sandwich complexes as nanoparticle precursors, the effectiveness of the "heat up" thermal decomposition of simple metal salts for the synthesis of large quantities high quality monodisperse iron oxide nanocrystals have left the hot-injection and single source routes largely by the wayside in terms of synthesis development.

However, the most notable example of the use of a single-source precursor was the isolation of the active complex in the Sun and Zeng synthesis; iron oleate (figure 5.3). Park *et al*. synthesised iron oleate from iron(III) chloride and sodium oleate in a solvent mixture of water, ethanol and *n*-hexane.[45] This salt metathesis reaction is driven by the formation of sodium chloride, and the relative solubility of sodium chloride in water versus the solubility of iron oleate in hexane, both of which are high (figure 5.3). Although a non-toxic brown solid, iron oleate is unpleasant to handle due to its waxy nature. The rheology of the product is due to solvent from the preparation residing in the solid.

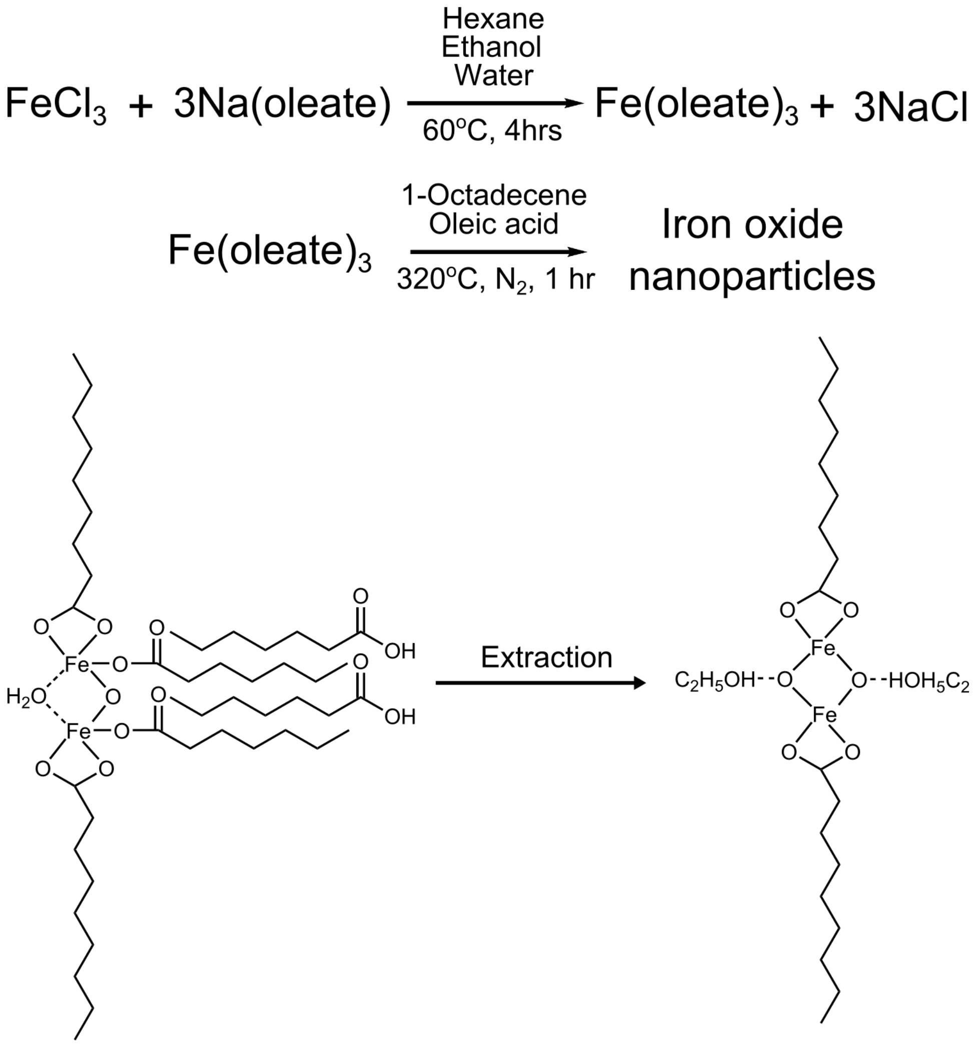

**Figure 5.3**: Top: Salt metathesis reaction in the formation of iron oleate from iron(III) chloride and sodium oleate, giving iron oleate and sodium chloride. Middle: thermal decomposition conditions for the synthesis of iron oxide nanoparticles as described by Park *et al.*[45] Bottom: The effect on the structure of the iron oleate complex after extraction with ethanol and acetone post synthesis. Adapted from ref.[143]

The original Park synthesis has been interrogated by several groups, with different parameters investigated. For example, the role of surfactants such as sodium oleate and oleic acid on the resultant nanocrystals has been shown to influence the shape and size of the products, as has changing the solvent.[143,353,354] Reaction times and temperatures have also been investigated, with longer times, perhaps unsurprisingly, yielding larger nanocrystals and more polydisperse products.[45]

Bronstein *et al*. investigated the effect of the composition of the iron oleate complex structure and composition of the nanocrystals.[143] They found that the structure of the iron oleate complex varied depending on the amount of solvent left in the complex. They postulate that ethanol is able to form a complex with iron centres instead of oleic acid if an extraction step (washing with ethanol and acetone) is undertaken. The authors also suggest that water (monohydrate) is also able to reside in the structure, but is removed as evidenced by FTIR on drying *in vacuo* at 70 ºC. This causes nucleation to occur at a higher temperature, and the authors postulate that the temperature barrier in the "heat-up" method between the nucleation and growth phases can be broken down, leading to polydisperse products.

Lynch *et al*. used the decomposition of iron oleate in 1-octadecene to investigate the effects of bubbles in the solvent on the nucleation and growth of iron oxide nanocrystals.[355] The authors vary reaction temperatures while changing the solvent, as refluxing solvents effervesce in solution. They also "artificially" produced bubbles at lower temperatures by purging the solution with argon gas, finding that bubbles promote singular primary nucleation events, thus reducing the polydispersity of the product. The bubbles absorb latent heat given off by exothermic reactions in solution, with greater energy being given off by nucleation (multiple bond formation) than growth (single bond formation) and so the bubbles drive nucleation.

The decomposition of metal oleate complexes is not limited to iron oxides- many other transition metal oxides and composite oxides have been produced, with a diverse range of shapes reported (figure 5.4).[45,60,353,356]

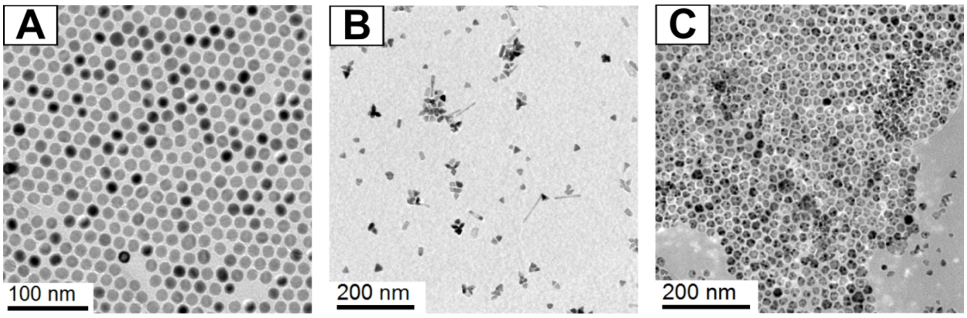

**Figure 5.4**: A) Spherical iron oxide nanoparticles from the decomposition of iron(III) oleate, B) anisotropic cobalt oxide nanoparticles from the decomposition of cobalt(II) oleate and C) hexagonal zinc oxide nanoparticles from the decomposition of zinc(II) oleate.

## 5.2 Magnetic hyperthermia

Magnetic hyperthermia is an experimental cancer treatment which involves the use of an alternating (AC) magnetic field to heat magnetic nanoparticles and cause either thermal ablation or induce an immunogenic response.[4,357,358] This avenue has been pursued by academic as well as commercial researchers due to its potential to be much less invasive than surgery and to drastically reduce the undesirable side-effects of treatments such as chemotherapy.

Before selecting a magnetic hyperthermia agent, one must first look at the mechanism of magnetic hyperthermia, and the effect nanoparticle size and composition has on those mechanisms. Other factors to consider are: the toxicity of the nanoparticle itself, the ability of the body to clear nanoparticles from the blood *via* the reticular endothelial system, the frequency of magnetic field used, the nanoparticle ligands and coatings, and the problem of localisation of the nanoparticles at the tumour site.[129,330,359–361]

Magnetite $Fe_3O_4$ is ferrimagnetic in the bulk, and a has net magnetisation due to unequal and opposed magnetic moments. Magnetic domains (regions in a magnetic material which has uniform magnetisation) form due to a need for a material to minimise its internal energy. This internal energy arises from the size of a magnetic field which will extend from a domain free material, requiring high magnetostatic energy stored in the field. To reduce this, a material forms opposing domains which reduce the size of the magnetic field and therefore the energy.

Hysteresis is an important property exhibited by magnetic materials. If a magnetic field is applied to a magnetic material, all of the magnetic domains of the material align with the applied field, known as the saturation magnetisation. An opposing magnetic field is then applied, and magnetic domains begin to align with the opposing field. however, once aligned, there is an energy associated with re-orientating the magnetic domains in the material. This leads to coercivity ($H_C$), magnetic remanence and the hysteresis loop (figure 5.5).

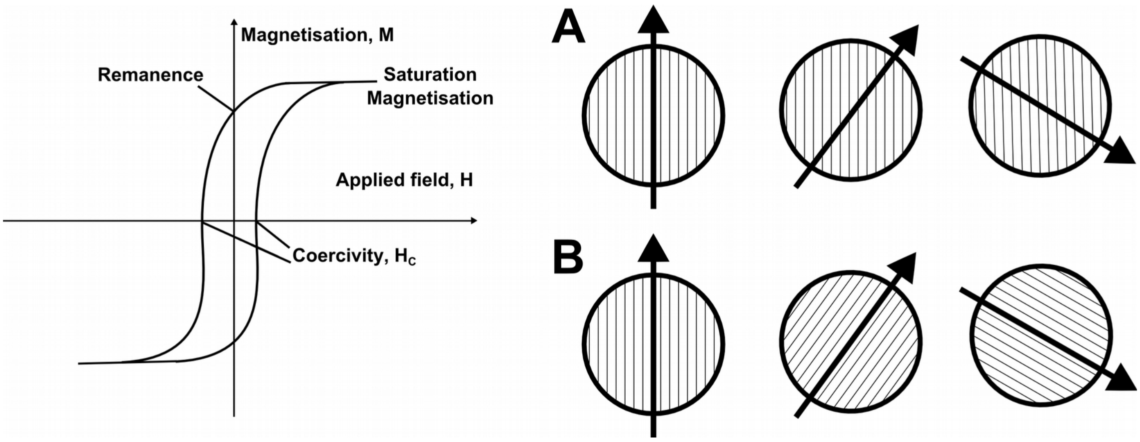

**Figure 5.5**: (Above left): The magnetic hysteresis loop showing the effect of an applied magnetic field on magnetisation, with magnetic remanance and coercivity labelled. (Above right): a representation of the two main methods of heat generation in magnetic hyperthermia, A) Neél and B) Brownian relaxation. Reproduced from ref.[115]

In every magnetic material, there is a point at which magnetic domains cease to exist as the size of the material decreases. Nanoparticles therefore become single domain and as such, align immediately to a magnetic field without hysteresis. Coercivity decreases in nanoparticles below this size until it becomes zero (~20 nm for $Fe_3O_4$) and thus superparamagnetic.[126] At this size, thermal energy (above the Neél transition temperature) is large enough to overcome the magnetic anisotropy barrier and flip between energy minima spontaneously. If a magnetic field is applied which oscillates faster than the relaxation time of the nanoparticles' magnetic moment, the magnetic anisotropy barrier is overcome and nanoparticles flip (relax) between energy minima. The energy required to do this is released as heat through the two mechanisms of particle relaxation: Neél (where the magnetic moment rotates and the particle remains fixed) and Brownian (the magnetic moment remains fixed with respect to the crystalline axis and the particle rotates) (figure 5.5).

The effectiveness of nanoparticles for magnetic hyperthermia are compared in the literature using two common parameters: Specific absorption rate (SAR) and intrinsic loss power (ILP). SAR depends both on frequency and strength of applied magnetic field (equation 14). The fundamental problem with this parameter is that it is difficult to reproduce both field strength and frequency from instrument to instrument. [113,114,362]

$$SAR = \frac{\Delta T}{\Delta t} . \frac{C}{m_{Fe}}$$ Equation 14

Where: “ΔT/Δt” is the initial temperature rise, “C” is the heat capacity of the fluid per unit mass and “mFe” is the mass of iron in the fluid per unit mass.

ILP is a modification of SAR which is less extrinsic, thus increasing comparability. However, there are limitations concerning range of field frequency applied (< 1 MHz), nanoparticle polydispersity index (must be < 0.1) and field strength (must be greater than the saturation field of the nanoparticles) (equation 15).[128]

$$ILP = \frac{SAR}{fH^2}$$ Equation 15

Where: “f” is frequency and “H” is the strength of the applied AC field. Hyperthermia experiments were carried out using a Magnetic Alternating Current Hyperthermia system designed and built by Resonant Circuits Ltd. The temperature was monitored using a fluoroptic temperature probe (Luxtron FOT Lab Kit, Lumasense California USA).

## 5.3 Problem overview

The synthesis of iron oxide nanomaterials from inexpensive, readily available precursors is highly desirable in order for applications such as magnetic hyperthermia, catalysis, data storage and drug delivery to be successful and commercially viable. Ease of synthesis could also lead this synthesis to be performed in poorer countries for iron oxide's use in water filters *etc*.[363] The following results and discussion explores the synthesis of iron oxide nanomaterials from high street reagents, taking into account cost and suitability of the product for magnetic hyperthermia. Experimental methods for this chapter are found in section 2.2.2. From section 5.1, it is clear that the easiest and most effective method for the production of monodisperse iron oxide nanocrystals is the method developed by Park *et al*., based on the decomposition of iron oleate.[45] This was the starting point.

## 5.4 Results and discussion

### 5.4.1 Replacing the reactants

When examining the synthesis of iron oxide nanoparticles developed by Park *et al.*,[45] it is clear that the synthesis and composition of the iron fatty acid precursor is critical. Although listed in section 2.2.2, a table of the precursors for this reaction as synthesied in the paper and their replacements in this study is listed below:

| Reagent | Vendor | Price per gram (£ GBP) | High-street reagent | Vendor | Price per gram (£ GBP) |
|---|---|---|---|---|---|
| Iron(III) chloride hexahydrate (ACS reagent grade) | VWR International Ltd. | 0.08* | Iron tablets | Boots Ltd. | 0.12 |
| Sodium oleate (≥82% fatty acid content) | Sigma-Aldrich | 0.03* | "Basics soap" | J. Sainsbury Ltd. | 0.0013 |
| Oleic acid (techn. grade 90%) | Sigma-Aldrich | 0.03* | Olive oil | J. Sainsbury Ltd. | 0.0038 |
| 1-octadecene (techn. grade 90%) | Sigma-Aldrich | 0.54* | Shark Liver oil | Shark Liver oil UK Ltd. | 0.23 |

**Table 5.1**: Associated costs and suppliers of reagents. An asterisk "*" indicates prices exclusive of value added tax.

When looking at alternatives for the iron source, it should be in high enough quantities to make the process viable, so fortified cereals or Irn-Bru ® whose typical iron content is too low were discounted. Iron supplements however offer a cheap source of iron, are readily available and are easy to handle, coming in solid pill form. The iron in the chosen supplements purchased from Boots Ltd., and contain iron(II) fumarate (not iron(III), so target was $Fe_2O_3$) at 14 mg of iron per tablet. The tablets were easily homogenised using a pestle and mortar and dissolved readily in the water/ethanol/hexane mixture utilised for the synthesis.

Other ingredients that made up the tablet such as the caking agent, dicalcium phosphate did have an effect on results and will be discussed later.

Oleic acid is a common constituent of many oils in nature.[364] As such, olive oil is an excellent source which is over 65% oleic acid, with the other 35% composed of long chain lipids and fatty acids. Sodium oleate proved difficult to substitute, but sodium salts of fatty acids are commonly used in cosmetic products, particularly as ionic surfactants in soaps. Sodium palmitate is a fatty acid salt commonly found in soaps and analagous to sodium oleate in terms of carbon chain length, so homogenised soap was used.

As for the solvent, a number of oils were considered and evaluated, including lavender oil, almond oil, shark liver oil and olive oil. It was found experimentally that almond and lavender oil, despite containing high boiling point compounds such as terpenes (for example linalool, a major typical constituent of lavender oil, boiling point 198 – 199 °C) were unsuitable as solvents. This was due to the volatile components lowering the boiling point and a vigorous reflux to be formed in the flask. This prevented the reaction from reaching the nucleation temperature (estimated to be around 300 °C) and thus no nanocrystals were formed. Pure olive oil (although necessary as a source of oleic acid) produced a carbonized mixture from which particles could not be isolated. However, shark liver oil was found to be a good substitute for 1-octadecene due to the presence of long-chain lipids such as squalene (boiling point 285 °C).

The constituents of shark liver oil itself vary according to the depths the shark normally resides.[365–368] Deep-sea sharks can approach neutral buoyancy through storage of low density lipids stored in the liver. A large contributor is squalene (density 0.858 g/ml at 25 °C and increases at cold, deep sea temperatures) which has been shown to influence iron oxide nanoparticle shape.[369] Other constituents include: diacyl glyceryl ether, triacylgycerol and wax esters, all of which could potentially contribute to directional growth of nanoparticles.[333,334,370,371]

### **5.4.2 Analysis of precursor species**

The synthesis of iron palmitate utilised the same salt metathesis reaction and conditions used for the synthesis of iron oleate (see section 2.2.1.2). Iron palmitate was characterised by IR spectroscopy and its decomposition temperature and behaviour analysed by TGA (figure 5.6). These results are compared directly to iron oleate synthesised according to Park *et al*.[45]

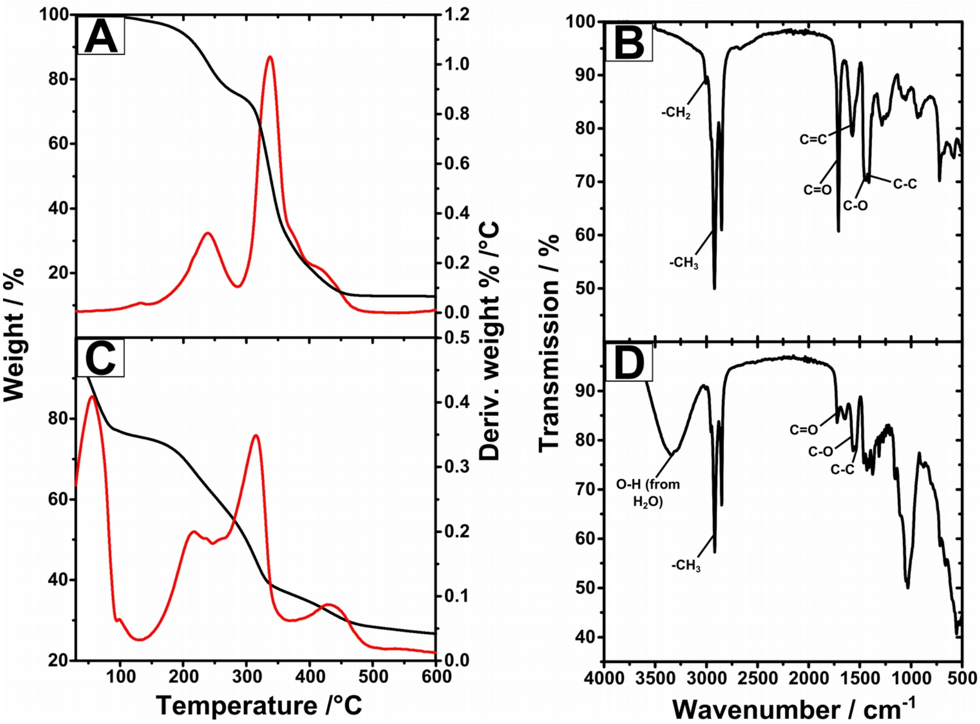

**Figure 5.6**: Thermogravimetric analysis and infrared spectroscopic analysis of iron oleate and iron palmitate precursors. A) Thermogravimetric analysis with first derivative of iron oleate, B) IR spectrum of iron oleate, C) Thermogravimetric analysis with first derivative of iron palmitate and D) IR spectrum of iron palmitate.

The decomposition of iron palmitate and iron oleate species was followed by TGA. Both iron oleate and iron palmitate samples had very similar decomposition profiles. The primary decomposition temperatures varied slightly between the two samples, but resided between 190 and 210 °C, after which rapid decomposition occurred. There was a significant loss of mass in the iron palmitate sample between 30 and 80 °C, which is associated with the evaporation of residual ethanol from the washing process (figure

5.3).

IR analysis of both compounds showed many common features, including -$CH_2$ and -$CH_3$ stretches at *ca.* 2920 $cm^{-1}$ and *ca.* 3000 $cm^{-1}$, carbonyl stretches at 1710 $cm^{-1}$ and 1719 $cm^{-1}$ for iron oleate and iron palmitate respectively. These stretches are shifted from carbonyl stretches of the native sodium oleate (1557 $cm^{-1}$) and soap (1557 $cm^{-1}$) respectively, which is indicative of conjugation.[45] It is noteworthy the broad band at *ca.* 3500 $cm^{-1}$ is from residual water left in the structure, which possibly contributed to the initial steep TGA profile of the iron palmitate sample. It has been shown that the presence of water in the iron oleate structure raises the decomposition temperature, separating the growth and nucleation phases, therefore reducing nanoparticle polydispersity.[143]

### **5.4.3 Analysis of nanoparticles produced**

Colloidal iron oxide nanoparticles were prepared using the high temperature thermal decomposition of iron palmitate and iron oleate species in the presence of surfactants. Reaction solutions turned from brown to black during the reaction, indicating the formation of colloidal nanoparticles. Nanoparticles were isolated by precipitation with ethanol and centrifugation and dispersed readily in *n*-hexane. It is noteworthy that obtained samples had significant organic components which were difficult to remove without the use of magnetic separation.

It is noteworthy that by varying the amount of oleic acid used in the synthesis, the particle size could be tuned, with particle size increasing with smaller amounts of oleic acid (*viz* olive oil). Average nanoparticle sizes were calculated from TEM micrographs, which were calculated to be ~12.7, 5.8 and 3.6 nm for 1.2, 6, 24 mmol of oleic acid in olive oil respectively, when decomposing 2 g of iron palmitate.

Three different samples of iron oxide nanoparticles were prepared to illustrate the effects replacing reagents had on the overall products, as illustrated in figure 5.7. Sample (I) are nanoparticles prepared from laboratory reagents according to the procedure reported by Park. Sample (II) and (III) are both prepared from high street reagents, only differing in the solvent used for the decomposition step.

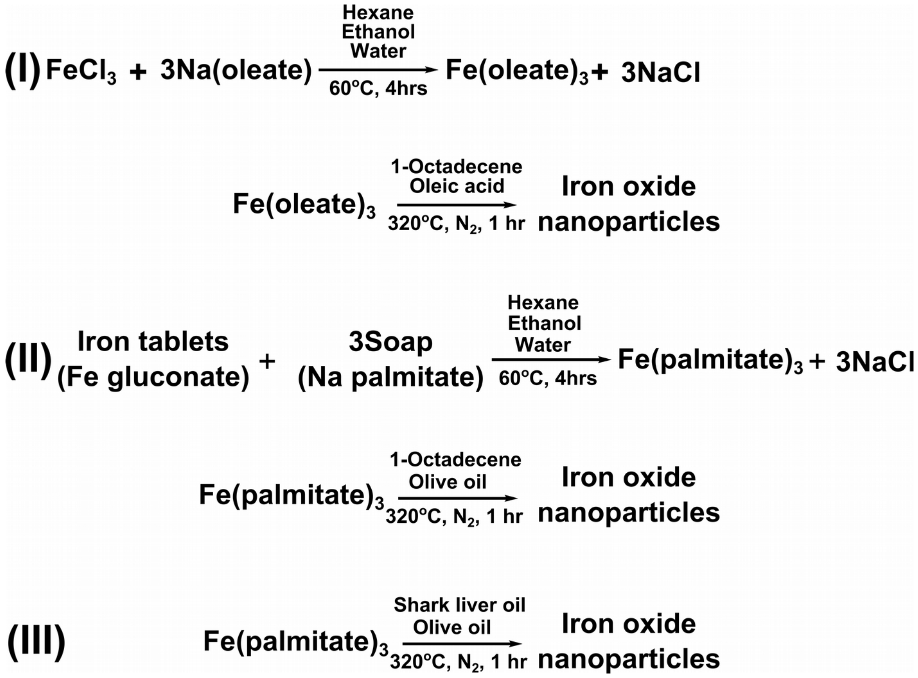

**Figure 5.7**: Sample (I) is the route to iron oxide nanoparticles proposed by Park *et al*.[45] Sample (II) is the synthesis of iron palmitate from high street sources and its subsequent decomposition in 1-octadecene and Sample (III) the decomposition of iron palmitate in shark liver oil.

TEM analysis showed a high degree of monodispersity in all samples of iron oxide nanoparticles. The shape of the nanoparticles was predominantly spherical using iron oleate or iron palmitate as the iron precursor. It was found that the solvent affected the final shape of the products. When a high ratio of oleic acid to iron palmitate was used for the decomposition in shark liver oil, directional growth of nanorods, as well as iron oxide nanoparticles, was observed (figure 5.8). These nanorods were highly crystalline, readily dispersible in organic solvents and exhibited directional growth. The nanorods however, were not composed of iron oxide, moreover of rhenanite ($\beta$-$NaCaPO_4$), determined by EDS and XRD. Ingredients from the initial iron tablets such as calcium phosphate and sodium chloride contributed to the nanorod formation. This is possibly due to the aforementioned organic species present in shark liver oil.

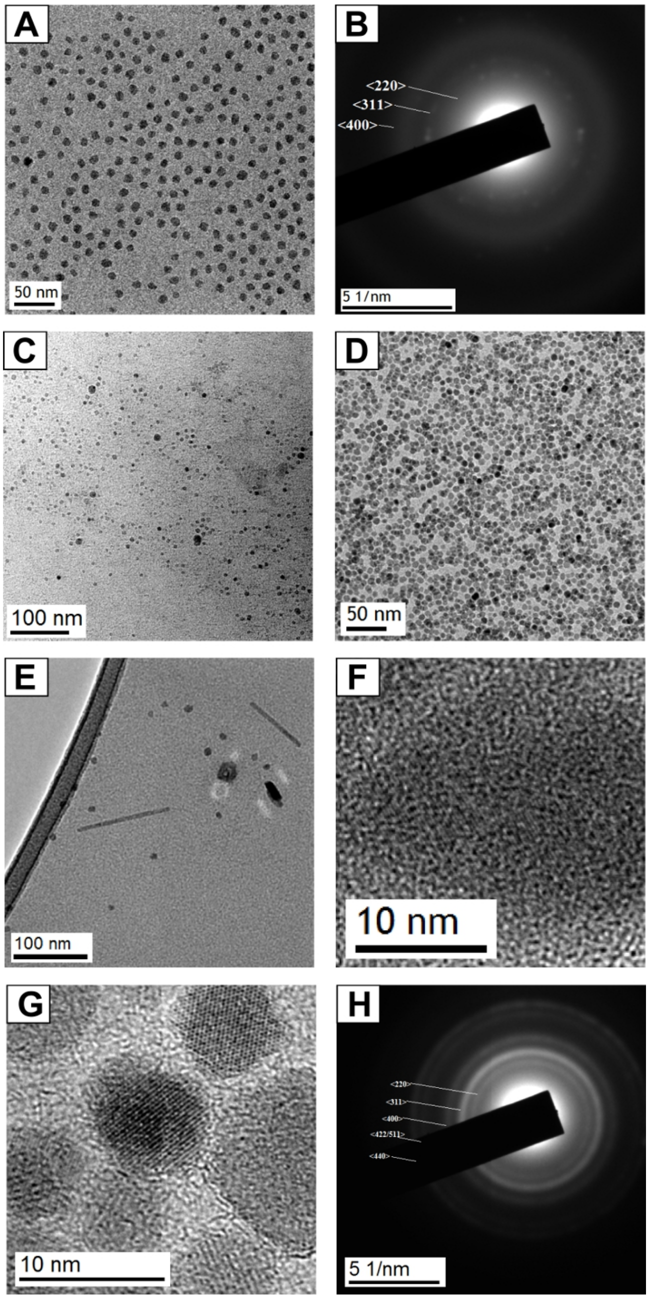

**Figure 5.8**: A) Iron oxide nanoparticles from the decomposition of iron palmitate in 1-octadecene (Sample (II)). B) SAED of iron oxide nanoparticles from the decomposition of iron palmitate in 1-octadecene. C) Iron oxide nanoparticles from the decomposition of iron palmitate in shark liver oil (Sample (III)). D) Iron oxide nanoparticles synthesised according to *Park et al.* Sample (I)). E) Iron oxide obtained from a 1:1 molar ratio of olive oil (oleic acid) to iron palmitate in shark liver oil. F) HRTEM micrograph of a single iron oxide nanoparticle from a 1:1 ratio of iron palmitate shark liver oil. G) HRTEM of D). H) SAED of D).

HRTEM analysis of obtained iron oxide nanoparticles showed highly crystalline products with *d*-spacings of: 0.2124 nm (sample (I)), 0.2081 nm (sample (II)) and 0.2695 nm (sample (III)) and 0.3282 nm for the rhenanite nanorods. These correspond to the <111> (magnetite), <400> (magnetite) and <311> (magnetite).[45]

EDS analysis detailed the elemental composition of the nanoparticles, confirming the presence of iron and oxygen. EDS and XPS analyses also highlighted additional elements acquired from the initial iron tablets such as phosphorus and calcium (*vide infra,* figure 5.9). Oxygen is a standard contaminant for EDS (picked up from oxidised carbonaceous species on the grids and indeed from carboxylate ligands themselves) so elemental atomic % comparisons are unreliable. In this instance EDS and XPS are used to confirm the presence of elements. Both EDS spectra showed the same thing; the presence of iron and oxygen.

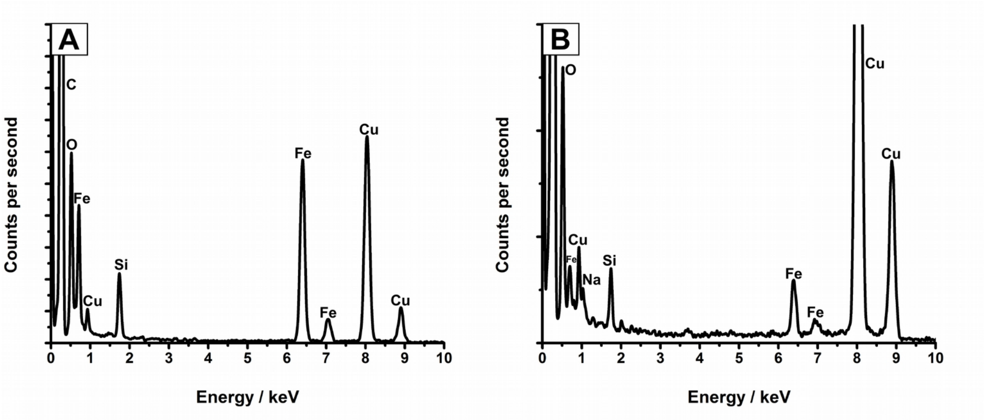

**Figure 5.9**: EDS spectra of: A) Iron oxide nanoparticles synthesised from the decomposition of iron oleate and B) from the decomposition of iron palmitate in shark liver oil.

FTIR analysis of the iron oxide nanoparticles showed features from both the precursors, notably -$CH_3$ and -$CH_2$ stretches at *ca.* 2920 $cm^{-1}$ and *ca.* 2960 $cm^{-1}$. The carbonyl stretches appear at 1714 $cm^{-1}$ and 1744 $cm^{-1}$ respectively for sample I and sample III respectively. The shift from the values obtained carbonyl stretches at and for iron oleate (1710 $cm^{-1}$) and iron palmitate respectively (1719 $cm^{-1}$) seem to indicate a change in carboxylate coordination for sample (III) but not for sample (I) (figure 5.10).[45,248]

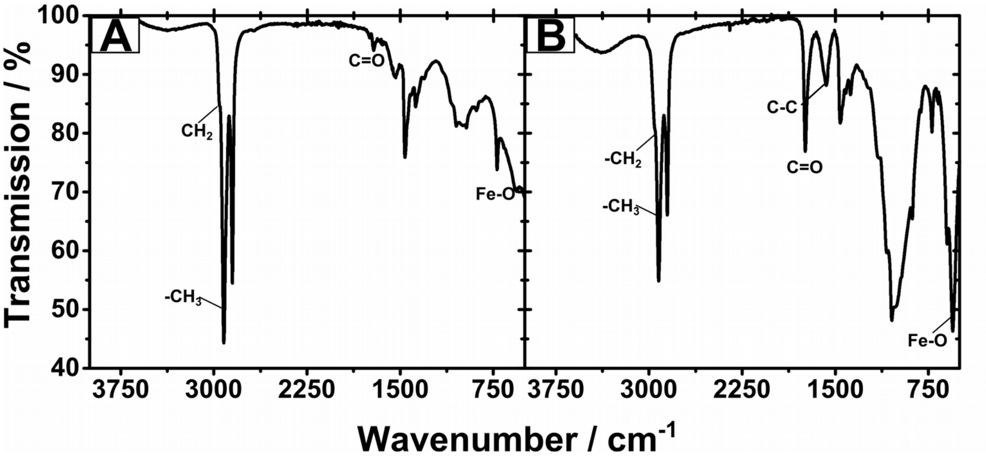

**Figure 5.10**: An FTIR comparison of A) iron oxide nanoparticles prepared from iron oleate (sample I) and B) iron oxide nanoparticles prepared from iron palmitate in shark liver oil (sample III).

XPS analyses (figure 5.11) revealed that the surface composition of the nanoparticles was influenced heavily by ingredients in the precursor, namely dicalcium phosphate (E341) which is used as a tableting agent. Calcium has been shown to be an effective dopant for iron oxide and iron oxide surfaces have high affinity for phosphorus containing ligands, hence the high level of surface doping.[372–374] EDS analysis showed that Ca and P were possible dopants for the iron, constituting *ca.* 4% of the total nanoparticle mass versus Fe. This would adversely affect the XRD pattern however, so it is more likely that alkyl calcium and phosphorus species are present in the nanoparticle dispersion or "nestling" in the ligand layer.

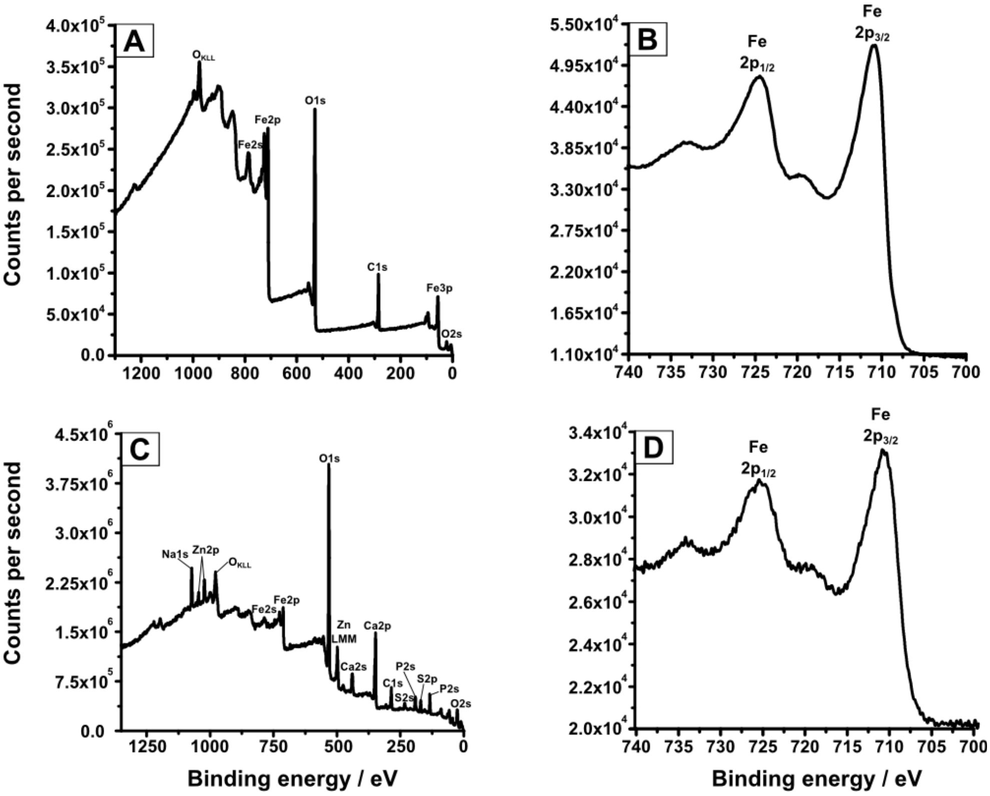

**Figure 5.11**: A) Survey and B) Fe2p scans of iron oxide nanoparticles synthesised from the decomposition of iron oleate and C) Survey and D) Fe2p scans of iron oxide nanoparticles synthesised from the decomposition of iron palmitate in shark liver oil.

Particle composition was also analysed by XRD. XRD analysis yielded a pattern consistent with that of an inverse spinel structure $\gamma$-$Fe_2O_3$/$Fe_3O_4$; however, it was not possible to discern between the two structures due to the high degree of similarity between the profiles of these two structures. The nanostructures obtained from a 1:1 molar ratio of olive oil to iron palmitate indicated the presence of a multiphase system as seen from XRD analysis. The sample was found to be mainly constituted by two phases due to the presence of peaks consistent with the diffraction pattern of $\gamma$-$Fe_2O_3$/$Fe_3O_4$ and also peaks corresponding to the orthorhombic structure of rhenanite (figure 5.12).

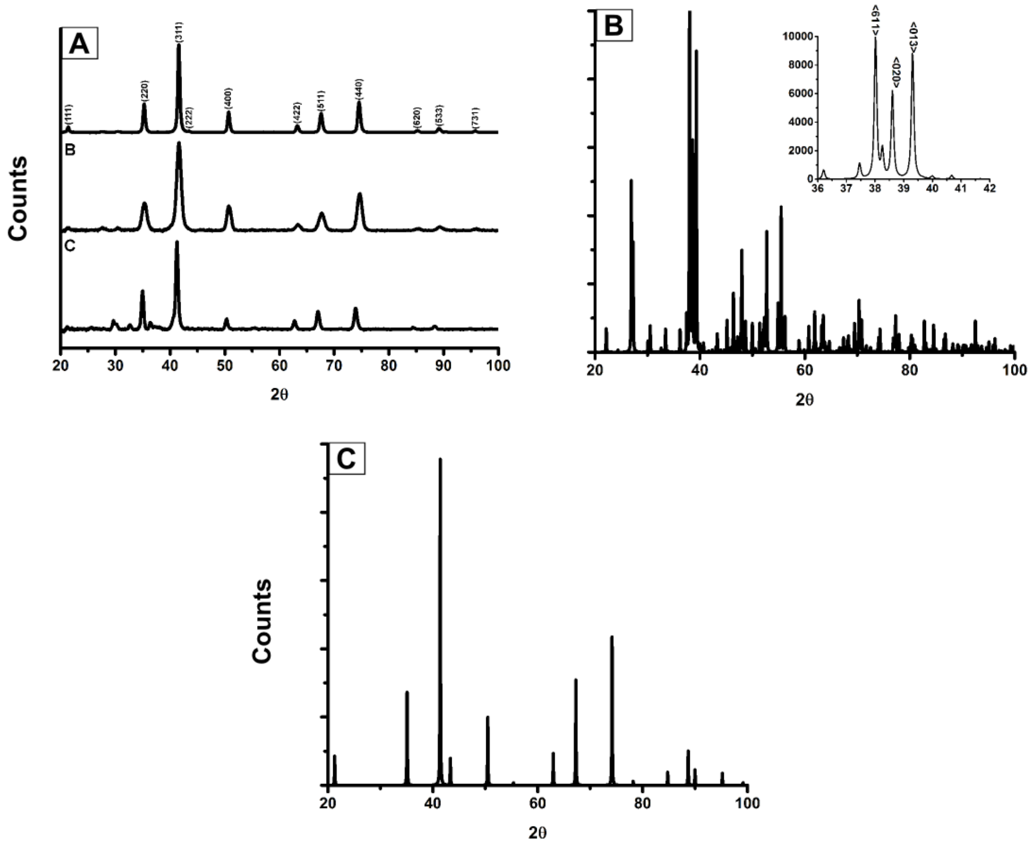

**Figure 5.12**: A) (Top): Labelled XRD pattern of a magnetite $Fe_3O_4$ standard powder, (middle): iron oxide nanoparticles obtained from the decomposition of iron oleate and (bottom): iron oxide nanoparticles obtained from the decomposition of iron palmitate in 1-octadecene. B) iron oxide nanoparticles obtained from the decomposition of iron palmitate in shark liver oil with a standard XRD pattern of β-rhenanite (ICSD no. 35629) (inset) C) Standard XRD pattern of magnetite $Fe_3O_4$ (ICSD no. 64829).

$^{57}$Fe Mössbauer spectroscopy was used to determine iron oxidation states in the samples (see section 2.1.3.5). All Mössbauer spectra were taken at room temperature. Sample I gave a very broad single peak, with wings extending out to ± 10 mm/s. The latter indicates the presence of magnetic hyperfine absorption, as would be expected in a magnetic iron oxide (such as maghemite or magnetite) below its superparamagnetic blocking temperature. The very broad nature of the absorption could be due to temporal or structural factors, or both – *i.e.* temporal as in magnetic relaxation on the nanosecond timescale of the Mössbauer measurement, or structural as in the crystallinity, size or defect structure of the particles. Further experiments would be needed to clarify this, with a variable temperature Mössbauer spectrometer (figure 5.13).

Mössbauer analysis of Sample (III) shows the superposition of two doublets – one of which has parameters typical of $Fe^{3+}$ (isomer shift $\delta = 0.30 \pm 0.07$ mm/s and quadrupole splitting $\Delta = 0.70 \pm 0.17$ mm/s), and another with parameters typical of $Fe^{2+}$ ($\delta = 1.18 \pm 0.04$ mm/s and $\Delta = 2.27 \pm 0.08$ mm/s). The latter was not expected, and was hypothesised to be due to the presence of a paramagnetic $Fe^{2+}$ species, such as unreacted iron palmitate/iron gluconate from the iron tablets/ iron palmitate precursor. The Mössbauer spectrum of a sample of homogenised iron tablets, shown in figure 6A), did indeed show such a $Fe^{2+}$ species, with parameters ($\delta = 1.20 \pm 0.01$ mm/s and $\Delta = 2.23 \pm 0.01$ mm/s) comparable to those observed in the product. From this analysis, we can say that although there some unreacted percursor, an appreciable amount of the precursor has formed magnetite and/or maghemite nanoparticles. The fact that these appear as a $Fe^{3+}$ doublet rather than a magnetic sextet is most likely due to the small particle size, so that the room temperature Mössbauer measurement is above the superparamagnetic blocking temperature of the nanoparticles. Sample II showed much the same in terms of species present, with a similar $Fe^{3+}$ spectrum ($\delta = 0.30 \pm 0.07$ mm/s and quadrupole splitting $\Delta = 0.68 \pm 0.17$ mm/s) with contribution from $Fe^{2+}$ species ($\delta = 1.18 \pm 0.01$ mm/s and $\Delta = 2.27 \pm 0.01$ mm/s). These results demonstrate the similarities of the iron oxide species produced through the decomposition of iron palmitate in 1-octadecene and shark liver oil respectively.

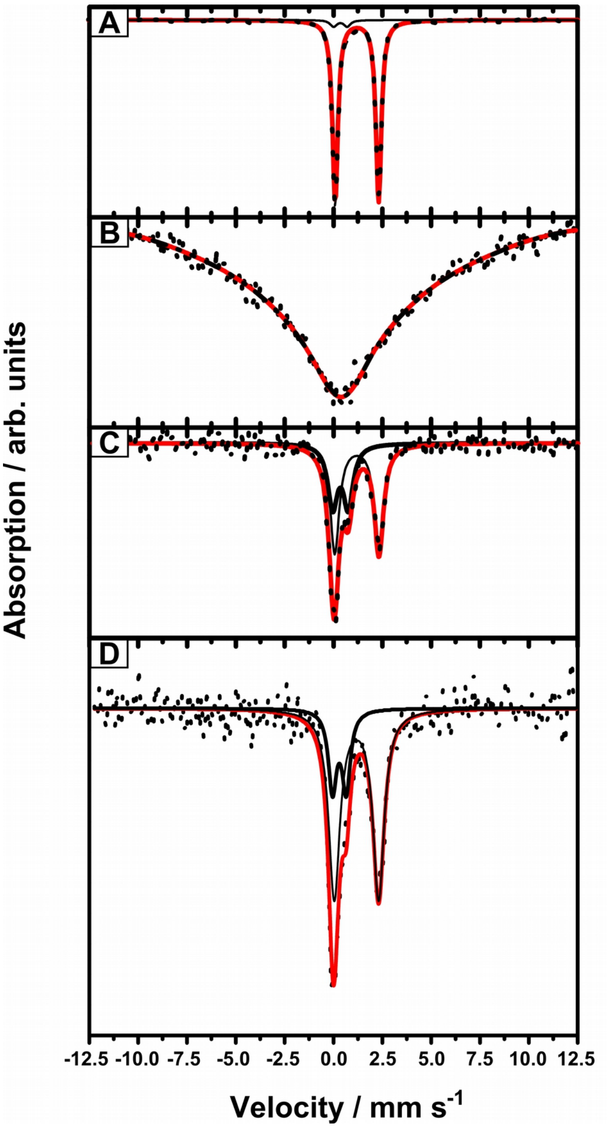

**Figure 5.13**: $^{57}$Fe Mössbauer spectra of: A) homogenised iron tablets, B) iron oxide nanoparticles from standard reagents (Sample (I)), C) iron oxide nanoparticles from the decomposition of iron palmitate in shark liver oil (Sample (III)) and (D) iron oxide nanoparticles from iron palmitate decomposed in 1-octadecene (Sample II). The red trace represents the fit with the thick black line the $Fe^{3+}$ doublet component and the thin black line the $Fe^{2+}$ doublet component.

In order for magnetic nanoparticles to be tested accurately for magnetic fluid hyperthermia, they needed to be transferred to water. This was accomplished through the use of a pro-amphiphilic polymer; poly(maleic anhydride-*alt*-octadecene).[151]

Briefly, oleic acid coated nanoparticles were dissolved in chloroform and stirred with a solution of poly(maleic anhydride-*alt*-octadecene) also in chloroform. Chloroform is polar compared to other organic solvents, and as such, encourages van der Waals hydrophobic interactions between the oleic acid hydrophobic "tails" and the hydrophobic parts of poly(maleic anhydride-*alt*-octadecene). The chloroform was evaporated slowly and the nanoparticle residue dried *in vacuo*. An aqueous solution of 0.1 mol $dm^{-3}$ tetramethylammonium hydroxide was used to open the maleic anhydride rings on the polymer, thus imparting water dispersibility to the nanoparticles. Water is a highly polar solvent, and as such the hydrophobic-hydrophobic van der Waals interactions between polymer and oleic acid is highly favourable. With the maleic anhydride rings opened, the nanoparticles become electrostatically stabilised and subject to DLVO theory.[151,375]

Heat loss dissipation measurements of sample (III) dispersed in water showed a temperature rise of 1.8 ºC at a prepared concentration of 2.3 mg/mL, whilst Sample (I) showed a temperature of 2.1 ºC at a prepared concentration of 6.1 mg/mL with ILP values of 1.9 and 0.4 $nHm^2$ /kg respectively, placing them towards the market leaders within the range of commercially available magnetic fluid hyperthermia agents.[128] Sample (II) showed signs no of heat dissipation on exposure to the AC magnetic field (figure 5.14).

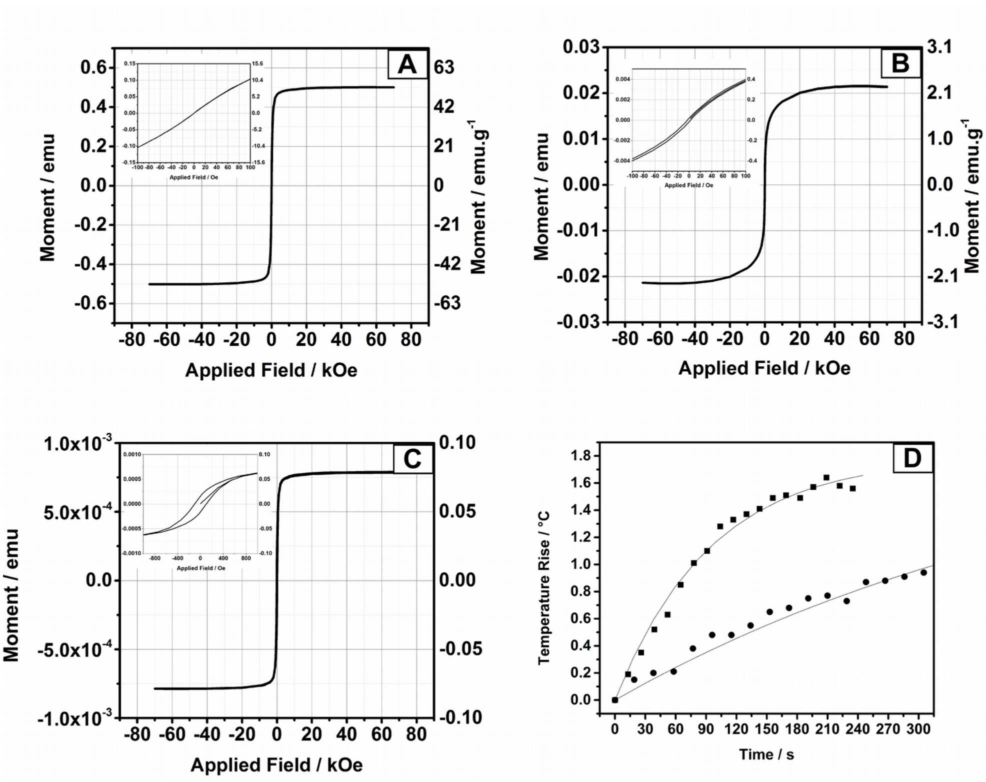

**Figure 5.14**: SQUID magnetic hysteresis loops of: iron oxide nanoparticles from standard reagents (Sample (I)) A), iron oxide nanoparticles from iron palmitate decomposed in 1-octadecene (Sample (II)) B) and iron oxide nanoparticles obtained from the decomposition of iron palmitate in shark liver oil (Sample (III)) C). D) shows magnetic hyperthermia heating of water-transferred iron oxide nanoparticles from Sample (I) (bottom) and nanoparticles from sample (III) (top). Insets are magnifications of the hysteresis loops, showing minimal coercivity.

SQUID magnetometry shows that Sample (I) and (II) are superparamagnetic at 300K. The shark liver oil samples exhibited signs of ferromagnetic behaviour with a normalised remanance M/M_s = 0.2 and a coercivity of 100 Oe. Samples (I), (II) and (III) have saturation magnetisation values of 52, 2.2 and 0.1 emu/g respectively (figure 5.14).

The heating vs. SQUID results for sample (III) are somewhat surprising due to the good heating properties vs. poor magnetic moment. Although classified as rhenanite by XRD and EDS, it is reasonable to assume the rods observed in sample (III) probably have some magnetic iron content. It has been shown that nanomaterials with large shape anisotropy such as rods composed of magnetic materials can exhibit heating properties not commensurate with their magnetic moments.[376,377]

## 5.5 Conclusion

In this chapter, the synthesis of iron oxide nanomaterials from readily available high street sources was demonstrated. The synthesis occurs in two steps, namely the synthesis of the precursor, iron palmitate, and then its decomposition in the presence of surfactants and high boiling point solvents, again shop bought. The results from these syntheses were compared to standard techniques, and the associated costs compared (Table 5.1). Iron oxide nanomaterials can be produced at a far lower cost than standard literature techniques, at the Chemist's discretion due to the availability of the reagents used.

The nanomaterials were characterised using a variety of techniques including: XRD, XPS, EDS, TEM, Mössbauer spectroscopy, TGA, ATR-FTIR, SQUID, and magnetic hyperthermia measurements. High quality, monodisperse iron oxide nanocrystals were also obtained from the decomposition of iron palmitate in 1-octadecene and shark liver oil, both displaying a degree of heating on exposure to an AC magnetic field. However, further work is needed to characterise the nanorods observed in sample (III), such as EELS/EDS-HRTEM elemental mapping. Optimisation of the nanoparticle syntheses in order to improve performance in magnetic fluid hyperthermia is also a direction for future work.

The inexpensive iron oxide nanomaterials obtained have tremendous scope for the transfer of this reaction to batch or mass production, for use in numerous applications from medical devices to catalysis. The good performance of the synthesised materials in magnetic hyperthermia tests, and the Food and Drug administration approved nature of the reagents give scope for the further development of cost-effective iron oxide nanomaterials, potentially for applications such as water filters in the developing world, allowing for synthesis at the point of use.

# Chapter 6: Conclusions and future work

## 6.1 Conclusions

The work presented in this thesis stems from distinct areas in the field of nanoparticulate research, namely nanoparticle composites, semiconductor quantum dots and magnetic nanocrystal synthesis.

The inspiration for the work in chapter 3 stems from the fact that there are few examples of superhydrophobic-photocatalytic surfaces, not least ones that could potentially be scaled up and used for anti-microbial applications in hospitals, clean-room facilities *etc*. The incorporation of functionalised titania nanoparticles into superhydrophobic poly(dimethylsiloxane) films *via* a one-pot AACVD reaction forms a photocatalytic-superhydrophobic surface, ideally suited to such applications. It is also in the vanguard of polymeric superhydrophobic surfaces, as the superhydrophobicity is undiminished after UV (254 nm) irradiation, a requirement of the photocatalytic activity of the titania nanoparticles. Photocatalytic activity was tested using dye degradation studies of Resazurin under 254 nm irradiation. The titania nanoparticle- PDMS surface is unmatched in terms of ease of synthesis and retention of superhydrophobicity post-irradiation, and represents a new class of anti-bacterial self-cleaning surfaces.

The one-pot AACVD method was extended to a variety of nanoparticles, thus producing a general method for the incorporation of hydrophobically ligated nanoparticles into superhydrophobic surfaces. However, the high temperatures required for the synthesis (monomer curing takes place at 360 °C) rendered a poly(dimethylsiloxane)-quantum dot surface impossible as the quantum dots oxidised at the high temperature. Certain types of nanoparticle, such as gold, interfered with the platinum based curing mechanism of the polymer, and as such prevented the formation of a superhydrophobic surface. This problem was surmounted by coating the gold with silica coated functionalised with trimethoxy(octadecyl)silane. Iron oxide nanoparticles were also incorporated, creating, to the best of the author's knowledge, the first magnetic nanoparticle-superhydrophobic polymer surface. Catalytic activity for the liberation of hydrogen gas from ammonia-borane was demonstrated using the nickel nanoparticle-PDMS film. This method opens up a plethora of superhydrophobic nanoparticulate composites, with the synergistic effects of the superhydrophobic polymeric matrix and incorporated nanoparticle properties open to future exploitation.

Chapter 4 details the development of cadmium selenide quantum dots as vectors for the photo-induced release of catalytically active $Cu^+$ ions. The quantum dots have a CdSe/ZnS-CuS core/shell structure, created by the decomposition of a mixture of zinc(II) and copper(II) diethyldithiocarbamate species in the presence of surfactants. The vector-release system is the first of its kind, and indeed one of the few examples of the use of quantum dots as a catalyst for organic transformations. $Cu^+$ is released into solution *via* photo-oxidation of the ZnS-CuS shell, a process elucidated by ICP-AES. The core/shell structure of the quantum dot was determined by EDS and XPS, as well as inferences made using photoluminescence spectroscopy, particularly the reduction in photoluminescence quantum yield and a second, low-energy signature in the photoluminescence emission profile. The quantum dots were shown to be highly effective in catalysing Huisgen “click” chemistry between benzyl azide and phenylacetylene. The catalysts are recoverable *via* centrifugation, exhibit high turnover frequencies compared to heterogeneous catalysts. It is stressed that these quantum dot catalyst vectors represent a bridge between homogeneous and heterogeneous catalysis and a new class of materials.

The synthesis of iron oxide nanoparticles *via* a new, inexpensive route is detailed in chapter 5. The grounding for this chapter builds on the work by Park *et al.* [45] in 2003, who outline a synthesis for the mass production of monodisperse nanocrystals from metal oleate precursors. The synthesis uses the framework laid down by Park *et al.*

and adapts it to reagents obtained form the high street. For example, the iron oleate complex is replaced by iron palmitate synthesised from soap and iron tablets using the same procedure. The resultant iron oxide nanoparticles from the decomposition of the as-synthesised iron palmitate were transferred to water *via* an amphiphilic polymer and effectively tested as magnetic fluid hyperthermia agents. The synthesised materials performed in the same range as commercially available magnetic hyperthermia agents, and due to their low cost and ease of synthesis, have potential for point of use synthesis for water filtration and therapy in the developing world.

## 6.2 Future work

The potential to expand on any one of the chapters in this thesis is enormous. The development of superhydrophobic antimicrobial surfaces is very attractive for a plethora of applications, and a film which is robust, adherent, superhydrophobic and self-cleaning with anti-microbial capability is highly desirable. Due to ease of synthesis and in particular, retention of superhydrophobicity post-irradiation, the superhydrophobic-nanoparticulate materials developed herein compare very favourably to contemporary literature examples, and represent a new class of superhydrophobic material. Therefore, the next stage would be to improve the adherence of the polymer to different substrates such as steel, plastics and glass before stringent anti-microbial testing. If the superhydrophobic polymer-nanoparticle composites were to be used in self-cleaning, energy efficient windows, perhaps combined with thermochromic nanoparticles, the issue of opacity must be addressed.

Although yet to be completed, work into the development of a general method for the synthesis of CdSe/ZnS-MS and InP/ZnS-MS (M for metal) quantum dots is nearing completion. The doping, achieved by metal-dithiocarbamates, has yielded some novel crystal structures as well as imparting interesting photoluminescence properties and improving the quantum yields of the quantum dots. The result which has proven to be the most interesting is the CdSe/ZnS-HgS system, which red-shifts the photoluminescence emission profile by 200 - 400 nm depending on the level of doping. This represents a facile way of producing infrared emitting quantum dots for quantum dot sensitised solar cells, from standard CdSe cores. Measurement of quantum yields and photoluminescence lifetimes is also ongoing.

The catalytic potential of doped-shell quantum dots is also an area under development, with potential photo-activated water-splitting devices for hydrogen production to the fore. Other metal dithiocarbamate complexes such as platinum, samarium or palladium dithiocarbamate species represent pathways for the development of photo-activated quantum dot catalyst vectors in fine chemical syntheses or polymerisations- currently an area of rapid growth and development.

The work in chapter 5 is yet to be optimised; the effect of additional constituents at many stages of the nanoparticle synthesis are yet to be analysed fully, although the possibility of the synthesis based wholly on inexpensive reagents for effective magnetic hyperthermia agents has been realised. Further development would involve further reduction in cost by varying the reagents and the optimisation of nanoparticles produced by this method for magnetic fluid hyperthermia, and reducing the complexity of the synthesis by reducing the temperatures and apparatus involved. Cheap iron oxide nanoparticles may also find use in the developing world for use in water filtration.[378]

# Bibliography

[1] P. Mulvaney, *MRS Bull.* **2001**, *26*, 1009–1014.

[2] M. Faraday, *Philos. Trans. R. Soc. Lond.* **1857**, *147*, 145–181.

[3] G. A. Ozin, A. Arsenault, L. Cademartiri, *Nanochemistry: A Chemical Approach to Nanomaterials*, Royal Society Of Chemistry, **2008**.

[4] J. Bear, G. Charron, M. T. Fernández-Argüelles, S. Massadeh, P. McNaughter, T. Nann, in *BetaSys Syst. Biol. Regul. Exocytosis Pancreat. ß-Cells*, Springer New York, **2011**, pp. 185–220.

[5] L. K. Bogart, G. Pourroy, C. J. Murphy, V. Puntes, T. Pellegrino, D. Rosenblum, D. Peer, R. Lévy, *ACS Nano* **2014**, 3107–3122.

[6] N. Li, P. Zhao, D. Astruc, *Angew. Chem. Int. Ed.* **2014**, *53*, 1756–1789.

[7] D. Schmaljohann, *Adv. Drug Deliv. Rev.* **2006**, *58*, 1655–1670.

[8] G. Reiss, A. Hütten, *Nat. Mater.* **2005**, *4*, 725–726.

[9] B. D. Terris, T. Thomson, *J. Phys. Appl. Phys.* **2005**, *38*, R199.

[10] S. Ahn, S. Y. Jung, S. J. Lee, *Adv. Funct. Mater.* **2013**, *23*, 2212–2217.

[11] G.-H. Kim, B. Walker, H.-B. Kim, J. Y. Kim, E. H. Sargent, J. Park, J. Y. Kim, *Adv. Mater.* **2014**, *26*, 3321–3327.

[12] J. Y. Kim, O. Voznyy, D. Zhitomirsky, E. H. Sargent, *Adv. Mater.* **2013**, *25*, 4986–5010.

[13] J. Pichaandi, F. C. J. M. van Veggel, *Coord. Chem. Rev.* **2014**, *263–264*, 138–150.

[14] J. Tang, E. H. Sargent, *Adv. Mater.* **2011**, *23*, 12–29.

[15] C. Ratanatawanate, Y. Tao, K. J. Balkus, *J. Phys. Chem. C* **2009**, *113*, 10755–10760.

[16] R. Shomura, K. J. Chung, H. Iwai, M. Higuchi, *Langmuir* **2011**, *27*, 7972–7975.

[17] S. T. Selvan, T. T. Y. Tan, D. K. Yi, N. R. Jana, *Langmuir* **2010**, 11631–11641.

[18] P. Hazarika, S. M. Jickells, D. A. Russell, *The Analyst* **2009**, *134*, 93.

[19] D. Astruc, F. Lu, J. R. Aranzaes, *Angew. Chem. Int. Ed.* **2005**, *44*, 7852–7872.

[20] R. Narayanan, M. A. El-Sayed, *J. Phys. Chem. B* **2005**, *109*, 12663–12676.

[21] R. Schlögl, S. B. Abd Hamid, *Angew. Chem. Int. Ed.* **2004**, *43*, 1628–1637.

[22] Z. Kang, C. H. A. Tsang, N.-B. Wong, Z. Zhang, S.-T. Lee, *J. Am. Chem. Soc.* **2007**, *129*, 12090–12091.

[23] K. L. Vigor, P. G. Kyrtatos, S. Minogue, K. T. Al-Jamal, H. Kogelberg, B. Tolner, K. Kostarelos, R. H. Begent, Q. A. Pankhurst, M. F. Lythgoe, et al., *Biomaterials* **2010**, *31*, 1307–1315.

[24] W. Bücking, S. Massadeh, A. Merkulov, S. Xu, T. Nann, *Anal. Bioanal. Chem.* **2010**, *396*, 1087–1094.

[25] Y.-H. Chan, J. Chen, Q. Liu, S. E. Wark, D. H. Son, J. D. Batteas, *Anal. Chem.* **2010**, *82*, 3671–3678.

[26] R. Freeman, T. Finder, L. Bahshi, R. Gill, I. Willner, *Adv. Mater.* **2012**, *24*, 6416–6421.

[27] E. J. W. Verwey, J. T. G. Overbeek, *J. Colloid Sci.* **1955**, *10*, 224–225.

[28] B. Derjaguin, L. Landau, *Prog. Surf. Sci.* **1993**, *43*, 30–59.

[29] D. J. Shaw, *Introduction to Colloid and Surface Chemisty*, Elsevier Limited, Oxford ; Boston, **1992**.

[30] K. Nose, Y. Soma, T. Omata, S. Otsuka-Yao-Matsuo, *Chem. Mater.* **2009**, *21*, 2607–2613.

[31] D. Ling, M. J. Hackett, T. Hyeon, *Nano Today* **2014**, DOI 10.1016/j.nantod.2014.06.005.

[32] A. Desireddy, B. E. Conn, J. Guo, B. Yoon, R. N. Barnett, B. M. Monahan, K. Kirschbaum, W. P. Griffith, R. L. Whetten, U. Landman, et al., *Nature* **2013**, *501*, 399–402.

[33] M. R. Dewi, G. Laufersky, T. Nann, *RSC Adv.* **2014**, *4*, 34217–34220.

[34] H. Zhang, J. Jang, W. Liu, D. V. Talapin, *ACS Nano* **2014**, DOI 10.1021/nn502470v.

[35] K. An, S. G. Kwon, M. Park, H. B. Na, S.-I. Baik, J. H. Yu, D. Kim, J. S. Son, Y. W. Kim, I. C. Song, et al., *Nano Lett.* **2008**, *8*, 4252–4258.

[36] A. Tavakoli, M. Sohrabi, A. Kargari, *Chem. Pap.* **2007**, *61*, 151–170.

[37] M. Gheisari, M. Mozaffari, M. Acet, J. Amighian, *J. Magn. Magn. Mater.* **2008**,

*320*, 2618–2621.

[38] M. Ullmann, S. K. Friedlander, A. Schmidt-Ott, *J. Nanoparticle Res.* **2002**, *4*, 499–509.

[39] V. Amendola, M. Meneghetti, G. Granozzi, S. Agnoli, S. Polizzi, P. Riello, A. Boscaini, C. Anselmi, G. Fracasso, M. Colombatti, et al., *J. Mater. Chem.* **2011**, *21*, 3803–3813.

[40] S. E. F. Kleijn, S. C. S. Lai, M. T. M. Koper, P. R. Unwin, *Angew. Chem. Int. Ed.* **2014**, *53*, 3558–3586.

[41] K. S. Suslick, M. Fang, T. Hyeon, *J. Am. Chem. Soc.* **1996**, *118*, 11960–11961.

[42] S. Laurent, D. Forge, M. Port, A. Roch, C. Robic, L. Vander Elst, R. N. Muller, *Chem. Rev.* **2008**, *108*, 2064–2110.

[43] S. Sun, H. Zeng, *J. Am. Chem. Soc.* **2002**, *124*, 8204–8205.

[44] S. Sun, H. Zeng, D. B. Robinson, S. Raoux, P. M. Rice, S. X. Wang, G. Li, *J Am Chem Soc* **2003**, *126*, 273–279.

[45] J. Park, K. An, Y. Hwang, J.-G. Park, H.-J. Noh, J.-Y. Kim, J.-H. Park, N.-M. Hwang, T. Hyeon, *Nat. Mater.* **2004**, *3*, 891–895.

[46] Y. K. Jung, J. I. Kim, J.-K. Lee, *J. Am. Chem. Soc.* **2009**, *132*, 178–184.

[47] K. Tao, H. Dou, K. Sun, *Chem. Mater.* **2006**, *18*, 5273–5278.

[48] T. Ahn, J. H. Kim, H.-M. Yang, J. W. Lee, J.-D. Kim, *J Phys Chem C* **2012**, *116*, 6069–6076.

[49] R. Hong, T. Pan, J. Qian, H. Li, *Chem. Eng. J.* **2006**, *119*, 71–81.

[50] V. K. LaMer, *Ind. Eng. Chem.* **1952**, *44*, 1270–1277.

[51] V. K. LaMer, R. H. Dinegar, *J. Am. Chem. Soc.* **1950**, *72*, 4847–4854.

[52] S. G. Kwon, Y. Piao, J. Park, S. Angappane, Y. Jo, N.-M. Hwang, J.-G. Park, T. Hyeon, *J. Am. Chem. Soc.* **2007**, *129*, 12571–12584.

[53] E. E. Finney, R. G. Finke, *J. Colloid Interface Sci.* **2008**, *317*, 351–374.

[54] J. van Embden, J. E. Sader, M. Davidson, P. Mulvaney, *J. Phys. Chem. C* **2009**, *113*, 16342–16355.

[55] M. Ramalakshmi, P. Shakkthivel, M. Sundrarajan, S. M. Chen, *Mater. Res. Bull.* **2013**, *48*, 2758–2765.

[56] C. Blanco-Andujar, D. Ortega, Q. A. Pankhurst, N. T. K. Thanh, *J. Mater. Chem.* **2012**, *22*, 12498–12506.

[57] M. Brust, M. Walker, D. Bethell, D. J. Schiffrin, R. Whyman, *J. Chem. Soc. Chem. Commun.* **1994**, 801–802.

[58] R. Sardar, A. M. Funston, P. Mulvaney, R. W. Murray, *Langmuir* **2009**, *25*, 13840–13851.

[59] D. Maity, S. N. Kale, R. Kaul-Ghanekar, J.-M. Xue, J. Ding, *J. Magn. Magn. Mater.* **2009**, *321*, 3093–3098.

[60] S. Ehlert, T. Lunkenbein, J. Breu, S. Förster, *Colloids Surf. Physicochem. Eng. Asp.* **2014**, *444*, 76–80.

[61] T.-D. Nguyen, T.-O. Do, *Langmuir* **2009**, *25*, 5322–5332.

[62] G. Oskam, F. de J. P. Poot, *J. Sol-Gel Sci. Technol.* **2006**, *37*, 157–160.

[63] A. Sobhani, M. Salavati-Niasari, M. Sobhani, *Mater. Sci. Semicond. Process.* **2013**, *16*, 410–417.

[64] D. C. Onwudiwe, P. A. Ajibade, *Int. J. Mol. Sci.* **2011**, *12*, 5538–5551.

[65] Y. Xie, L. Carbone, C. Nobile, V. Grillo, S. D'Agostino, F. Della Sala, C. Giannini, D. Altamura, C. Oelsner, C. Kryschi, et al., *ACS Nano* **2013**, *7*, 7352–7369.

[66] S. Carenco, C. Boissiere, L. Nicole, C. Sanchez, P. Le Floch, N. Mezailles, *Chem. Mater.* **2010**, *22*, 1340–1349.

[67] M. Salavati Niasari, F. Davar, N. Mir, *Polyhedron* **2008**, *27*, 3514–3518.

[68] S. M. Hosseinpour-Mashkani, M. Ramezani, *Mater. Lett.* **2014**, *130*, 259–262.

[69] S. Xu, S. Kumar, T. Nann, *J. Am. Chem. Soc.* **2006**, *128*, 1054–1055.

[70] N. O. Boadi, M. A. Malik, P. O'Brien, J. A. M. Awudza, *Dalton Trans.* **2012**, *41*, 10497–10506.

[71] V. Roullier, F. Grasset, F. Boulmedais, F. Artzner, O. Cador, V. Marchi-Artzner, *Chem. Mater.* **2008**, *20*, 6657–6665.

[72] B. O. Dabbousi, J. Rodriguez-Viejo, F. V. Mikulec, J. R. Heine, H. Mattoussi, R. Ober, K. F. Jensen, M. G. Bawendi, *J. Phys. Chem. B* **1997**, *101*, 9463–9475.

[73] K. O. Abdulwahab, M. A. Malik, P. O'Brien, G. A. Timco, F. Tuna, R. E. P.

Winpenny, R. A. D. Pattrick, V. S. Coker, E. Arenholz, *J. Mater. Chem. C* **2014**, *2*, 6781–6789.

[74] P. Samokhvalov, M. Artemyev, I. Nabiev, *Chem. – Eur. J.* **2013**, *19*, 1534–1546.

[75] S. Jun, E. Jang, *Angew. Chem. Int. Ed.* **2013**, *52*, 679–682.

[76] L. Qu, X. Peng, *J. Am. Chem. Soc.* **2002**, *124*, 2049–2055.

[77] S. Flamee, M. Cirillo, S. Abe, K. De Nolf, R. Gomes, T. Aubert, Z. Hens, *Chem. Mater.* **2013**, *25*, 2476–2483.

[78] J. Zhang, C. Xi, C. Feng, H. Xia, D. Wang, X. Tao, *Langmuir* **2014**, *30*, 2480–2489.

[79] X. Ye, Y. Gao, J. Chen, D. C. Reifsnyder, C. Zheng, C. B. Murray, *Nano Lett.* **2013**, *13*, 2163–2171.

[80] S. R. K. Perala, S. Kumar, *Langmuir* **2013**, DOI 10.1021/la401604q.

[81] N. R. Jana, X. Peng, *J. Am. Chem. Soc.* **2011**, *125*, 14280–14281.

[82] S. Liu, G. Chen, P. N. Prasad, M. T. Swihart, *Chem. Mater.* **2011**, *23*, 4098–4101.

[83] J. Zheng, C. Zhou, M. Yu, J. Liu, *Nanoscale* **2012**, *4*, 4073.

[84] J. Turkevich, P. Stevenson, J. Hillier, *Discuss. Faraday Soc.* **1951**, 55–75.

[85] L. Wang, J. Bai, P. Huang, H. Wang, L. Zhang, Y. Zhao, *Electrochem. Commun.* **2006**, *8*, 1035–1040.

[86] L. Olofsson, T. Rindzevicius, I. Pfeiffer, M. Käll, F. Höök, *Langmuir* **2003**, *19*, 10414–10419.

[87] Y.-C. Yeh, B. Creran, V. M. Rotello, *Nanoscale* **2012**, *4*, 1871–1880.

[88] E. B. Dickerson, E. C. Dreaden, X. Huang, I. H. El-Sayed, H. Chu, S. Pushpanketh, J. F. McDonald, M. A. El-Sayed, *Cancer Lett.* **2008**, *269*, 57–66.

[89] J.-F. Soulé, H. Miyamura, S. Kobayashi, *J. Am. Chem. Soc.* **2011**, *133*, 18550–18553.

[90] S. Panigrahi, S. Basu, S. Praharaj, S. Pande, S. Jana, A. Pal, S. K. Ghosh, T. Pal, *J. Phys. Chem. C* **2007**, *111*, 4596–4605.

[91] Y. Zhang, X. Cui, F. Shi, Y. Deng, *Chem. Rev.* **2012**, *112*, 2467–2505.

[92] G. Mie, *Ann. Phys.* **1908**, *330*, 377–445.

[93] L. M. Liz-Marzán, *Chem. Commun.* **2012**, *49*, 16–18.

[94] T. Pradeep, Anshup, *Thin Solid Films* **2009**, *517*, 6441–6478.

[95] A. I. Ekimov, A. A. Onushchenko, *Sov. J. Exp. Theor. Phys. Lett.* **1981**, *34*, 345.

[96] L. E. Brus, *J. Chem. Phys.* **1984**, *80*, 4403–4409.

[97] L. Brus, *J. Phys. Chem.* **1986**, *90*, 2555–2560.

[98] C. B. Murray, D. J. Norris, M. G. Bawendi, *J. Am. Chem. Soc.* **1993**, *115*, 8706–8715.

[99] F. C. J. M. van Veggel, *Chem. Mater.* **2014**, *26*, 111–122.

[100] I. L. Medintz, H. T. Uyeda, E. R. Goldman, H. Mattoussi, *Nat. Mater.* **2005**, *4*, 435–446.

[101] J. K. Jaiswal, E. R. Goldman, H. Mattoussi, S. M. Simon, *Nat. Methods* **2004**, *1*, 73–78.

[102] J. J. Li, Y. A. Wang, W. Guo, J. C. Keay, T. D. Mishima, M. B. Johnson, X. Peng, *J. Am. Chem. Soc.* **2003**, *125*, 12567–12575.

[103] X. Gao, Y. Gui, R. M. Levenson, L. W. K. Chung, S. Nie, *Nat. Biotechnol.* **2004**, *22*, 969–976.

[104] E. B. Voura, J. K. Jaiswal, H. Mattoussi, S. M. Simon, *Nat. Med.* **2004**, *10*, 993–998.

[105] H. Fu, S.-W. Tsang, *Nanoscale* **2012**, *4*, 2187–2201.

[106] C. Lorbeer, J. Cybinska, A.-V. Mudring, *J. Mater. Chem. C* **2014**, *2*, 1862–1868.

[107] C. Kirchner, T. Liedl, S. Kudera, T. Pellegrino, A. Muñoz Javier, H. E. Gaub, S. Stölzle, N. Fertig, W. J. Parak, *Nano Lett.* **2005**, *5*, 331–338.

[108] A. M. Derfus, W. C. W. Chan, S. N. Bhatia, *Nano Lett.* **2004**, *4*, 11–18.

[109] P. T. K. Chin, C. de Mello Donegá, S. S. van Bavel, S. C. J. Meskers, N. A. J. M. Sommerdijk, R. A. J. Janssen, *J. Am. Chem. Soc.* **2007**, *129*, 14880–14886.

[110] D. C. J. Neo, C. Cheng, S. D. Stranks, S. M. Fairclough, J. S. Kim, A. I. Kirkland, J. M. Smith, H. J. Snaith, H. E. Assender, A. A. R. Watt, *Chem. Mater.* **2014**, *26*, 4004–4013.

[111] S. Xu, Synthesis of High Quality Low-Toxic Semiconductor Nanocrystals, Thesis, University of East Anglia, **2008**.

[112] J. van Embden, J. Jasieniak, D. E. Gómez, P. Mulvaney, M. Giersig, *Aust. J.*

*Chem.* **2007**, *60*, 457–471.

[113] T. Atsumi, B. Jeyadevan, Y. Sato, K. Tohji, *J. Magn. Magn. Mater.* **2007**, *310*, 2841–2843.

[114] R. Hergt, R. Hiergeist, I. Hilger, W. A. Kaiser, Y. Lapatnikov, S. Margel, U. Richter, *J. Magn. Magn. Mater.* **2004**, *270*, 345–357.

[115] A. E. Deatsch, B. A. Evans, *J. Magn. Magn. Mater.* **2014**, *354*, 163–172.

[116] K. Yan, P. Li, H. Zhu, Y. Zhou, J. Ding, J. Shen, Z. Li, Z. Xu, P. K. Chu, *RSC Adv.* **2013**, *3*, 10598–10618.

[117] S. H. Gage, B. D. Stein, L. Z. Nikoshvili, V. G. Matveeva, M. G. Sulman, E. M. Sulman, D. G. Morgan, E. Y. Yuzik-Klimova, W. E. Mahmoud, L. M. Bronstein, *Langmuir* **2013**, *29*, 466–473.

[118] F. Khan, G. Süss-Fink, *Eur. J. Inorg. Chem.* **2012**, *2012*, 727–732.

[119] S. Shylesh, V. Schünemann, W. R. Thiel, *Angew. Chem. Int. Ed.* **2010**, *49*, 3428–3459.

[120] M.-L. Chen, Y.-J. He, X.-W. Chen, J.-H. Wang, *Langmuir* **2012**, *28*, 16469–16476.

[121] J. Dobson, *Drug Dev. Res.* **2006**, *67*, 55–60.

[122] S.-H. Hu, C.-H. Tsai, C.-F. Liao, D.-M. Liu, S.-Y. Chen, *Langmuir* **2008**, *24*, 11811–11818.

[123] H. Na, I. Song, T. Hyeon, *Adv. Mater.* **2009**, *21*, 2133–2148.

[124] Y. Jun, Y.-M. Huh, J. Choi, J.-H. Lee, H.-T. Song, KimKim, S. Yoon, K.-S. Kim, J.-S. Shin, J.-S. Suh, et al., *J. Am. Chem. Soc.* **2005**, *127*, 5732–5733.

[125] C. F. G. C. Geraldes, S. Laurent, *Contrast Media Mol. Imaging* **2009**, *4*, 1–23.

[126] D. Mathew, R. Juang, *Chem. Eng. J.* **2007**, *129*, 51–65.

[127] R. Hergt, S. Dutz, M. Röder, *J. Phys. Condens. Matter* **2008**, *20*, 385214.

[128] M. Kallumadil, M. Tada, T. Nakagawa, M. Abe, P. Southern, Q. A. Pankhurst, *J. Magn. Magn. Mater.* **2009**, *321*, 1509–1513.

[129] J. W. J. Bergs, N. A. P. Franken, J. Haveman, E. D. Geijsen, J. Crezee, C. van Bree, *Int. J. Hyperthermia* **2007**, *23*, 329–341.

[130] X. Ji, R. Shao, A. M. Elliott, R. J. Stafford, E. Esparza-Coss, J. A. Bankson, G.

Liang, Z.-P. Luo, K. Park, J. T. Markert, et al., *J. Phys. Chem. C* **2007**, *111*, 6245–6251.

[131] X. Wang, J. Zhuang, Q. Peng, Y. Li, *Nature* **2005**, *437*, 121–124.

[132] S. Palchoudhury, Y. Xu, A. Rushdi, R. A. Holler, Y. Bao, *Chem. Commun.* **2012**, *48*, 10499–10501.

[133] C. Schieber, A. Bestetti, J. P. Lim, A. D. Ryan, T.-L. Nguyen, R. Eldridge, A. R. White, P. A. Gleeson, P. S. Donnelly, S. J. Williams, et al., *Angew. Chem. Int. Ed.* **2012**, *51*, 10523–10527.

[134] J. Luo, H. Wei, Q. Huang, X. Hu, H. Zhao, R. Yu, D. Li, Y. Luo, Q. Meng, *Chem. Commun.* **2013**, *49*, 3881–3883.

[135] D. B. Williams, C. B. Carter, *Transmission Electron Microscopy: A Textbook for Materials Science*, Springer, New York, **2011**.

[136] J. F. Watts, J. Wolstenholme, *An Introduction to Surface Analysis by XPS and AES*, Wiley-Blackwell, **2003**.

[137] M. Newville, *Rev. Mineral. Geochem.* **2014**, *78*, 33–74.

[138] E. A. V. Ebsworth, D. W. H. Rankin, S. Cradock, *Structural Methods in Inorganic Chemistry*, Wiley-Blackwell, Oxford Oxfordshire ; Boston, **1986**.

[139] M. McElfresh, *Fundamentals of Magnetism and Magnetic Measurements*, Quantum Design, **1994**.

[140] A. C. Jones, M. L. Hitchman, *Chemical Vapour Deposition: Precursors, Processes and Applications Edition*, Royal Society Of Chemistry, Cambridge, UK, **2008**.

[141] R. Quesada-Cabrera, C. Sotelo-Vazquez, J. C. Bear, J. A. Darr, I. P. Parkin, *Adv. Mater. Interfaces* **2014**, DOI 10.1002/admi.201400069.

[142] M. Lattuada, T. A. Hatton, *Langmuir* **2007**, *23*, 2158–2168.

[143] L. M. Bronstein, X. Huang, J. Retrum, A. Schmucker, M. Pink, B. D. Stein, B. Dragnea, *Chem. Mater.* **2007**, *19*, 3624–3632.

[144] P. D. Cozzoli, A. Kornowski, H. Weller, *J. Am. Chem. Soc.* **2003**, *125*, 14539–14548.

[145] Z. Zhang, S. Brown, J. B. M. Goodall, X. Weng, K. Thompson, K. Gong, S.

Kellici, R. J. H. Clark, J. R. G. Evans, J. A. Darr, *J. Alloys Compd.* **2009**, *476*, 451–456.

[146] R. G. Palgrave, I. P. Parkin, *J. Am. Chem. Soc.* **2006**, *128*, 1587–1597.

[147] J. R. Dethlefsen, A. Døssing, *Nano Lett* **2011**, *11*, 1964–1969.

[148] R. Golding, C. Harris, K. Jessop, W. Tennant, *Aust. J. Chem.* **1972**, *25*, 2567–2576.

[149] G. Hogarth, *Progress in Inorganic Chemistry: Volume 53*, **2005**.

[150] S. Xu, J. Ziegler, T. Nann, *J. Mater. Chem.* **2008**, *18*, 2653–2656.

[151] E. E. Lees, T.-L. Nguyen, A. H. A. Clayton, B. W. Muir, P. Mulvaney, *ACS Nano* **2009**, *3*, 2049–2049.

[152] M. Darbandi, R. Thomann, T. Nann, *Chem. Mater.* **2005**, *17*, 5720–5725.

[153] I. Pastoriza-Santos, J. Pérez-Juste, L. M. Liz-Marzán, *Chem Mater* **2006**, *18*, 2465–2467.

[154] A. Kafizas, I. P. Parkin, *J. Mater. Chem.* **2010**, *20*, 2157–2169.

[155] P.-Z. Li, A. Aijaz, Q. Xu, *Angew. Chem. Int. Ed.* **2012**, *51*, 6753–6756.

[156] C. R. Crick, I. P. Parkin, *J. Mater. Chem.* **2009**, *19*, 1074–1076.

[157] C. R. Crick, I. P. Parkin, *Chem. – Eur. J.* **2010**, *16*, 3568–3588.

[158] S. Yang, J. Ju, Y. Qiu, Y. He, X. Wang, S. Dou, K. Liu, L. Jiang, *Small* **2014**, *10*, 294–299.

[159] K. Li, X. Zeng, H. Li, X. Lai, H. Xie, *Mater. Lett.* **2014**, *120*, 255–258.

[160] Z. Sun, T. Liao, K. Liu, L. Jiang, J. H. Kim, S. X. Dou, *Small* **2014**, *10*, 3001–3006.

[161] E. Celia, T. Darmanin, E. Taffin de Givenchy, S. Amigoni, F. Guittard, *J. Colloid Interface Sci.* **2013**, *402*, 1–18.

[162] Y.-L. Zhang, H. Xia, E. Kim, H.-B. Sun, *Soft Matter* **2012**, *8*, 11217–11231.

[163] C. R. Crick, S. Ismail, J. Pratten, I. P. Parkin, *Thin Solid Films* **2011**, *519*, 3722–3727.

[164] B. Bhushan, Y. C. Jung, *Prog. Mater. Sci.* **2011**, *56*, 1–108.

[165] R. N. Wenzel, *Ind. Eng. Chem.* **1936**, *28*, 988–994.

[166] A. B. D. Cassie, S. Baxter, *Trans. Faraday Soc.* **1944**, *40*, 546–551.

[167] D. Quere, M. Reyssat, *Philos. Trans. R. Soc. Math. Phys. Eng. Sci.* **2008**, *366*, 1539–1556.

[168] B. J. Privett, J. Youn, S. A. Hong, J. Lee, J. Han, J. H. Shin, M. H. Schoenfisch, *Langmuir* **2011**, *27*, 9597–9601.

[169] J.-S. Chung, B. G. Kim, S. Shim, S.-E. Kim, E.-H. Sohn, J. Yoon, J.-C. Lee, *J. Colloid Interface Sci.* **2012**, *366*, 64–69.

[170] Y. Chen, Y. Zhang, L. Shi, J. Li, Y. Xin, T. Yang, Z. Guo, *Appl. Phys. Lett.* **2012**, *101*, 033701.

[171] Q. F. Xu, Y. Liu, F.-J. Lin, B. Mondal, A. M. Lyons, *ACS Appl. Mater. Interfaces* **2013**, *5*, 8915–8924.

[172] L. Cao, A. K. Jones, V. K. Sikka, J. Wu, D. Gao, *Langmuir* **2009**, *25*, 12444–12448.

[173] S. A. Kulinich, S. Farhadi, K. Nose, X. W. Du, *Langmuir* **2011**, *27*, 25–29.

[174] J. Wang, X. Chen, Y. Kang, G. Yang, L. Yu, P. Zhang, *Appl. Surf. Sci.* **2010**, *257*, 1473–1477.

[175] M. Zhang, S. Wang, C. Wang, J. Li, *Appl. Surf. Sci.* **2012**, *261*, 561–566.

[176] J. Ge, Y.-D. Ye, H.-B. Yao, X. Zhu, X. Wang, L. Wu, J.-L. Wang, H. Ding, N. Yong, L.-H. He, et al., *Angew. Chem. Int. Ed.* **2014**, *53*, 3612–3616.

[177] Y. Lu, S. Sathasivam, J. Song, F. Chen, W. Xu, C. J. Carmalt, I. P. Parkin, *J. Mater. Chem. A* **2014**, *2*, 11628–11634.

[178] C. R. Crick, J. A. Gibbins, I. P. Parkin, *J. Mater. Chem. A* **2013**, *1*, 5943–5948.

[179] P. M. Barkhudarov, P. B. Shah, E. B. Watkins, D. A. Doshi, C. J. Brinker, J. Majewski, *Corros. Sci.* **2008**, *50*, 897–902.

[180] X. Xu, Z. Zhang, F. Guo, J. Yang, X. Zhu, *Appl. Surf. Sci.* **2011**, *257*, 7054–7060.

[181] M. C. Draper, C. R. Crick, V. Orlickaite, V. A. Turek, I. P. Parkin, J. B. Edel, *Anal. Chem.* **2013**, *85*, 5405–5410.

[182] Y. Li, F. Liu, J. Sun, *Chem. Commun.* **2009**, 2730–2732.

[183] Q. An, W. Xu, L. Hao, Y. Fu, L. Huang, *J. Appl. Polym. Sci.* **2013**, *128*, 3050–3056.

[184] I. Yilgor, S. Bilgin, M. Isik, E. Yilgor, *Polymer* **2012**, *53*, 1180–1188.

[185] M. Yu, G. Gu, W.-D. Meng, F.-L. Qing, *Appl. Surf. Sci.* **2007**, *253*, 3669–3673.

[186] H. M. Shang, Y. Wang, S. J. Limmer, T. P. Chou, K. Takahashi, G. Z. Cao, *Thin Solid Films* **2005**, *472*, 37–43.

[187] S. A. Mahadik, M. S. Kavale, S. K. Mukherjee, A. V. Rao, *Appl. Surf. Sci.* **2010**, *257*, 333–339.

[188] Y. Zhao, Z. Xu, X. Wang, T. Lin, *Langmuir* **2012**, *28*, 6328–6335.

[189] B. Leng, Z. Shao, G. de With, W. Ming, *Langmuir* **2009**, *25*, 2456–2460.

[190] H. Zhou, H. Wang, H. Niu, A. Gestos, X. Wang, T. Lin, *Adv. Mater.* **2012**, *24*, 2409–2412.

[191] T. Liu, B. Yin, T. He, N. Guo, L. Dong, Y. Yin, *ACS Appl. Mater. Interfaces* **2012**, *4*, 4683–4690.

[192] X. L. Sun, Z. P. Fan, L. D. Zhang, L. Wang, Z. J. Wei, X. Q. Wang, W. L. Liu, *Appl. Surf. Sci.* **2011**, *257*, 2308–2312.

[193] J. T. Han, Y. Zheng, J. H. Cho, X. Xu, K. Cho, *J. Phys. Chem. B* **2005**, *109*, 20773–20778.

[194] X. Liu, B. Dai, L. Zhou, J. Sun, *J. Mater. Chem.* **2009**, *19*, 497–504.

[195] M. E. Buck, S. C. Schwartz, D. M. Lynn, *Chem. Mater.* **2010**, *22*, 6319–6327.

[196] X. Wang, Y. Shen, A. Xie, L. Qiu, S. Li, Y. Wang, *J. Mater. Chem.* **2011**, *21*, 9641–9646.

[197] I. Bernagozzi, S. Torrengo, L. Minati, M. Ferrari, A. Chiappini, C. Armellini, L. Toniutti, L. Lunelli, G. Speranza, *Colloid Polym. Sci.* **2012**, *290*, 315–322.

[198] Y. Ma, X. Cao, X. Feng, Y. Ma, H. Zou, *Polymer* **2007**, *48*, 7455–7460.

[199] J. Bravo, L. Zhai, Z. Wu, R. E. Cohen, M. F. Rubner, *Langmuir* **2007**, *23*, 7293–7298.

[200] M. Thieme, F. Streller, F. Simon, R. Frenzel, A. J. White, *Appl. Surf. Sci.* **2013**, *283*, 1041–1050.

[201] P. Pareo, G. L. De Gregorio, M. Manca, M. S. Pianesi, L. De Marco, F. Cavallaro, M. Mari, S. Pappadà, G. Ciccarella, G. Gigli, *J. Colloid Interface Sci.* **2011**, *363*, 668–675.

[202] X. Lu, L. Li, W. Zhang, C. Wang, *Nanotechnology* **2005**, *16*, 2233.

[203] E. Burkarter, C. K. Saul, F. Thomazi, N. C. Cruz, L. S. Roman, W. H. Schreiner, *Surf. Coat. Technol.* **2007**, *202*, 194–198.

[204] R. Weng, H. Zhang, X. Liu, *AIP Adv.* **2014**, *4*, 031327.

[205] N. D. Boscher, V. Vaché, P. Carminati, P. Grysan, P. Choquet, *J. Mater. Chem. A* **2014**, *2*, 5744–5750.

[206] J. Fresnais, J. P. Chapel, F. Poncin-Epaillard, *Surf. Coat. Technol.* **2006**, *200*, 5296–5305.

[207] H. C. Barshilia, N. Gupta, *Vacuum* **2014**, *99*, 42–48.

[208] N. Vandencasteele, B. Broze, S. Collette, C. De Vos, P. Viville, R. Lazzaroni, F. Reniers, *Langmuir* **2010**, *26*, 16503–16509.

[209] F. Henry, F. Renaux, S. Coppée, R. Lazzaroni, N. Vandencasteele, F. Reniers, R. Snyders, *Surf. Sci.* **2012**, *606*, 1825–1829.

[210] Y. Y. Yan, N. Gao, W. Barthlott, *Adv. Colloid Interface Sci.* **2011**, *169*, 80–105.

[211] H. Yan, K. Kurogi, H. Mayama, K. Tsujii, *Angew. Chem. Int. Ed.* **2005**, *44*, 3453–3456.

[212] K. Kurogi, H. Yan, H. Mayama, K. Tsujii, *J. Colloid Interface Sci.* **2007**, *312*, 156–163.

[213] H. Yan, Y. Hattori, J. Fujisato, N. Toshima, *Polym. J.* **2007**, *39*, 652–653.

[214] M. Nicolas, *J. Colloid Interface Sci.* **2010**, *343*, 608–614.

[215] M. Drábik, O. Polonskyi, O. Kylián, J. Čechvala, A. Artemenko, I. Gordeev, A. Choukourov, D. Slavínská, I. Matolínová, H. Biederman, *Plasma Process. Polym.* **2010**, *7*, 544–551.

[216] F. Wang, S. Yu, J. Ou, M. Xue, W. Li, *J. Appl. Phys.* **2013**, *114*, 124902–124902–6.

[217] K. K. S. Lau, J. A. Caulfield, K. K. Gleason, *Chem. Mater.* **2000**, *12*, 3032–3037.

[218] J. Wang, X. Song, R. li, J. Shen, G. Yang, H. Huang, *Appl. Surf. Sci.* **2012**, *258*, 9782–9785.

[219] C. R. Crick, I. P. Parkin, *Chem. Commun.* **2011**, *47*, 12059–12061.

[220] C. R. Crick, I. P. Parkin, *J. Mater. Chem. A* **2012**, *1*, 799–804.

[221] N. D. Boscher, C. J. Carmalt, I. P. Parkin, *J. Mater. Chem.* **2006**, *16*, 122–127.

[222] N. D. Boscher, C. J. Carmalt, I. P. Parkin, *Chem. Vap. Depos.* **2006**, *12*, 54–58.

[223] N. D. Boscher, C. S. Blackman, C. J. Carmalt, I. P. Parkin, A. G. Prieto, *Appl. Surf. Sci.* **2007**, *253*, 6041–6046.

[224] N. D. Boscher, C. J. Carmalt, I. P. Parkin, *Eur. J. Inorg. Chem.* **2006**, *2006*, 1255–1259.

[225] C. P. Stallard, M. M. Iqbal, M. M. Turner, D. P. Dowling, *Plasma Process. Polym.* **2013**, *10*, 888–903.

[226] H. Kong, J. Jang, *Langmuir* **2008**, *24*, 2051–2056.

[227] J. Song, H. Kang, C. Lee, S. H. Hwang, J. Jang, *ACS Appl. Mater. Interfaces* **2012**, *4*, 460–465.

[228] F. Caruso, A. Susha, M. Giersig, H. Möhwald, *Adv. Mater.* **1999**, *11*, 950.

[229] F. Caruso, M. Spasova, A. Susha, M. Giersig, R. A. Caruso, *Chem. Mater.* **2001**, *13*, 109–116.

[230] M. J. Joralemon, S. McRae, T. Emrick, *Chem. Commun.* **2010**, *46*, 1377–1393.

[231] G. Palui, F. Aldeek, W. Wang, H. Mattoussi, *Chem. Soc. Rev.* **2014**, DOI 10.1039/C4CS00124A.

[232] M. Fernández-Argüelles, A. Yakovlev, R. Sperling, C. Luccardini, S. Gaillard, A. Medel, *Nano Lett.* **2007**, *7*, 2613–2617.

[233] P. N. Manoudis, A. Tsakalof, I. Karapanagiotis, I. Zuburtikudis, C. Panayiotou, *Surf. Coat. Technol.* **2009**, *203*, 1322–1328.

[234] C. Liu, N. Wang, Y. Long, *Appl. Surf. Sci.* **2013**, *283*, 222–226.

[235] M. Y. Yüce, A. L. Demirel, *Eur. Phys. J. B* **2008**, *64*, 493–497.

[236] L. Cao, D. Gao, *Faraday Discuss.* **2010**, *146*, 57–65.

[237] P. Samyn, G. Schoukens, H. V. den Abbeele, L. Vonck, D. Stanssens, *J. Coat. Technol. Res.* **2011**, *8*, 363–373.

[238] M. D. McConnell, A. W. Bassani, S. Yang, R. J. Composto, *Langmuir* **2009**, *25*, 11014–11020.

[239] P. R. Gil, L. L. del Mercato, P. del Pino, A. Muñoz Javier, W. J. Parak, *Nano*

*Today* **2008**, *3*, 12–21.

[240] L. Hong, T. Pan, *J. Microelectromechanical Syst.* **2010**, *19*, 246–253.

[241] M. Motornov, R. Sheparovych, R. Lupitskyy, E. MacWilliams, S. Minko, *J. Colloid Interface Sci.* **2007**, *310*, 481–488.

[242] B. J. Sparks, E. F. T. Hoff, L. Xiong, J. T. Goetz, D. L. Patton, *ACS Appl. Mater. Interfaces* **2013**, *5*, 1811–1817.

[243] O. Kylián, M. Petr, A. Serov, P. Solař, O. Polonskyi, J. Hanuš, A. Choukourov, H. Biederman, *Vacuum* **2014**, *100*, 57–60.

[244] X. Y. Ling, I. Y. Phang, G. J. Vancso, J. Huskens, D. N. Reinhoudt, *Langmuir* **2009**, *25*, 3260–3263.

[245] Y. Rahmawan, L. Xu, S. Yang, *J. Mater. Chem. A* **2013**, *1*, 2955–2969.

[246] I. Karapanagiotis, P. N. Manoudis, A. Savva, C. Panayiotou, *Surf. Interface Anal.* **2012**, *44*, 870–875.

[247] H. Kong, J. Jang, *Chem. Commun.* **2006**, 3010–3012.

[248] D. H. Williams, I. Fleming, *Spectroscopic Methods in Organic Chemistry 5/e*, McGraw-Hill Higher Education, **1995**.

[249] R. Buonsanti, V. Grillo, E. Carlino, C. Giannini, M. L. Curri, C. Innocenti, C. Sangregorio, K. Achterhold, F. G. Parak, A. Agostiano, et al., *J. Am. Chem. Soc.* **2006**, *128*, 16953–16970.

[250] S. Kundu, A. Kafizas, G. Hyett, A. Mills, J. A. Darr, I. P. Parkin, *J. Mater. Chem.* **2011**, *21*, 6854–6863.

[251] A. Kafizas, I. P. Parkin, *J. Am. Chem. Soc.* **2011**, *133*, 20458–20467.

[252] A. E. Henkes, Y. Vasquez, R. E. Schaak, *J. Am. Chem. Soc.* **2007**, *129*, 1896–1897.

[253] M. F. Sarac, W.-C. Wu, J. B. Tracy, *Chem. Mater.* **2014**, DOI 10.1021/cm4034353.

[254] Z. Han, F. Qiu, R. Eisenberg, P. L. Holland, T. D. Krauss, *Science* **2012**, *338*, 1321–1324.

[255] P. Reiss, M. Protière, L. Li, *Small* **2009**, *5*, 154–168.

[256] R. Xie, U. Kolb, J. Li, T. Basché, A. Mews, *J. Am. Chem. Soc.* **2005**, *127*, 7480–

7488.

[257] D. V. Talapin, I. Mekis, S. Götzinger, A. Kornowski, O. Benson, H. Weller, *J. Phys. Chem. B* **2004**, *108*, 18826–18831.

[258] X. Peng, M. C. Schlamp, A. V. Kadavanich, A. P. Alivisatos, *J. Am. Chem. Soc.* **1997**, *119*, 7019–7029.

[259] A. Eychmüller, A. Mews, H. Weller, *Chem. Phys. Lett.* **1993**, *208*, 59–62.

[260] L. Cao, S. Huang, S. Lü, J. Lin, *J. Colloid Interface Sci.* **2005**, *284*, 516–520.

[261] H. Zhu, A. Prakash, D. N. Benoit, C. J. Jones, V. L. Colvin, *Nanotechnology* **2010**, *21*, 255604.

[262] X. Liu, Y. Jiang, F. Fu, W. Guo, W. Huang, L. Li, *Mater. Sci. Semicond. Process.* **2013**, *16*, 1723–1729.

[263] P. S. Nair, T. Radhakrishnan, N. Revaprasadu, G. Kolawole, P. O'Brien, *J. Mater. Chem.* **2002**, *12*, 2722–2725.

[264] W. Haiss, N. T. K. Thanh, J. Aveyard, D. G. Fernig, *Anal. Chem.* **2007**, *79*, 4215–4221.

[265] J. R. Lakowicz, *Principles of Fluorescence Spectroscopy 3rd*, Springer, **2006**.

[266] J. Hao, J. Zhou, C. Zhang, *Chem. Commun.* **2013**, *49*, 6346–6348.

[267] H. Sun, F. Zhang, H. Wei, B. Yang, *J. Mater. Chem. B* **2013**, *1*, 6485–6494.

[268] M. Protière, P. Reiss, *Small* **2007**, *3*, 399–403.

[269] P. M. Allen, W. Liu, V. P. Chauhan, J. Lee, A. Y. Ting, D. Fukumura, R. K. Jain, M. G. Bawendi, *J. Am. Chem. Soc.* **2010**, *132*, 470–471.

[270] H. Shen, X. Bai, A. Wang, H. Wang, L. Qian, Y. Yang, A. Titov, J. Hyvonen, Y. Zheng, L. S. Li, *Adv. Funct. Mater.* **2014**, *24*, 2367–2373.

[271] S. V. Kershaw, A. S. Susha, A. L. Rogach, *Chem. Soc. Rev.* **2013**, *42*, 3033–3087.

[272] L. Spanhel, M. Haase, H. Weller, A. Henglein, *J. Am. Chem. Soc.* **1987**, *109*, 5649–5655.

[273] K. R. Gopidas, M. Bohorquez, P. V. Kamat, *J. Phys. Chem.* **1990**, *94*, 6435–6440.

[274] P. V. Kamat, *J. Am. Chem. Soc.* **1991**, *113*, 9705–9707.

[275] P. V. Kamat, N. M. Dimitrijevic, *J. Phys. Chem.* **1989**, *93*, 4259–4263.

[276] P. Mulvaney, M. Giersig, A. Henglein, *J. Phys. Chem.* **1992**, *96*, 10419–10424.

[277] A. R. Kortan, R. Hull, R. L. Opila, M. G. Bawendi, M. L. Steigerwald, P. J. Carroll, L. E. Brus, *J. Am. Chem. Soc.* **1990**, *112*, 1327–1332.

[278] D. V. Talapin, A. L. Rogach, A. Kornowski, M. Haase, H. Weller, *Nano Lett.* **2001**, *1*, 207–211.

[279] M. A. Hines, P. Guyot-Sionnest, *J. Phys. Chem.* **1996**, *100*, 468–471.

[280] S. Kudera, M. Zanella, C. Giannini, A. Rizzo, Y. Li, G. Gigli, R. Cingolani, G. Ciccarella, W. Spahl, W. J. Parak, et al., *Adv. Mater.* **2007**, *19*, 548–552.

[281] H. Shen, H. Wang, Z. Tang, J. Z. Niu, S. Lou, Z. Du, L. S. Li, *CrystEngComm* **2009**, *11*, 1733–1738.

[282] D. V. Talapin, J. H. Nelson, E. V. Shevchenko, S. Aloni, B. Sadtler, A. P. Alivisatos, *Nano Lett.* **2007**, *7*, 2951–2959.

[283] M. Booth, R. Peel, R. Partanen, N. Hondow, V. Vasilca, L. J. C. Jeuken, K. Critchley, *RSC Adv.* **2013**, *3*, 20559–20566.

[284] Q. Zhao, X. Rong, H. Ma, G. Tao, *J. Mater. Sci.* **2013**, *48*, 2135–2141.

[285] J. Zhang, Y. Tang, K. Lee, M. Ouyang, *Science* **2010**, *327*, 1634–1638.

[286] Z. Pan, H. Zhang, K. Cheng, Y. Hou, J. Hua, X. Zhong, *ACS Nano* **2012**, *6*, 3982–3991.

[287] J. McBride, J. Treadway, L. C. Feldman, S. J. Pennycook, S. J. Rosenthal, *Nano Lett.* **2006**, *6*, 1496–1501.

[288] R. Xie, U. Kolb, T. Basché, *Small* **2006**, *2*, 1454–1457.

[289] L. Carbone, C. Nobile, M. De Giorgi, F. D. Sala, G. Morello, P. Pompa, M. Hytch, E. Snoeck, A. Fiore, I. R. Franchini, et al., *Nano Lett.* **2007**, *7*, 2942–2950.

[290] D. V. Talapin, R. Koeppe, S. Götzinger, A. Kornowski, J. M. Lupton, A. L. Rogach, O. Benson, J. Feldmann, H. Weller, *Nano Lett.* **2003**, *3*, 1677–1681.

[291] S. Park, B. L. Clark, D. A. Keszler, J. P. Bender, J. F. Wager, T. A. Reynolds, G. S. Herman, *Science* **2002**, *297*, 65–65.

[292] M. Ristov, G. Sinadinovski, I. Grozdanov, M. Mitreski, *Thin Solid Films* **1989**, *173*, 53–58.

[293] W. K. Bae, K. Char, H. Hur, S. Lee, *Chem. Mater.* **2008**, *20*, 531–539.

[294] H. Lee, M. Wang, P. Chen, D. R. Gamelin, S. M. Zakeeruddin, M. Grätzel, M. K. Nazeeruddin, *Nano Lett.* **2009**, *9*, 4221–4227.

[295] L. D. Nyamen, A. A. Nejo, V. S. R. Pullabhotla, P. T. Ndifon, M. A. Malik, J. Akhtar, P. O'Brien, N. Revaprasadu, *Polyhedron* **2014**, *67*, 129–135.

[296] N. Revaprasadu, M. A. Malik, P. O'Brien, G. Wakefield, *J. Mater. Res.* **1999**, *14*, 3237–3240.

[297] M. A. Malik, N. Revaprasadu, P. O'Brien, *Chem. Mater.* **2001**, *13*, 913–920.

[298] M. A. Malik, P. O'Brien, N. Revaprasadu, *Chem. Mater.* **2002**, *14*, 2004–2010.

[299] T. Trindade, P. O'Brien, *J. Mater. Chem.* **1996**, *6*, 343–347.

[300] M. Green, P. O'Brien, *Chem. Commun.* **1998**, 2459–2460.

[301] H. Wang, H. Nakamura, M. Uehara, Y. Yamaguchi, M. Miyazaki, H. Maeda, *Adv. Funct. Mater.* **2005**, *15*, 603–608.

[302] W. Luan, H. Yang, N. Fan, S.-T. Tu, *Nanoscale Res. Lett.* **2008**, *3*, 134.

[303] D. Dorfs, A. Eychmüller, *Nano Lett.* **2001**, *1*, 663–665.

[304] A. Mews, A. Eychmüller, M. Giersig, D. Schooss, H. Weller, *J. Phys. Chem.* **1994**, *98*, 934–941.

[305] J. Zhao, M. A. Holmes, F. E. Osterloh, *ACS Nano* **2013**, *7*, 4316–4325.

[306] Y. Liu, P. Wu, *ACS Appl. Mater. Interfaces* **2013**, *5*, 3362–3369.

[307] P. V. Kamat, J. A. Christians, J. G. Radich, *Langmuir* **2014**, *30*, 5716–5725.

[308] R. Ullah, J. Dutta, *J. Hazard. Mater.* **2008**, *156*, 194–200.

[309] T. Nann, S. K. Ibrahim, P.-M. Woi, S. Xu, J. Ziegler, C. J. Pickett, *Angew. Chem. Int. Ed.* **2010**, *49*, 1574–1577.

[310] J. Zuloaga, E. Prodan, P. Nordlander, *Nano Lett.* **2009**, *9*, 887–891.

[311] Q. Zhang, H.-Y. Wang, X. Jia, B. Liu, Y. Yang, *Nanoscale* **2013**, *5*, 7175–7183.

[312] M. Warrier, M. K. F. Lo, H. Monbouquette, M. A. Garcia-Garibay, *Photochem. Photobiol. Sci.* **2004**, *3*, 859–863.

[313] H. Li, R. Liu, S. Lian, Y. Liu, H. Huang, Z. Kang, *Nanoscale* **2013**, *5*, 3289–3297.

[314] K. M. Gattas-Asfura, R. M. Leblanc, *Chem. Commun.* **2003**, 2684.

[315] A. W. Wills, M. S. Kang, A. Khare, W. L. Gladfelter, D. J. Norris, *ACS Nano* **2010**, *4*, 4523–4530.

[316] O. Ehlert, A. Osvet, M. Batentschuk, A. Winnacker, T. Nann, *J. Phys. Chem. B* **2006**, *110*, 23175–23178.

[317] E. Kuçur, W. Bücking, R. Giernoth, T. Nann, *J. Phys. Chem. B* **2005**, *109*, 20355–20360.

[318] W. Q. Peng, G. W. Cong, S. C. Qu, Z. G. Wang, *Opt. Mater.* **2006**, *29*, 313–317.

[319] V. Babentsov, J. Riegler, J. Schneider, O. Ehlert, T. Nann, M. Fiederle, *J. Cryst. Growth* **2005**, *280*, 502–508.

[320] E. Kuçur, J. Riegler, G. A. Urban, T. Nann, *J. Chem. Phys.* **2003**, *119*, 2333.

[321] D. H. Son, S. M. Hughes, Y. Yin, A. P. Alivisatos, *Science* **2004**, *306*, 1009–1012.

[322] M. H. B. Stowell, T. M. McPhillips, D. C. Rees, S. M. Soltis, E. Abresch, G. Feher, *Science* **1997**, *276*, 812–816.

[323] R. H. Nagaraj, D. R. Sell, M. Prabhakaram, B. J. Ortwerth, V. M. Monnier, *Proc. Natl. Acad. Sci.* **1991**, *88*, 10257–10261.

[324] P.-Y. Liu, N. Jiang, J. Zhang, X. Wei, H.-H. Lin, X.-Q. Yu, *Chem. Biodivers.* **2006**, *3*, 958–966.

[325] M. A. Tasdelen, Y. Yagci, *Tetrahedron Lett.* **2010**, *51*, 6945–6947.

[326] T. W. Clarkson, L. Magos, *Crit. Rev. Toxicol.* **2006**, *36*, 609–662.

[327] R. M. Cornell, U. Schwertmann, *The Iron Oxides: Structure, Properties, Reactions, Occurrences and Uses*, John Wiley & Sons, **2006**.

[328] Y. M. Wang, X. Cao, G. H. Liu, R. Y. Hong, Y. M. Chen, X. F. Chen, H. Z. Li, B. Xu, D. G. Wei, *J. Magn. Magn. Mater.* **2011**, *323*, 2953–2959.

[329] O. V. Melnikov, O. Y. Gorbenko, M. N. &Mcaron;arkelova, A. R. Kaul, V. A. Atsarkin, V. V. Demidov, C. Soto, E. J. Roy, B. M. Odintsov, *J. Biomed. Mater. Res. A* **2009**, *91A*, 1048–1055.

[330] S. E. Barry, *Int. J. Hyperthermia* **2008**, *24*, 451–466.

[331] X. Wen, J. Yang, B. He, Z. Gu, *Curr. Appl. Phys.* **2008**, *8*, 535–541.

[332] P. Guardia, J. Pérez-Juste, A. Labarta, X. Batlle, L. M. Liz-Marzán, *Chem.*

*Commun.* **2010**, *46*, 6108.

[333] M. V. Kovalenko, M. I. Bodnarchuk, R. T. Lechner, G. Hesser, F. Schäffler, W. Heiss, *J. Am. Chem. Soc.* **2007**, *129*, 6352–6353.

[334] L. M. Bronstein, J. E. Atkinson, A. G. Malyutin, F. Kidwai, B. D. Stein, D. G. Morgan, J. M. Perry, J. A. Karty, *Langmuir* **2011**, *27*, 3044–3050.

[335] Y. V. Kolen'ko, M. Bañobre-López, C. Rodríguez-Abreu, E. Carbó-Argibay, A. Sailsman, Y. Piñeiro-Redondo, M. F. Cerqueira, D. Y. Petrovykh, K. Kovnir, O. I. Lebedev, et al., *J. Phys. Chem. C* **2014**, *118*, 8691–8701.

[336] C. Ravikumar, R. Bandyopadhyaya, *J. Phys. Chem. C* **2011**, *115*, 1380–1387.

[337] L. Zhou, B. He, J. Huang, *ACS Appl. Mater. Interfaces* **2013**, *5*, 8678–8685.

[338] T. Hyeon, S. S. Lee, J. Park, Y. Chung, H. B. Na, *J. Am. Chem. Soc.* **2001**, *123*, 12798–12801.

[339] J. Park, E. Lee, N.-M. Hwang, M. Kang, S. C. Kim, Y. Hwang, J.-G. Park, H.-J. Noh, J.-Y. Kim, J.-H. Park, et al., *Angew. Chem. Int. Ed.* **2005**, *44*, 2872–2877.

[340] B. Bateer, C. Tian, Y. Qu, S. Du, T. Tan, R. Wang, G. Tian, H. Fu, *CrystEngComm* **2013**, *15*, 3366–3371.

[341] T.-D. Nguyen, *Nanoscale* **2013**, *5*, 9455–9482.

[342] W. Cai, J. Wan, *J. Colloid Interface Sci.* **2007**, *305*, 366–370.

[343] R. H. Gonçalves, C. A. Cardoso, E. R. Leite, *J. Mater. Chem.* **2010**, *20*, 1167–1172.

[344] C. Qin, C. Li, Y. Hu, J. Shen, M. Ye, *Colloids Surf. Physicochem. Eng. Asp.* **2009**, *336*, 130–134.

[345] Z. Li, Q. Sun, M. Gao, *Angew. Chem. Int. Ed.* **2005**, *44*, 123–126.

[346] Y. Wang, S. Maksimuk, R. Shen, H. Yang, *Green Chem.* **2007**, *9*, 1051–1056.

[347] P. D. McNaughter, J. C. Bear, D. C. Steytler, A. G. Mayes, T. Nann, *Angew. Chem. Int. Ed.* **2011**, *50*, 10384–10387.

[348] H. Qu, H. Ma, A. Riviere, W. Zhou, C. J. O'Connor, *J Mater Chem* **2012**, *22*, 3311–3313.

[349] C.-H. Ho, C.-P. Tsai, C.-C. Chung, C.-Y. Tsai, F.-R. Chen, H.-J. Lin, C.-H. Lai, *Chem. Mater.* **2011**, *23*, 1753–1760.

[350] D. A. J. Herman, P. Ferguson, S. Cheong, I. F. Hermans, B. J. Ruck, K. M. Allan, S. Prabakar, J. L. Spencer, C. D. Lendrum, R. D. Tilley, *Chem. Commun.* **2011**, *47*, 9221–9223.

[351] K. Abdulwahab, M. A. Malik, P. O'Brien, K. Govender, C. A. Muryn, G. A. Timco, F. Tuna, R. E. P. Winpenny, *Dalton Trans.* **2012**, *42*, 196–206.

[352] K. O. Abdulwahab, M. A. Malik, P. O'Brien, G. A. Timco, F. Tuna, C. A. Muryn, R. E. P. Winpenny, R. A. D. Pattrick, V. S. Coker, E. Arenholz, *Chem. Mater.* **2014**, *26*, 999–1013.

[353] M. R. Buck, A. J. Biacchi, R. E. Schaak, *Chem. Mater.* **2014**, DOI 10.1021/cm4041055.

[354] W. Jiang, Y. Wu, B. He, X. Zeng, K. Lai, Z. Gu, *J. Colloid Interface Sci.* **2010**, *347*, 1–7.

[355] J. Lynch, J. Zhuang, T. Wang, D. LaMontagne, H. Wu, Y. C. Cao, *J. Am. Chem. Soc.* **2011**, *133*, 12664–12674.

[356] Y. Ohno, K. Tomita, Y. Komatsubara, T. Taniguchi, K. Katsumata, N. Matsushita, T. Kogure, K. Okada, *Cryst. Growth Des.* **2011**, *11*, 4831–4836.

[357] A. Ito, H. Honda, T. Kobayashi, *Cancer Immunol. Immunother.* **2006**, *55*, 320–328.

[358] M. W. Dewhirst, *Int. J. Hyperthermia* **2008**, *24*, 449–450.

[359] Y. Bae, R. A. Buresh, T. P. Williamson, T.-H. H. Chen, D. Y. Furgeson, *J. Controlled Release* **2007**, *122*, 16–23.

[360] P. Cherukuri, E. S. Glazer, S. A. Curley, *Adv. Drug Deliv. Rev.* **2010**, *62*, 339–345.

[361] L. Lartigue, C. Innocenti, T. Kalaivani, A. Awwad, M. del M. Sanchez Duque, Y. Guari, J. Larionova, C. Guérin, J.-L. G. Montero, V. Barragan-Montero, et al., *J. Am. Chem. Soc.* **2011**, *133*, 10459–10472.

[362] L. A. Thomas, L. Dekker, M. Kallumadil, P. Southern, M. Wilson, S. P. Nair, Q. A. Pankhurst, I. P. Parkin, *J. Mater. Chem.* **2009**, *19*, 6529.

[363] V. Chandra, J. Park, Y. Chun, J. W. Lee, I.-C. Hwang, K. S. Kim, *ACS Nano* **2010**, *4*, 3979–3986.

[364] J. A. Young, *J. Chem. Educ.* **2002**, *79*, 24.

[365] B. M. Wetherbee, P. D. Nichols, *Comp. Biochem. Physiol. B Biochem. Mol. Biol.* **2000**, *125*, 511–521.

[366] M. J. Bakes, P. D. Nichols, *Comp. Biochem. Physiol. B Biochem. Mol. Biol.* **1995**, *110*, 267–275.

[367] J. C. Cain, R. A. Morton, *Biochem. J.* **1955**, *60*, 274–283.

[368] I. Batista, M. L. Nunes, *Fish. Res.* **1992**, *14*, 329–334.

[369] A. Shavel, B. Rodriguez-González, M. Spasova, M. Farle, L. Liz-Marzán, *Adv. Funct. Mater.* **2007**, *17*, 3870–3876.

[370] C. Yang, J. Wu, Y. Hou, *Chem. Commun.* **2011**, *47*, 5130–5141.

[371] J. Cheon, N.-J. Kang, S.-M. Lee, J.-H. Lee, J.-H. Yoon, S. J. Oh, *J. Am. Chem. Soc.* **2004**, *126*, 1950–1951.

[372] L. J. Berchmans, M. Myndyk, K. L. Da Silva, A. Feldhoff, J. Šubrt, P. Heitjans, K. D. Becker, V. Šepelák, *J. Alloys Compd.* **2010**, *500*, 68–73.

[373] R. Dom, R. Subasri, K. Radha, P. H. Borse, *Solid State Commun.* **2011**, *151*, 470–473.

[374] Y. Sahoo, H. Pizem, T. Fried, D. Golodnitsky, L. Burstein, C. N. Sukenik, G. Markovich, *Langmuir* **2001**, *17*, 7907–7911.

[375] T. Pellegrino, L. Manna, S. Kudera, T. Liedl, D. Koktysh, A. L. Rogach, S. Keller, J. Rädler, G. Natile, W. J. Parak, *Nano Lett.* **2004**, *4*, 703–707.

[376] F. Dumestre, B. Chaudret, C. Amiens, M. Respaud, P. Fejes, P. Renaud, P. Zurcher, *Angew. Chem. Int. Ed.* **2003**, *42*, 5213–5216.

[377] T. M. Whitney, P. C. Searson, J. S. Jiang, C. L. Chien, *Science* **1993**, *261*, 1316–1319.

[378] A. Ghosh, S. Chakrabarti, U. C. Ghosh, *Chem. Eng. J.* **2014**, *248*, 18–26.

## Appendix

List of publications associated with this thesis

[1] **"Superhydrophobic Photocatalytic Surfaces through Direct Incorporation of Titania Nanoparticles into a Polymer Matrix by Aerosol Assisted Chemical Vapor Deposition" -** C. R. Crick, **J. C. Bear**, A. Kafizas, I. P. Parkin, *Adv. Mater.* **2012**, *24*, 3505–3508.

[2] **"A general method for the incorporation of nanoparticles intosuperhydrophobic films by aerosol assisted chemical vapour deposition" -** C. R. Crick, **J. C. Bear**, P. Southern, I. P. Parkin, *J. Mater. Chem. A* **2013**, *1*, 4336–4344.

[3] **"Copper-Doped CdSe/ZnS Quantum Dots: Controllable Photoactivated Copper(I) Cation Storage and Release Vectors for Catalysis" - J. C. Bear**, N. Hollingsworth, P. D. McNaughter, A. G. Mayes, M. B. Ward, T. Nann, G. Hogarth, I. P. Parkin, *Angew. Chem. Int. Ed.* **2014**, *53*, 1598–1601.

[4] "**Doping Group IIB metal ions into quantum dot shells via the one-pot decomposition of metal-dithiocarbamates**" - **J.C. Bear**, N. Hollingsworth, A.R. Roffey, P.D. McNaughter, A. G. Mayes, M.S. Frost, D.E. Whitehead, T.J. Macdonald, T. Nann, W.H. Ng, A.J. Kenyon, G. Hogarth and I.P. Parkin, *Adv. Opt. Mater.* **2014** (Manuscript in preparation).

[5] "FD 175: **Iron oxide nanoparticles for magnetic hyperthermia from readily available materials**" - **J.C. Bear**, B. Yu, C. Blanco-Andujar, P. D. McNaughter, P. Southern, M-K. Mafina, Q. A. Pankhurst and I. P. Parkin, *Faraday Discuss.* **2014** (accepted).